



# New Technology for Imaging Atmospheric Cherenkov Telescopes and Underwater Neutrino Detectors

Richard James White

*Submitted in accordance with the requirements for  
the degree of Doctor of Philosophy.*

September, 2007

The University of Leeds

School of Physics & Astronomy

The candidate confirms that the work submitted is his own and that appropriate credit  
has been given where reference has been made to the work of others.

This copy has been supplied on the understanding that it is copyright material  
and that no quotation from the thesis may be published without proper acknowledgment.



# Abstract

The study of processes that take place in physical conditions which cannot be reproduced in Earth-based laboratories is of great importance to physics. Underwater Neutrino Detectors (UNDs) and Imaging Atmospheric Cherenkov Telescopes (IACTs) probe the cosmos searching for neutrinos and VHE  $\gamma$ -rays from distant accelerators hoping to find an answer to an age long riddle - the origin of cosmic rays (CR).

The origin of CRs is discussed in this work and the need for next generation Cherenkov detectors in  $\gamma$ -ray and neutrino astrophysics introduced. New technology is developed to facilitate larger, more sensitive, cost effective IACTs and extend the window of opportunity with current detectors to include new, exotic, physics such as the detection of direct Cherenkov light and intensity interferometry. Instrumentation is developed for use in the IACT array VERITAS to enable high-speed topological triggering of candidate images and a future high density camera. In VERITAS the telescopes are connected at the hardware level to an array trigger system for the stereoscopic detection of  $\gamma$ -ray initiated extensive air showers. This approach greatly reduces the number of background images recorded by the instrument and consequently reduces the detector energy threshold and improves the sensitivity. A Digital Asynchronous Transceiver (DAT) is presented for the distribution of array level signals within VERITAS. The resulting increase in system performance is reported using observations of the  $\gamma$ -ray standard candle, the Crab Nebula. The application of the technology developed here is not limited to IACTs and, due to the similar exploitation of Cherenkov light, the applicability to the future UNDs are also considered.



*Physics is very muddled again at the moment; it is much too hard for me anyway, and I wish I were a movie comedian or something like that and had never heard anything about physics!*

(Wolfgang Pauli)



# Contents

List of figures . . . . .	xx
List of tables . . . . .	xxi
List of Abbreviations . . . . .	xxiii
Personal Contribution . . . . .	xxvii
Acknowledgements . . . . .	xxix
Preface . . . . .	xxxii
<b>1 The Origin of Cosmic Rays and the Age of Cherenkov Telescopes</b>	<b>1</b>
1.1 The Origin of Cosmic Rays . . . . .	2
1.2 $\gamma$ -rays and Neutrino Production Mechanisms . . . . .	8
1.3 The Detection of Astrophysical $\gamma$ -Rays and Neutrinos . . . . .	10
1.4 Current Generation Cherenkov Telescopes . . . . .	14
1.5 The Next Generation of IACTs and UNDs . . . . .	23
1.6 New Technology for IACTs and UNDs . . . . .	27
<b>2 Extensive Air Showers, Cherenkov Radiation and the Imaging Atmospheric Technique</b>	<b>29</b>
2.1 The Development of Extensive Air Showers . . . . .	30
2.2 Cherenkov Radiation . . . . .	33
2.3 The Imaging Atmospheric Cherenkov Technique . . . . .	40

<b>3</b>	<b>VERITAS</b>	<b>53</b>
3.1	Introduction to VERITAS . . . . .	54
3.2	Mechanical Structure and Optics . . . . .	55
3.3	The Camera . . . . .	57
3.4	Trigger Chain . . . . .	60
3.5	Data Acquisition . . . . .	70
3.6	Calibration . . . . .	75
3.7	Data Analysis and Simulations . . . . .	77
<b>4</b>	<b>Transmission of Fast Analogue Signals Over Optical Fibre</b>	<b>79</b>
4.1	Introduction . . . . .	79
4.2	VCSELs . . . . .	81
4.3	Link Specification . . . . .	83
4.4	Implementation . . . . .	84
4.5	Selection and Qualification . . . . .	90
4.6	Performance . . . . .	94
4.7	Temperature Compensation . . . . .	113
4.8	Conclusion . . . . .	116
<b>5</b>	<b>High-Speed Topological Triggering with FPGAs</b>	<b>119</b>
5.1	Introduction . . . . .	119
5.2	FPGA Basics . . . . .	123
5.3	An FPGA Based Topological Trigger . . . . .	124
5.4	The Splitter Input Card with Spartan-II (SSICXv1) . . . . .	125
5.5	The Splitter Input Card with Virtex-4 (SSICXv2) . . . . .	128
5.6	The Signal Splitter Output Card with Virtex-4 (SSOCX) . . . . .	135

5.7	Conclusions . . . . .	136
<b>6</b>	<b>Parallel Distribution of Asynchronous Optical Signals</b>	<b>139</b>
6.1	Introduction to the DAT . . . . .	140
6.2	Specification . . . . .	141
6.3	The Principle of Exclusive OR Encoding . . . . .	142
6.4	The Beginning Stages of the DAT . . . . .	144
6.5	Developing the DAT . . . . .	148
6.6	FPGA Design . . . . .	154
6.7	Performance . . . . .	163
6.8	The Integration of the DAT within VERITAS . . . . .	179
6.9	Dynamic Phase Shift . . . . .	180
6.10	Conclusions . . . . .	183
<b>7</b>	<b>Benefits of Stereoscopic Observations with a Hardware Array Trigger</b>	<b>187</b>
7.1	Introduction . . . . .	188
7.2	The Crab Nebula . . . . .	188
7.3	Observations . . . . .	189
7.4	Simulations . . . . .	193
7.5	Telescope Calibration . . . . .	194
7.6	Image Reconstruction . . . . .	196
7.7	Shower Reconstruction . . . . .	198
7.8	$\gamma$ -Ray Selection . . . . .	201
7.9	Background Estimation and Signal Extraction . . . . .	206
7.10	Summary and Conclusions . . . . .	218
<b>8</b>	<b>Conclusions and Outlook</b>	<b>223</b>

<b>Appendices</b>	<b>232</b>
<b>A Technical Details of the Optical Link Test Setup and Equipment</b>	<b>233</b>
A.1 The Bias Current Scan Test Setup . . . . .	233
A.2 Optical Link Test Setup and Equipment . . . . .	235
<b>B Details of the Analogue Fibre Noise Calculations</b>	<b>237</b>
B.1 Thermal Noise . . . . .	237
B.2 Shot Noise . . . . .	238
B.3 Relative Intensity Noise . . . . .	238
B.4 Noise Analysis . . . . .	239
<b>C Details of the Commercial Hardware used in the DAT</b>	<b>241</b>
C.1 The Parallel Optical Link . . . . .	241
C.2 The MPO Cabling System . . . . .	243
<b>D Details of the DAT Test Setup</b>	<b>247</b>
<b>E The Components of Jitter</b>	<b>249</b>
E.1 Duty Cycle Distortion (DCD) Jitter . . . . .	249
E.2 Data Dependent Jitter (DDJ) . . . . .	250
E.3 Periodic Jitter (PJ) . . . . .	252
E.4 Dual-Data-Rate Flip-Flop Jitter (DDRFFJ) . . . . .	255
<b>F Further DAT Results</b>	<b>257</b>
<b>G Integration of the DAT within VERITAS</b>	<b>271</b>
G.1 Onsite Installation and Evaluation of the DAT . . . . .	271
G.2 Software for the DAT . . . . .	274



# List of Figures

1.1	The measured CR spectral energy distribution. . . . .	3
1.2	H.E.S.S. $\gamma$ -ray images of (a) RXJ1713.7-3946 and (b) RXJ0852.0-4622. . .	5
1.3	(a) A simple model of an AGN. (b) The plasma jet emanating from the core of M87. . . . .	7
1.4	UND detection principle. . . . .	13
1.5	The sensitivity of several high-energy IACT observatories produced using Monte-Carlo $\gamma$ -ray simulations and appropriate detector simulations. . .	15
1.6	World map showing the current major IACTs and UNDs. . . . .	17
1.7	(a) An artists impression of ANTARES 12-string detector. (b) A downward going muon reconstructed from ANTARES data. . . . .	22
2.1	Schematic illustration of the development of an EAS. . . . .	31
2.2	The development of 100 GeV $\gamma$ -ray (left) and 100 GeV proton (right) induced air showers in Corsika. . . . .	34
2.3	A charged particle travelling through a medium at a non-relativistic velocity, (a), and relativistic velocity, (b), emitting Cherenkov light, (c). . .	35
2.4	Cherenkov emission spectrum. . . . .	37
2.5	Cherenkov light pools at ground level from showers initiated by (a) a 300 GeV $\gamma$ -ray and (b) a 500 GeV proton. . . . .	37

2.6	Relation between $E_{th}^{Che}$ , $R_c$ and the height $h$ of emission. . . . .	38
2.7	(a) Cherenkov radiation cones, (b) resulting photon distribution and (c) modified lateral distribution. . . . .	39
2.8	EAS-camera image mapping. . . . .	42
2.9	Cherenkov images captured by a VERITAS telescope. . . . .	49
3.1	Images of VERITAS . . . . .	54
3.2	The VERITAS four telescope array. . . . .	55
3.3	(a) The azimuth and (b) elevation residuals. (c) Average mirror reflectivity as a function of wavelength. . . . .	56
3.4	(a) A close-up view of the hexagonal VERITAS mirror facets. (b) The VERITAS PSF. . . . .	59
3.5	(a) The VERITAS camera box. (b) The VERITAS light cones. . . . .	59
3.6	The simplified VDAQ and trigger chain. . . . .	61
3.7	The working principle of (a) a traditional threshold discriminator, and (b) the VERITAS CFD. . . . .	63
3.8	VERITAS PST pixel mapping. . . . .	64
3.9	The VERITAS SS crate. . . . .	65
3.10	The VERITAS SSIC and SSOC. . . . .	65
3.11	The transit times of signals through the T2 signal splitter crate. . . . .	67
3.12	A VERITAS PST CAMAC module. . . . .	68
3.13	(a) VERITAS FADC trace. (b) VERITAS bias curve for two different topological trigger configurations. . . . .	73
3.14	Illustration of VERITAS dead time. . . . .	74
3.15	(a) The single pe response for one PMT at standard operating gain. (b) The charge distribution across the camera for a CR event. . . . .	76

4.1	Typical structure of a VCSEL. . . . .	82
4.2	ZL60052 VCSELs. . . . .	85
4.3	(a) A female E2000 connector. (b) A schematic of the ball lens integrated into the ZL60052 VCSEL. . . . .	86
4.4	The first, (a), and second, (b), optical link transmitter prototypes. . . . .	86
4.5	The VERITAS camera box. . . . .	87
4.6	A schematic drawing of the second transmitter. . . . .	88
4.7	Circuit diagram for the second transmitter. . . . .	89
4.8	The 12 channel optical link receiver with 1 E2000 input connector and 2 Lemo output connectors per channel, from the top, (a), and front, (b). . . . .	91
4.9	Results of the bias current scan tests on two HFE4085-321 VCSELs as used in the MAGIC telescope. . . . .	93
4.10	Results of the bias current scan tests on two of the ZL60052 VCSELs used in this work. . . . .	94
4.11	(a) $I_l$ as a function of $V_l$ . (b) $P_l$ , as a function of $I_l$ . . . . .	95
4.12	VCSEL effective resistance as a function of $I_b$ , (a), and temperature, (b). . . . .	96
4.13	(a) A close up of Figure 4.11(b). (b) $I_t$ as a function of temperature. . . . .	97
4.14	(a) The fibre coupled slope efficiency, $s_l$ . (b) $s_l$ as a function of temperature. . . . .	98
4.15	The stability of the output pulse area at room temperature, (a), and as the temperature is varied according to a sine-wave profile (red)(b). . . . .	99
4.16	(a) Linearity and (b) SNR of the analogue optical link. . . . .	101
4.17	(a) Linearity of the analogue optical link as varies with temperature, (a), and $I_b$ , (b). . . . .	105
4.18	Gain of the analogue optical link as a function of $I_b$ . . . . .	106

4.19	(a) RMS noise measurements compared to the relative components of the noise model. (b) RMS noise measurements and model calculations for various temperatures and values of $I_b$ . . . . .	107
4.20	Frequency response of the analogue optical link. . . . .	109
4.21	Transit time across the analogue optical link whilst varying the transmitter temperature, then the fibre temperature compared to that across coax. . . . .	111
4.22	(a) Pulses before and after transmission over the optical link and coax. (b) The FWHM and $T_r$ of a pulse after transmission over coax. and the optical link as a function of the coax., fibre and transmitter temperature. . . . .	112
4.23	(a) The Fourier spectrum of a 10 MHz input and output signal. (b) The power of the first two harmonics and the THD. . . . .	113
4.24	(a) $A_{out}$ as a function of $I_b$ at 0°C, 20°C and 40°C. (b) $A_{out}$ as a function of $I_b$ and temperature. . . . .	114
4.25	(a) The required $I_b$ to maintain a constant gain. (b) The stability of $A_{out}$ with and without temperature compensation. . . . .	115
5.1	Examples of the 2, 3 and 4-fold patterns required to trigger the PST logic. . . . .	121
5.2	VERITAS T2 bias curves for varying CFD output widths. . . . .	122
5.3	The control structure of the intended FPGA based PST system. . . . .	125
5.4	(a) The SSICXv1 with Spartan-II FPGA. (b) SSICXv1 onsite test setup. . . . .	126
5.5	The top layer of the PCB routing for the SSICXv2. . . . .	128
5.6	(a) The SSICXv2 with onboard Virtex-4 FPGA. (b) A close up of the Virtex-4 FPGA. . . . .	129
5.7	(a) SSICXv2 trigger efficiency as a function of input pulse width. (b) Accidental trigger rate as a function of input pulse width. . . . .	132
5.8	(a) SSICXv2 trigger efficiency as a function of input pulse frequency. (b) Accidental trigger rate as a function of input pulse frequency. . . . .	134

5.9	The SSOCX prototype board. . . . .	135
6.1	(a) A female MPO 12 channel fibre optic connector. (b) The PAROLI 2 <sup>®</sup> transmitter and receiver. . . . .	141
6.2	XOR encoding principle. . . . .	143
6.3	The DAT -V1 VME modules (centre) seated in a CERN V430 VME crate.144	
6.4	Distribution of arrival times for a 1 MHz, 200 ns wide pulse at the DAT- RX channel 3 output relative to the input. . . . .	146
6.5	The first DAT-V2 pair. . . . .	150
6.6	Functional diagram of the DAT modules depicting the data flow from transmitter to receiver including signal standards. . . . .	151
6.7	The DAT-V2 boards with MPO terminated cable connected causing the PAROLI to become unseated from the DB. . . . .	153
6.8	The modified front panel and DB design for the DAT-V3 modules with rubber bend-protection on the fibre removed by Sachsenkabel. . . . .	154
6.9	ISE schematic of the XOR decoding, see Section 6.6.2. . . . .	155
6.10	FPGA data routing. . . . .	156
6.11	Resulting LVDS FPGA output waveforms from a simulation of the DAT- TX. . . . .	158
6.12	FPGA clock routing. . . . .	159
6.13	Response of the DDRFF. . . . .	160
6.14	Capabilities of the Spartan-3 DCM. . . . .	161
6.15	Illustration of the DCM fixed phase shift attribute. . . . .	162
6.16	The DCM reset circuit. . . . .	163
6.17	The components of jitter. . . . .	165
6.18	The dual-Dirac model. . . . .	167

6.19	(a) The DC% dependence of the encoded clock on the input state of the data. (b) The DC% when the input data is held high vs. low. . . . .	170
6.20	An example of the jitter distribution in arrival times from a 1 MHz, 200 ns wide input pulse over 2 m of fibre optic cable. . . . .	171
6.21	$T_{ar}$ histograms with dual-Dirac fits for channel 9 of the prototype pair of DAT-V2 modules connected with 2 m of fibre. . . . .	171
6.22	$T_{cc}$ of channel 5 of the DAT-V2 prototype modules relative to channel 2, (a), and 8, (b). . . . .	175
6.23	Distribution of arrival times (a), and p-p jitter (b), for 25 measurements spaced equally across 50 minutes . . . . .	177
6.24	(a) Short term temperature stability of the VME crate. (b) Peak-to-peak jitter as a function of VME crate temperature. . . . .	178
6.25	Long term stability of the DAT modules as captured by the oscilloscope, (a), and added to a histogram, (b). . . . .	179
6.26	Onsite installation of the DAT-V2 modules. . . . .	180
6.27	(a) The DAT-RX DCM dynamic phase shift setup. (b) The resulting relationship between PHASE_SHIFT and the DAT-RX channel 1 output. . . . .	181
6.28	(a) Figure 6.29(b) on a smaller time-scale. (b) The centre of the dynamic phase-shift alignment window. . . . .	182
7.1	(a) Composite image of the Crab Nebula. (b) The Crab Nebula spectrum. . . . .	189
7.2	Array trigger rate for a Crab Nebula data run taken during good (a) and bad (b) weather. . . . .	190
7.3	Bias curves taken with T1, T2 and T3. . . . .	192
7.4	System trigger rate as a function of the array trigger coincidence window. . . . .	193
7.5	(a) The distribution of the mean relative gains for all channels of T1. (b) The average trace arrival time over all channels before and after calibration. . . . .	195

7.6	The image of a CR in the VERITAS T1 camera (a) before and (b) after cleaning. . . . .	197
7.7	Geometric definition of the parameters used to describe the image of a Cherenkov shower in the focal plane of an IACT. . . . .	198
7.8	Image parameter distributions. . . . .	200
7.9	(a) Simple source location reconstruction using intersection of axes. (b) Simple core location reconstruction using intersection of axes. . . . .	201
7.10	Reconstructed core locations on the ground for (a) a two telescopes and (b) a three telescopes, obtained with hardware array trigger Wobble runs. . . . .	203
7.11	The length/size distributions for parameterised data before cuts. . . . .	205
7.12	Single telescope $\alpha$ distribution from analysis with EventDisplay. . . . .	207
7.13	Significance maps, 2D analysis, single telescope, Pairs mode. . . . .	209
7.14	Software Stereo $\theta^2$ distribution, Pairs mode. . . . .	210
7.15	Significance map and distribution, 2D analysis, two telescopes, Pairs mode, software array trigger. . . . .	211
7.16	Schematic illustration of (a) reflected region background mode and (b) the Ring Background Model. . . . .	213
7.17	$\theta^2$ distribution, stereo observations, Wobble mode, T1 and T2, hardware array trigger. . . . .	214
7.18	2D map of the reconstructed arrival directions after $\gamma$ -ray selection cuts, T1 and T2, hardware array trigger . . . . .	215
7.19	Integrated signal (a) and background (b) maps resulting from the RBM applied to Figure 7.18, two telescopes, hardware stereo. . . . .	216
7.20	Excess map, RBM, two telescopes, hardware stereo. . . . .	216
7.21	Significance map and distribution, 2D analysis, two telescopes, Wobble mode, hardware stereo. . . . .	217

7.22	$\theta^2$ distribution, three-telescopes, Wobble mode, T1, T2 and T3, hardware array trigger (2/3), reflected region background estimation model. . . . .	218
7.23	Significance map and distribution, 2D analysis, three telescopes, Wobble mode, hardware array trigger. . . . .	219
8.1	Kifune Plot: The total number of sources detected as a function of time for X-ray, $\gamma$ -ray and VHE $\gamma$ -ray astronomy. . . . .	224
A.1	The bias current scan test setup. . . . .	234
A.2	The optical link test setup. . . . .	235
C.1	(a) PAROLI demo. boards. (b) 12 channel MPO to E2000 fanout cable. . . . .	242
C.2	The pinning of the Spartan-3 XC3S50 FPGA. . . . .	245
D.1	The test setup used to evaluate the performance of the DAT modules. . . . .	248
E.1	DCD: The encoding and decoding of a falling data edge for several possible clock-to-data alignments at the transmitter. . . . .	251
E.2	DCD: The encoding and decoding of a falling data edge for several more clock-to-data alignments at the transmitter continued from Figure E.2. . . . .	253
E.3	Scenarios for the possible occurrence of crosstalk induced jitter. . . . .	255
F.1	<b>Arrival Times, 2 m of Fibre.</b> . . . .	259
F.2	<b>Arrival Times, 60 m of Fibre.</b> . . . .	260
F.3	<b>Pulse Width Distortion, 2 m of Fibre.</b> . . . .	262
F.4	<b>Pulse Width Distortion, 60 m of Fibre.</b> . . . .	263
F.5	<b>Channel-to-Channel Jitter Relative to Channel 2, 2 m of Fibre.</b> . . . .	265
F.6	<b>Channel-to-Channel Jitter Relative to Channel 2, 60 m of Fibre.</b> . . . .	266
F.7	<b>Channel-to-Channel Jitter Relative to Channel 8, 2 m of Fibre.</b> . . . .	269

**F.8 Channel-to-Channel Jitter Relative to Channel 8, 60 m of Fibre.** 270

G.1 (a) The DAT layout between T1 and T2 using E2000 patch-panels. (b)  
The alternative of using 12 channel MPO ribbon-fibre cables. . . . . 273

G.2 Skew across the 30 fibres between T1 and T2 after termination in the  
E2000 patch panels. . . . . 274

# List of Tables

6.1	The functionality of an XOR gate. . . . .	143
6.2	Channel by channel performance of the DAT-V1 over a 2 m fibre optic link. . . . .	148
6.3	DDRFF functionality. . . . .	159
6.4	$T_{ar}$ , DAT-V2 over 2 m of fibre. . . . .	172
6.5	$T_{pw}$ , DAT-V2 over 2 m of fibre. . . . .	173
6.6	$T_{cc2}$ , DAT-V2 over 2 m of fibre. . . . .	176
7.1	The image parameters used in this analysis. . . . .	199
7.2	Quality cuts used to reject poorly reconstructed events. . . . .	202
7.3	The non-optimised single telescope selection cuts used in this work. . . . .	203
7.4	The non-optimised scaled $\gamma$ -ray selection cuts used in this work for stereo- data analysis. . . . .	204
7.5	Analysis results for all Crab Nebula observations in this work . . . . .	219
F.1	<b>Arrival Times, 60 m of Fibre.</b> . . . .	258
F.2	<b>Pulse Width Distortion, 60 m of Fibre.</b> . . . .	261
F.3	<b>Channel-to-Channel Jitter Relative to Channel 2, 60 m of Fibre.</b> . . . .	264
F.4	<b>Channel-to-Channel Jitter Relative to Channel 8, 2 m of Fibre.</b> . . . .	267
F.5	<b>Channel-to-Channel Jitter Relative to Channel 8, 60 m of Fibre.</b> . . . .	268



# List of Abbreviations

ARS	Analogue Ring Sampler
a.s.l.	Above Sea Level
AGN	Active Galactic Nuclei
ANTARES	Astronomy with a Neutrino Telescope and Abyss Enviromental Research
BGA	Ball Gate Array
CFD	Constant Fraction Discriminator
C.L.	Confidence Level
cPCI	Compact Peripheral Component Interface
CR	Cosmic Ray
CSR	Control Status Register
CTA	Cherenkov Telescope Array
DAQ	Data Aquisition
DAT	Digital Asynchronous Transceiver
DB	Daughter Board
DBR	Distributed Bragg Reflector
d.c.	Digital Counts
DC%	Duty Cycle
DDRFF	Double Data Rate Flip Flop
DIL	Dual InLine
GND	Ground
GRB	Gamma-Ray Burst
EAS	Extensive Air Shower
EC	External Compton
ECL	Emitter Coupled Logic

EM	Electromagnetic
FADC	Flash Analogue to Digital Converter
FiFo	First in First out
FoV	Field of View
FPGA	Field Programmable Gate Array
FWHM	Full Width at Half Maximum
$\gamma$ -ray	Gamma Ray
HE	High Energy
H.E.S.S.	High Energy Stereoscopic System
HV	High Voltage
IC	Inverse Compton
I/O	Input/Output
HG	High Gain
IACT	Imaging Atmospheric Cherenkov Telescope
KM3NeT	Kilometer Cubed Neutrino Telescope
L1	VERITAS Level 1 trigger
L2	VERITAS Level 2 trigger
L3	VERITAS Level 3 trigger
LA	Logic Analyser
LED	Light Emitting Diode
LCM	Local Control Module
LG	Low Gain
LVPECL	Low Voltage Positive Emitter Coupled Logic
LVDS	Low Voltage Differential Signal
MAGIC	Major Atmospheric Gamma Imaging Cherenkov
MSL	Mean Scaled Length
MSO	Mixed Signal Oscilloscope
MSW	Mean Scaled Width

NECL	Negative Emitter Coupled Logic
NSB	Night Sky Background
OM	Optical Module
opamp	Operational Amplifier
PAROLI	Parallel Optical Link
PCB	Printed Circuit Board
PDF	Probability Density Function
PDM	Pulse Delay Module
pe	Photoelectron
PECL	Positive Emitter Coupled Logic
PMT	Photo-Multiplier Tube
PSF	Point Spread Function
PST	Pattern Selection Trigger
SAM	Swift Analogue Memory
SCM	String Control Module
SS	Signal Splitter
SSC	Synchrotron Self-Compton
SSIC	SS Input Card
SSICX	SSIC with Xilinx FPGA
SSOC	SS Output Card
SSOCX	SSOC with Xilinx FPGA
SNR	Signal to Noise Ratio
S.N.R.	Supernovae Remnant
T1, T2, T3, T4	VERITAS telescopes 1, 2, 3 and 4
THD	Total Harmonic Distortion
TTL	Transistor-Transistor Logic
UND	Under water Neutrino Detector
VDAQ	VERITAS DAQ

VEGAS	VERitas Gamma-ray Analysis Suite
VERITAS	Very Energetic Radiation Imaging Telescope Array System
VHDL	Very High Speed Integrated Circuit Hardware Description Language
VHE	Very High Energy
VCSEL	Vertical Cavity Surface Emitting Laser
XOR	Exclusive OR

# Personal Contribution

The initial stage of development for the analogue optical link were done with the help of Isobel Bond. The later concepts used for the single channel transmitter prototype were imagined and then designed by myself and Joachim Rose. I developed the design and produced a circuit diagram which was used by Hytec Electronics to build the prototype. The tests performed in Munich were done completely by myself, but I am hugely grateful to David Paneque for his help with the test setup (and especially with LabView).

I designed and tested all the high-speed FPGA based trigger prototypes used in Chapter 5. Furthermore I was responsible for the wire-wrapping and timing measurements for the signal splitter crate used in the second VERITAS telescope. I joined the development of the DAT modules detailed in Chapter 6 after the design of the DAT-V1 modules and was jointly responsible for their testing. I played a key role in the design of the DAT-V2 modules, and was responsible for FPGA pinning. I was solely responsible for the FPGA development and the testing of the DAT-V2 and DAT-V3 modules, which took up a large proportion of this PhD. I was also responsible for the integration of the modules within VERITAS and this occupied the majority of a second site visit. I served as a "DAT expert" during observing and was on-call to help with any technical problems. I developed the VME software used to run the DATs based on the structure developed by Scott Wakely and Liz Hays for VDAQ. The work done on the DAT modules has been written up as a journal paper and an ICRC contribution and has been presented in talks and posters at collaboration meetings and several other conferences. I performed all of the analysis in Chapter 8 with both EventDisplay and VEGAS. The results obtained with multiple telescopes connected with a hardware implemented array trigger were compared to those obtained by other collaboration members and posted on the internal VERITAS website.



# Acknowledgements

I would like to thank my supervisor, Joachim Rose, for the (stream-of-consciousness) contributions to all that I have done over the past few years. I am indebted to Stella Bradbury for the invaluable help, support and cakes that she has provided during my time in the department. I would like to thank Lee Thompson for his support and encouragement from Sheffield, and everyone in the office in Leeds who have endured my obsession with instrumentation and ever increasingly grumpy demeanour over the months preceding the submission of this work.

I am hugely grateful for the support I have received from the VERITAS collaboration and would, in particular, like to thank Liz Hays for her time and patience with all that is *VME*. I am grateful to my parents for the support, financial and otherwise, during the last four years. I would like to thank Jamie Holder for everything he has taught me, including who would win between a badger and a whale in a fight (you see it all depends on the environment: underwater the whale has a clear advantage, but on land it could go either way). Renato Pallassini on for putting me up (and putting up with me) in the final five weeks of this work. Paul Ogden, Andrew Price and Richard Oliver for the constant supply of advice and resistors. Peter Marshall for not only indulging me, but helping to make the ideas a reality. Kurt Baldwin, Michael Daniel and everyone else who has bravely read past this page and provided much appreciated feedback. Chris and Jan for welcome breaks away from physics in Plymouth. Jerry, Paddy and Dan for keeping me, at least mildly, sane over all these years and Sonya Bezboraiah for her ever brutal methods of bringing me back down to Earth.

My eternal gratitude and love to Nichola, who has advised, cajoled, criticized, tended, and tolerated me during the course of my research.

And finally this list would not be complete without thanking Jack Klugman for regular doses of morality in an increasingly immoral world: "Don't you see Sam?! He died

eating radioactive tuna fish! We gotta warn everyone in the neighbourhood!".

# Preface

The origin of CRs is an unresolved enigma at the heart of astrophysics. At the centre of the problem lies a huge dynamic range of fluxes spanning decades of energy, from 100 GeV to over 100 EeV. In Chapter 1 the current state of the problem is outlined and the role of IACTs and UNDs introduced. CR production is accompanied by the generation of  $\gamma$ -rays and neutrinos. Hence, ground-based  $\gamma$ -ray astronomy provides an indirect test of CR accelerator models and crucially the ability to detect super nova remnants (SNR) with energies of  $\sim 50$  GeV to  $\sim 100$  TeV, unreachable with space-based detectors, such as GLAST. A positive neutrino signal from a source would provide definitive evidence for the acceleration of CRs, and so UNDs will play a crucial role in the determination and characterisation of their origin.

The Cherenkov imaging technique is now recognised as one of the most sensitive tools for astroparticle physics and has become a valuable astronomical discipline in its own right. IACTs aim to reconstruct the direction and energy of an incident  $\gamma$ -ray by imaging the Cherenkov light resulting from a particle shower following an interaction with an air nucleus in the upper atmosphere. Chapter 2 describes the nature of these showers and the detection principle. A number of new instruments utilising the latest innovations in technology are coming into operation and offer unprecedented performance and a wealth of scientific results. In addition to the origin of CRs, IACTs aim to address issues including the nature of jets in Active Galactic Nuclei (AGN), the intensity of the cosmic infrared background light, the nature of dark matter and  $\gamma$ -ray bursts.

The first stage of the VERITAS project will use four telescopes at a site in Arizona. Each telescope will consist of a 12 m diameter segmented reflector instrumented with a 499 element PMT imaging camera. The first of these telescopes became operational in February 2005. One year later, two telescopes were operating in stereo, in part due to technology developed in this work. Two trips were made to the VERITAS site to

install hardware and observe with the telescopes during the course of this work and VERITAS-4 saw first light in April 2007.

Even with the improvements in sensitivity provided by new instruments like VERITAS, the fundamental limits of the technique have not yet been reached. New technology for the current and next generation of IACTs will extend the energy range to overlap with space-based detectors, increase the sensitivity to probe weaker and more distant sources, and increase the angular resolution to map in detail the morphology of galactic SNR. Furthermore, new technology may be utilised to adapt IACTs to operate in parallel with normal  $\gamma$ -ray observations to observe exotic physics. This could include: the measurement of the CR spectrum through so called direct Cherenkov light, the discovery of evaporating black holes, intensity interferometry, and even the optical search for extraterrestrial life.

The key to ground based  $\gamma$ -ray astronomy is the use of the atmosphere as a detector medium vastly larger than can be created artificially. This aspect is also common to UNDs, where the expanse of the medium greatly surpasses that of manmade detectors such as Super Kamiokande. UNDs rely on the Cherenkov light from a muon resulting from the interaction of a muon neutrino with matter to reconstruct the neutrino energy and direction. The detection principle is describe in Chapter 1. In this work technology developed primarily for IACTs is also evaluated for use in the proposed UND, KM3NeT. Towards the end of this work the KM3NeT collaboration began a three year design study for the construction of a cubic kilometre detector in the Mediterranean.

The VERITAS cameras contains 499 pixels, each individually readout over coaxial cable. For future detectors higher density cameras of  $\sim 2000$  pixels will be essential to increase the field of view (FoV) and angular resolution. The current, coaxial, scheme is not suitable for such an extrapolation due to the high weight of the cables and the limited space within the telescope frame to route them. VCSELs are low power, low cost, readily available laser diodes capable of transmitting nanosecond rise-time signals over hundreds of meters of optical fibre with virtually no attenuation. They are therefore a natural candidate for use within the readout system of next generation IACT arrays, and UNDs. In chapter 4 a VCSEL based analogue transmission scheme is developed.

The results indicate improvements, both in the available VCSELs and the transmission circuit over existing schemes.

Cherenkov telescopes typically use multi-level trigger systems to reject fluctuations in background light. In the case of VERITAS there exists a high speed topological telescope level Pattern Selection Trigger (PST), requiring a coincidence between an amount of neighbouring pixels in a camera, and an array level trigger, requiring a coincidence between several telescopes. In chapter 3 the VERITAS trigger system is described in detail and in chapter 5 the idea of high-speed topological triggering is expanded upon by implementing the PST functions within FPGA based prototypes.

The VERITAS array trigger requires the distribution of multiple, fast, digital pulses between telescopes to enable the stereoscopic detection of  $\gamma$ -ray initiated extensive air showers observed by several telescopes simultaneously. This problem is tackled in Chapter 6, where a VME implemented Digital Asynchronous Transceiver (DAT), is presented. The DAT modules rely on parallel optical links and PAROLI modules, which uses VCSELs to transmit pulses encoded via FPGA implemented combinatorial logic. In this way asynchronous pulses may be sent in parallel without introducing dead time into the system. The solution introduces a minimal jitter into the trigger chain and has been installed in VERITAS between all four telescopes.

The DAT modules connect the VERITAS telescopes at the hardware level, and as such enable the use of the array trigger. This in turn reduces the background of the instrument and allows one to decrease the energy threshold and improve the sensitivity of the system. The benefits of using a hardware implemented array trigger are assessed in Chapter 7, where single telescope data is compared to that taken with multiple telescopes using both a software and hardware implemented array trigger by analysing observations of the Crab Nebula taken during the commissioning stages of VERITAS.

Conclusions are drawn as to the impact of these technologies within VERITAS, future IACT arrays, UNDs and other areas of astroparticle physics in Chapter 8. The performance and limitations of this work are summarised and possible areas for future development are highlighted.



# Chapter 1

## The Origin of Cosmic Rays and the Age of Cherenkov Telescopes

---

The origin of the relativistic Cosmic Rays (CRs) bombarding the earth isotropically over ten decades of energy has remained an outstanding mystery since Victor Hess first reported the phenomena in 1912 [81]. The astrophysical acceleration of these particles is widely believed to be accompanied by the production of both Very High Energy (VHE)  $\gamma$ -rays and neutrinos. Imaging Atmospheric Cherenkov Telescopes (IACTs) and Underwater Neutrino Detectors (UNDs)<sup>1</sup> are essential in the determination of the origin of CRs and the nature of their progenitors.

In this chapter the measured CR spectrum is described and the potential acceleration sites of CRs are introduced. The  $\gamma$ -ray and neutrino production mechanisms associated with CRs are outlined before the detection methods for these multi-messenger particles are presented and the principles of underwater neutrino and atmospheric Cherenkov detection discussed. The current and next generation IACTs and UNDs are described and the new technology developed in this work is introduced.

---

<sup>1</sup>UND will also be used to refer to neutrino detectors under the ice.

## 1.1 The Origin of Cosmic Rays

### 1.1.1 The Spectrum and Composition of Cosmic Rays

The measured CR spectral energy distribution, shown in Figure 1.1, extends to over 100 EeV, well above the energies attainable in terrestrial particle accelerators. CRs therefore may offer a unique insight into extreme physical processes. Two spectral breaks can be distinguished in the otherwise smooth spectrum: the *knee* at  $10^{15}$  eV and the *ankle* at  $10^{18}$  eV. It is now widely accepted that CRs below the knee are produced within our galaxy (see Section 1.1.2). The origin of the knee and the source of CRs at higher energies is still uncertain (see Section 1.1.3).

Complex galactic magnetic fields deflect CRs randomly from their paths trapping them within the galaxy for a time. The effect is dependent on the gyro-radius of the particle, which is proportional to the particle's energy and inversely proportional to the particle's charge and the galactic magnetic field strength. At higher energies protons have increasing gyro-radii and therefore escape the galaxy more easily. Protons will escape more easily than heavier nuclei such as iron at a given energy. In the widely used leaky box model CRs propagate within the galaxy through a homogeneous interstellar medium (ISM) with a constant probability of escape [62].

The composition of CRs is similar to that of matter in the solar system, consisting mainly of high energy nuclear particles, predominantly protons, but also helium nuclei ( $\alpha$ -particles) and a small abundances of heavier nuclei [115]. There is also a small amount ( $\sim 1\%$ ) of electrons and a tiny  $\gamma$ -ray constituent. The largest composition differences between the measured CR flux and that at the source can be attributed to spallation in the ISM. Nuclei such as Li, Be and B are enhanced in the CR flux by the disintegration of the CNO group. The measured ratio of such secondary to primary CRs indicates the amount of matter traversed and the time spent in the galaxy.

### 1.1.2 Galactic Cosmic Rays and Supernovae Remnants

The lack of features in the energy spectrum up to  $10^{15}$  eV strongly suggests a common origin for these CRs. It is currently believed that diffuse shock acceleration in shell-type S.N.R.s within the galaxy is responsible for the observed flux until at least the knee [85].

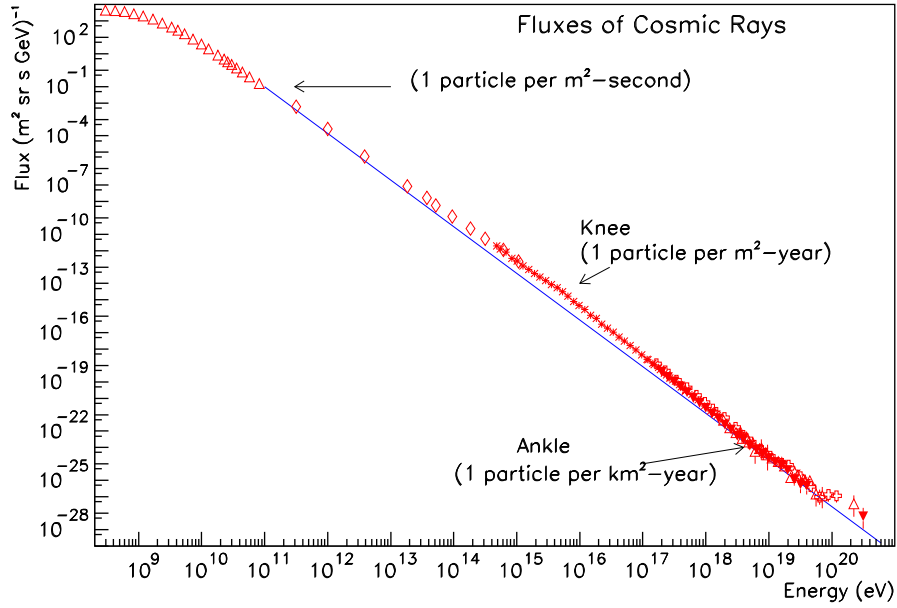


Figure 1.1: *The measured CR spectral energy distribution from [46] containing data from seven different sources. The solid (blue) line shows a constant power law for comparison.*

Under this scenario VHE  $\gamma$ -rays and neutrinos would be produced by the interaction of CRs with dense local matter.

S.N.R.s may be divided into two groups: plerions and shell-type. In shell type S.N.R.s a large shell of hot material is produced by the expanding shock and a ring structure is observed due to limb brightening. Plerions, or pulsar wind nebulae (PWN), are powered by a relativistic particle outflow of electrons and positrons from a central rapidly rotating neutron star (pulsar). The line between plerions and shell-type S.N.R. is blurred and gives rise to a third, composite, category which appear plerion-like and shell-like depending upon the wavelength at which they are observed.

In plerions particles are accelerated to non-thermal energies in the termination shock between the relativistic outflow of electrons from the pulsar and the outer nebula. The pulsars within plerions are highly magnetised and should exhibit a pulsed component of radiation together with an steady component from the shock region. The detection of steady emission from the Crab Nebula as the first VHE  $\gamma$ -ray source in 1989 by the Whipple collaboration [173] confirmed these predictions. The Crab Nebula, as the brightest stable VHE  $\gamma$ -ray source, remains the best-studied object of this class of par-

ticle accelerators and will be considered in more detail in Chapter 7. Although claims have been made for a hadronic component at the high energy end of the spectrum, the energy distribution of photons from plerions is typically well described by leptonic models, and they do not present a promising site for the origin of CRs.

Predictions of the CR flux in the shell-type S.N.R.s from first order Fermi acceleration [59] (see [30] and [54] for a comprehensive review) match the measured CR spectrum well. Furthermore shell-type S.N.R. may be the only class of galactic object with sufficient power to supply the observed energy density of the cosmic radiation. After estimating the energy loss and leakage from the galaxy Ginzburg [66] suggests a total power of  $\sim 10^{33}$  W to source the galactic CRs. Supernovae in our galaxy are estimated to occur approximately every 50 years producing typically  $10^{43}$  J of kinetic energy. The usable power output from supernovae is therefore  $10^{34}$  W. Thus only  $\sim 10\%$  of the supernovae energy must go directly into CR acceleration to provide the required energy. The recent discovery and morphological mapping of shell-like TeV emission from RXJ1713.7-3946 [12] and RXJ0852.0-4622 [11] indeed confirm that shell-type S.N.R. are capable of multi-TeV particle acceleration at their shock-fronts, see Figure 1.2. Such VHE emission may be due to the acceleration of electrons, via Inverse Compton (IC) scattering or to hadron acceleration, via pion decay (see Section 1.2). The shape of the  $\gamma$ -ray spectrum strongly indicates such a hadronic origin. Observations of synchrotron emission in the X-ray band have provided strong evidence for the existence of 100 TeV electrons in shell-type S.N.R.s, see for example [107]. In both cases large uncertainties on crucial parameters, like the magnetic field strength and the effective ambient density, hamper decisive conclusions. Furthermore even if these specific S.N.R.s do accelerate CRs, the question remains to what extent? And are S.N.R.s as a class responsible for CR acceleration within the galaxy? More S.N.R. and their surroundings must be observed to link emission regions of VHE  $\gamma$ -rays to regions of known density. The measured  $\gamma$ -ray spectrum has been used to estimate the expected neutrino flux in next generation UNDs. Such predictions remain upper-limits, relying heavily on assumptions about the relative leptonic/hadronic contribution to the measured  $\gamma$ -ray spectrum. The challenge remains to disentangle the leptonic contribution to the measured VHE  $\gamma$ -ray flux, from that potentially due to hadrons.

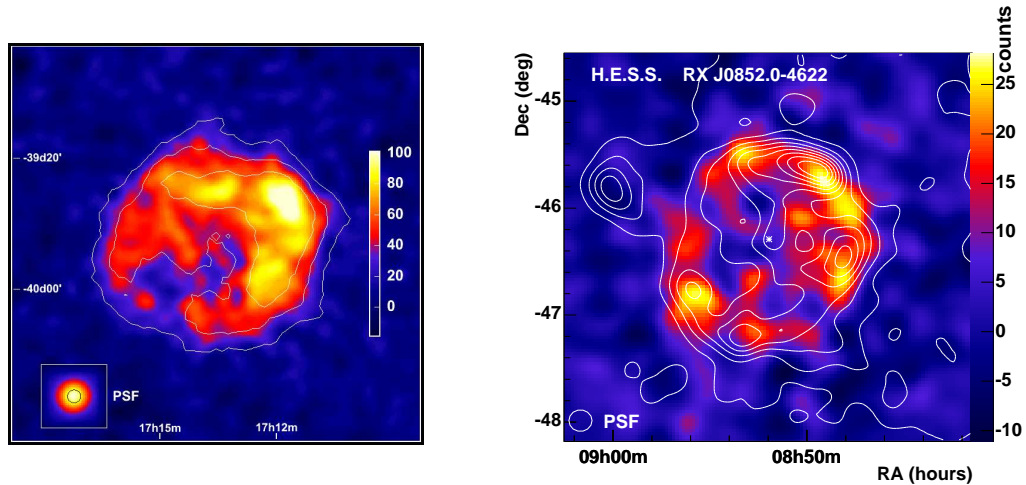


Figure 1.2: (a) H.E.S.S.  $\gamma$ -ray image of RXJ1713.7-3946 from [10]. The linear colour scale is in units of excess counts. The white contour lines indicate the significance of the different features, the levels are linearly spaced and correspond to 5, 10, and 15  $\sigma$ . (b) H.E.S.S.  $\gamma$ -ray image of RXJ0852.0-4622 from [11]. The lines denote equidistant contours of smoothed ( $\sigma = 0.1^\circ$ ) X-ray data from the ROSAT All Sky Survey.

### 1.1.3 Acceleration beyond the Knee

Diffuse shock acceleration in S.N.R.s can only reasonably explain the origin of CRs to a maximum energy  $\sim 3 \times 10^{15}$  eV. Beyond this the fluxes of the individual components from S.N.R. should turn down more steeply than indicated by the total measured flux in Figure 1.1. After a slight steepening at the knee the total flux looks deceptively smooth to at least  $10^{17}$  eV. The CR flux beyond the knee becomes dominated by heavier nuclei such as carbon and iron. The extended gradual fall-off between the knee and the ankle raises many questions and an overall scheme which credibly addresses and unifies acceleration below, across and beyond the knee remains elusive.

Above the ankle at  $3 \times 10^{18}$  eV the spectrum flattens again and the composition becomes dominated by protons. This strongly suggests an extragalactic origin, since even the heaviest nuclei of this energy could not be contained by the galactic magnetic field. If CRs above the ankle are extragalactic then they can be expected to exhibit a characteristic cut-off due to photo-pion production with the Cosmic Microwave Background (CMB), see Section 1.1.4.

Active Galactic Nuclei (AGN) are extragalactic CR candidates. In AGN the central

region is observed to outshine the billions of stars in the galaxy itself. Emission is observed to be bright at all wavelengths and the luminosity is highly variable. Radio loud AGN exhibit long jets of radio-emitting material originating from a very compact nucleus, commonly believed to be a super-massive black hole. Figure 1.3(a) shows a simplified AGN model. The radio emission is attributed to synchrotron radiation (see Section 1.2) from high energy electrons in magnetic fields.

Radio-loud AGN provided the most exciting, and unexpected, results for the first generation of ground-based  $\gamma$ -ray telescopes. The detection of strong, rapidly variable emission from six of these objects (including Mkr421, [150] and Mkr501, [151]) led to the definition of a new class of "TeV blazar", believed to be AGN with the axis of their jets oriented very closely with the line of sight. This unique orientation Doppler boosts the  $\gamma$ -ray luminosity along the direction of the jet increasing the probability of detection. Off-axis radio-loud AGN with their primary jet at  $>20^\circ$  to the observer, simply known as radio galaxies are potentially promising sources of CRs. Radio galaxies exhibit jets with spectacular lobes far outside the visible part of the galaxy, with radio emission thousands of times that of a normal galaxy, indicating the presence of relativistic particles. The nearby radio galaxy M87 (Figure 1.3(b)), which contains a super-massive black hole of mass  $2 - 3 \times 10^9 M_\odot$  and with jet angle  $30-35^\circ$  has been detected at VHE by the HEGRA collaboration [7] at a marginal significance of  $4.1\sigma$ . The limited number of excess events makes it difficult to draw conclusions from the spectral analysis. To fully assess the possibility of a hadronic emission mechanism within AGN jets requires time dependent observations of the spectral energy distribution in X-rays,  $\gamma$ -rays and ultimately a detection or upper limit in neutrinos.

Starburst galaxies are galaxies harbouring regions of intensive star formation, associated with a dense ISM and an unusually high supernova rate. Such regions are expected to have extremely high levels of CR production, given the theorised relation between S.N.R. and CR acceleration, and are a promising CR alternative to AGN. The CR interaction rate may produce a detectable level of VHE  $\gamma$ -rays. Diffuse emission from the starburst galaxy NGC 253 was reported by the CANGAROO collaboration [97] in excess of 500 GeV. A far more sensitive search using the H.E.S.S. array [18] reported upper limits far below the flux estimates of CANGAROO. Searches by the Whipple-

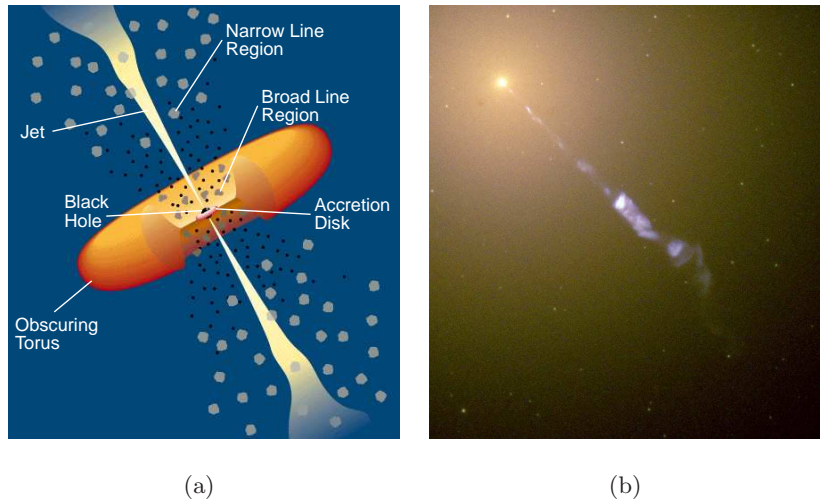


Figure 1.3: (a) A simple model of an AGN (not to scale). (b) The plasma jet emanating from the core of M87, taken from Hubble Heritage Team (<http://heritage.stsci.edu>).

10 m telescope of the starburst galaxies IC342, M81, M82, and NGC3079 are reported in [134] with upper limits placed on all four objects.

#### 1.1.4 The Role of $\gamma$ -rays and Neutrinos

The main complication in determining the production sites and acceleration mechanism of CRs arises from the deflection of charged particles in interstellar magnetic fields. Our galaxy ( $\sim 20$  kpc diameter) is penetrated by a magnetic field of  $\sim 10^{-11}$  T, thus a proton with energy below  $10^{17}$  eV will lose information about its primary source direction within 1 kpc. In addition at VHE (above  $10^{20}$  eV), the HE protons see the CMB as  $\gamma$ -ray photons with sufficient energy to produce pions via  $\Delta$  resonance and are strongly absorbed (the GZK effect [70; 197]). The observation of CRs with energies greater than the GZK limit, at  $10^{20}$  eV, is an outstanding problem as there appears to be no sources within the cut-off distance ( $\sim 100$  Mpc) capable of producing them. Another probe is needed in order to trace the sources of CRs.

Fortunately the acceleration of CRs is accompanied by the subsequent production of photons and neutrinos. These multi-messengers propagate to Earth unaffected by magnetic fields. Thermal processes may produce photons as energetic as X-rays, with up to  $\sim 50$  keV, but  $\gamma$ -rays are indicative of non-thermal processes.  $\gamma$ -rays may be referred to

as medium energy (0.1 - 30 MeV), HE (30 MeV - 100 GeV), or VHE (100 GeV - 100 TeV). Higher energy X-rays exhibiting a power law spectrum also hint at a non-thermal origin and a site of electron acceleration. Such a flux is accompanied by the production of  $\gamma$ -rays via non-thermal bremsstrahlung and IC scattering of lower energy photons. If a site is capable of accelerating electrons, it may also prove capable of accelerating protons, and in turn produce  $\gamma$ -rays via pion decay. Thus X-ray sources provide promising  $\gamma$ -ray candidates. It may therefore seem that photons are the most obvious messengers for astrophysical sources. However, photons can be absorbed in the hot dense sources of interest and at energies above a few TeV interact with the infrared and CMB producing electron positron pairs. The effect is energy dependent and strongly depends on the nature of the spectrum and the distance to the source. The effect rapidly decreases below  $\sim 200$  TeV, due to the threshold for pair production, and detectors with a lower energy threshold are better suited for observing distant sources.

Neutrinos are distinct from other particles. They are electrically neutral and weakly interacting and can therefore travel enormous distances without being absorbed or deflected. They can escape from the dense cores of violent sources and provide the only direct information about processes driving particle acceleration. It is even feasible that there exists astrophysical sources containing CR acceleration where there is no measured non-thermal photon flux due to absorption within the source or before reaching Earth.

## 1.2 $\gamma$ -rays and Neutrino Production Mechanisms

### 1.2.1 $\gamma$ -Rays, and other photons

Non-thermal photons may be produced via IC scattering, indicating a site of leptonic acceleration, and by pion decay, a result of hadronic acceleration.

#### 1.2.1.1 Photons from the acceleration of Electrons

Electrons accelerated within an astrophysical object will spiral around the source's magnetic field lines emitting photons. This process is known as synchrotron radiation and results in a population of photons ranging from radio to X-ray. HE photons in the X-ray to  $\gamma$ -ray regime are produced when low energy photons gain an energy boost by interact-

ing with a relativistic electron via IC scattering. A possible source for these lower energy photons is synchrotron radiation produced by the same population of charged particles. In this Synchrotron Self-Compton (SSC) model the energy distribution of synchrotron radiation and secondary HE  $\gamma$ -rays would be highly correlated in energy, intensity and time. Alternatively an external population of low energy photons may provide the population required for  $\gamma$ -rays via IC. In this case the  $\gamma$ -ray emission is independent of the accelerated charged particles and instead reflects the medium surrounding the jet. This is known as the External Compton model (EC).

### 1.2.1.2 Photons from the acceleration of Protons

Relativistic protons and nuclei create secondary pions and kaons in inelastic collisions with matter. The neutral pions decay almost immediately predominantly into two  $\gamma$ -rays<sup>2</sup> and thus provide the main channel for the conversion of kinetic energy of hadrons to  $\gamma$ -rays. In the energy range above 1 GeV the  $\gamma$ -ray spectrum can closely follow the (power law) spectrum of the parent protons. Thus VHE  $\gamma$ -rays carry information about the acceleration spectrum of the progenitor particles, though be it convolved with the secondary,  $\gamma$ -ray spectrum.

$\gamma$ -rays may also result from the interaction of high energy protons with ambient photons. Mannheim, [123], proposes that peaks in AGN emission spectra in X-rays and  $\gamma$ -rays may both be explained by synchrotron radiation, but by different populations of electrons. A beam of protons of energies  $>10^{17}$  travelling down the AGN jet may interact with the ambient photons near the AGN core through the process  $p\gamma \rightarrow \pi N$  producing neutral pions, which decay to  $\gamma$ -rays, and charged pions, which create electromagnetic showers. The observed  $\gamma$ -ray emission is then a result of synchrotron radiation of electrons with energies  $>10^{16}$  eV in these showers.

## 1.2.2 Neutrinos

Neutrinos may be produced as a consequence of Dark Matter annihilation, the collapse of massive stars, and the astrophysical acceleration of hadrons. This latter mechanism is of interest to the origin of CRs.

---

<sup>2</sup>The  $\pi^0$  mesons have a mean life time of  $8.4 \times 10^{-17}$  s and form photons with branching ratio of 99%.

The interaction of relativistic hadrons with matter and photons results not only in the production of neutral pions but also in a population of charged pions which decay primarily into muons and muon neutrinos (with a likelihood of >99.98%). The muons then decay to electrons and electron neutrinos as shown below.

$$\begin{aligned} \text{hadrons} &\rightarrow \pi^+ \rightarrow \mu^+ + \nu_\mu \rightarrow e^+ + \nu_\mu + \bar{\nu}_\mu + \nu_e \\ &\rightarrow \pi^- \rightarrow \mu^- + \bar{\nu}_\mu \rightarrow e^- + \nu_\mu + \bar{\nu}_\mu + \bar{\nu}_e \end{aligned}$$

## 1.3 The Detection of Astrophysical $\gamma$ -Rays and Neutrinos

### 1.3.1 HE $\gamma$ -Rays

The Earth's atmosphere is opaque to  $\gamma$ -rays and to observe them directly a detector must be carried above the atmosphere. This was traditionally done using balloons and more recently, from around 1972, by satellites. Optical, radio, infrared and even X-ray astronomy all utilise reflection to concentrate incoming photons onto a small detector element. Above a few MeV, there is no efficient way of reflecting  $\gamma$ -rays. Add to this the need to screen detectors to remove the background flux in all but the direction of pointing, and the effective aperture of a space-borne  $\gamma$ -ray telescope is seldom greater than 1 m<sup>2</sup> and often only a few cm<sup>2</sup> and therefore limited to the regimes of HE and below.

$\gamma$ -rays detected directly utilise scintillation, for example by RXTE for X-ray/ME  $\gamma$ -ray detection, photoelectric ionisation in a semiconductor, used in INTEGRAL, and Compton scattering in the case of COMPTEL onboard NASA's Compton  $\gamma$ -Ray Observatory (CGRO). However, arguably the most important process is pair-production, in which HE  $\gamma$ -rays above 30 MeV create an electron-positron pair that in turn are tracked using a spark chamber. By recording the trails a 3-dimensional picture of the pair as it travels through the chamber is built up. The paths of the pair determine the direction of the incoming photon and the energy of the electron and positron give the energy of the incoming photon. The Energetic Gamma Ray Experiment Telescope (EGRET) on CGRO was such a telescope and the future the Gamma-Ray Large Area Space Telescope (GLAST) mission will also use a pair production telescope.

EGRET was one of the four scientific instruments on CGRO satellite and detected HE  $\gamma$ -rays with energy from 30 MeV to 30 GeV. EGRET produced a catalogue of 271 HE  $\gamma$ -ray point sources. More than half of these remain unidentified with respect to objects in other wavelength bands, mainly due to the relatively poor angular resolution of the instrument ( $5.8^\circ$  at 100 MeV). The identified sources are mostly blazars, with a few pulsars and other types of objects. The improved angular resolution ( $3.5^\circ$  at 100 MeV) promised by GLAST in comparison to EGRET will be important for resolving the morphology of sources and disentangling confusion and identification of counterparts. Additionally the increase in sensitivity (about 50 times that of EGRET at 100 MeV) and extension to  $>100$  GeV will provide an overlap with IACTs promising spectral measurements in an energy regime where differences between hadronic and leptonic  $\gamma$ -ray production mechanisms are significant. The launch of GLAST is scheduled for early 2008.

### 1.3.2 VHE $\gamma$ -Rays

At the VHE level the direct detection of  $\gamma$ -rays becomes unfeasible due to the prohibitively large cost of satellite experiments. However at these energies the opacity of the atmosphere may be utilised to observe  $\gamma$ -rays from ground based detectors via the secondary particles produced air-showers initiated in the upper atmosphere. In an IACT a large reflector is used to focus Cherenkov light produced in air-showers to a highly pixellated camera. An image of the air-shower is recorded by fast electronics and distinguished from background events via a multi-level trigger system. The IACT principle is described in detail in Section 2.3.

IACTs are not the only way to observe VHE  $\gamma$ -rays from the ground. At energies above  $\sim 10$  TeV the amount of charged particles reaching ground level from an EAS is large enough to reconstruct the primary energy and direction via an array of particle detectors. These may be water Cherenkov tanks, as in the case of Milagro [161], or densely packed arrays of scintillation detectors, as in the case of the Tibet air-shower array [19]. Although a few  $\gamma$ -rays from the strongest TeV sources have been detected by both Milagro and the Tibet array, such air shower particle detectors are limited by their ability to distinguish  $\gamma$ -rays from hadrons. They are, however able to operate

continuously and monitor a large section of the sky. The current emphasis in the field is to reduce the energy threshold to overlap with that of IACTs in order to operate in an energy band where there are known sources.

An alternative way of utilising Cherenkov light to detect VHE  $\gamma$ -rays relies upon large arrays of optical heliostats, built as light collectors for solar energy power-stations. Three examples are: STACEE (Albuquerque, New Mexico) [164], Solar Two (Barstow, California) [199], and CELESTE (Pyrenees, France) [51]. These instruments are not in ideal locations, but due to their large mirror collection area, offer the possibility of low energy thresholds (down to  $\sim 30$  GeV). The contribution of light from background hadrons (as described in Chapter 2, Section 2.3.9) is extremely low at these energies. Even though these instruments have an extremely small FoV, and are unsuitable for extended source observations, they may make significant contributions to distant, point-like, sources with steep spectra such as AGN.

### 1.3.3 Neutrinos

The neutrino is a unique probe of the universe and provides complementary information to photons and charged particles. This neutral particle is not deviated by magnetic fields thereby in principle allowing a precise astronomy to be achieved. Further, as the neutrino is only sensitive to the weak interaction, it is essentially unaffected during its journey from the source to the detector. Unfortunately, the very properties which make the neutrino such an interesting messenger also mean that it is notoriously difficult to detect experimentally; the weakness of its interaction implies that exceptionally large detector volumes, of the order of a  $\text{km}^3$ , are required.

At low energies (below  $\sim 20$  MeV) cosmic neutrinos are observable in man-made detectors placed deep underground to reduce the flux downward going CR muons. Experiments such as Super-Kamikande have observed neutrinos from the Sun and the 1987a supernova explosion [171]. This technique is limited by the extreme cost of building a large detector deep under the surface of the planet, and is not scalable to higher energies. However since the Earth acts as a shield against all particles except neutrinos, a neutrino detector placed in a body of water or ice looking downwards may exploit the natural environment to achieve much larger detector volumes therefore probing higher

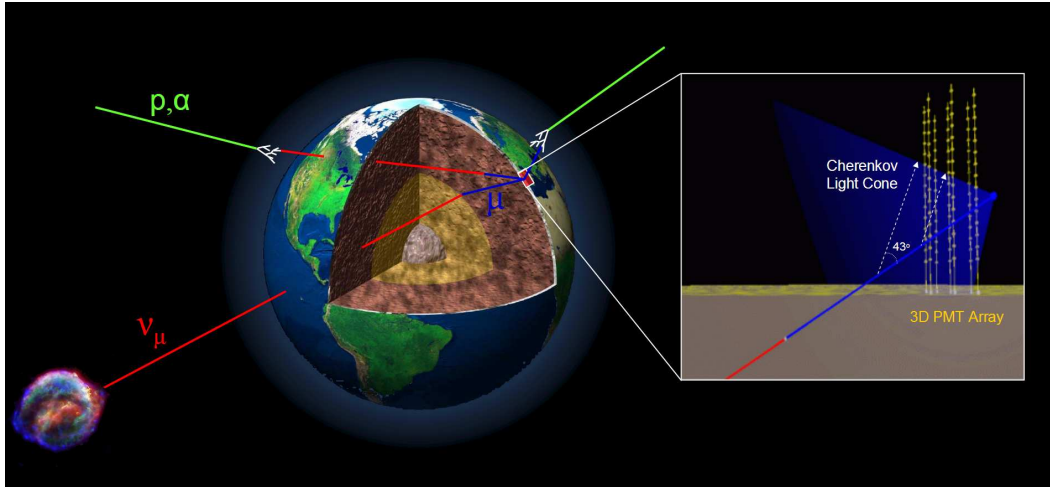


Figure 1.4: *Cosmic neutrinos traverse the Earth and interact to produce muons (lower left), which are in turn observed by a UND via Cherenkov light (right, inset). The UND is placed deep under water or ice and faces downwards to minimise the background from muons produced by CRs from above (upper right). There is a significant background from neutrinos produced on the far side of the planet in CR air-showers that traverse the Earth and produce muons in the same way as cosmic neutrinos (upper left).*

energies. In such an experiment the detection of an upward-going muon may be regarded as a signature of a muon-neutrino interaction in the matter below the detector. The detectors themselves are typically arrays of PMTs in water or ice through which the muon emits Cherenkov light. The detection of this light allows the determination of the muon trajectory and subsequently the original neutrino direction and energy. This technique requires discriminating upward going muons against the much higher flux of downward atmospheric muons (see Figure 1.4). To reduce the background, the detector is installed in a deep site under a layer of water or ice, a feature that results in a costly, complicated installation procedure and requires robust specialist technology for the detector elements. In addition to downward going muons, CR initiated air-showers on the other side of the planet also produce neutrinos that result in Cherenkov signals in the detector volume identical to those from cosmic neutrinos. This background may only be reduced by directional restrictions, since the CR flux is isotropic.

In addition to underwater and ice telescopes cosmic neutrinos may be detected using several other techniques including radio Cherenkov detection (e.g. RICE [108]), surface

detectors, horizontal air showers, and acoustic detection [100].

## 1.4 Current Generation Cherenkov Telescopes

In this section the current IACTs and UNDs are introduced and their performance summarised. The IACT technique is covered in more detail in Chapter 2 and VERITAS is described fully in Chapter 3.

### 1.4.1 Imaging Atmospheric Cherenkov Telescopes

The first successful application of the imaging technique was realised by the Whipple collaboration, who used a 10 m diameter light collector and an array of PMTs to record images of the angular distribution of Cherenkov light produced by air showers [172]. The shape and orientation of the images were used to efficiently select  $\gamma$ -ray initiated air shower candidate events from among the otherwise overwhelming background of CR initiated events [84]. Arrays of IACTs provide a further increase in sensitivity and in angular and energy resolution, as demonstrated by the HEGRA experiment [149]. The stereoscopic imaging atmospheric Cherenkov technique is now being exploited using large reflectors by four projects worldwide (see Figure 1.6): MAGIC [116] and VERITAS [174] in the Northern hemisphere and H.E.S.S. [87] and CANGAROO III [109] in the South. H.E.S.S. was the first of these to come online and recent observations have produced a wealth of new discoveries, an excellent review of which can be found in [16; 86]. For the development of new technology it is useful to understand the instrumentation, and in particular the read out and triggering schemes, used in these detectors. The sensitivity of various IACTs are presented in Figure 1.5, including the expected sensitivity of MAGIC-II, H.E.S.S. Phase II. Also included are the sensitivities for several possible geometric configurations of the proposed Cherenkov Telescope Array (CTA) (see Section 1.5). The sensitivity is defined as the minimum  $\gamma$ -ray flux required to obtain a  $5\sigma$  excess over background events in 50 hours of observing.

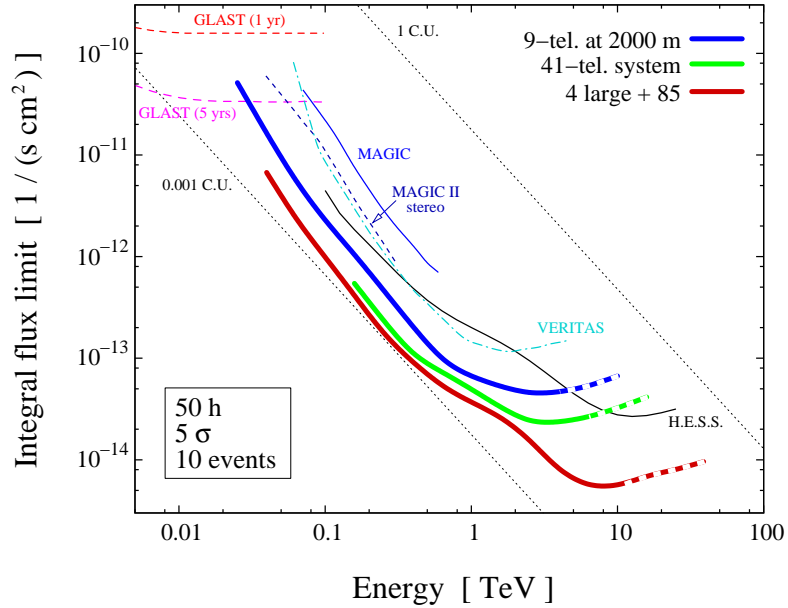


Figure 1.5: *The sensitivity of several high-energy observatories produced using Monte-Carlo  $\gamma$ -ray simulations and appropriate detector simulations. Indicated sensitivities assume 50 hours of observations and a minimum  $5\sigma$  detection. The thick, solid blue, green and red lines show the expected sensitivity of CTA for several possible geometric configurations. Taken from [29].*

#### 1.4.1.1 MAGIC

The MAGIC, or Major Atmospheric Gamma Imaging Cherenkov, telescope, located on the Canary island of La Palma (2200 m a.s.l.), was completed in 2003. MAGIC is the most technologically daring of the current generation IACTs and aims primarily to provide an increase in sensitivity at lower energies than previous experiments [132]. A 17 m diameter reflector and high photon detection efficiency result in an energy threshold of around 25 GeV [44]. The optical support structure is made from carbon fibre epoxy tubes and is light enough to be repositioned within to any position in the sky within 20 s, useful in the search for  $\gamma$ -ray bursts (GRBs).

The 239 m<sup>2</sup> reflector consists of 964 mirror elements arranged parabolically to minimise spread in the arrival time of photons at the camera plane. The curvature of the individual mirror tiles is spherical, and their focal lengths are increased following their radial position on the dish, increasing the cost of production. They contain heating elements to avoid dew and snow and are attached to the frame using an active control

system to align the mirrors remotely (a similar method has been adopted by H.E.S.S., see Section 1.4.1.2).

Reflected photons are recorded by a  $3.5^\circ$  FoV hexagonal camera in the focal plane composed of 397  $0.1^\circ$  PMTs surrounded by 180  $0.2^\circ$  PMTs. The PMTs have hemispherical windows and only 6 dynodes to minimize the time response width. The PMT photo conversion efficiency has been enhanced up to 30% and extended to the UV by coating the window with wavelength shifter [143] and coupling them to Winston cones (hexagonally shaped light guides). The MAGIC telescope is capable of operating during moon time unlike VERITAS or H.E.S.S.. To make this possible the PMT gains are reduced and a 1 GHz bandwidth transimpedance amplifier provides an additional signal gain of  $\sim 8$  with an output noise low enough to still resolve the single pe. PMT signals are transferred in their analogue form via optical fibres [142] to the electronics room some 100 m away using a transmission scheme based upon work originally done by Lorenz et. al. [117] and later developed for the Whipple-10 m telescope [49]. Such a scheme is developed further in this work and the MAGIC fibre-optic transmission system is discussed in more detail in Chapter 4. In the electronics room the signals are split into three channels, one into the trigger channel and two into the acquisition system for digitisation with different gains. The analogue signals are continuously digitized by 8 bit 300 MHz Flash ADCs providing a series of 3.3 ns slices of the original pulse [25]. The high gain (HG) signal is further amplified whilst the low gain (LG) signal is delayed and digitised in the same FADC channel as the HG signal. Due to the low attenuation of the fibre-optic transmission scheme the narrow PMT pulses (2-3 ns FWHM) are stretched before digitisation to  $\sim 6$  ns (FWHM) to ensure at least four points are sampled.

When a trigger arrives at the FADC modules, the FADC chip stops digitizing, the position of the signal in a ring-buffer is determined and 30 time slices of 1-Byte (15 for HG and 15 for LG) are written into the FiFo buffer for each pixel. This operation is performed at a maximum rate of 80 MBytes/s; which results in a dead time of  $\sim 20 \mu\text{s}$ . This corresponds to about 2% dead time at the design trigger rate of 1 kHz. The time and trigger information for each event are recorded by dedicated digital modules which are read out together with the FADC boards.

The trigger decision is generated by a three level system [131]. Level 0 simply requires

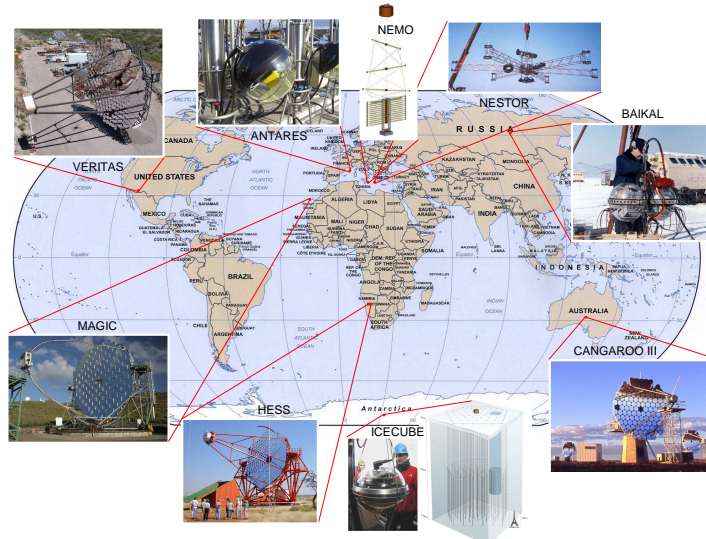


Figure 1.6: World map showing the current major IACTs UNDs.

the signal in a given pixel to exceed an adjustable threshold. The trigger signals are routed into 19 overlapping patches of 36 pixels covering the 325 innermost PMTs and the level 1 trigger requires a coincidence between 4 adjacent pixels within a few nanoseconds. The level 2 trigger consists of multiple layers of programmable SMART modules. In the first layer the level 1 information for each trigger cell is divided into three 12-pixels regions and fed into 19 such modules. Patterns of fired pixels that have passed the level 0 discriminator threshold can be selected locally in one SMART and coded in a 6-bit word. The outputs from the 19 modules of the first stage are fed into a second and a third stage in a tree-like structure, in order to apply topological cuts. The information available at level 2 is the digital image filtered by the level 1. The level 2 can apply cuts on the event topology based on the number of pixels, the shape and other parameters. Currently the level 2 is not used during observations. The potential use for background rejection is under investigation.

#### 1.4.1.2 H.E.S.S.

The first phase of the High Energy Stereoscopic System (H.E.S.S.) consists of an array of four IACTs located 1800 m a.s.l in Namibia. The system started operation with one telescope in summer 2002, was completed with the installation of the fourth telescope in

December 2003 and has been used for routine data taking since then [27]. The array is arranged in a square with 120 m sides, spaced to maximise the effective collection area whilst ensuring light from  $\gamma$ -ray induced air showers is seen by more than one telescope.

The optical system of each telescope is based on a segmented reflector with  $f/d \sim 1.2$  and a reflective area of 107 m<sup>2</sup>. The 380 spherical mirror facets have identical focal lengths of 15 m and are arranged in a Davies-Cotton layout with an opening diameter of 13 m. The 1.4 m diameter camera images Cherenkov light over a 5° FoV and contains 960 42 mm diameter PMT pixels each subtending an angle of 0.16°. The specified point spread function is 0.03° (RMS) for parallel light in the focal plane [43]. Winston cones are again used to close the gaps between the circular pixels.

The complete electronics for image digitisation, read out and triggering are integrated into the camera, constructed using a series of modular 'drawers', each containing 16 PMTs and associated electronics which slide into the camera body. Individual photons are recorded using the PMTs with a quantum efficiency of 25% [8]. The signal pulse from the PMT is fed into three different channels, one into the trigger channel of the camera and two into the acquisition system with different gains. By using a HG and a LG channel the linear response of the PMT is increased to a dynamic range of up to 2000 pe. The analogue PMT signal is sampled in an Analogue Ring Sampler (ARS) initially developed by the CEA for the ANTARES experiment. The sampling is performed at a rate of 1 GHz and the analogue voltage levels are stored in a ring buffer consisting of 128 capacitor cells. The camera is triggered by a coincidence of signals above a threshold of around 5 p.e. detected in 3 to 5 pixels in overlapping 8x8 pixel sectors [61]. The fast circuitry provides an effective coincidence window of about 1.5 ns due to the sorting of PMTs according to transit time and the close proximity of the trigger logic to the PMTs.

Following a camera trigger signal, which takes 70-80 ns, the ARS sampling is stopped, the capacitor cells are addressed one by one and a multiplexer distributes the signal from 4 ARS chips (8 PMTs) into one 12-bit ADC. Normally 16 cells are converted into charge equivalent ADC counts in the range where the Cherenkov signal is expected on the basis of the trigger timing which takes around 270  $\mu$ s. The digitised signals are stored and processed in a FPGA on each acquisition card. In the normal read out mode (charge

mode), the 16 samples are summed to give two ADC values per pixel (HG and LG). The position of this 16 sample read out window is verified frequently using the 'sample mode' facility of the ARSs. In this mode, the charge of the 16 cells in 1 ns intervals is read and stored. The pulse shape can be then studied, as well as the read out timing. The position of the charge peak in the read out window is used to adjust the timing. Pre-processed digital data from the drawers are sent to 8 FiFo memories located in a cPCI (Compact Peripheral Component Interface) crate which requires a further 140  $\mu$ s. Once a camera triggers on a shower image, it alerts a central trigger station. If two or more telescopes trigger simultaneously, providing stereo images of an air shower, a trigger confirmation is sent back to the telescope, and read out via a bus into the local processor of the camera, which only takes around 4.5  $\mu$ s. The total dead time for an event read out is dominated by the digitisation, pre-processing and read out time and is around 445  $\mu$ s. If no coincidence between telescopes occurs, the camera trigger is vetoed by the central trigger and the dead time is 5.5  $\mu$ s, dominated by the round-trip time to the central trigger. Telescopes that do not form a local trigger do not participate in the read out initiated by an array trigger, reducing dead time, but at the expense of potentially useful information.

#### 1.4.1.3 VERITAS

The VERITAS telescopes are discussed in detail in Chapter 3, a brief summary is given here for context and comparison. At the time of completion of this thesis, the VERITAS array consisted of three operating telescopes, with a fourth telescope in the commissioning phase. The array is temporarily located at the Basecamp of the Fred Lawrence Whipple Observatory on Mount Hopkins in Arizona at an altitude of 1270 m. Each telescope has a mirror diameter of 12 m giving a total mirror area of over 100 m<sup>2</sup>. The focal plane cameras comprise 499 pixels in a close packed hexagonal array. The data acquisition consists of custom built 500 MHz FADCs which sample the Cherenkov light pulse in the pixels every 2 ns. The telescopes operate with an array trigger, which requires at least two telescopes to trigger within a 100 ns coincidence window. After a telescope trigger the FADC sampling continues, and (unlike H.E.S.S.) no dead time occurs at this stage.

#### 1.4.1.4 CANGAROO-III

The CANGAROO-III (Collaboration of Australia and Nippon for a Gamma- Ray Observatory in the Outback) project [56; 99] consists of four Cherenkov telescopes located near Woomera, South Australia, at an altitude of just 160 m. Each telescope has a diameter of 10 m giving a total mirror area of 57 m<sup>2</sup>. The mirrors are mounted on a parabolic reinforced plastic frame with a focal length of 8 m. The telescopes are arranged in a diamond formation of side 100 m. They are operated in pseudo-stereo mode, using software GPS time stamp matching to combine telescope events into array events offline.

### 1.4.2 Underwater Neutrino Detectors

The Dumand experiment based in Hawaii was the first attempt to construct a UND, [166; 181]. Although the project was cancelled in 1996, a great deal of technological experience and knowledge of the under water environment was gained. It now seems that Dumand was simply ahead of its time, [153], and required technology that is only today becoming readily available and affordable.

#### 1.4.2.1 Baikal, NEMO, and NESTOR

There are currently several UNDs in construction or operation, as shown in Figure 1.6. In the northern hemisphere there are three detectors at different sites in the Mediterranean and one in Lake Baikal, Siberia. The deep sea provides a clear natural medium with relatively small amounts of photon scattering. A large amount of scattering reduces the number of Cherenkov photons recorded for a given muon and spreads their arrival times out, reducing the ability to accurately reconstruct the trajectory. The Baikal neutrino telescope [21], consists of 200 PMTs on 8 detectors strings at a depth of 1300 m. This relatively shallow depth is reflected in a higher CR muon background rate and a shorter optical photon absorption length than found in the deep sea. Unlike the sea however, the lake freezes in winter offering a hard platform for deployment. ANTARES has made the most progress of the three Mediterranean projects (see Section 1.4.2.3), and is currently in the commissioning stage due for completion in 2007. Nestor and

Nemo both operate at deeper sites than ANTARES, though largely remain exercises in research and development. The current European effort has been combined for a three year research project into a cubic kilometre scale detector, KM3NeT.

#### 1.4.2.2 AMANDA and IceCube

In the southern hemisphere the troublesome deployment associated with the sea is avoided by situating the detector elements in the ice of the Antarctic, where US scientific facilities provide a pre-existing infrastructure. Ice at a depth of several kilometres below the South Pole has much longer absorption lengths than the water in the deep sea. Thus individual PMTs can be spaced further apart and therefore increasing the size of the detector. There is also no bioluminescence from radioactive decay and living creatures in the ice, a constant source of  $\sim 50$  kHz background noise in the sea. However scattering is much more pronounced in ice than in water, which has a significant effect on the ability to reconstruct muon directions. Additionally the ice suffers from inhomogeneities such as air bubbles and layers of dust that make simulation difficult.

The IceCube Neutrino Detector [101; 158] is currently under construction at the South Pole. An extension from its predecessor, the Antarctic Muon And Neutrino Detector Array (AMANDA) [75], IceCube is being constructed by deploying thousands of spherical optical modules (OMs) containing PMTs at depths between 1,450 and 2,450 m. The sensors are deployed on strings of sixty modules each, into holes in the ice melted using a hot water drill. IceCube will be the world's first cubic kilometre scale neutrino detector and will operate for 20 years once complete offering unprecedented sensitivity. However, the angular resolution will be limited by the intrinsic properties of ice. A next generation northern hemisphere UND should not only complement the sky coverage of IceCube, but may also surpass the performance.

#### 1.4.2.3 ANTARES

The ANTARES experiment or, rather dubiously, Astronomy with a Neutrino Telescope and Abyss environmental RESearch, will consist of an array of approximately 900 PMTs in 12 vertical strings, spread over an area of about  $0.1 \text{ km}^2$  as shown in Figure 1.7. The detector comprises of OM grouped together in triplets to form stories interconnected

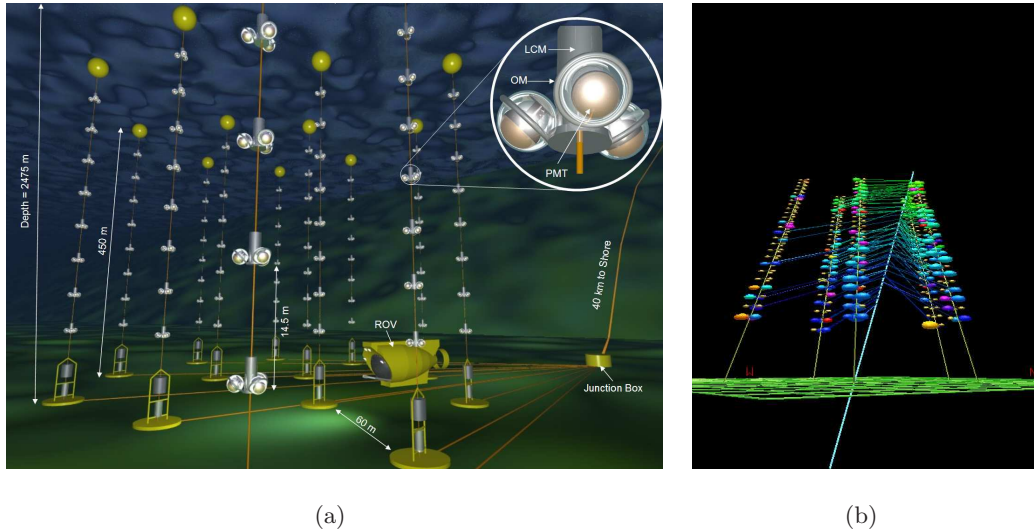


Figure 1.7: (a) An artists impression of ANTARES 12-string detector with a single storey inset, a composite of images from F.Montanet, CNRS/IN2P3 and UJF. (b) A downward going muon reconstructed from data taken with the current 5-string detector. The colour of the hits encodes the time, while the size is a measure of the charge in each PMT.

with an electro-mechanical cable. Each of the 12 strings contains 25 such storeys vertically spaced in 14.5 m steps and horizontally separated by 60 m. Each OM consists of a 10" Hamamatsu PMT, HV power supply, various sensors, and the associated electronics, housed in a pressure-resistant glass sphere. The OMs in a storey are arranged with the axis of PMTs  $45^\circ$  below the horizontal.

At every storey, there is a local control module (LCM), which contains custom built electronics, including an FPGA and six Analogue Ring Sampler (ARS) chips, to capture and store waveforms, pulse heights and timing information, and at the base of each string there is a string control module (SCM) [6]. An acoustic system provides real-time positioning of the detector elements to a precision of a few centimetres and a system of optical beacons, developed at the University of Sheffield [2], allows in-situ time calibration. The individual SCMs are linked to a common junction box by electro-optical cables which are connected using a submarine. A standard deep sea telecommunication cable links the junction box with a shore station where the data are filtered and recorded. The trigger logic in the sea is simple and flexible. Each ARS is set to a typical threshold of 0.3 p.e., and integrated over 35 ns gate. The first-level trigger requires a coincidence

between any two OMs in a single storey. The second-level trigger is based on combinations of first-level triggers. Following a second-level trigger the full detector will be read out. A more refined third-level trigger, imposing tighter time coincidences over larger numbers of OMs, may be made in a farm of processors on shore. The read out rate from the full detector is expected to be several kHz, and the corresponding data recording rate less than 100 Hz.

The main electro-optical cable and the junction box have been operating in situ since their installation in 2002. A series of prototype lines have allowed verification of the technological choices. A Mini-Instrumentation Line with Optical Modules (MILOM) connected in March 2005 [5; 162] has provided continuous real-time monitoring of environmental parameters such as sea current speed and direction, OM counting rates and seismological activity. The first two full-size production lines were successfully connected in March and September 2006 respectively followed by lines 3, 4 and 5 in early 2007. The remaining 7 lines will be deployed during 2007. Figure 1.7(b) shows an example of a downward going muon reconstructed with the first 5 ANTARES lines.

## 1.5 The Next Generation of IACTs and UNDS

Even with the great improvements promised by the current generation of IACTs in operation or under construction the field has not yet reached the fundamental limits of sensitivity and UNDS are generations away from achieving a comparable sensitivity. Next generation telescopes in both fields will be designed to optimise performance across a chosen energy range and this choice will directly effect the technological requirements of the detector. New technology is required to make the next generation of Cherenkov telescopes physically possible, cost effective and may provide versatility and performance across an extended energy range. In the case of UNDS the effect of key factors such as geometry and PMT choice on performance as a function of energy is still very much open. The KM3NeT collaboration aims to understand such issues before making a design choice within the next two years [110]. During this research and development period new technology must be explored to facilitate the deployment, read out and triggering of this potentially huge detector. In particular the effect of new technology on the performance and cost of a given detector geometry must be evaluated. The

principle issue of energy domain has been considered greatly in the development of next generation IACTs. The ultimate goal of which is a dramatic improvement in flux sensitivity (down to  $10^{-14}$  erg/cm<sup>2</sup>s) in the energy regime of 0.1 to 10 TeV and an aggressive extension of the energy domain down to  $\sim 0.03$  TeV (30 GeV) and up to 300 TeV. CTA is in the very early stages of a design study and aims to reach a high level of sensitivity across a wide range of energies by constructing a hybrid array of many medium size telescopes ( $\sim 100 \times 12$  m diameter) and several large telescopes ( $\sim 10 \times 30$  m diameter).

## 1.5.1 Requirements for Next Generation of IACTs

### 1.5.1.1 Increasing the TeV Sensitivity

In the TeV region (300 GeV - 30 TeV) the desired sensitivity of  $10^{-14}$  erg/cm<sup>2</sup> may be reached by extending the number of medium size telescopes (with opening diameters of  $\sim 10$ -12 m) in stereoscopic arrays. An IACT array with this sensitivity and a FoV  $\geq 5^\circ$  should provide extensive sky surveys of areas such as the galactic plane. Although no new technology is directly required for this extension, the physics possibilities could be greatly expanded by implementing high-speed advanced triggering scenarios. This is a very expensive way of extending the field, and any new technology that reduces the cost of a single IACT without reducing the performance would help to realise this scenario.

### 1.5.1.2 Lowering the Energy Threshold

In order to probe the sub-TeV regime (30 GeV - 300 GeV) the energy threshold, generally defined as the energy at which the  $\gamma$ -ray rate becomes maximum when observing the Crab Nebula, must be lowered. This can be done by using a very large  $\geq 20$  m-diameter reflector and by increasing the collection efficiency of the detector. As the reflector size increases so does the off-axis optical aberrations and the IACT FoV becomes limited. Whilst this does not particularly affect point source observations, it significantly hampers the morphological mapping of extended sources and limits the  $\gamma$ -ray detection area at high energies. The Small Telescope Array (STAR)[57] proposes achieving a large effective aperture by using many small telescopes, thereby avoiding both the cost ( $\sim \$1$ -2

million for the equivalent area covered by a 30 m dish costing \$6 million) and limited FoV associated with large ( $\sim 30$  m) dishes. STAR would function by combining Cherenkov light from a sub-set of these smaller telescopes to trigger as one larger telescope. In one realisation 144 x 2.5 m dishes placed close together are combined to produce a collection area equivalent to a single 30 m dish. A  $5^\circ$  FoV is easily obtainable with cameras as small as 22 cm, which provide prime targets for the development of new technology. Since each sub-array of telescopes will be spread over a 35 m circular area relative signal delays will be required based upon telescope location and source position before forming a trigger, a unique problem that FPGA based delay and trigger modules, such as those developed in Chapter 5, would prove useful for. The energy threshold of STAR could be as low as 20-40 GeV. Even lower energies (down to 5 GeV) may be reached by constructing large dish ( $\geq 20$  m) IACT arrays at higher altitudes (5 km a.s.l.), where there are more Cherenkov photons from lower energy  $\gamma$ -rays, such as the proposed *5at5 project* [17].

### 1.5.1.3 Probing Higher Energies

The tendency of  $\gamma$ -ray fluxes to decrease dramatically with energy above 10 TeV means that large arrays of IACTs are required to probe this range. Since images from higher energy  $\gamma$ -rays land further from the camera centre large FoV cameras are required. Such an array would also provide a tool for detailed morphological and spectrometric measurements in the 3 TeV to 10 TeV range. One design under consideration is the  $\gamma$ -Ray Astrophysical Telescope Imaging System (GRATIS), consisting of 37 x 5.4 m diameter telescopes with  $4^\circ$  FoV), covering 1 km<sup>2</sup> in a 200 m spaced hexagonal lattice [42] offering reasonable sensitivity from 300 GeV to over 100 TeV at a total estimated cost of  $\sim 17$  million.

## 1.5.2 The Immediate Future of IACTs

Whilst there are several IACT projects proposed in the long-term, including the Cherenkov Telescope Array (CTA) and a *beyond* VERITAS project, the immediate future will see extensions to the MAGIC and H.E.S.S. by 2009.

### 1.5.2.1 MAGIC II

A second 17 m telescope (MAGIC-II) is under construction at the same site as the first telescope on the Roque de los Muchachos, La Palma, Canary Islands [130]. The second telescope is situated at a distance of 80 m from the first telescope. This distance was optimized after a detailed Monte Carlo simulation. The imaging camera is designed with advanced photon detector HPDs which have a quantum efficiency of 50% around 500 nm [78]. The signals will be read out by ultra-fast FADC systems of 2.5 GSa/s [22] to reduce background photons from the night sky and to achieve a better gamma / hadron separation by utilising the time profile of the Cherenkov light. MAGIC-II aims to lower the threshold energy by a factor of two with advanced photon detectors and an ultra fast read out system. The stereo configuration with two telescopes will increase the sensitivity to fainter sources and the quality of the experimental data.

The VCSELs used in the analogue read out scheme of MAGIC have been upgraded, thanks partly to work done in this thesis (see Chapter 4), and promise improved linearity, dynamic range and experience less noise problems. The dead time problems associated with a hardware implemented multiple telescope trigger system (see Chapter 3 Section 3.5) are avoided by transporting all signals from both telescopes to a single location allowing a very short trigger round-trip time.

### 1.5.2.2 H.E.S.S. Phase II

An extension to H.E.S.S. consisting of a very large (28 m diameter) telescope is planned for completion in 2008 costing approximately \$8 million [93]. This Phase-II telescope will utilise improvements in technology to decrease the dead time and increase read out speed and will feature a total mirror area of  $\sim 600 \text{ m}^2$  to improve image quality and p.e. statistics in the 100 GeV range down to 20 GeV. The Davies-Cotton reflector arrangement (see Chapter 2 for a description of this geometry) used in the Phase I telescopes is replaced with a parabolic reflector. Whilst the Davies-Cotton design offers improved off-axis imaging it does so at the expense of a dispersion in the arrival time of photons at the camera (5 ns for a 12 m dish) which grows linearly with dish size and for a 28 m reflector is unacceptable. The camera contains 2000 pixels of equivalent absolute size to the Phase-I cameras resulting in a size of  $0.07^\circ$  at the  $\sim 35 \text{ m}$  focal length. The

FoV is reduced to  $3^\circ$  from  $5^\circ$  due to the increased off-axis aberrations associated with the larger reflector. The read out scheme remains integrated into the camera and will use an improved analogue memory ASIC known as the SAM (Swift Analogue Memory) chip, a new iteration of the ARS, which also offers an attractive read out option for KM3NeT. The integration times for single pixels are around 10-15 ns.

The relatively slow read out of the ARS chips and the multiplexing of several channels to a single ADC limits the read out rate in the Phase-I cameras to about 1 kHz. The SAM chips sample at up to 2.5 GHz with a 256 sample depth and several external 12-bit ADCs at a rate of 20 MSa/s are used in parallel for each channel to increase the read out rate up to 50 kHz, and 3 kHz on average. Differential signal routing replaces the TTL based layout to reduce noise and larger FPGAs facilitate signal pre-processing including peak-detection, possible signal sampling, and an adaptive integration window. Full waveform sampling at GHz frequencies is achievable with both the ARS and SAM chips and may provide valuable information, but would require significant increases in read out bandwidth and data storage. This is a key limitation of digitisation within the camera.

## 1.6 New Technology for IACTs and UNDS

Current and future Cherenkov telescopes will benefit from the development of new technology across several areas. This work concentrates on the analogue read out of PMT pulses over fibre, high-speed topological pattern trigger electronics, and the optical distribution of fast digital pulses.

A key issue in the design of next generation Cherenkov telescopes is where and at what point to digitise the data. In ANTARES data is digitised at the LCM in the ARS chips. The same chips are used in H.E.S.S. to digitise data in the camera of each IACT. This local digitisation is slow, leading to increased dead time, and only records a total charge over the integration gate. Dead time is minimised in VERITAS by transporting the analogue PMT signals over bulky coaxial cable to the electronics room, where they are digitised by FADCs. Due to the physical weight and size of the coaxial cable this read out scenario is simply not scalable to larger cameras. In

Chapter 4 the possibility of transporting analogue pulses over fibre optic cable using low power VCSELS is investigated. Such a scheme is in place on the MAGIC IACT, and improvements in VCSEL technology measured during this work have aided in the development of the analogue transmission system for MAGIC II.

Multi-level, high speed schemes are currently used in both IACTs and UNDS to reduce the accidental trigger rate due to background light. Both VERITAS and ANTARES require coincident signals from a number of PMTs in a certain geometric pattern to form a trigger. The current VERITAS pattern trigger scheme routes 463 pixels to CAMAC modules in overlapping patches of 59 via a signal splitter crate. This bulky solution requires two large electronics crates, dozens of ribbon cable interconnects, and a minimum overlap of 10 ns between individual pixel triggers to form a coincidence. To ensure that the pulses arrive simultaneously at a given module each of the 59 signals must be connected with an individually calculated length of wire. For next generation detectors, with higher density cameras this becomes unfeasible. In Chapter 5 an FPGA based PST is developed to potentially improve and extend the functionality of the current VERITAS system and which is suitable for a future, much larger, camera. The FPGA technology used is easily adaptable to UNDS and extendable to larger IACT cameras and a variety of exotic triggering scenarios.

The use of VCSELS and FPGA technology is brought together for the development of the DAT modules in Chapter 6. These VME modules are used within VERITAS to distribute fast trigger pulses and housekeeping information between telescopes over optical fibre without dead time. They are a key feature of the array trigger system and enable the stereoscopic triggering of  $\gamma$ -ray initiated extensive air showers observed by several telescopes simultaneously.

## Chapter 2

# Extensive Air Showers, Cherenkov Radiation and the Imaging Atmospheric Technique

---

Above an energy of  $\sim 50$  GeV an incident  $\gamma$ -ray near the top of the Earth's atmosphere will interact to produce a cascade of secondary particles known as an Extensive Air Shower (EAS). Such phenomena are not limited to photons and an incoming CR will suffer a similar fate. Charged particles within these showers radiate Cherenkov light which may be focussed by an IACT to produce an image of the shower. This idea was introduced in Chapter 1 and the current IACTs were described. The development of EASs, the nature of the Cherenkov light within them, and the Imaging Atmospheric Technique will be considered in detail here. The IACT array, VERITAS, will be described in Chapter 3. The relationship between the physical properties of an IACT, such as collection area, and the signal-to-noise ratio (SNR) are considered in this chapter, and will be crucial in assessing the effect of new technology on telescope performance in later chapters.

## 2.1 The Development of Extensive Air Showers

Hadronic showers, and in particular those initiated by protons, constitute the majority of EASs in the atmosphere and, as it will be seen in Section 2.3.9.2, provide the overwhelming background in ground-based  $\gamma$ -ray astronomy. Whilst a  $\gamma$ -ray induced EAS consists almost entirely of electromagnetic (EM) secondary products an EAS resulting from a CR also contains a large hadronic component.

A simple qualitative description of an EAS is useful and will be given here. When working with EAS it is convenient to consider position in the atmosphere in terms of  $\text{g cm}^{-2}$  of air mass above the position. The relationship between  $\text{g cm}^{-2}$  and altitude above sea level (a.s.l.) is approximately exponential, with sea level corresponding to  $\sim 1000 \text{ g cm}^{-2}$ .

### 2.1.1 Photon Induced Extensive Air Showers

A  $\gamma$ -ray of sufficient energy entering the atmosphere will interact within the Coulomb field of an atmospheric nucleus to produce an electron-positron ( $e^+e^-$ ) pair. The production of a muon-antimuon pair is also possible, though greatly suppressed due to the high mass, and therefore low production cross-section, of the muon as compared to the electron ( $\sigma_{e^+e^-}/\sigma_{\mu^+\mu^-} \sim 45 \times 10^3$ ). The resulting  $e^+e^-$  pair will lose energy continuously, but in relatively small amounts, by ionization in atomic collisions. The electron and positron may be suddenly deflected by the Coulomb field of a nucleus radiating a large fraction of energy in the form of a  $\gamma$ -ray through bremsstrahlung. Figure 2.1(left) shows schematically these initial stages in the development of a photon induced EAS.

Pair production and radiation continue and the number of  $\gamma$ ,  $e^+$  and  $e^-$  grows exponentially around the forward direction of the original  $\gamma$ -ray, sharing out its total energy. Multiple Coulomb (elastic) scattering of the electrons and positrons deflects the secondary particles away from the direction of the primary photon, or shower axis. This scattering is more severe than the angular deviations introduced into a particle's path by bremsstrahlung and pair production and therefore dominates the lateral distribution of particles at a given height (see Section 2.2.2). The particles form a disk a few meters thick that propagates through the atmosphere at a speed close to  $c$ . As the

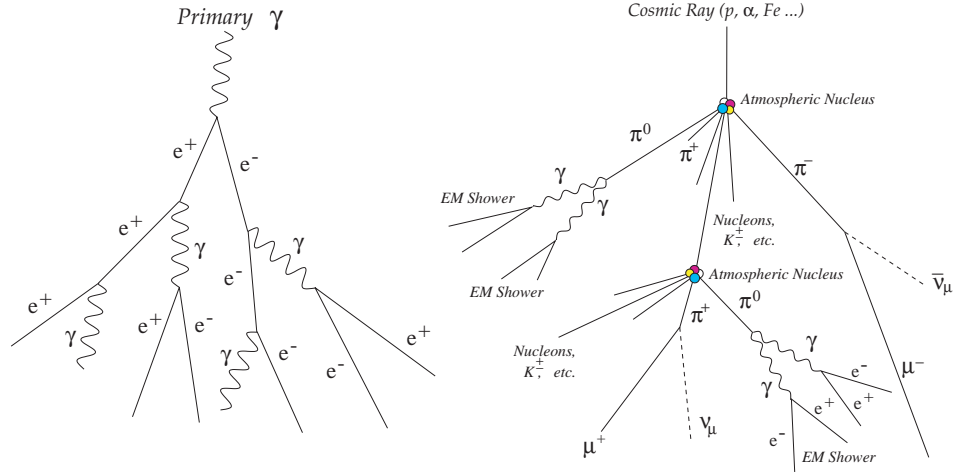


Figure 2.1: *Schematic illustration of the development of an EAS: induced by a  $\gamma$ -ray (left) and induced by a charged CR (right). Taken from [141].*

EAS proceeds, the energy of the secondary particles decreases. At a critical energy,  $E_c$  ( $\sim 83$  MeV in air), an electron loses equal amounts of energy per radiation length by the processes of ionization and radiation. In addition the mean photon energy drops towards twice the rest mass of an electron. The cross-section for pair-production becomes approximately equivalent to that for Compton scattering and, at lower energies, photoelectric absorption. Thus the shower reaches a maximum development at  $E_c$ . At larger depths the number of particles falls off and the shower is exhausted. A description of bremsstrahlung, pair-production, elastic scattering, ionisation, and Compton scattering may be found in many texts including [182].

EM cascade theory has been studied in much detail and an early comprehensive review was given by Rossi and Greisen [157], then in more depth in [156]. Greisen applied cascade theory to EAS in [69] as did Hillas in [82]. The relatively simple model of Heitler may be used to determine many general features of EM showers, including the position and number of particles at the shower maximum (see [63] and [115] for a review). As an illustration a vertically incident 1 TeV  $\gamma$ -ray initiated EAS reaches a maximum of  $\sim 10^4$  particles at  $\sim 350$  g cm $^{-2}$  ( $\sim 8$  km a.s.l.). Monte Carlo simulations, such as Corsika [80], have provided the most complex study of air showers.

### 2.1.2 Hadron Induced Extensive Air Showers

The majority of air showers produced in the Earth's atmosphere are initiated not by  $\gamma$ -rays, but rather by hadronic CRs. These particles, most of which are protons, collide with an atmospheric nucleus, producing secondary particles which in turn interact giving rise to a hadronic cascade as shown in Figure 2.1(right). At each successive generation approximately half of the available energy continues in nuclear particles, the bulk of which is carried by a single leading nucleon along the shower axis. The balance of the incident energy produces pions and kaons. Pions account for 90% of the EAS particles and are produced in equal abundances of  $\pi^+$ ,  $\pi^-$  and  $\pi^0$ , each population containing approximately one sixth of the secondary particles' total energy.

The neutral pions decay almost instantly, even allowing for relativistic effects at the highest energies into two photons. The photons generate EM sub showers by the interaction mechanisms described in the previous section. The charged pions have a much longer lifetime ( $2.6 \times 10^{-8}$  s at rest as compared to  $8.4 \times 10^{-17}$  s) and at energies above  $\sim 100$  GeV are likely to suffer nuclear collisions rather than decay. These interactions give rise to hadronic sub showers in the cascade. Deeper into the atmosphere, at lower energies (less than  $\sim 20$  GeV), the charged pions decay to muons ( $\mu^\pm$ ). As decay dominates over nuclear collisions the shower is brought to a halt. The  $\mu^\pm$  generated in pion decays do not interact strongly and lose energy mainly by ionisation. Above  $\sim 1$  GeV they penetrate to ground level. Below  $\sim 1$  GeV the muons decay to electrons adding a fractional amount to the total electromagnetic component of the EAS.

Although simple models of hadronic showers are available [62], again complex Monte Carlo simulations provide the best models of hadronic interactions. Note, however, that even the most advanced Monte Carlo tools rely on the extrapolation of measurements made in colliders to the higher energies found in the atmosphere.

### 2.1.3 Differences between Photonic and Hadronic EAS

The interaction length of a proton in air is  $\sim 80$  g cm $^{-2}$  compared to  $\sim 36$  g cm $^{-2}$  for a  $\gamma$ -ray. Therefore hadronic showers are initiated deeper into the atmosphere than their EM counterparts. In addition, the interaction length of the pions in hadronic cascades

( $107 \text{ g cm}^{-2}$ ) is longer than the that for pair-production ( $47 \text{ g cm}^{-2}$ ) and the radiation length for bremsstrahlung ( $37 \text{ g cm}^{-2}$ ). Thus, on average, a hadronic EAS will develop lower in the atmosphere than an EM EAS.

The average rest mass energy per particle is much greater in a hadronic EAS than in the purely EM case. The lateral distribution is therefore not dominated by multiple Coulomb scattering, but rather the extreme transverse momentum kick associated with pion production ( $\sim 0.4 \text{ GeV}/c$ ). Accordingly a hadronic EAS will exhibit a larger lateral spread than a EM EAS initiated by a primary particle of equivalent energy. The longitudinal and lateral development of a 100 GeV photon initiated EAS is compared to that initiated by an equivalent energy CR in Figure 2.2. Complex multi-particle processes are involved in the development of a hadronic EAS, whereas an EM EAS is dominated by simple three-particle processes such as bremsstrahlung and pair-production. EM showers are therefore more regular with smaller fluctuations than hadronic showers.

## 2.2 Cherenkov Radiation

When a charged particle passes through a dielectric medium with a velocity greater than the group velocity of light in the medium, light with a continuous spectrum is emitted along the track of the particle. This process is known as the Cherenkov effect and was discovered by its namesake in 1934. The theory of Cherenkov radiation was tackled a few years later by Frank and Tamm, and a comprehensive review is given by Jelley in [98]. In this section the role of Cherenkov radiation in the ground based observation of high-energy  $\gamma$ -rays and the underwater detection of neutrinos is examined.

### 2.2.1 The Nature of Cherenkov Radiation

A charged particle moving inside a dielectric medium with velocity  $v = \beta c$  emits Cherenkov light when  $\beta > 1/n$ , where  $c$  is the speed of light in a vacuum and  $n$  is the refractive index of the medium. As the particle travels it disrupts the local EM field in the medium. Electrons in the atoms of the medium are displaced and polarized by the passing EM field creating electric dipoles. In a dielectric material photons are emitted as the dipoles re-orientate and the electrons restore themselves to equilibrium after the

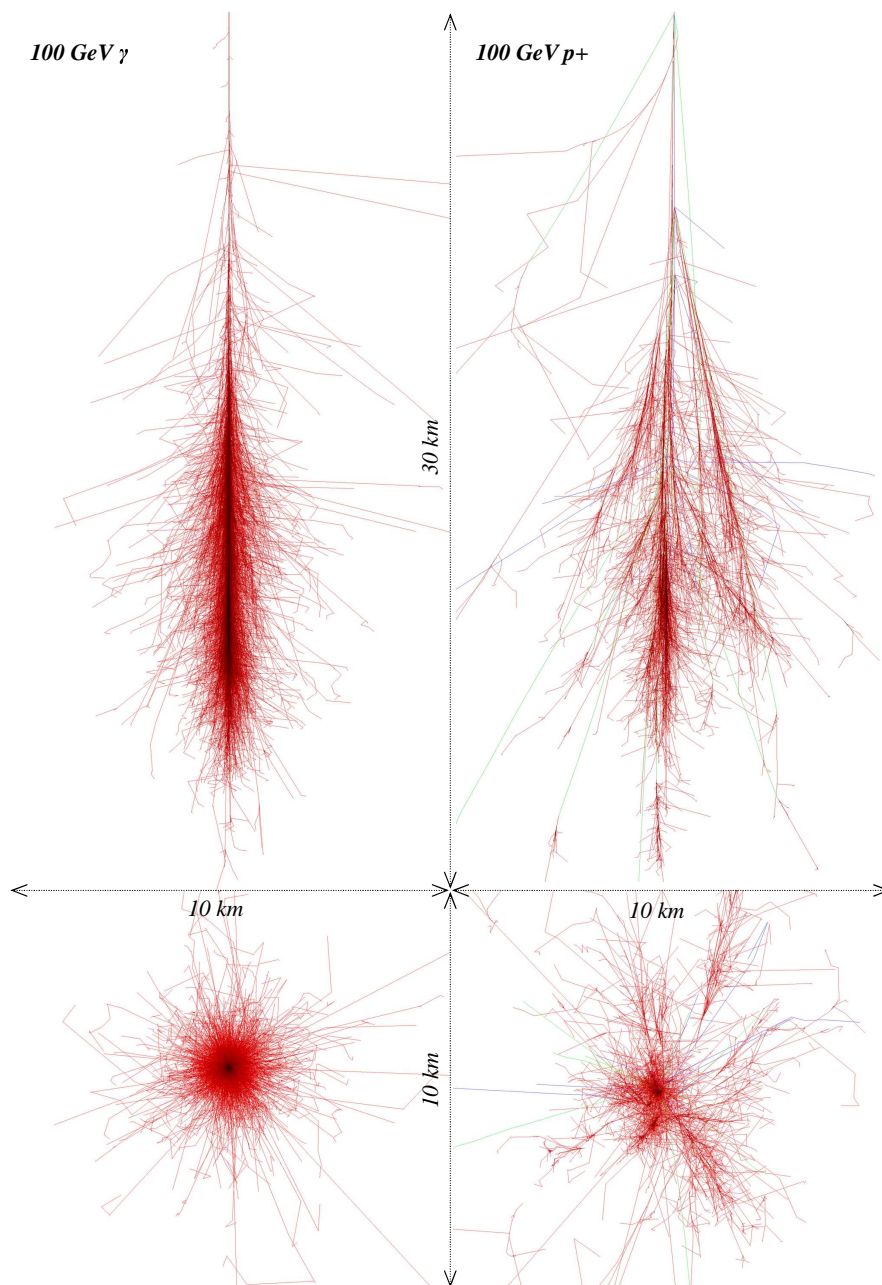


Figure 2.2: The development of 100 GeV  $\gamma$ -ray (left) and 100 GeV proton (right) induced air showers. The upper panels show the longitudinal development of a cascade, and the lower panels the lateral distribution. These images were produced using Corsika with a fixed interaction height of 30 km a.s.l. Red tracks are used to indicate electrons, positrons and  $\gamma$ -rays. Adapted from F. Schmidt, "CORSIKA Shower Images", <http://www.ast.leeds.ac.uk/~fs/showerimages.html>.

disruption has passed. At non-relativistic speeds these photons interfere destructively between the centres of emission and no radiation is detected as shown in Figure 2.3(a). However, once the velocity of the particle exceeds the phase velocity of light ( $\beta > 1/n$ ) the situation depicted in Figure 2.3(b) is obtained. Under this scenario the particle is travelling faster than its own EM field and the emission interferes constructively at the wave front according to Huygen's principle as shown in Figure 2.3(c). The Cherenkov wave front propagates at a fixed angle with respect to the charged particle's trajectory given by:

$$\cos \theta = 1/(\beta n). \quad (2.1)$$

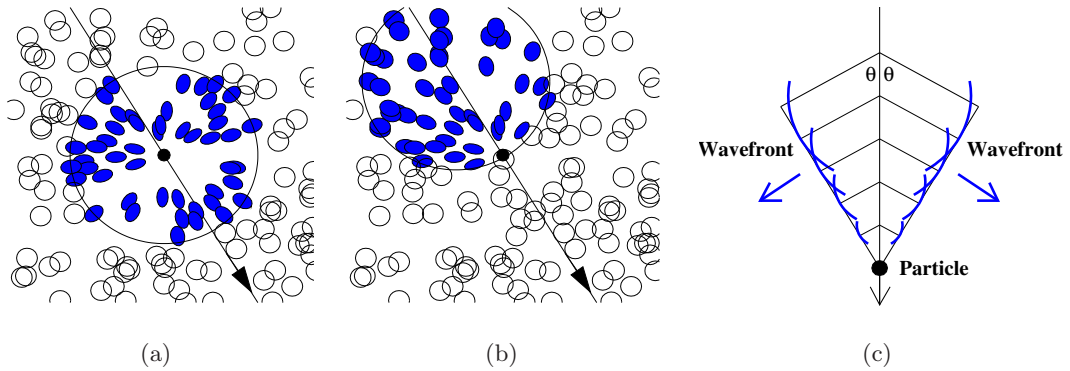


Figure 2.3: A charged particle travelling through a medium at a non-relativistic velocity (a) and relativistic velocity (b). In the non-relativistic case the orientation of the polarised atoms results in destructive interference. In the relativistic case the polarised atoms align, allowing constructive interference and resulting in Cherenkov radiation emitted at an angle  $\theta$  to the direction of the charged particle (c). Taken from [41].

It is apparent that the maximum emission angle occurs when the particle is ultra relativistic and  $\beta = 1$  given by:  $\theta_{max} = \cos^{-1}(1/n)$ . In water, where  $n = 1.33$ ,  $\theta_{max}$  is  $41^\circ$ , whereas for air at sea level,  $n = 1.00029$ , and  $\theta_{max}$  is correspondingly only  $1.3^\circ$ .

The minimum particle energy required for the production of Cherenkov light is given by:

$$E_{min} = \gamma_{min} m_0 c^2 = \frac{m_0 c^2}{\sqrt{1 - 1/n^2}}, \quad (2.2)$$

where  $m_0$  is the rest mass of the charged particle. In water the threshold energy for electrons, muons and protons is 0.76 MeV, 159 MeV and 210 MeV respectively, and for air the corresponding values are 21 MeV, 4.4 GeV and 39 GeV (again at sea level).

The number of photons emitted by a particle of charge  $z$  per unit path length and wavelength is:

$$\frac{dN^2}{dx d\lambda} = \frac{2\pi\alpha z^2}{\lambda^2} \left(1 - \frac{1}{\beta^2 n^2}\right), \quad (2.3)$$

where  $\alpha$  is the fine structure constant ( $e^2/\hbar c = 1/137$ ). Due to the wavelength dependence of the refractive index the condition for Cherenkov emission can only be satisfied in the UV to near IR region of the spectrum (300 nm to 600 nm) in both water and air. In addition the  $1/\lambda^2$  dependence of the number of photons emitted causes the Cherenkov emission to peak at the shorter wavelengths, in the UV region.

In water the refractive index does not vary along the length of the particle track whereas in air the refractive index depends upon the height at which the light is emitted (see the proceeding section). Additionally Cherenkov light in water need only travel tens of meters before reaching the detector, whereas in air the light will typically travel ten kilometres. The Cherenkov yield at ground level is greatly reduced by a combination of Raleigh scattering, Mie scattering and absorption in the Ozone layer resulting in a spectrum peaking at around 330 nm (see Figure 2.4). A relatively small amount of attenuation and scattering in water also alters the Cherenkov spectrum seen by a UND, which peaks in the blue, near 470 nm, where the water is most transparent.

### 2.2.2 Cherenkov Radiation in Extensive Air Showers

In an EAS electrons and positrons are the main sources of Cherenkov light. As mentioned in the previous section the threshold for this is 21 MeV at sea level. This increases to 37 MeV at 8 km altitude due to the variation in the refractive index of air with height a.s.l. In the simplest model (see [88]) this may be represented by:

$$n = 1 + \eta_h = (1 + \eta_0) \exp(-h/h_0), \quad (2.4)$$

where  $\eta_0 = 2.9 \times 10^{-4}$ ,  $h_0 = 7.1$  km and  $1 + \eta_h$  is the refractive index at height  $h$ .

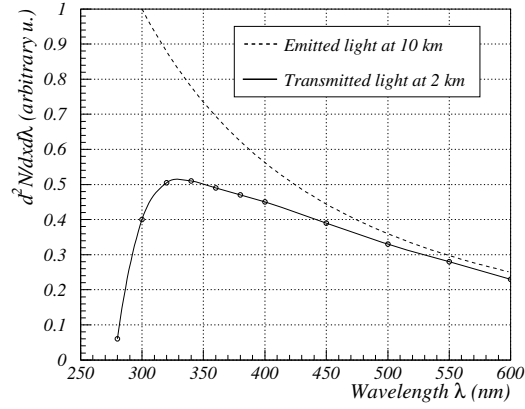


Figure 2.4: The intrinsic Cherenkov emission spectrum compared to the spectrum after absorption in the atmosphere. Taken from [50].

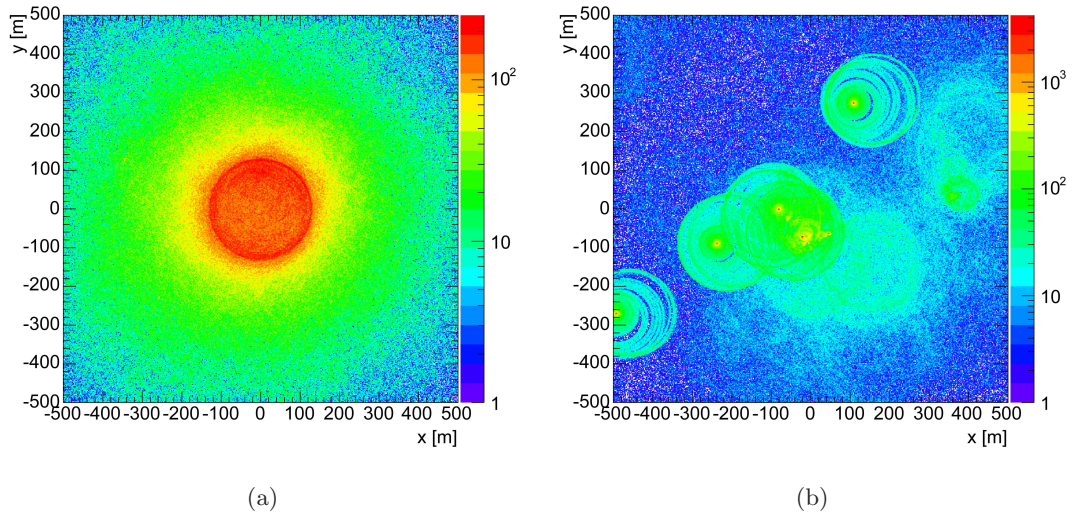


Figure 2.5: Cherenkov light pools at ground level from showers initiated by (a) a 300 GeV  $\gamma$ -ray and (b) a 500 GeV proton. Figure courtesy of G. Maier.

Assuming  $\eta_h \ll 1$  the Cherenkov threshold energy and maximum emission angle at height  $h$  may be written as:

$$E_{th}^{Che} = \frac{m_0 c^2}{\sqrt{2\eta_h}} \quad \theta_{max} = \sqrt{2\eta_h}. \quad (2.5)$$

Figure 2.6 shows the variation of Cherenkov emission angle and threshold with height

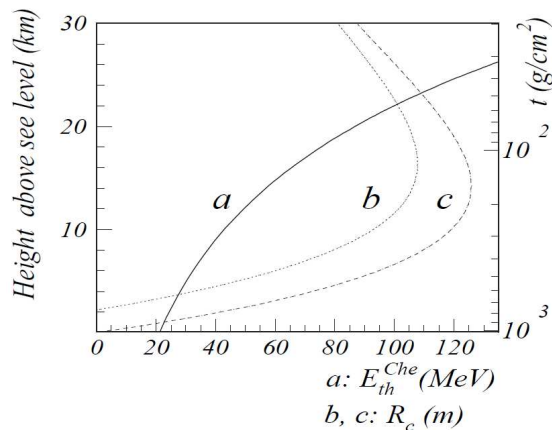


Figure 2.6: (a) Relation between  $E_{th}^{Che}$  and the height of emission  $h$ ; (b) Relation between  $R_c$  at  $h_{obs} = 2200$  m and  $h$ ; (c) Relation between  $R_c$  at  $h_{obs} = 0$  m and the height  $h$ .

a.s.l. for an ultra relativistic, vertically incident electron. Note that at a height of  $\sim 8$  km, corresponding to the point at which a 1 TeV  $\gamma$ -ray induced EAS reaches maximum development, the Cherenkov threshold ( $\sim 21$  MeV) is well below the critical energy ( $\sim 83$  MeV). Hence Cherenkov light continues to be generated after the shower begins to die out.

It follows directly from  $\theta_{max}$  that the radius of the Cherenkov pool from emission at height  $h$  is given by:

$$R_c = (h - h_{obs}) \tan(\theta_{max}), \quad (2.6)$$

where  $h_{obs}$  is the height at which the pool is observed. The dependence of  $R_c$  on  $h$ , again for an ultra-relativistic, vertically incident electron is also shown in Figure 2.6. The radius of the Cherenkov pool reaches a maximum for light emitted between 10 km and 20 km a.s.l. Assuming the trajectory remains vertical with no lateral displacement, then as the electron proceeds towards ground the Cherenkov angle opens, focussing the radiation into a narrow annulus at  $R_c \sim 120$  m, see Figure 2.7(a)(b). Of course the single electron would not survive the entire path length; it would fall below the Cherenkov threshold due to radiation and ionisation losses long before reaching the Earth's surface. However, the same geometric Cherenkov pattern is observed from the many  $e^\pm$  of an EM shower, assuming the charged particles propagate close to the direction of the primary,

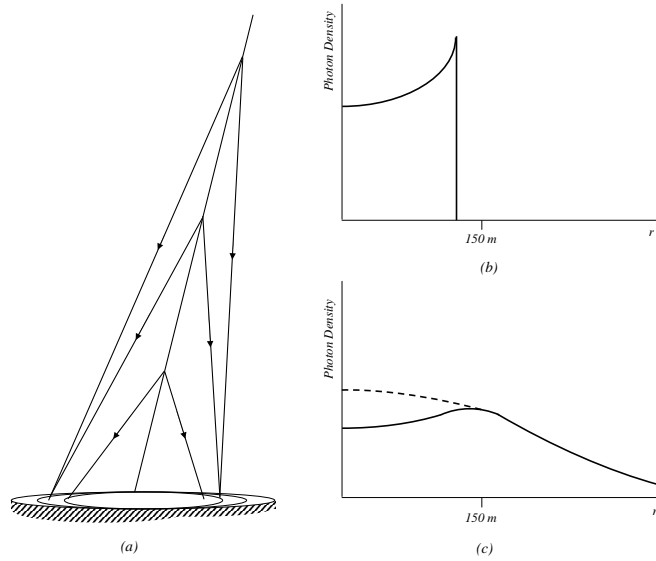


Figure 2.7: (a) Cherenkov radiation cones from particles moving down the shower axis (angles exaggerated) and (b) resulting photon distribution. (c) Modified lateral distribution when particles are scattered about the axial direction (schematic). Reproduced from [83]

and therefore each other. In reality multiple Coulomb scattering diverts the particles from this ideal trajectory. The Cherenkov ring is broadened, but does not disappear for showers that develop high enough in the atmosphere where the  $e^\pm$  have energies above  $\sim 1$  GeV [83]. At lower altitudes, and therefore lower average particle energies, the  $e^\pm$  are more scattered and the Cherenkov ring is washed out. The pattern is further distorted when the tail of the shower penetrates the observation level, increasing the intensity of the light pool close to the shower axis. The Cherenkov ring is therefore most prominent for lower energy  $\gamma$ -rays, which interact high in the atmosphere and produce showers that die out far above the observation level. The broadening of the Cherenkov ring is illustrated schematically in Figure 2.7(c). Around 50% of the total Cherenkov light is contained within the 'hump' of this ring and originates from charged particles radiating at heights between 6 km and 10 km. Recall that a 1 TeV  $\gamma$ -ray induced shower reaches maximum development at  $\sim 8$  km.

As mentioned in the preceding section, on average, a hadronic EAS will develop lower in the atmosphere than an EAS induced by a  $\gamma$ -ray. Therefore the Cherenkov emitting

charged component will be carried much closer to the observation level. The Cherenkov light pool is correspondingly more intense near the shower axis for a hadronic EAS and the ring structure is absent. Figure 2.5 shows the resulting distribution of Cherenkov light at ground level (2200 m a.s.l.) for a 300 GeV photon and 500 GeV proton initiated EAS. The Cherenkov pool of a hadronic EAS is also more irregular than that originating from a  $\gamma$ -ray. As discussed in Section 2.1.2 only one third of the primary hadron's energy is contained in EM sub showers, so a hadron will produce a less intense light pool than a  $\gamma$ -ray of equivalent energy. Hadronic cascades contain particles capable of Cherenkov emission other than electrons and positrons, such as muons which penetrate to ground level. The muons land over a wide area, due to the lateral spread of the hadronic EAS, creating localised hot spots of Cherenkov light about their impact points and thus adding further to the irregularities in the light pool of a hadronic EAS.

## 2.3 The Imaging Atmospheric Cherenkov Technique

The first detection of Cherenkov light produced by CR air showers in the atmosphere was made over half a century ago [64]. Today the basic detection method remains essentially unchanged and has been demonstrated by collaborations worldwide to successfully discriminate  $\gamma$ -rays from the overwhelming CR background. In this section the IACT technique and the detector elements are introduced. IACT performance is described in terms of collection area, angular resolution and energy threshold. Crucial differences between signal and background images are illustrated.

### 2.3.1 The Detection Principle

As discussed in the previous section a  $\gamma$ -ray incident on the Earth's atmosphere will result in a pool of Cherenkov light approximately 150 m in radius on the ground for an observation level of 2 km a.s.l.; depending on the incident direction of the primary particle. An appropriately oriented reflector placed within the Cherenkov pool shaped to focus the light onto a pixellated camera at the focal plane which is read out to fast counting electronics is used to record an image of the shower. The shape, orientation and size of the image may be used to determine the nature, direction and energy of the

primary particle.

Collectors are either parabolic or spherical. In both cases large reflectors are constructed from many smaller mirror segments. Unlike those used in optical astronomy the mirrors in an IACT may be fairly crude, and exhibit a reflectivity of around 90% at best. The camera typically consists of many tightly packed PMTs fitted with Winston cones to increase the collection efficiency. PMTs have a very fast time response ( $\sim 2$  ns) and are used to increase the SNR by exploiting the characteristically short duration of Cherenkov light from an EAS. The analogue signals from the camera may be transmitted to a counting house before digitisation, or digitised in the camera itself. Either way fast electronics are required to accurately reconstruct the fast PMT signals. The rate of data acquisition is generally controlled by a multi-level trigger system.

### 2.3.2 Collection Area

The collection area of a space-based  $\gamma$ -ray observatory is less than  $1 \text{ m}^2$ , and due to the ever decreasing flux of  $\gamma$ -rays with energy they are unsuitable for VHE observations. Unlike space-based observatories the atmospheric Cherenkov technique does not rely upon the primary photon interacting directly with the detector. Instead the IACT must simply lie within the Cherenkov light pool to record an image of the EAS resulting from an incident  $\gamma$ -ray. In relation to its size an IACT may therefore obtain an enormous collection area of  $\sim 5000 \text{ m}^2$ . The collection area is affected by photon energy and the zenith angle of observations. A more energetic primary photon will cover a broader distribution of Cherenkov photons on the ground, resulting in a larger collection area. Similarly, photons with a large zenith angle will have a larger area on the ground, but at the cost of a decrease in the density of Cherenkov photons per square meter.

### 2.3.3 Imaging

Figure 2.8 illustrates the principle of Cherenkov imaging for an EAS parallel to the optical axis of the telescope. Cherenkov light emitted from  $A$  and  $B$  hits the reflector at angles  $\phi_1$  and  $\phi_2$  and is projected on a camera in the focal plane at a corresponding distance from the focal point. Note that due to the finite angular acceptance of the camera the longitudinal extent of the EAS may not be mapped in its entirety. Light

from the top of the EAS is incident to the reflector at smaller angles and is mapped to the centre of the camera, whereas light from the bottom of the EAS lands near the edge of the camera. The length of the image in the camera therefore depends on the range:  $\Delta\phi = \phi_2 - \phi_1$ . The lateral extent of Cherenkov light in the EAS, emitted between  $C$  and  $D$ , forms the width of the image in the camera. The image is roughly elliptical and its orientation indicates the direction of the shower axis.

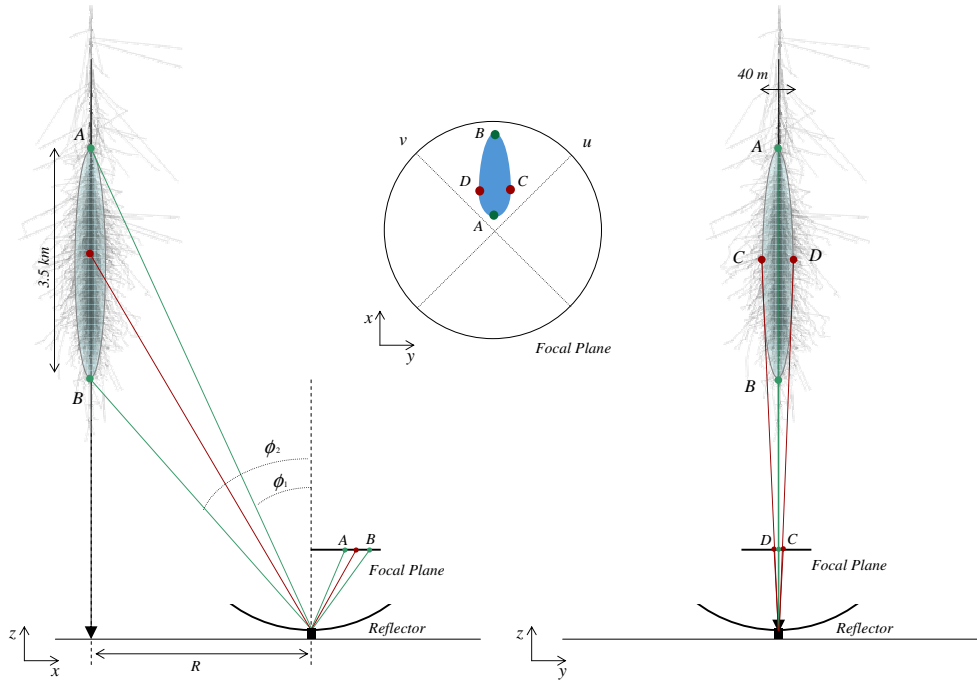


Figure 2.8: An EAS parallel to the IACT optical axis produces an image in a camera at the focal plane (centre) with a length corresponding to the longitudinal component (left) and a width related to the lateral spread of the EAS (right). The mapping is not linear so the image in the camera is asymmetric relative to the original distribution.

The image axis in the focal plane points, on the camera centre side, to the image of the shower impact point on ground and, on the other, towards the source position. The image is distorted by the asymmetric distribution of Cherenkov light in the EAS, aberrations in the reflector, non-linear mapping, and a finitely pixellated camera. As the EAS moves further from the telescope light from  $A$  and  $B$  intersects the reflector further from the optical axis. The angles  $\phi_1$  and  $\phi_2$  increase by different amounts. Thus the image moves towards the camera edge and  $\Delta\phi$  increases so that the image becomes elongated. As the shower is tilted in the  $x, z$  plane the image shape and distance from the camera centre changes. The image rotates around the camera centre as the shower is rotated about the telescope's optical axis. The angle the shower makes with the vertical in the  $y, z$  plane,  $\theta_y$ , offsets the head of the image from the camera centre, whilst the tail remains at the same point. The axis of the elliptical image therefore forms an angle,  $\alpha$ , with a line drawn from the camera centre to the centre of gravity of the image. The IACT technique relies on the ability to correctly isolate  $\gamma$ -ray induced images in the camera. The "Hillas parameters" describe the shape, orientation and light content of the shower images and, developed by A.M. Hillas in 1985 [84], are still the standard method to describe and distinguish between  $\gamma$ -ray and hadronic images. In Chapter 7 the Hillas parameters and their use will be expanded upon.

#### 2.3.4 The Cherenkov *Flash*

The average flux of Cherenkov photons from EAS is hugely outweighed by background light from the night sky. Cherenkov flashes are only detectable as they consist of light emitted from an ensemble of many particles and are of a very short duration. A 1 TeV  $\gamma$ -ray will typically produce a Cherenkov flash lasting 5 ns with a flux of  $\sim 50$  photons  $\text{m}^{-2}$  within 100 m of the shower axis at ground level (2000 m a.s.l.). An IACT with a FoV of  $1^\circ$  will, when correctly oriented, capture the full angular extent of this pulse, whilst only collecting 1 - 2 NSB photons in the 5 ns sampling window. Thus the ability to detect a weak Cherenkov pulse, from a low energy  $\gamma$ -ray, is limited by fluctuations in the NSB. Assuming an integration time,  $\tau$ , greater than the Cherenkov flash time, the SNR is given by:

$$\frac{S}{N} = \frac{S}{\sqrt{B}} = \int_{\lambda_1}^{\lambda_2} C(\lambda) \sqrt{\frac{\eta(\lambda)A(\lambda)}{B(\lambda)\tau\Omega}} d\lambda, \quad (2.7)$$

where  $C(\lambda)$  is the Cherenkov photon flux within the wavelength sensitivity range of the PMT ( $\lambda_1 - \lambda_2$ ),  $A(\lambda)$  is the mirror collection area, which depends on the mirror reflectivity and hence wavelength, and  $\eta(\lambda)$  is the wavelength dependent quantum efficiency of the PMT.  $B(\lambda)$  is the emission spectrum of the night sky background and  $\Omega$  is the solid angle.

The energy threshold of the detector is typically defined as the peak in the differential trigger rate and therefore depends on the spectrum of the source under observation. In ground-based  $\gamma$ -ray astronomy the energy threshold is typically defined by observing the VHE  $\gamma$ -ray standard candle, the Crab Nebula (see Chapter 7). The energy threshold, prior to analysis, is related to the SNR and may be described as:

$$E_{th} \propto \frac{1}{C(\lambda)} \sqrt{\frac{B(\lambda)\tau\Omega}{\eta(\lambda)A(\lambda)}}. \quad (2.8)$$

### 2.3.5 Photon Collection

The collecting reflector of an IACT typically consists of many smaller mirror segments. These may be square, hexagonal or circular, and are arranged either according to the Davies-Cotton design [48] or on a parabolic dish. Whereas light from a parabolic reflector arrives isochronously at the focal point, the Davies-Cotton design injects a time difference between light arriving at different collector radii. The effect of this time difference is discussed in [179]. In the parabolic case, a large parabolic surface is made from segments of the parabola. Many individual segments are required to correctly reproduce the parabola when assembled and this approach is costly. The Davies-Cotton design requires small segments of a sphere of radius  $2R$  be arranged on a frame comprising a much larger angular section of a sphere of radius  $R$ . Each mirror segment is tilted such that the normal to its centre points to the centre of the sphere of radius  $R$ . In this way each facet has a focal length  $f = 2R/2$  at a common point. The frame is constructed with a chosen opening diameter,  $D$ , and the resulting *f-number* is given by  $R/D$ . The Whipple-10 m telescope has an *f-number* of  $f/0.7$ .

A Davies-Cotton collector is subject to spherical aberrations as a function of the point of impact across each facet. It is therefore desirable to use small facets. Spherical aberrations are further reduced across each facet by increasing  $R$ . This has the additional advantage of increasing the overall collector  $f$ -number reducing the off-axis aberrations known as *coma*, which causes light from a point source, such as a star, to form an increasingly comet-like shape in the focal plane as the point source moves away from the optical axis. Parabolic reflectors do not suffer spherical aberrations, but are subject to greater *coma* aberrations. An  $f/2.0$  parabolic reflector will suffer a spread of  $0.04^\circ$  RMS at an incident angle of  $3^\circ$ , whereas a Davies-Cotton reflector will only be spread out to  $0.03^\circ$  RMS.

As collectors become larger the time dispersion associated with the Davies-Cotton design becomes unacceptably large. Parabolic reflectors must therefore be used but due to the large *coma* aberrations the FoV of the camera must be limited. In the case of H.E.S.S. Phase II, the camera FoV is reduced from  $5^\circ$  to  $3^\circ$  when increasing the reflector aperture from a 13 m Davies-Cotton reflector to a 28 m parabolic design. Whilst increasing the reflector area decreases the energy threshold, it prohibits the use of wide FoV cameras ( $\sim 10^\circ$ ), which are desirable to increase the sensitivity to higher energy  $\gamma$ -rays. Therefore the design modifications required to extend the energy range to lower and to higher regimes with a single telescope are diametrically opposed.

### 2.3.6 Sensitivity

The statistical reliability of  $\gamma$ -ray detections must be assessed as random fluctuations in the expected number of background events may mimic a source of VHE  $\gamma$ -rays. The statistical presence of a signal over the expected background may be described by equation 17 in Li and Ma 1983, [113] (see Section 7.9.1), in which the number of recorded events from the direction of the source is given by  $N_{on}$  and the number of background events, recorded off source, is given by  $N_{off}$ . Here an event is an image selected as  $\gamma$ -ray like, generally on the basis of selection cuts made on the Hillas parameters. The significance of a detection is given in units of standard deviation, where it is assumed that the fluctuations in background are Gaussian distributed. The observation window (typically a cone of opening angle  $\sim 1^\circ$  around the source position in the camera) in

which  $N_{on}$  is measured contains both signal and background events. The background expected to fall within the  $N_{on}$  region may be estimated as  $\kappa N_{off}$ , where  $\kappa$  reflects the ratio of time spent on-source to the time spent off-source, and is used to calculate an excess number of counts in the source region  $N_\gamma = N_{on} - \kappa N_{off}$ . It is this excess that is evaluated to assess the statistical presence of a VHE  $\gamma$ -ray source.

The number of standard deviations required to reliably claim detection of a source with modern instruments is generally taken as 5. The sensitivity of a given detector may then be described as the minimum flux required to produce a  $5\sigma$  detection in 50 hrs from a source with a  $\gamma$ -ray spectral index equivalent to that of the Crab Nebula, and requiring at least 10 excess events. This required flux may be given as:  $F_\gamma(E) = \frac{N_S}{A_\gamma(E)\tau}$ , where  $S$  is the required number of source  $\gamma$ -rays,  $A_\gamma(E)$  is the effective collection area of the detector for  $\gamma$ -rays and  $\tau$  is again the integration time.  $N_S$  may be obtained from the Li and Ma significance calculation by assuming  $N_{on} = N_S + N_B$  and  $N_{off} = N_B/\kappa$  given an expected number of background events in the on-source region of  $N_B = F_{CR}(E)A_{CR}(E)\tau\Omega$ , where  $F_{CR}(E)$  is the flux of CR,  $A_{CR}(E)$  is the effective collection area of the detector for CRs and  $\Omega$  is the size of the observation cone in steradians.

$A_\gamma(E)$  and  $A_{CR}(E)$  must be obtained from a large database of Monte Carlo simulations of extensive air showers induced by protons and  $\gamma$ -rays propagated through a detector simulation to determine the telescope response. The estimation of  $A_\gamma(E)$  and  $A_{CR}(E)$  relies upon the assumed  $\gamma$ -ray source and CR background spectral indices.

At low energies  $A_\gamma(E)$  drops and the background dominates causing a drop in sensitivity, represented by an up-turn in the curves shown in Figure 1.5. At high energies the background rapidly falls off and the area reaches a steady plateau, but the ever diminishing flux of VHE  $\gamma$ -rays causes the sensitivity curve to again turn up.

### 2.3.7 Angular and Energy Resolution

Due to the narrow emission angles in EM interactions, and the relative weakness of the Earth's magnetic field, IACTs achieve a high level of angular resolution. A shower can typically be reconstructed to within  $0.2^\circ$  of the incident direction of the primary  $\gamma$ -ray using a single, 10 m, telescope and down to  $0.1^\circ$  ( $0.05^\circ$  at optimum elevations) with a telescope array. With the statistics obtained from a few hundred excess  $\gamma$ -rays a source

location may be reconstructed to within a few arc minutes. The energy of a given  $\gamma$ -ray event is proportional to the light content of the image in a camera. The inherent ambiguity between image brightness, distance and energy (i.e. is an image faint because the EAS is distant, or small?) is overcome by using the images from several telescopes to accurately determine the location of the shower core.

The angular and energy resolution are estimated by propagating a set of Monte-Carlo simulations of  $\gamma$ -ray induced EASs through a detector simulation and measuring the RMS spread of the reconstructed source positions for all showers. Angular and energy resolution generally improve as a function of  $\gamma$ -ray energy. Higher energy  $\gamma$ -rays form larger images in the camera plane resulting in a more accurate determination of the shower direction and primary energy. A higher energy  $\gamma$ -ray is also more likely to illuminate a greater number of telescopes, further improving the reconstruction of the arrival direction and energy.

### 2.3.8 Stereoscopy

The most significant barrier to reducing the energy threshold using the imaging atmospheric technique to a regime below 200 GeV is the population of local muons. These can generate small, compact images in the focal plane almost indiscernible from those due to low energy  $\gamma$ -rays (see Section 2.3.9.4 and Figure 7.6). The use of multiple, appropriately spaced telescopes removes the contribution of these *local muons*, which are typically only seen by one telescope. To achieve this an array trigger requiring coincident events between multiple telescopes must be employed. This may be implemented off-line in software via GPS time stamping, or in real-time using hardware and requiring the telescopes to be connected to a central location. The benefits of such an array trigger are the subject of Chapter 7. The use of multiple telescopes also improves angular resolution and energy resolution, allowing both the shower core position on the ground and the source position in the sky to be determined.

### 2.3.9 Background Rejection

A major obstacle in ground based  $\gamma$ -ray astronomy is the huge abundance of camera images produced by background light. The background may be divided into four contribu-

tions: the night sky background (NSB), hadrons, muons and electrons. The background due to the diffuse  $\gamma$ -ray flux (both galactic and extra-galactic) above 30 GeV is about five orders of magnitude less than that from CRs [95; 163] and is therefore neglected here, though this becomes important in the detection of extended sources.

### 2.3.9.1 NSB

The NSB comprises diffuse and non-diffuse contributions. The diffuse component principally consists of zodiacal light (sunlight scattered by interplanetary dust) and airglow from atoms in the upper atmosphere excited by solar UV radiation during the day. Fluctuations in the diffuse NSB may cause individual pixels in the camera to trigger and add light to images from Cherenkov emission. The non-diffuse component of NSB comes from bright stars in the field of view. This contribution is predictable, and will trigger a single pixel for an extended period of time.

For an IACT with an alt-az mount the star will move across the camera as the telescope tracks a nearby point in the sky. Either the affected pixels are automatically suppressed by reducing the supply voltage due avoid damage, or the pixels are identified as over-active in the offline analysis.

Typically a telescope level multiplicity trigger, requiring that more than one pixel contains a signal over a given threshold for a given time, reduces the single pixel rate of  $\sim 1$  MHz to an overall camera rate of 250 Hz, which is in turn dominated by the hadronic background (see below). Thus, whilst NSB is present in recorded images it is extremely unlikely that NSB alone will trigger a telescope to read out. In a system with non-negligible read out dead time it is desirable to select coincident events at the hardware level in this way, which has the additional advantage of greatly reducing the network, disc space, and CPU time requirements of the system.

The distortion in the shape and light content of a Cherenkov image by NSB affects the event reconstruction and background separation capabilities of an IACT. It is therefore important to minimise the length of the read out window in time to accept the minimum amount of NSB whilst capturing the complete Cherenkov pulse. It is obvious that any broadening of the pulse by the PMTs or the read out system results in a longer sampling window, which consequently contains a larger NSB contribution. The addition of NSB

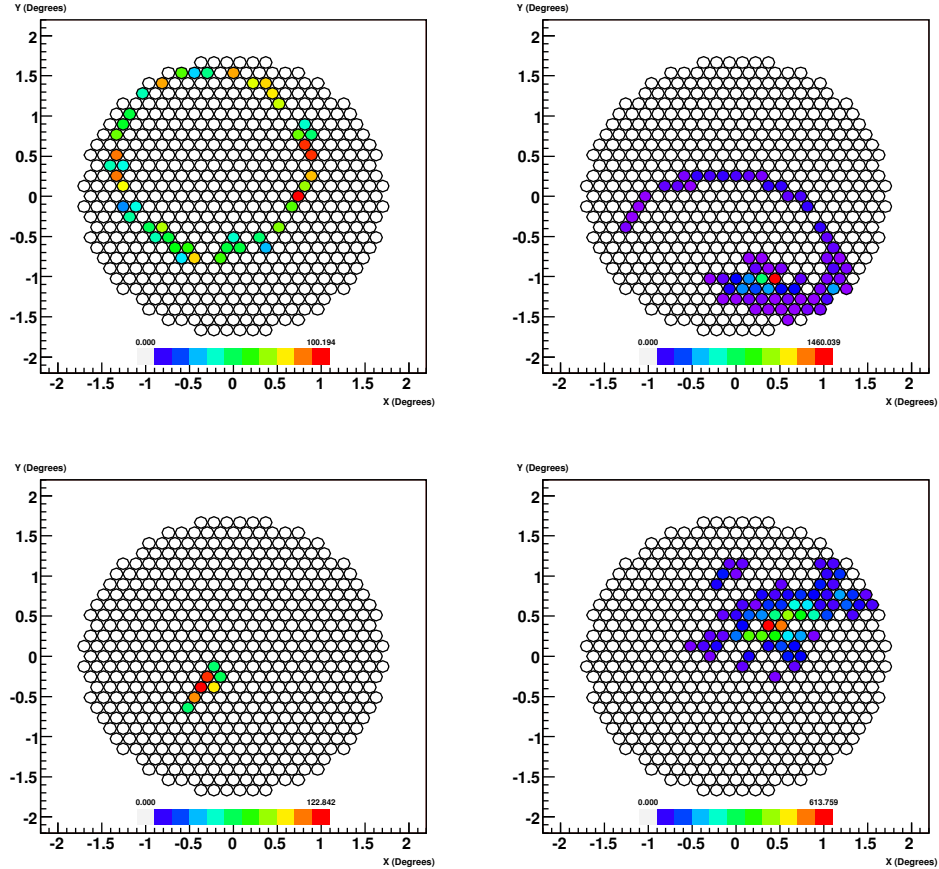


Figure 2.9: *Cherenkov images captured by a VERITAS telescope (see Chapter 3). Top-Left: local muon with a distinct ring. Top-right: CR and muon ring in a single image. Bottom-Left: Probable  $\gamma$ -ray. Bottom-right: CR. Taken from [41].*

to images from low energy  $\gamma$ -rays is a limiting factor in the energy threshold of the detector.

### 2.3.9.2 Hadrons

The overwhelming flux of hadronic CRs over  $\gamma$ -rays between 100 MeV and 10 TeV is dominated by protons and helium nuclei. These initiate EASs as described in Section 2.1.2 and result in EM sub-showers that produce images in the camera of an IACT similar to those due to  $\gamma$ -rays. These are not rejected by a simple multiplicity trigger as with NSB. Figure 7.6 shows the image from a hadronic CR compared to that from a presumed  $\gamma$ -ray.

The incident CR flux is isotropic due to deflection by galactic magnetic fields, hence hadronic images in an IACT will be randomly orientated in the camera.  $\gamma$ -ray images will all have the same orientation with the point closest to the camera centre pointing towards the source location. The Hillas parameter describing the orientation of the image,  $\alpha$ , may therefore be used to reject CRs from all but the source direction (see Chapter 7). Furthermore, hadron-induced showers have longer longitudinal and wider lateral particle distributions than EM showers of the same primary energy. The images recorded in the camera are therefore typically longer and wider than those due to  $\gamma$ -rays. Cuts on the Hillas parameters: length, width and size, further reduce the CR background. Nevertheless, due to the large statistical fluctuations, and outnumbering  $\gamma$ -ray showers by a factor of  $10^4$ , hadronic showers will occasionally produce images in the camera from the source direction that resemble  $\gamma$ -rays of a higher energy, passing the cuts on the Hillas parameters. Also real  $\gamma$ -ray events may be thrown away by stringent cuts, and the optimisation process becomes a balancing act. Hadrons therefore constitute the most important background for IACTs.

#### 2.3.9.3 Electrons

A cosmic electron with an energy above  $\sim 5$  GeV will produce an EAS identical in nature to that initiated by a photon of equivalent energy upon entering the atmosphere. Neglecting the effect of the Earth's magnetic field, electrons arrive isotropically and produce images of similar length, width and size to those due to  $\gamma$ -rays in the camera of a IACT. Thus they may only be rejected by their orientation in the camera. However, the differential flux of CR electrons above 10 GeV drops rapidly as a power-law with an index of -3.2. Thus, at higher energies the contribution of electrons to the overall background is negligible. At energies of around 50 GeV cuts on the orientation reduce the electron background to around a fifth of the hadronic contribution. As IACTs push for lower energy thresholds, towards the 10 GeV region, the background from cosmic electron induced showers will become increasingly troublesome.

#### 2.3.9.4 Muons

Early in a hadronic EAS pions lose energy through nuclear collisions. Further into the shower, decay becomes likely and muons are produced. Low energy muons below  $\sim 1$  GeV produced very deep into the EAS will not reach the Cherenkov threshold and are susceptible to decay. However, between  $\sim 1$  GeV and  $\sim 20$  GeV pions decay to muons with enough energy to produce Cherenkov light and high enough Lorentz factors to survive to ground level. These secondary muons produce pools of Cherenkov light with radii up to around 80 m over a large range of impact points and angles. A small fraction may reach a telescope and mimic the  $\gamma$ -ray showers. Most muons produce arcs in the camera of an IACT. Muons landing close to the telescope with small impact radii may produce full rings, as shown in Figure 7.6. Ellipses fitted to these muon images have a large *length* to *size* ratio, and may be rejected through cuts on the Hillas parameters (see Chapter 7). However, this rejects signals from low energy  $\gamma$ -rays, which also result in camera images with a high *length* to *size* ratio. This problem is avoided in arrays of telescopes. As long as the IACTs are spaced further than  $\sim 80$  m apart (depending on the size and angular acceptance of the IACT) and the array level trigger requires a coincidence between at least two telescopes, the local muons do not trigger the read out of the array. This condition also significantly lowers the hadronic background contribution, since the Cherenkov pool in such showers is less homogeneous than in purely EM EASs and the chance of a coincidence is correspondingly reduced. The effect of this array trigger condition on the muon and hadron rejection capabilities and the sensitivity and energy threshold of a telescope array are examined in Chapter 7.



## Chapter 3

# VERITAS

---

In Chapter 1 the principle of underwater neutrino detection and the atmospheric Cherenkov technique were introduced. The current and future detectors were described and the areas of technological interest for this work highlighted. New technology is developed primarily for VERITAS and as such the IACT technique was described fully in Chapter 2. A detailed technical description of VERITAS is presented in this chapter and the calibration schemes and data analysis methods are outlined. In Chapter 7 the single telescope and array performance of VERITAS are obtained from observations of the Crab Nebula.

The Very Energetic Radiation Imaging Telescope Array System or VERITAS is, in its current incarnation, an array of four 12 m-diameter IACTs located at the base camp of the Fred Lawrence Whipple Observatory in Southern Arizona at an elevation of 1270 m. The four telescope VERITAS array saw first light on April 28 2007. VERITAS offers a natural northern-hemisphere counterpart, of comparable sensitivity, to H.E.S.S., and greater sensitivity at higher energies than MAGIC.

### 3.1 Introduction to VERITAS

VERITAS grew out of the Whipple collaboration [172] [173] and currently has around 65 members in more than 20 institutions. The collaboration has a history of technological innovation and the detector is designed to allow changes, upgrades and experimentation to open the window to new methods of background rejection and exotic physics. The University of Leeds has contributed a large amount of hardware development to VERITAS, including the level 2 (L2) trigger system and the DAT modules.

Originally consisting of seven telescopes, funding problems led the collaboration to reduce the array to four telescopes in 2002 [174]. Several sites were considered for the project until the foundations for the first four telescopes were laid in Horseshoe Canyon at Kitt Peak.



Figure 3.1: (a) The first VERITAS Telescope installed at the Whipple Observatory base camp. The control room housing the electronics and power supply systems is shown in the foreground. (b) The full VERITAS four telescope array from the air with the telescope separations marked.

In February 2003 a prototype was constructed at a temporary site at the Whipple Base Camp on Mt. Hopkins. It was operated initially in 2004 as a prototype, with one third of the mirror area and half of the PMTs of the completed telescope [170]. Due to problems with access to the Kitt Peak site the prototype was upgraded to the first full VERITAS telescope (T1) in February 2005 [91]. The second, T2, followed in October 2005 and stereo observations were taken using GPS timing to match events in software in December 2005. The first true stereo observations were taken in March 2006. The

third and fourth telescopes (T3 and T4) saw light in September 2006 and February 2007 respectively. The four telescopes completed an engineering stage in March 2007 and the array saw official first light in April 2007.



Figure 3.2: *The VERITAS four telescope array installed at the Fred Lawrence Whipple Observatory base camp in southern Arizona at an altitude of 1270 m.*

Figure 3.1 (a) shows the first complete VERITAS telescope in 2005. The building closest to the telescope contains the trigger and VERITAS data acquisition (VDAQ) electronics and is the control room from which the telescope is operated. The four telescope array is shown in Figure 3.2. The construction of the array at the Whipple Observatory Base Camp forced the telescopes to be spaced as shown in Figure 3.1 (b). Originally the telescopes were to be arranged in a mercedes star, each separated by 80 m. Simulations show the Base Camp geometry does not significantly effect the performance [121].

## 3.2 Mechanical Structure and Optics

The mechanical structure of the each VERITAS telescope consists of an altitude-over-azimuth positioner and a tubular steel Optical Support Structure (OSS). The camera is supported on a quadropod, and a mechanical bypass of the upper quadropod arm transfers this load directly to the counterweight support. The positioner is a commercial unit manufactured by RPM-PSI (Northridge, California); the OSS is a steel space frame, custom designed by M3 engineering (Tucson, Arizona) and fabricated by Amber Steel (Chandler, Arizona)[65]. The maximum slew speed was originally measured to be  $0.3^{\circ}\text{s}^{-1}$ . Tests with a modified drive system showed that it was possible to reach max-

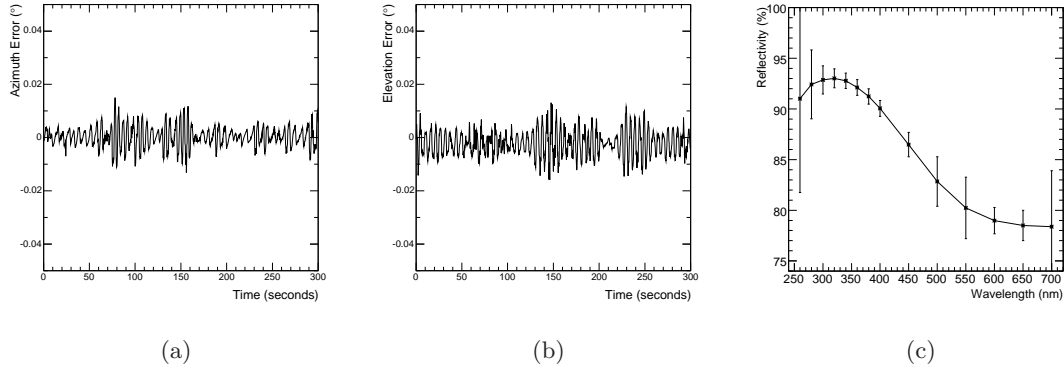


Figure 3.3: (a) The azimuth and (b) elevation residuals (difference between measured and requested position) for a short tracking run. (c) Average mirror reflectivity as a function of wavelength for photons normal to the mirror. Measurements were made in the laboratory after the mirrors were produced.

imum slew speeds of  $1^\circ\text{s}^{-1}$ , and this modified drive is now installed on all telescopes. The telescope encoder measurements are written to a VERITAS database at a rate of 4 Hz and indicate that the tracking is stable with a relative raw mechanical pointing accuracy of typically  $< \pm 0.01^\circ\text{s}^{-1}$  (Figure 3.3 (a), (b)).

OSS flexure and imperfections in the mechanics of the drive system lead to telescope misalignment. This misalignment can be corrected by applying a series of adjustments to the azimuth and elevation drives. The adjustments are calculated by pointing the telescope at a star whose exact location in the sky is known. A CCD camera is used to record an image of the star reflected onto a screen at the focal plane. The pointing of the telescope is adjusted, and further images recorded in an iterative procedure until the image of the star is coincident with the centre of the camera. The process is repeated for several stars at a range of elevations and azimuths and used to construct a ten parameter model of the OSS and drive system. These parameters are then used to correct the telescope’s pointing during observing.

The telescope reflectors are each comprised of 350 hexagonal mirror facets arranged in a Davies-Cotton design [48] to form a 12 m aperture with a 12 m focal length. A maximum spread of 5 ns is introduced into synchronous light normal to the reflector arriving at the focal plane, although work done during the early stages of this PhD suggests that

90% of the peak light intensity arrives within 2 ns [179]. Each facet (Figure 3.4 (a)) has an area of 0.322 m<sup>2</sup> resulting in a total reflector area of  $\sim 110$  m<sup>2</sup>. Hexagonal facets fit together in a honey-comb mesh and, unlike the H.E.S.S. circular facets, allow the full area of the OSS to be exploited. The facets themselves are made from glass, slumped and polished by DOTI (Roundrock, Texas) then cleaned, aluminized and anodized at the onsite optical coating laboratory. An aluminium layer is evaporated onto the glass to attain a thickness of approximately 1350 Å. Once the layer is set, a current is passed through the aluminium producing aluminium oxide. This adjusts the peak of the mirror reflectivity response curve to coincide with the peak in the Cherenkov spectrum from air showers at observing level. The reflectivity of the anodized coating at normal incidence is shown as a function of wavelength in Figure 3.3 (c); it is typically  $>90\%$  at 320 nm. Each facet has a  $24.0 \pm 0.2$  m radius of curvature and is mounted on the spherical front surface of the OSS (radius 12 m) using a triangular frame. Three adjustment screws allow each facet to be accurately aligned.

Reflector facets are aligned manually using a laser alignment system located at a distance of twice the focal length (24 m) from the centre of the reflector. The PSF response is shown in Figure 3.4 (b) and is measured to be  $0.06^\circ$  (FWHM) at the position of Polaris (elevation  $31^\circ$ ) degrading at higher elevations due to flexure of the OSS. The technique of bias alignment, wherein the mirror facets are aligned such that the PSF is optimum over the most useful observing range, has been successfully employed on the first VERITAS telescope to achieve a PSF of  $<0.06^\circ$  FWHM over the  $40^\circ$ - $80^\circ$  elevation range.

### 3.3 The Camera

The imaging camera of each VERITAS telescope consists of 499, 2.86 cm diameter PMT pixels (Photonis XP2970/02) housed in a 1.8 m square focus box (which allows for future expansion to increase the camera field-of-view). Each PMT has a quantum efficiency  $>20\%$  at 300 nm. The angular pixel spacing is  $0.15^\circ$ , giving a total field-of-view of  $\sim 3.5^\circ$ . Reflecting light cones are installed on the camera face and increase the overall photon collection efficiency by  $\sim 30\%$ . The front face of the T1 camera and the light cones are shown in Figure 3.5. The low noise, high gain PMTs with a fast rise time ( $<2$  ns) are required to detect the extremely faint and brief flashes of Cherenkov photons (3-4 ns).

The fast rise time also ensures a minimisation of the charge integration gate which leads to a maximisation of the signal to noise ratio.

The PMT high voltage (HV) is provided by a multi-channel modular commercial power supply (CAEN) which allows each PMT to be controlled individually. The HV is chosen to give a PMT gain of  $\sim 2 \times 10^5$ .

The signals are amplified by a high-bandwidth pre-amplifier integrated into the PMT base mounts requiring the signal be terminated with  $75 \Omega$ . These requirements will be crucial in the design of the analogue transmitter developed in Chapter 4. Average PMT currents are typically  $3 \mu\text{A}$  (for dark fields) to  $6 \mu\text{A}$  (for bright fields), corresponding to a night-sky photoelectron background of 100-200 MHz per PMT at this site. Each camera is fitted with a custom built system for monitoring the DC anode currents in the PMTs, read out at 10 Hz with an accuracy of  $0.5 \mu\text{A}$ . The current monitor system also provides power to the pre-amplifiers and provides power and read out channels for environmental sensors. There are 16 current monitor boards in a camera with 32 channels per board. The boards are daisy-chained, allowing for future expansion. Communication between the camera and the control room is via optical fibre.

The PMT analogue signals are sent via  $\sim 50$  m of  $75 \Omega$  coaxial cable to the telescope trigger and DAQ electronics housed in the control room. The choice of cable is driven by electrical and mechanical considerations [106]. Electrical tests on several cable candidates were performed by passing a short pulse through 50 m of cable and measuring the SNR. Increasing the SNR is equivalent to increasing the mirror area of the telescope. The cable weight is also an important consideration in the context of OSS flexure as approximately 6 km of cable is routed through the quadrapod arms. Using these factors and also considering cable diameter and cost, stranded core RG59(9803C) cable was chosen.

Environmental sensors monitor temperature and humidity changes in the cameras. Temperature changes can alter PMT gains by  $\sim 1\%/^{\circ}\text{C}$ , and PMT noise increases with temperature due to increased thermionic emission. Running the camera at high temperatures is also detrimental to many electronic components. During daytime testing camera temperatures can exceed  $50^{\circ}\text{C}$  in the Arizona summer heat, mostly due to the  $\sim 160$  W dissipated by the pre-amplifiers. Camera fans provide extra circulation, however this

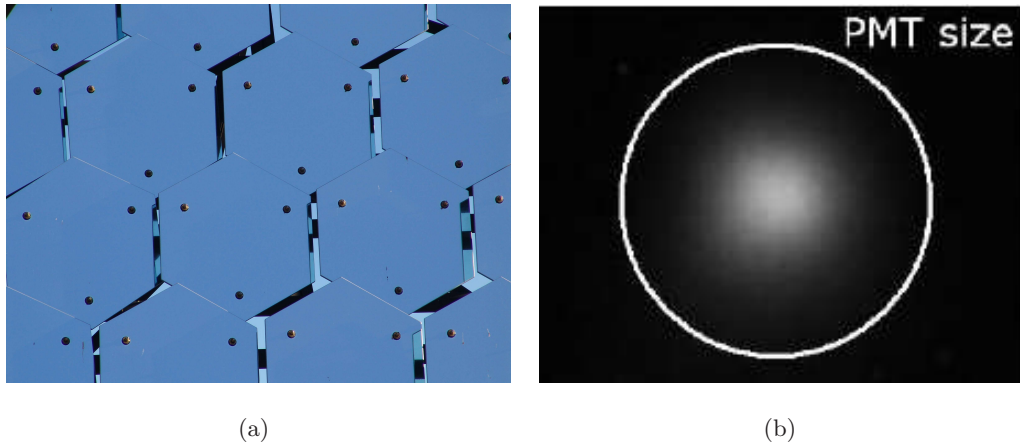


Figure 3.4: (a) A close-up view of the hexagonal VERITAS mirror facets. (b) An image of Polaris in the focal plane of the telescope recorded with a CCD camera. The point spread function is  $0.06^\circ$  FWHM. The circle indicates the size of a VERITAS PMT ( $0.15^\circ$  diameter).



Figure 3.5: (a) The 499 PMT pixel camera. The focus box is 1.8 m square. A remotely operated shutter usually covers the camera during daylight hours. (b) The light cones set into a plate which in turn attaches to the camera.

generally only permits camera operation for a few hours during daytime. It is important to monitor the humidity within the camera as moist air can become sufficiently conductive that arcing occurs between PMTs.

The VERITAS cameras are also fitted with a system for sending pulses directly into the PMT base [105]. These pulses simulate the Cherenkov light induced signal produced by the PMT and are used for testing and calibration. The charge injection system consists of a Programmable Pulse Generator (PPG) board with 16 fan-out/mask boards. The PPG can produce frequencies from 1 Hz to 1 MHz using an internal crystal oscillator. The clock can also be triggered with an external optical signal which allows precise timing of injected pulses between telescopes. The PPG board carries two pulse generators which can be used to set the pulse width from 1 ns to 10 ms and adjust the pulse height over 85 dB.

### 3.4 Trigger Chain

A multi-level trigger system is used within VERITAS to reduce the overwhelming NSB rate and the local muon contribution whilst efficiently recoding signals from  $\gamma$ -ray induced air showers. The pre-amplified PMT signals arrive at the control house and are input to VME implemented FADC modules, each of which accepts 10 channels as discussed in Section 3.5 and shown along side the trigger chain in Figure 3.6. Signals are split into the high and low gain channels, and a trigger channel. The trigger channel is fed into a Constant Fraction Discriminator (CFD), forming a level 1 (L1) trigger if the pulse height breaches a preset threshold. The 10 level 1 trigger channels are output in differential negative emitter coupled logic (NECL) form from an IDC header on the FADC module front panel. A signal splitter (SS) crate copies and maps the signals to the L2 Pattern Selection Trigger (PST) modules in patches corresponding to overlapping sections of the camera. An L2 trigger formed by a pre-programmed next-neighbour coincidence requirement is transmitted to the level 3 (L3) array trigger system in a central location using the DAT modules developed in Chapter 6. The array trigger system then returns a trigger if a preset number of telescopes have formed an L2 signal within an adjustable coincidence window.

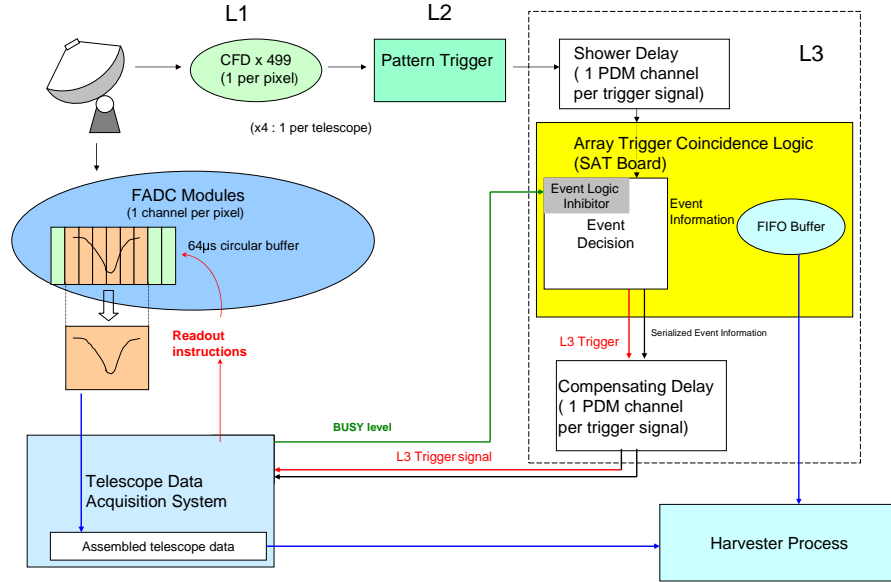


Figure 3.6: *The simplified VERITAS DAQ and trigger chain. Taken from [175].*

During the VERITAS commissioning stages the first telescope (T1) was operated at a 70 mV (6.7 pe) L1 threshold using a 3 fold L2 condition and the corresponding telescope trigger rate was  $\sim 150$  Hz. The L1 trigger rate, or single pixel rate, was  $\sim 50$  kHz. During the first stereo observations under the hardware implemented L3 trigger, two telescopes operate an array trigger rate of  $\sim 150$  Hz, corresponding to single telescope (L2) rates of  $\sim 1$ -2 kHz and single pixel rates of up to  $\sim 1$  MHz, for a L1 threshold of 50 mV (4.5 p.e.). Whilst the effect of the L3 on the array performance will be discussed in detail in Chapter 7, Figure 3.13(b) shows the effect of reducing the L1 threshold on single telescope trigger rate [90]. For low thresholds the NSB dominates and sets a sharp limit for each L2 trigger condition. Beyond this limit air showers, primarily hadronic, result in a steady trigger rate up to high thresholds.

### 3.4.1 Level 1 - The Constant Fraction Discriminators

The L1 trigger forms the first line of defence against the overwhelming NSB and PMT afterpulses. Signals below an adjustable threshold are rejected, lowering the overall telescope trigger rate to a manageable level and therefore directly affecting the energy

threshold of the detector.

Traditional discriminators trigger at a set voltage threshold which introduces a dependence of signal peak height and trigger time, an effect called time walk (see Figure 3.7(a)). Precise timing between the L1 trigger channels is desirable to define the FADC read out window to within a few ns and reduce the coincidence resolving time of the L2 PST and consequently the energy threshold of the detector. The larger the required overlap between pixel, the more likely that random NSB fluctuations will create a false L2 trigger. To achieve precise timing, each channel is equipped with a custom-designed constant fraction discriminator (CFD) [74] which has a trigger time independent of the input pulse height.

The CFD works by splitting the input signal into three. Whilst one third is delayed and inverted, another is attenuated with a fraction  $f$ . These are summed to create a zero crossing discriminator (ZCD). The third signal is fed into a traditional discriminator with a programmable threshold up to 140 mV corresponding to around 15 pe. The ZCD clocks the threshold discriminator decision into a flip-flop. The flip flop is reset after an adjustable time creating a programmable output width with a 12 step range between 4 ns and 25 ns, typically set to 10 ns. A 3-bit, 6 ns programmable delay is provided for each channel so as to correct for systematic differences in the relative signal paths due to cable length differences and the voltage-dependent PMT transit times.

Noise from fluctuations in the NSB distorts pulse shapes, affecting the rise and fall times and creating jitter in the ZCD. To counter this a small, constant voltage may be added to the ZCD input. Background light from stars and man-made pollution can not be eliminated and requires a larger offset to minimise the incurred jitter. Additionally the NSB may increase by a factor of four in the direction of the galactic plane. A large ZCD offset introduces a time walk into the CFD and may reject pulses strongly distorted by noise, decreasing the trigger efficiency of the detector. A novel circuit coupling the ZCD offset to the ZCD trigger rate is included in the CFD to optimise the balance between jitter, walk and trigger efficiency during real-time IACT operation. This feedback loop automatically adjusts the ZCD offset over  $\sim 1$  s when the noise level in the telescope FoV changes. For an input pulse of 6 pe and a trigger threshold of 5 pe in the presence of a, typical, NSB of 0.6 p.e./ns the jitter is reduced to  $\sim 0.75$  ns with no detriment to

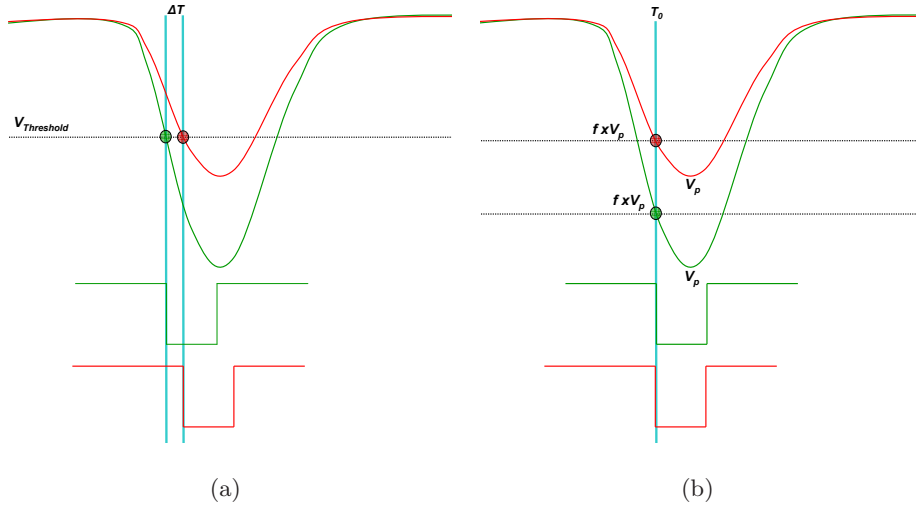


Figure 3.7: (a) The working principle of a traditional threshold discriminator. Pulses of different magnitudes arriving at the same time trigger the discriminator at different times incurring a time walk,  $\Delta T$ . (b) The same pulses trigger a CFD simultaneously at a time corresponding to a fraction,  $f \times V_p$ , of the pulse height,  $V_p$ .

the trigger efficiency at the cost of a  $\sim 0.8$  ns walk.

### 3.4.2 Level 2 - The Pattern Selection Trigger

The L2 topological trigger system reduces the rate of triggers due to random fluctuations in NSB and ion leakage within the PMTs and preferentially selects compact Cherenkov light images. A pre-programmed coincidence of 2, 3 or 4 CFD hits is required between adjacent pixels to form an L2 trigger. The required overlap time between adjacent CFD signals is  $\sim 6$  ns for T1 and  $\sim 10$  ns for T2, T3 and T4<sup>1</sup>. The innermost 463 camera pixels take part in the L2 trigger, and are divided into 19 overlapping patches of pixels. As shown in Figure 3.8(a) the first patch consists of 19 pixels at the centre of the camera, whilst the other 18 each span an elongated hexagon of 59 pixels. Pixels are copied and routed in these patches to the PST modules via a signal splitter housed in a custom built crate. The patches of 59 are internally copied and mapped to 5 overlapping hexagonal patches of 19 as shown in Figure 3.8(b).

<sup>1</sup>The PST modules in T2, T3 and T4 use a different model of comparator to that in T1 with a greater minimum overlap requirement. A different comparator is used simply due to the availability of components at the time of assembling the PST.

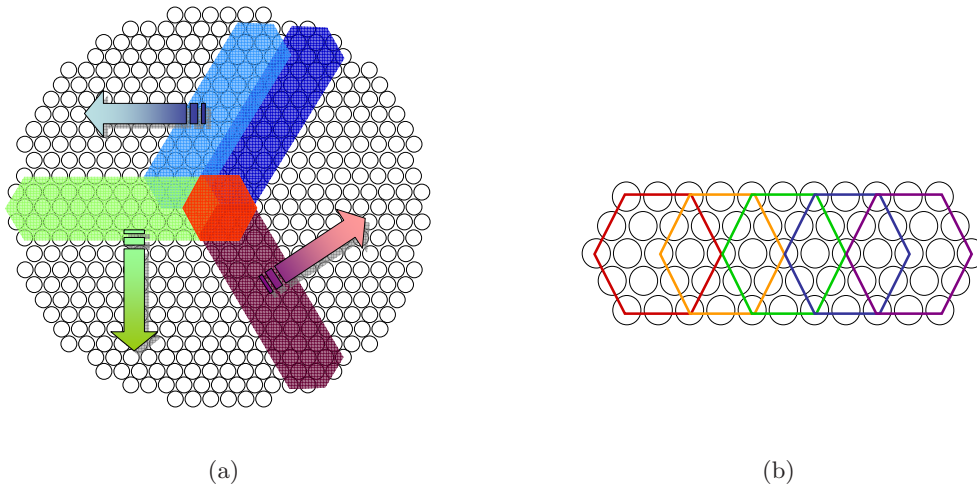


Figure 3.8: (a) The 19 overlapping patches of pixels covering 463 of the 499 PMT VERITAS camera. The first patch consists of 19 pixels arranged in a hexagon at the camera centre whilst the other 18 contain 59 pixels in elongated hexagons. (b) A patch of 59 pixels divided into 5 overlapping sections of 19 pixels within each PST module.

### 3.4.2.1 The Signal Splitter

The SS receives differential NECL inputs from the CFDs on the FADC boards across 24 input cards (SSICs) via two 20-way ribbon cables per card. The final SSIC uses only 3 of its inputs. The 20 differential NECL signals entering each SSIC are converted to TTL and routed through logic gates before conversion back to NECL and output to the backplane. The SSIC logic can be used to switch individual channels on or off and inject test pulses over a I<sup>2</sup>C-bus from an in-crate pulse generator. The pulse generator produces pulses with a width of 20 ns to 80 ns and can be triggered in software via a TINI embedded controller, also included in the crate, or externally through front panel inputs (NIM, ECL or TTL) up to a maximum rate of  $\sim 5$  MHz.

The input signals are copied and re-distributed via multiple wire-wrapping in the back of the crate to 19 output cards (SSOCs). Over 1100 pairs of connections are made on the backplane and each piece of wire is approximately the same length to minimise the channel-to-channel skew. The SSOCs provide two 60-way outputs and contain hard-wired delays to further correct the channel-to-channel timing within each group of 30 outputs. The bottom channel of each SSOC is connected to GND. The SSOCs are



Figure 3.9: *The front, (a), and rear, (b), of the SS crate showing the intricate wire-wrapping on the backplane.*

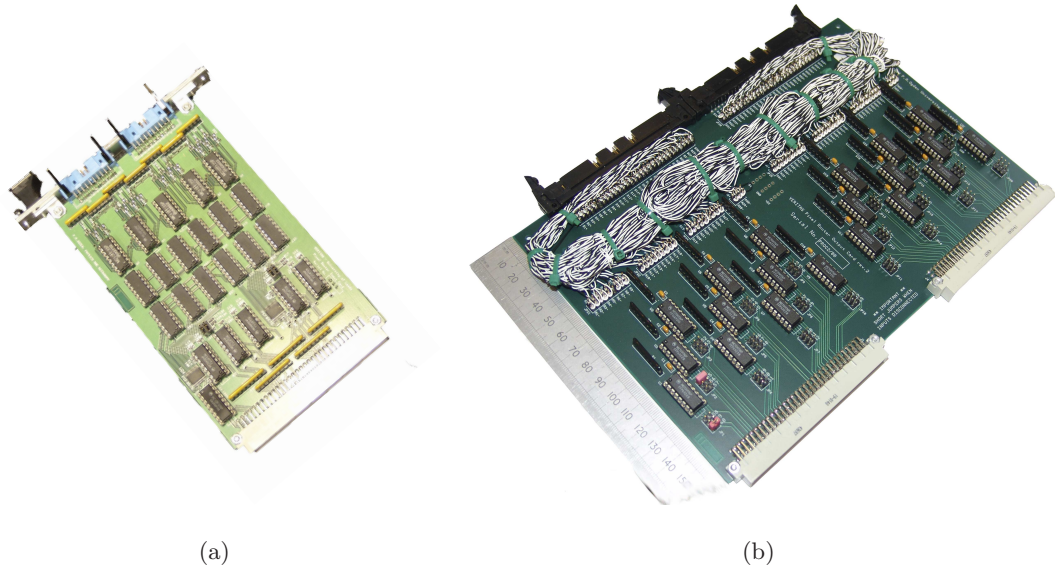


Figure 3.10: *A SSIC, (a), and SSOC with wire-wrapped delays, (b).*

connected in a one-to-one mapping to the PST modules via 30-way ribbon cables.

The delays needed on each SSOC channel must be individually calculated and implemented. A reference SSOC with a known, constant, amount of wire-wrapped delay on each channel is first used to measure the transit time through the crate of every output channel in every SSOC slot. Over 1000 measurements of the arrival time of the falling edge of a pulse relative to a the falling edge of a reference pulse at signal splitter in-

put are taken at the output for every channel. The temperature of the crate is kept constant at approximately 25°C by controlling the room temperature and using a fan-tray throughout the measurements. The measurements are then used to calculate the length of wire required on each output channel to correct the channel-to-channel skew<sup>2</sup>. All 19 SSOCs are wire-wrapped by hand and the measurements repeated to verify the alignment.

The delays for the SS installed in the VERITAS T2 telescope were calculated and hard-wired as part of the trigger development work for this thesis. The results are shown in Figure 3.11, and indicate an initial channel-to-channel skew with a range of 5.48 ns, which was reduced to 1.48 ns. The remaining skew is due to differences between the reference card and the other output cards, temperature variations and human error. The typical jitter introduced to a signal by the signal splitter was less than 200 ps (RMS). These results were typical of those obtained for the other three signal splitter crates. The SS characteristics and performance are discussed further in the context of the development of a high-speed topological trigger in Chapter 5.

### 3.4.2.2 The Pattern Selection Trigger

The 19 PST modules (see Figure 3.12) are housed in a CAMAC crate. The first PST module corresponds to the innermost patch of 19 camera pixels whilst the other 18 each receive signals from 59 pixels. The patches of 59 are internally copied and mapped to 5 overlapping hexagonal patches of 19 as shown in Figure 3.8(b). The system contains a memory look-up which can be pre-programmed in a few minutes to recognise patterns of triggered pixels in the camera of any 2, 3 or 4 adjacent pixels.

The differential NECL input signals are converted to TTL and each patch of 19 is summed and input to a majority logic comparator to check if there are more than any 2, 3 or 4 signals present. The comparator decision signal is used to latch the original 19 bit pattern into the address lines of a 512 kbit static RAM chip. Thus, the time consuming memory look-up operation only occurs if this voltage comparator fires.

This memory chip is programmed such that the  $2^{19}$  memory locations, corresponding

---

<sup>2</sup>Note that in this thesis the term *skew*, will refer to the difference in the average arrival time between two or more signals.

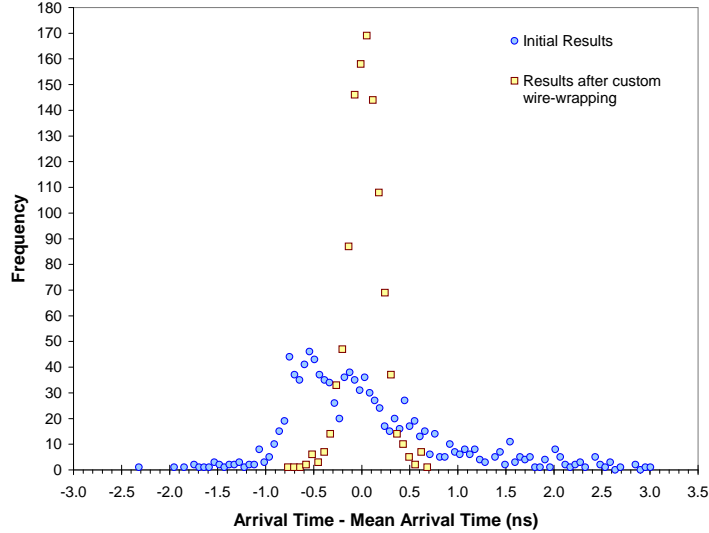


Figure 3.11: *The transit times of signals through the T2 signal splitter crate, relative to the average transit time, before (squares) and after (circles) hard-wired delay corrections.*

to all possible pixel combinations, contain a flag indicating adjacency or otherwise. If the pattern reaches an address indicating a valid pattern a FLAGOUT signal is set on the back pins of the module. The FLAGOUT signal is created by latching the memory look-up decision with a delayed version of the majority logic comparator signal, ensuring a jitter of  $<1$  ns (RMS) relative to the NECL inputs. The rear panel of the modules contains a 40-way connector. The lowest pins of this provides an NECL FLAGOUT signal, the propagation delay corrected logical OR of all the patch flags. This signal is passed to the rear panel of a custom built OR module. If any PST module is triggered then the OR module provides NIM outputs via the front panel. One of these outputs is the L2 trigger signal which is passed to the L3 system.

The PST system is similar to that used successfully on the Whipple-10 m telescope but with an improved channel-to-channel timing jitter [33]. The system offers versatility over previous attempts due to its reprogrammable nature. The PST modules used in T1 require an overlap time between adjacent CFD signals of  $\sim 6$  ns. The other three telescopes contain PST modules with alternative comparators which require a longer overlap of  $\sim 10$  ns between adjacent CFD signals. Each module requires around 10 s to



Figure 3.12: A *VERITAS* PST CAMAC module.

reprogram, or 3 minutes for the entire CAMAC crate. This will normally only be needed following a power reset. The PST returns a positive trigger decision after  $\sim 65$  ns and can then be reset via a NIM or ECL fast-clear input in  $\sim 22$  ns.

### 3.4.3 Level 3 - The Array Trigger

Cherenkov light from muons with large impact parameters form images in the camera plane virtually identical to those from VHE  $\gamma$ -ray initiated air showers. At low energies these "local" muons dominate the background. Local muons only produce Cherenkov light over a large enough area to trigger a single telescope. An array of telescopes may therefore remove local muons by requiring a coincidence between multiple telescopes to form an overall trigger.

For the first few months of operation T1 and T2 operated independently and coincident events were identified offline using the GPS timestamps as described in Section 3.5. In March 2006 a hardware array trigger system was installed which corrects the single telescope triggers for changing time delays due to the source movement across the sky. The performance benefits of a hardware implemented array trigger are investigated in Chapter 7.

The L3 array trigger system receives and, where appropriate, delays the L2 trigger inputs from the individual telescopes before transmitting a decision back to the telescopes. It also assigns a unique 32-bit event number to every event resulting from a L3 trigger

decision. This event number, along with a 16-bit summary of telescope trigger information, is sent back to the telescopes. In addition the array trigger logs rates and timing information for the L2 inputs. This additional information is stored in log files once a second and is accessible off-line via the VERITAS database that also stores information on the run, FADC and CFD settings (see Section 3.5) and telescope position.

Signals are distributed throughout the array over fibre-optic cabling via the custom built DAT modules developed for this thesis (see Chapter 6). The DAT modules allow the parallel distribution of 11 channels of data in each direction between a telescope and the array trigger. The devices are dead time free and introduce a nominal jitter 0.8 ns (95% C.L.) on a average channel and a maximum skew of 1.6 ns between the 11 channels.

There are a number of delays which are required by the array trigger system. The L2 signals are delayed to compensate for the different cable lengths associated with the physical geometry of the array. This equalises the L2 pulse arrival time from each telescope.

Since the telescopes will, in general, be located at different distances from the shower axis, Cherenkov light from an EAS will not arrive isochronously at each telescope. To compensate for this, signals are delayed by an amount depending on the elevation and azimuth of the telescopes. These delays are corrected approximately every ten seconds. The telescope tracking software writes the tracking data to the VERITAS database from which the array trigger can read the telescope tracking positions. The array system also generates L3 events at a rate of 1 Hz to trigger FADC read out in the absence of local triggers to record the electronic pedestal in the data stream. These signals do not require delays.

The time-corrected signals are passed to coincidence logic and only events which trigger a preset number of telescopes within a programmable coincidence window of 10-250 ns (typically set to 100 ns) are read out. The system divides the full-four telescope array into a set of mutually exclusive sub arrays and produces a decision independently for each sub array. Individual sub arrays may take data independently, without affecting the trigger dead time (the time in which L3 cannot process L2 trigger inputs). This architecture is achieved using a 6u, 3 slot wide, VME implemented Sub Array Trigger (SAT) Board which can take input from up to eight telescopes. The SAT board contains

a set of eight identical decision blocks embedded in a single Altera Stratix FPGA. The blocks themselves are identical and may be configured to use or ignore any combination of telescope inputs and return a coincidence decision. Each block thus corresponds to a particular sub array.

In order to minimise the read out dead time it is necessary to minimise the size of the FADC read out window. To do this without losing shower information, the timing edge of the L3 trigger which is sent to each telescope must be precise to within 2 ns. The array trigger achieves this low level of jitter by using the incoming L2 signal itself to generate the timing edge. The incoming L2 trigger signal is split in two, with one copy going to the array trigger coincidence logic and the other being delayed for use as a timing edge. This delay, along with the compensating and shower delays, is achieved using custom built Pulse Delay Modules (PDMs). Pulses on each of the PDM input channels may be programmable delayed independently in steps of 2 ns.

The array trigger system can accept incoming L2 triggers at up to  $\sim 100$  kHz and is dead for 100 ns between consecutive signals (given by the coincidence window). Whilst an L3 decision will be reached within 250 ns, the total array trigger dead time is  $\sim 1$   $\mu$ s (not including the waiting period for telescopes to complete read out which is part of the telescope dead time). The array trigger system therefore contributes a negligible amount to the desired telescope dead time of  $<10\%$  at a trigger rate of 1 kHz (see Section 3.5) [89].

### 3.5 Data Acquisition

The VERITAS data acquisition chain (VDAQ), shown in Figure 3.6, is centred around a custom-built 500 MHz FADC system [35] which provides a digital version of the PMT pulse in 2 ns slices. Each PMT signal is digitized with an 8-bit dynamic range and a memory depth of upto 64  $\mu$ s. Typically a FADC window of 24 samples, corresponding to 48 ns, is read out. The signals are split into HG and LG channels. The HG channel is digitised by default and if the dynamic range is exceeded an analogue switch connects the FADC chip to the delayed LG path. The electronic noise is small, with a sample-to-sample standard deviation  $\sim 0.5$  digital counts and an event-to-event standard deviation

over a 10 sample integration window of  $\sim 1.5$  digital counts. Figure 3.13(a) shows a typical FADC trace in a signal channel

The FADC read out window size and position are programmable and a 24 sample read out on all 500 channels results in a data size of 13.5 kb per event and a dead time of  $\sim 7\%$  at 250 Hz. This implies nearly 5 GB of data per 28 minute run for a single telescope. At this rate the array produces 20 GB per run. To reduce the energy threshold of the array it is necessary to reduce the minimum pulse size required to trigger a given pixel, consequently increasing the trigger rate. To maintain a low dead time for trigger rates up to 1 kHz, a zero suppression scheme has been implemented in which only those channels with a peak signal larger than some preset value are read out, reducing the data size by a factor of  $>4$ .

The FADCs for each telescope are situated in four custom VME crates where they are read out by local single board computers (VME-DACQ). Each of the four FADC crates carries custom built clock-trigger boards which provide synchronous distribution of clock, trigger signals and scalars for latching the event time and live time. A master clock-trigger board provides a 500 MHz clock used to phase lock the other three clock-trigger boards to within 200 ps. The clock-trigger boards also form a wired-OR to generate the telescope busy flag when the buffered FADC memory is being read out. The L3 trigger and event number are received by the master clock-trigger board and fanned out to the slave clock-trigger boards and to an Auxiliary Crate. Once a crate receives the trigger, it sets the wired-OR bus high to indicate that it is busy. If any of the crates are busy the telescope is set as busy, indicating that it is incapable of receiving further L3 triggers. The VME-DACQ computers read out the data from the clock-trigger boards and the contents of the FADC ring buffer memory using a Chain Block Transfer(CBLT) and stores them in a buffer. When the CBLT is complete the wired-OR for that crate is disengaged. Once all the wired-ORs are disengaged, the telescope busy is unset and the telescope is ready to receive the next L3 trigger.

Buffered events from the VME-DACQ computers are transferred via a Scaleable Coherent Interface (SCI) to an event-building computer where they are integrated, tested and passed onto the online analysis system and data harvester.

The four FADC crates each dissipate over 2 kW and are cooled using a chilled water

system. Monitoring of the FADC temperatures is accomplished using thermometers mounted directly on the boards which are read out using a multi-channel Keithly voltmeter which in turn is read out via serial interface and reported to the array control software.

The VERITAS FADCs give two principal benefits over simple charge integrating ADCs. Firstly, they allow the application of digital signal processing techniques, (for example, actively placing and minimizing the charge integration gate thus improving the signal/noise per PMT and lowering the effective energy threshold of the detector). Secondly, they provide measurements of the time distribution of the Cherenkov photons across the image which may help to reject the hadronic CR background showers and improve the accuracy of  $\gamma$ -ray shower parameter reconstruction [89].

With conventional triggered ADCs a single IACT may achieve a reasonable dead time by delaying a signal above a threshold in its analogue form until the local trigger initiates digitisation. In this case the telescope is dead from the point of receiving the local trigger until digitisation and read out is complete. If no trigger occurs the data is not digitised and no dead time is incurred. If more than one telescope exists it is desirable to form coincident triggers between them. Under this scenario analogue delays are not feasible requiring hundreds of meters of cabling and subjecting the signal to a large amount of dispersion. Instead when a local trigger is obtained digitisation begins and the telescope becomes dead. Whilst awaiting an array trigger the data is digitised and stored in a temporary buffer. If an array trigger is returned the data is read out and again the telescope is dead from the time of the local trigger until the read out process is complete. The majority of local triggers however are not accompanied by an array counterpart. If no array trigger is forthcoming the read out of data is vetoed requiring the digitisation and storage system to be reset. Under this scenario the telescope is dead from the point of the local trigger until a veto signal is returned and the acquisition reset. The theoretical minimum dead time associated with this process is twice the signal travel time between the two most widely separated telescopes or about  $2 \mu\text{s}$ .

The H.E.S.S. collaboration use ADCs to read out data and achieve the required delay to form a local trigger by using ARS chips, allowing the digitisation system to be integrated into the camera. To avoid a bottle-neck at the read out stage that increases the dead

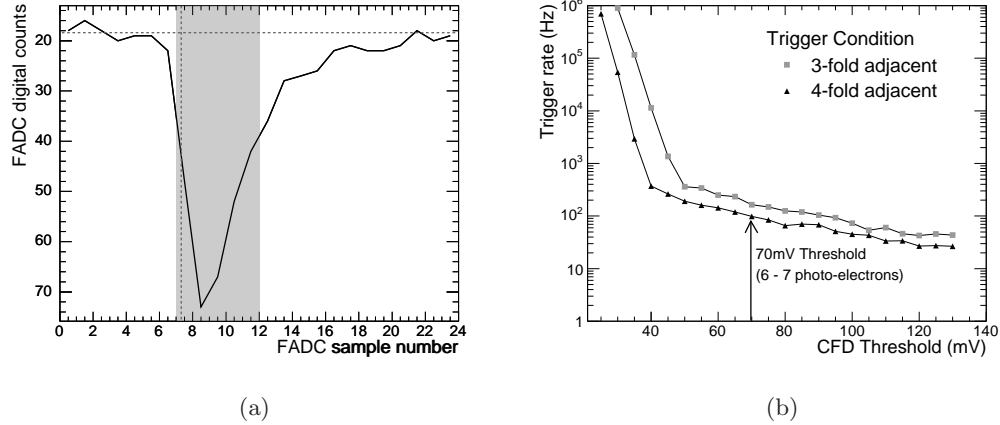


Figure 3.13: (a) A FADC trace produced by Cherenkov light from a CR air shower in a single signal channel. The dashed horizontal line is the electronic pedestal level, the dashed vertical line shows the pulse arrival time and the shaded area indicates a 10 ns (5 FADC samples) integration window. (b) The trigger rate as a function of CFD threshold, or bias curve, for two different topological trigger configurations.

time to an unacceptable level, the system is normally operated in charge-integrating mode. The analogue delay is not deep enough to await an array response (128 ns at 1 GHz) and so the local trigger halts the ARS chips and initiates the digitisation process. A veto halts and resets the system if no array trigger is forthcoming. Telescopes that do not participate in the array can not be read out.

The use of high-speed FADCs with deep digital delays permits a much longer time for development of an intelligent array trigger without incurring any dead time. A local trigger is generated and sent to the central location but is not required to initiate digitisation and instead output samples from each FADC channel are continuously written to a circulating memory. When an array trigger arrives writing ceases and the memory contents are read out in a window around the pulse position. In this pipe-line scenario the dead time is simply the time required to read out the window of FADC samples from the buffer. If no array trigger occurs the memory continues to circulate, the data is over written and the system incurs no dead time. As read out is independent of the local trigger, telescopes that did not participate in the array trigger may also be read out. Such a scheme requires fast digitisation and a deep enough memory to await array triggers. In order to improve the signal/noise per PMT and lower the effective energy

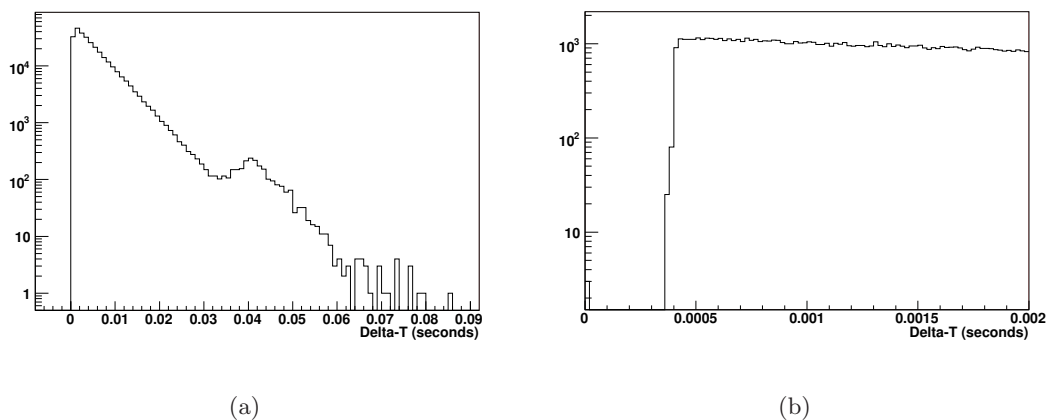


Figure 3.14: (a) Time difference between consecutive events with event rate in Hz on the y-axis. The excess at 0.04 s is caused by extra dead time associated with buffer transfers in the data acquisition system. (b) The time difference between consecutive events scaled down to a few milliseconds. The sharp cut-off at 0.4 ms indicates the system dead time.

threshold and dead time of the detector, it is necessary to minimise the FADC read out window. Thus, as will be addressed in Chapter 6, trigger pulses must be distributed throughout the array with minimal jitter to ensure the data is accurately located in the FADC buffers.

Each telescope is equipped with a Global Positioning System (GPS) clock providing a timestamp for each event which is accurate to within  $1 \mu\text{s}$ . This timestamp is routed via the Auxiliary Crate and the VME-DACQ software to the Event Builder where it is combined with the other telescope data to form telescope events. The array trigger has an independent GPS clock providing timestamps for each array trigger. These are combined with the telescope events by a computer known as the Harvester when the array events are built. In the absence of an array trigger, the GPS clocks allow events from T1 and T2 to be matched offline. The performance and limitations of this soft-array trigger are presented in Chapter 7. The GPS time stamps in the full array system result in a distribution of the exact time between events, known as a Delta-T distribution (see Figure 3.14), indicating the dead time of the array and showing up potential noise problems.

## 3.6 Calibration

The telescope calibration is divided into two sections. Absolute calibration is concerned with understanding the signal size produced by a single photon such that detector response and the energy scale can be accurately modelled in Monte Carlo simulations. Relative calibration involves measuring the various constants for each signal channel so as to flat-field the response of the camera in the data analysis. Data analysis and simulations will be described in Chapter 7 and it is prudent to introduce the calibration of the telescopes briefly beforehand.

### 3.6.1 Absolute Calibration

The overall photon conversion factor is a combination of the mirror reflectivity, the collection efficiency and quantum efficiency of the PMT photocathode, and the conversion factor of the electronics chain. The mirror reflectivity and PMT photocathode characteristics can be determined from laboratory measurements and manufacturer's specifications. The conversion factor of the electronics chain is defined as the average integral number of FADC counts produced by the generation of a single pe in the PMTs and measured in-situ. A nitrogen laser is used to deliver a  $\sim 4$  ns wide pulse to a dye module which fluoresces at 400 nm. This light is passed via optical fibre to a diffuser  $\sim 4$  m in front of the camera providing uniform illumination [77]. The camera face is covered by a semi-reflective Mylar sheet which shields the PMTs from background light and the laser pulse intensity is adjusted using filters to provide an average illumination of  $\sim 1$  p.e. per PMT. A delayed copy of the laser trigger is used to trigger the DAQ such that the signal arrives centred in the read out window. Figure 3.15(a) shows the histogram of the integrated FADC counts for a single PMT at standard operating gain. The conversion factor averaged over all PMTs is  $0.19 \pm 0.02$  p.e./digital count (d.c.).

Two complementary methods have been used to confirm the overall photon collection efficiency of the telescope. Single muons within the FoV produce sharply defined ring images and the expected amount of Cherenkov light per unit arc length can be accurately calculated, providing a well calibrated natural *test beam* [169]. A comparison of the total charge in simulated muons and in real muons selected from data taken with the first

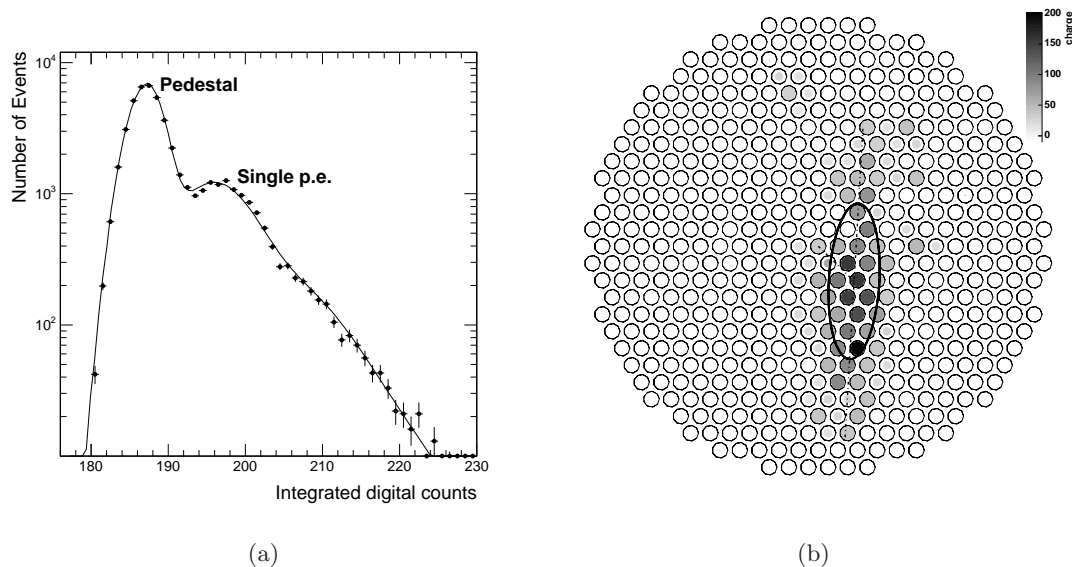


Figure 3.15: (a) The single pe response for one PMT at standard operating gain. The fit assumes a Poisson distribution of pe and a Gaussian distribution for the integrated charge produced by a single pe. The average conversion factor over all PMTs is  $0.19 \pm 0.02$  p.e./d.c. (b) The charge distribution across the camera for a CR event (the grey scale is in d.c.).

VERITAS telescope indicates that the total photon collection efficiency is well matched [94]. A novel alternative approach to absolute calibration, borrowed from atmospheric fluorescence detectors of ultra-high energy CRs [154], has also been tested. A calibrated laser pulse directed towards the zenith is used to produce a flash of Rayleigh scattered light with an intensity that can be calculated very accurately. Again, preliminary results indicate good agreement between simulations and data [160].

### 3.6.2 Relative Calibration

Prior to the parameterization of Cherenkov images in the camera in the data analysis chain, each signal channel must be calibrated. A pulse generator is used to trigger the DAQ at a rate of 3 Hz during the data taking in order to generate events with no Cherenkov light present. A histogram is constructed of the integrated number of d.c. in each FADC trace (for a given integration window size), the mean of this histogram is the electronic pedestal value and the width is the pedestal standard deviation providing a measure of the night sky background noise level. Pedestal values are currently calculated

once per 28 minute data run. The same laser system used for the single photoelectron calibration is used once per night to provide  $\sim 1000$  bright, uniform, time-coincident photon pulses across the camera. The mean of a histogram of the integrated signal in each FADC trace over these events measures the relative gain of the signal channels. Similarly, a histogram of the arrival time of the laser pulse in each trace measures the relative time offsets for each channel. Relative PMT gains are set to within  $\sim 10\%$  by adjusting the PMT high voltages. Approximately 95% of the signal channels show a relative time offset of less than  $\pm 3$  ns. This is due to uncertainty in the PMT transit time, coaxial cable length and trigger chain transit time. It may be compensated for in the trigger hardware at several points, such as in CFD delays or the SS wire wrapping.

### 3.7 Data Analysis and Simulations

Data analysis within VERITAS was pioneered by the EventDisplay package developed at the University of Leeds. This software now complements the VERITAS Gamma-Ray Analysis Suite (VEGAS), the standard analysis package for the collaboration.

Development work to define the optimum data analysis methods for VERITAS is ongoing. The data, in particular the FADC information, provide an opportunity for exploiting many techniques which have not been applicable to previous generations of Cherenkov telescopes. For example, the use of digital signal processing algorithms to parameterise the signal traces and the added dimension of detailed image timing information. The analysis used in Chapter 7 is based on a second moment analysis parameterisation of images in the camera, the results of which can be described by an ellipse as shown in Figure 3.15(b). Due to the purely EM nature of  $\gamma$ -ray initiated air showers,  $\gamma$ -ray Cherenkov images are expected to be more compact than CR images and can be preferentially selected by applying cuts based on the dimensions of the event ellipse (*length*, *width*) [84]. The parameter  $\alpha$  describes the orientation of the long axis of the image ellipse relative to the line joining the centre of the field-of-view and the ellipse centroid. Showers originating from a point source, such as the Crab Nebula, will be oriented with their long axes pointing back to the position of the source at the centre of the camera. The angular *distance* of the image from the source position is related to the distance of the shower core position on the ground. Finally, the ratio of the image

*length* to its total *size* (where *size* is the integrated charge over all PMT signals in the image) is used to discriminate  $\gamma$ -rays from the otherwise overwhelming background of local muons which generate short arcs in the camera with a constant size per unit arc length. Whilst the optimisation of these parameters for VERITAS is beyond the scope of this work, their use will be required in Chapter 7 to establish the benefits of a hardware implemented array trigger over single telescope observations.

To calculate source fluxes and energy spectra accurately it is necessary to develop a detailed model of the telescope performance to which simulated air showers are presented such that the telescope detection efficiencies can be calculated. A complete chain of Monte Carlo simulations has been developed [121]. It consists of air shower simulations with CORSIKA [80] and a detailed simulation of the telescope response (GrISU [55]). The agreement of the Monte Carlo simulations with observational data has been illustrated for the first VERITAS telescope in [89]. For the purposes of this work simulations will be used to confirm the performance increases promised by new technology and to complement the analysis of Crab Nebula observations.

## Chapter 4

# Transmission of Fast Analogue Signals Over Optical Fibre

---

The current VERITAS camera contains 499 pixels each individually read out over coaxial cable. For future IACT arrays higher density cameras of  $\sim 2000$  pixels will increase the FoV and angular resolution of the detector. The current coaxial scheme, as described in Section 3.3, is not suitable for such an extrapolation. In this chapter the use of VCSELs for the transmission of fast analogue signals over optical fibre is explored. Such a scheme is also of interest to UNDs, where the read out is potentially over distances of kilometres. Here focus is given to the transmitter circuit and a novel method of biasing the VCSEL above threshold. The VCSELs chosen offer improved stability over previous attempts and the sporadic changes in pulse area associated with laser mode-hopping previously seen are not experienced. The dependence of the transmitted pulse area on temperature is measured and methods of temperature compensation examined.

### 4.1 Introduction

As described in Section 3.3 short fast pulses, typically of 3-5 ns FWHM and 1-2 ns rise time, are transported from the 499 PMTs in each VERITAS camera over  $\sim 50$  m of

stranded 75  $\Omega$  RG59 coaxial cable [106] to the electronics trailer for digitisation by the 500 MSa/s FADCs [35]. Coaxial cable attenuates the pulse amplitude by  $\sim 25\%$  and imparts a dispersion of over 50% into the FWHM of a typical pulse (a single pe pulse of amplitude  $\sim 13.5$  mV and FWHM  $\sim 3$  ns results in a pulse of amplitude  $\sim 10$  mV and FWHM of  $\sim 6.5$  ns at the FADC input) [111]. In this chapter an alternative method of transporting fast analogue signals is presented. A transmitter converts the pulse into an optical form using a VCSEL (or Vertical Cavity Surface Emitting Laser). The signal is coupled into an optical fibre, transported, and converted back to an analogue electrical form using a photodiode at the receiver. In the case of VERITAS this would allow the FADC integration window to be shortened. In turn less noise would be integrated into the signal and the energy threshold of the detector would drop. Crucially optical links experience no crosstalk or electromagnetic pickup between channels, no grounding problems and are immune to lightning strikes.

VCSELs are low power, low cost, readily available laser diodes capable of transmitting nanosecond rise-time signals over hundreds of meters of optical fibre with virtually no attenuation [140]. They are a natural candidate for use within the read out system of next generation IACT arrays and UNDs. Typically employed in digital systems [71] (see Chapter 6), the use of VCSELs in analogue transmission schemes is novel, but not unique [53; 118]. The University of Leeds and MPI Munich successfully designed and built a prototype optical link system with VCSEL drivers to transmit PMT pulses in 2000 [155]. The system was installed on 111 outer pixels of the Whipple-10 m telescope [50]. A study of the shape of the analogue PMT signals in the data acquisition building showed that the pulse degradation was significantly lower in those channels transmitted by optical fibres; the FWHM of the fibre channels was 8 ns, whereas that of the coaxial cable channels was 12 ns<sup>1</sup>[49]. The VCSELs (HoneyWell HFE4085-321 [92]) experienced sporadic periods of gain and noise instability in which the optical output of the laser varied greatly on minute time scales by up to 50%. This behaviour was attributed to mode-hopping in which different spatial modes of the laser become active altering the amount of light coupled into the fibre [145]. Improvements were noted in the VCSELs (again Honeywell HFE4080-321) selected for the analogue read out scheme in the MAGIC telescope in

---

<sup>1</sup>The typical FWHM of the pulses produced by the PMT camera of the Whipple-10 m telescope is  $\sim 7$  ns.

2004 [117; 142] and attributed to improvements in the manufacturing process. However fluctuations of up to 39% in the output pulse amplitude and area were still evident in some of the VCSELS. A two-stage classification procedure was required to select VCSELS suitable for use in the camera and rejected approximately 30% of the original sample. In this way fluctuations in the output pulse area and amplitude were kept to an acceptable 12%. The result was the first stable, large-scale, VCSEL-based analogue transmission scheme. Further improvements in the VCSEL manufacturing technique suggest it is now timely to consider the next generation of analogue transmission scheme. In this work focus is given to the development of the transmitter, and the receiver design is nearly identical to that used in the Whipple-10 m system. The performance of VCSELS, transmitter and link as a whole is assessed.

## 4.2 VCSELS

Semiconductor laser diodes traditionally emit light parallel to the semiconductor wafer. These edge-emitting laser diodes, such as the Fabry-Perot diode, consist principally of a p-n junction and an optical waveguide with partially reflecting mirrors at either end. Forward biasing the diode junction produces spontaneous radiation following the recombination of electrons and holes. Light from this spontaneous emission is amplified by stimulated emission within a resonant optical cavity.

As the current is increased from zero the optical power is initially dominated by spontaneous emission, growing slowly and linearly with current. Eventually a *threshold current*,  $I_t$ , is reached above which stimulated emission dominates the optical power which increases by at least two magnitudes faster than below  $I_t$  [140]. In order to avoid switch-on delays, and ensure the transmission of small pulses, laser diodes are operated above  $I_t$  at the *bias current*,  $I_b$  [145].

Diode lasers with their lasing cavity in the plane of the semiconductor wafer must be diced individually from the wafer before testing can take place and emit an elliptical beam of light that lowers the coupling efficiency into the fibre. A VCSEL has a cavity perpendicular to the plane of the wafer and therefore avoids such problems. The typical structure of a VCSEL is shown in Figure 4.1. A Fabry-Perot cavity is formed by roughly

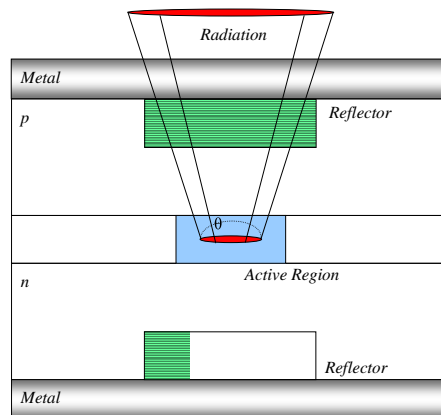


Figure 4.1: *Typical structure of a VCSEL. The reflectors are made from a stack of dielectric layers whose index of refraction alternates between high and low values resulting in a high reflection. The upper reflector is partially transmissive at the laser output wavelength.*

20 periods of alternating dielectric layers of high and low refractive index known as a Distributed Bragg Reflector (DBR). The upper reflector is partially transmissive at the wavelength defined by the Fabry-Perot cavity and the resonance of the DBR leading to vertical laser emission. The dimensions of the VCSEL are such that only one longitudinal mode is allowed. Typically several transverse modes are produced (multi-mode VCSEL) although VCSELs emitting one single transverse mode are available (single mode VCSEL). Multi-mode VCSELs, as used in this work, can exhibit a total optical output power of greater than 100 mW [45]. This increase in optical output power is accompanied by changes to the shape of the emission beam as multiple transverse modes become stimulated. Thus higher efficiency is possible with multi-mode VCSELs, but the fibre coupling efficiency is much more sensitive to misalignment and the optical spectrum no longer consists of a single frequency [114].

VCSELs exhibit several advantages over LEDs and traditional edge-emitting laser diodes for the transmission of fast pulses.

- The rotational symmetry of the cavity about the vertical axis creates a circular emission beam increasing the efficiency of optical coupling over edge-emitting lasers.
- The low beam divergence ( $\sim 15^\circ$ ) in comparison to LEDs ( $\sim 120^\circ$ ) and edge-

emitting laser diodes ( $\sim 40^\circ$ ) increases the efficiency of optical coupling.[140]

- The low lasing threshold current ( $\sim 3$  mA) in comparison to edge-emitting lasers ( $\sim 25$  mA) lowers the effect of self-heating and reduces power consumption [45]. Additionally the drive, or modulation currents are lower for VCSELs (a few  $\mu\text{A}$ ) compared to laser diodes (10-100  $\mu\text{A}$ ).
- VCSELs are capable of rise and fall times on the order of 100 ps, comparable to that of the latest edge-emitting lasers and much shorter than that of LEDs.
- The narrow spectral width of  $< 1$  nm is comparable to edge-emitting lasers and significantly narrower than LEDs ( $\sim 50$  nm) and minimises pulse dispersion within the fibre [60].
- Although VCSELs have a low threshold current they may be pulsed at up to 100-200 mA for short durations increasing the dynamic range for Cherenkov pulses [155].
- The cost of a connector-mounted VCSEL is comparable to that of a connector-mounted LED and approximately one-third that of an edge-emitting laser diode.

### 4.3 Link Specification

Although the analogue optical link developed here is of interest to future UNDs and IACTs the specification matches the current VERITAS read out scheme. In order to integrate the prototype transmitter into the camera without interfering with the current coaxial read out scheme the input must be of high-impedance. To match the pre-amplifier output the transmitter must accept pulses with amplitudes between 0 and -2.2 V and the link should operate at an overall gain of  $\sim 1$ . The minimum transmittable pulse height must be below that due to a single pe,  $\sim 10$  mV at the FADC input corresponding to  $\sim 13.5$  mV at the pre-amplifier output. VCSELs have large bandwidths in excess of 1 GHz, but the overall bandwidth of the link will be limited by the electronics in the transmitter and receiver. A fast PMT signal with a  $\sim 1$ -2 ns rise time requires a bandwidth of  $\sim 170$ -340 MHz to be correctly transmitted and correspondingly the VERITAS pre-amplifier has a bandwidth of 440 MHz for large signals. The VERITAS

FADCs sample at a rate of  $f_s=500$  MSa/s. The bandwidth of the signal at the FADC input must therefore be below the Nyquist frequency of  $f_s/2=250$  MHz to be correctly reconstructed. In the current VERITAS scheme the bandwidth of the signal leaving the pre-amplifier is degraded to well below this by the  $\sim 50$  m of coaxial cable (the rise time of a signal due to a single pe as sampled with the 500 Msp/s FADCs is  $\sim 6.5$  ns). The bandwidth of the optical link should exceed that of the coaxial scheme. If the bandwidth of the optical link exceeds the Nyquist frequency of the FADCs then pulse stretching (as used by the MAGIC collaboration upon encountering exactly this problem [44]) may be required to make proper use of the link within VERITAS. In future detectors it is expected that FADCs with a much higher sampling rate will be employed [40]. Finally, the transmitter must be small enough to physically fit into the VERITAS camera box, whilst the receiver can be a larger module as it will reside in the electronics trailer.

## 4.4 Implementation

The optical link consists of a transmitter, fibre and receiver. The transmitter generates a current proportional to the input signal voltage to drive the VCSEL. A bias current is also provided independently of this signal current to raise the VCSEL above threshold. Two iterations of transmitter prototype were constructed in this work. The receiver contains a PIN photodiode to convert the optical signal back to an electrical current. The receiver circuit outputs a voltage proportional to that current. A single iteration of the receiver is used in this work.

### 4.4.1 VCSEL, Fibre and Connectors

The ZL60052 VCSEL from Zarlink Semiconductor Inc., as pictured in Figure 4.2, was chosen for use in this work [136]. The laser is capable of rise and fall times as short as 100 ps and emits light at a peak wavelength of 850 nm with a maximum beam divergence of  $15^\circ$ . The ZL60052 has a lasing threshold of 1-4.5 mA but, crucially, can be operated at up to 200 mA for low duty cycles allowing a large dynamic range for Cherenkov pulses. The ZL60052 converts electrical current to optical power with an efficiency, known as the *slope efficiency*, of roughly 0.20 W/A. The VCSEL is coupled to

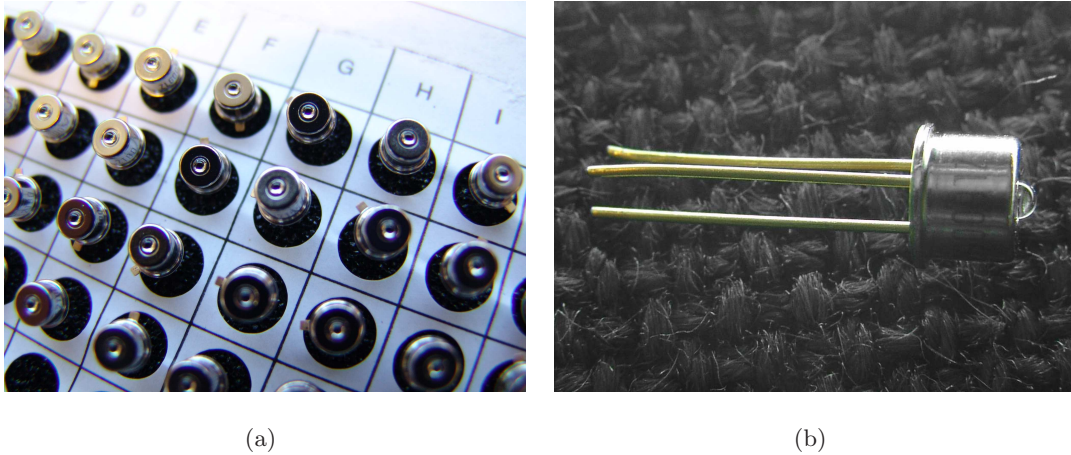


Figure 4.2: (a) The batch of 40 ZL60052 VCSELs from Zarlink Semiconductor Inc. purchased for this work. (b) A close up of a ZL60052 VCSEL with the integrated ball lens clearly visible.

a multi-mode, graded-index,  $62.5\ \mu\text{m}$  core optical fibre via an E2000 connector as shown in Figure 4.3(a). The E2000 connector includes a mechanism to automatically close the receptacle when the optical fibre is removed to ensure laser-eye safety and prevent dust from entering the precisely machined connector. The VCSEL is provided in TO-can and contains a spherical lens of 2 mm diameter at the can opening to focus emitted light onto the fibre as shown in Figure 4.3(b). The previously used Honeywell HFE4080-321 did not contain a spherical lens. The integrated spherical lens available on the ZL60052 is closer to the active area of the VCSEL and increases the amount of light coupled into the fibre when compared to the HFE4080-321 [114; 167].

#### 4.4.2 Transmitter

Figure 4.4(a) shows the first version of the transmitter constructed in this work. The four channel prototype uses two OPA695 current-feedback op-amps to invert and amplify the voltage signal creating a suitable current through the VCSEL. The bias current is supplied via two transistors and adjusted using a potentiometer. The design is very similar to that used in the MAGIC telescope, with additions to accommodate the VERITAS pre-amplifier output voltage range and high-impedance input requirement. This circuit exhibited many problems. Components were found to be incorrectly oriented (attributed to problems with the manufacturing process), the bias current range was

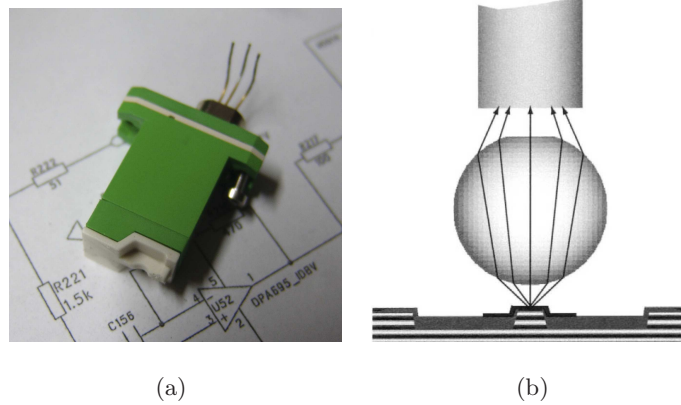


Figure 4.3: (a) A female E2000 connector with a ZL60052 VCSEL mounted inside. The metal spring-loaded clips close the connector when the fibre, terminated with a male E2000 connector is removed. (b) A schematic of the ball lens integrated into the ZL60052 VCSEL.

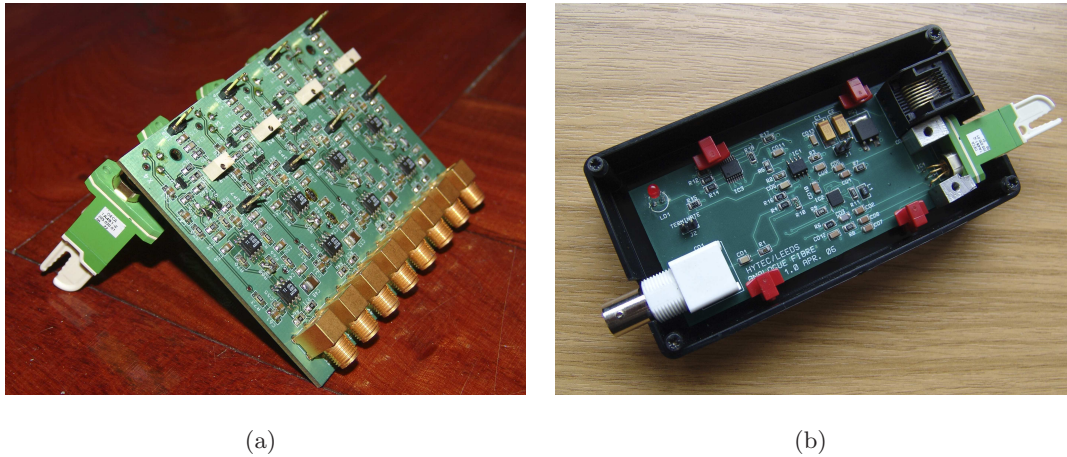


Figure 4.4: The first, (a), and second, (b), optical link transmitter prototypes.

limited and insufficient, and the output was extremely noisy. Rather than pursue this circuit design the decision was made to try a novel method of supplying the bias current via a digital laser driver chip and the second prototype was designed and constructed. The second version of the transmitter, shown in Figure 4.4(b), is a compact, single channel device and is used throughout the rest of this chapter for examining the performance of the optical link and will simply be referred to as *the transmitter*.

The VERITAS camera box is shown in Figure 4.5(a). The pre-amplifier outputs are routed to feed-through boards via the black coaxial cables shown in Figure 4.5(b).



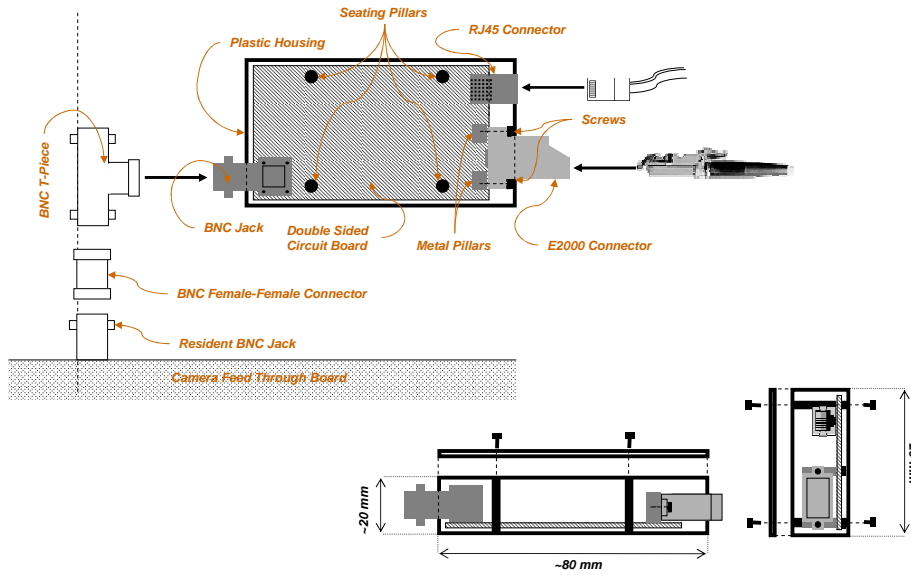


Figure 4.6: A schematic drawing of the second transmitter illustrating how the device could easily be installed within the VERITAS camera in parallel with the coaxial read out scheme.

( $26 \text{ pA}/\sqrt{\text{Hz}}$  and  $2.7 \text{ nV}/\sqrt{\text{Hz}}$  respectively) over the full output swing range of  $\pm 4.2 \text{ V}$ . The OPA695 is operated at unity gain and the output voltage therefore swings by  $2.2 \text{ V}$ , taking around  $0.5 \text{ ns}$ . The op-amp output is AC coupled to the VCSEL anode to isolate the DC voltage offset required to generate the bias current through the VCSEL.

An internal resistor between the H0 and L0 pins of the DS1859 creates a voltage at H0 that is used to set the value of the bias current via the BIASSET pin of the MAX3740A. The value of this resistance is controlled by a simple hexadecimal value accessible over an I<sup>2</sup>C interface, in turn accessed via a USB-to-I<sup>2</sup>C adapter and a small C++ program. The bias current is generated by the MAX3740A laser driver chip via an internal PNP transistor and output on the BIAS pin and connected to the VCSEL anode via an inductor (L1). The bias current may then be set between 1 and 15 mA. The MAX3740A BIASMON pin provides  $I_b/9$  and is monitored across R10 using the MON1 input of the DS1859. The DS1859 also monitors the temperature of the VCSEL. A look-up table of hexadecimal values, each corresponding to a resistance, and therefore a bias current, as a function of temperature can be loaded into the DS1859 to compensate for instabilities



The MAX3740A is used in digital circuits, and correspondingly the chip accepts a differential digital input signal on the +IN and -IN pins and drives a current through the VCSEL via the +OUT and -OUT pins. This feature may prove useful for calibration of the optical link when in situ. In this case the MAX3740A modulates the laser with a current set, in a similar way to the bias current, using the MODSET input and the H1 output of the DS1859.

The  $\pm 5$  V power is supplied via an RJ45 8-pin connector which also carries the I<sup>2</sup>C interface signals (SCL and SDA) and the optional MAX3740A digital inputs (+IN and -IN).

### 4.4.3 Receiver

The receiver, shown in Figure 4.8, uses a Mitel 1A354 [133] photodiode mounted in an E2000 housing to convert the optical signal into an electrical current with a responsivity of 0.45 A/W. The photodiode output is AC coupled to remove the DC offset created by the addition of the bias current at the transmitter. Two OPA695 current-feedback op-amps then create a voltage proportional to the photodiode current, inverting and multiplying the signal by a factor of 10 in the process. The predicted gain of the optical link is then given by the combination of VCSEL slope efficiency, photodiode responsivity and receiver amplification and is  $\sim 1$ . The receiver circuit is identical to that used in the Whipple-10 m system [49] with the exception of the faster opamp model used and the chosen feedback resistors. The receiver module requires a  $\pm 5$  V power supply, contains 12 channels and provides two copies of the output signal on single-pole Lemo connectors.

## 4.5 Selection and Qualification

As noted in Section 4.1 sporadic variations in the size of the transmitted pulse have been observed in the previous attempts at VCSEL based analogue transmission schemes. Therefore the ZL60052 VCSELs used in this work were subjected to a qualification procedure before selecting suitable lasers for mounting into E2000 connectors (a costly procedure -  $\sim 50$ E per piece). The qualification procedure consists of a *bias current scan test* as used by the MAGIC collaboration. The response of the VCSEL to a standard

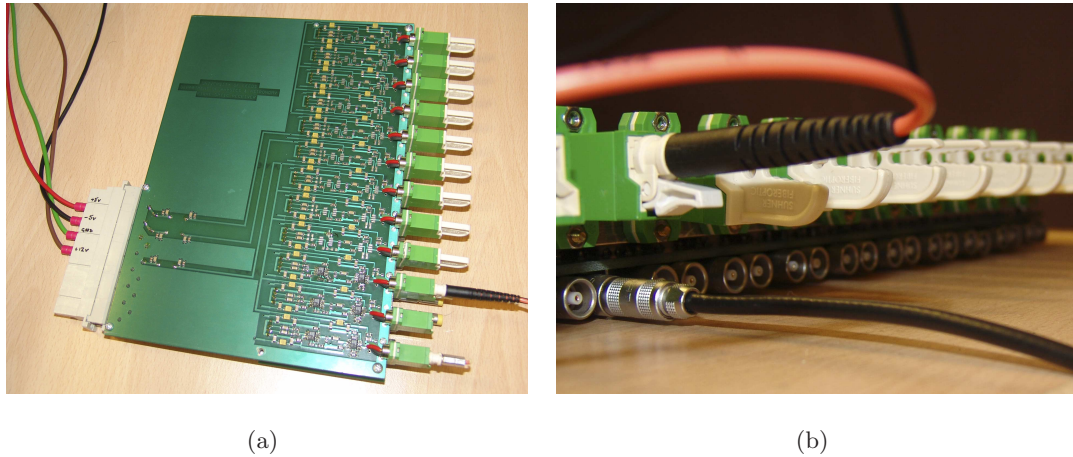


Figure 4.8: *The 12 channel optical link receiver with 1 E2000 input connector and 2 Lemo output connectors per channel, from the top, (a), and front, (b).*

input pulse is monitored as the bias current is altered and cuts are made to reject all but the most stable lasers. In this section the bias current scan testing procedure and results are described and compared to those obtained with the VCSELs used in the MAGIC telescope. This work took place in collaboration with MPI Munich during a visit in January 2005 and uses a dedicated VCSEL classification setup independent to the optical-link described in the previous section.

In VERITAS, and indeed all IACTs, the number of photons incident on a PMT photocathode within a given time is estimated by measuring the charge of the resulting PMT pulse over the same time period. The charge of the PMT pulse is in turn directly proportional to the area under that pulse. It is therefore the area of the pulse through the optical link, and the variations therein, that are used in this section and the rest of the chapter as a qualification of VCSEL and optical link performance.

#### 4.5.1 The Bias Current Scan Test

As mentioned in Section 4.3 the smallest pulse that may be expected to be transmitted over the optical link in the case of VERITAS is around  $\sim 10$  mV. Since the number of PMT pulses created in an IACT increases with decreasing energy and the SNR is expected to be worst for small pulses, the bias scan is performed on a 10 mV input pulse of FWHM 2.7 ns.

In the bias current scan test the response of the VCSELs is measured over bias currents ranging from 5.00 mA to 7.00 mA in steps of 0.05 mA. At each bias current, 120 measurements of the output pulse area are taken (a measurement every 2 seconds during 4 minutes). The standard deviation and the mean area in each 4 minute step are then computed. It is assumed that during normal operation the VCSELs will be set to a constant bias current of  $\sim 6$  mA and lasers are accepted or rejected based upon their performance in the bias current range 5.70-6.30 mA<sup>2</sup>. As previously noted the bias current scan test takes place prior to mounting the VCSELs in E2000 connectors (on what will be herein be referred to as *naked* VCSELs) to avoid the high price of encapsulating lasers that would later be rejected.

A dedicated test setup was used to perform the bias current scan test. In the absence of an E2000 connector and fibre the naked VCSELs are connected to the driver circuit and couple directly onto the PIN photodiodes on an adjacent receiver. The details of this measuring setup are given in Appendix A.1. VCSELs were rejected if either the relative charge noise exceeded 4.5% at a given bias current or if the pulse charge area varied by more than 3% between 0.05 mA steps. The relative noise is estimated as the standard deviation in the measured area divided by the mean measured area at a given bias current.

#### 4.5.2 Results of the Bias Current Scan Test

In the original bias current scan test performed on the VCSELs for the MAGIC telescope, 24% of the lasers (Honey Well HFE4085-321) were rejected (a second, long-term, test on the E2000 mounted VCSELs rejected an additional 7%)[141]. Figure 4.9(a) shows the mean area and relative noise as function of bias current for a HFE4085-321 VCSEL surviving the bias current scan test whilst Figure 4.9(b) shows the result for a less fortunate candidate. The relative noise in Figure 4.9(b) exceeds 4.5% and the output area changes by more than 3% over a 0.05 mA step due to a large peak near 6 mA and hence this VCSEL is rejected.

Figure 4.10(a) shows the result for a ZL60052 VCSEL obtained in this work. The

---

<sup>2</sup>As it will be seen in later sections selecting lasers that perform well at a fixed bias current is not sufficient to deal with instabilities introduced by temperature changes.

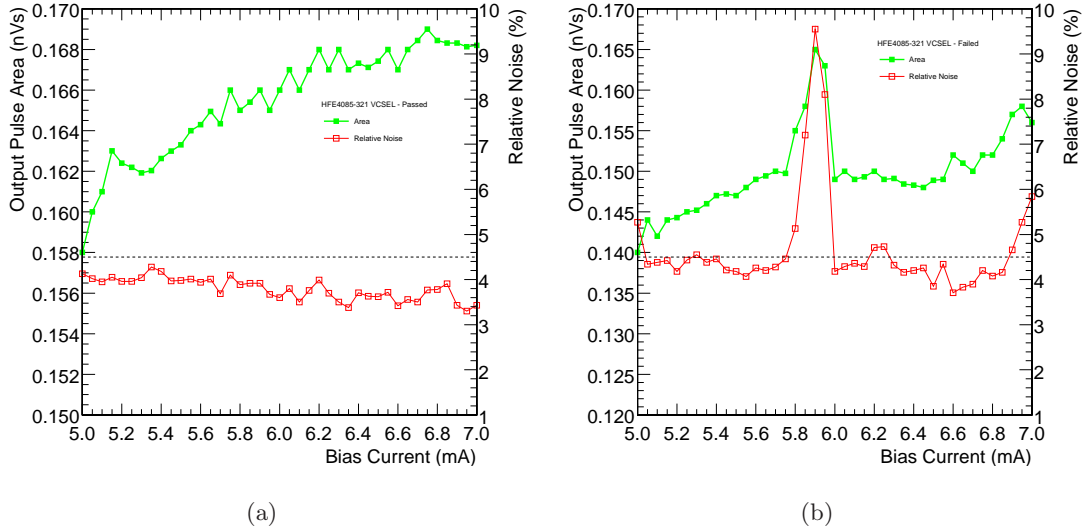


Figure 4.9: Results of the bias current scan tests on two HFE4085-321 VCSELs as used in the MAGIC telescope. VCSEL (a) passes the test whilst VCSEL (b) fails due to a resonant peak close to 6 mA.

output area appears more stable than for the HFE4085-321 and the relative noise is lower. Only 3 of the sample of 38 VCSELs tested<sup>3</sup> were rejected ( $\sim 8\%$ ), the result from one such VCSEL is shown in Figure 4.10(b). Even in the rare case of a VCSEL failing no large peaks are observed. The mode-hopping previously seen has been resolved, either through improvements in the VCSEL manufacturing process or the introduction of the integrated spherical lens. Examining the original tests performed with HFE4085-321 VCSELs more closely reveals that the total sample of 970 VCSELs were tested in 3 batches delivered from the manufacturer from March 1999 to September 2002. The number of VCSELs failing the bias current scan decreased from 36% to 21% over this period, and therefore the improvement in VCSEL behaviour seen here is not entirely unexpected. The implications of this result are significant. The optical link should not be limited by mode-hopping as the Whipple-10 m system was. In addition there is no need to incur the time and expense of rejecting  $\sim 30\%$  of the VCSELs in order to guarantee large-peak-free behaviour as was the case in the MAGIC telescope system.

<sup>3</sup>The alert reader may have noticed that in Figure 4.2(a) it is noted that a batch of 40 VCSELs were purchased, however two of these were destroyed accidentally in learning how to use the test setup correctly.

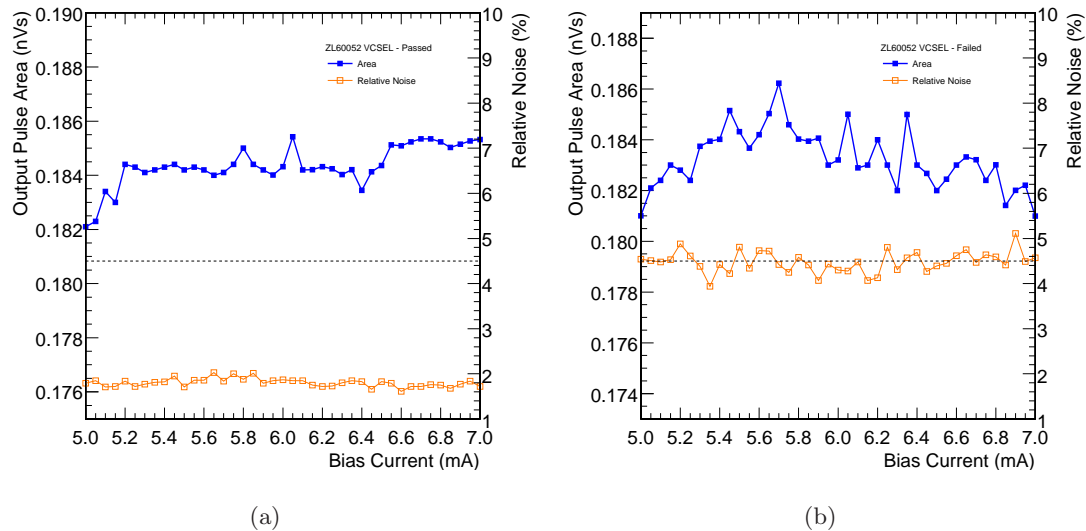


Figure 4.10: Results of the bias current scan tests on two of the ZL60052 VCSELs used in this work. Again VCSEL (a) passes the test whilst VCSEL (b) fails as the relative noise level exceeds 4.5% but no large peaks are visible,

The absence of resonant peaks observed in this work in January 2005 was verified by the MAGIC group in a set of bias current scan tests performed on a variety of newly available VCSELs and reported in October 2006 [23]. It is no longer necessary to operate the VCSELs at a fixed bias current of 6 mA to ensure a stable behaviour. As it will be seen in Section 4.7 it is crucial that the bias current can be altered to compensate for changes in the optical output of the VCSEL due to variations in temperature.

## 4.6 Performance

In this section a detailed account of the performance of the optical link is given. A single ZL60052 VCSEL which passed the bias scan test previously described was mounted into an E2000 connector and soldered onto the transmitter. The transmitter was connected to the receiver via 100 m of optical fibre and the receiver output was monitored using a mixed-signal oscilloscope (MSO). This section begins by establishing the relationship between current and optical power of the specific VCSEL used in the transmitter. The linearity and noise of the link are then examined before the link bandwidth is determined. Finally the pulse-shape distortion and harmonic distortion are examined. The equipment

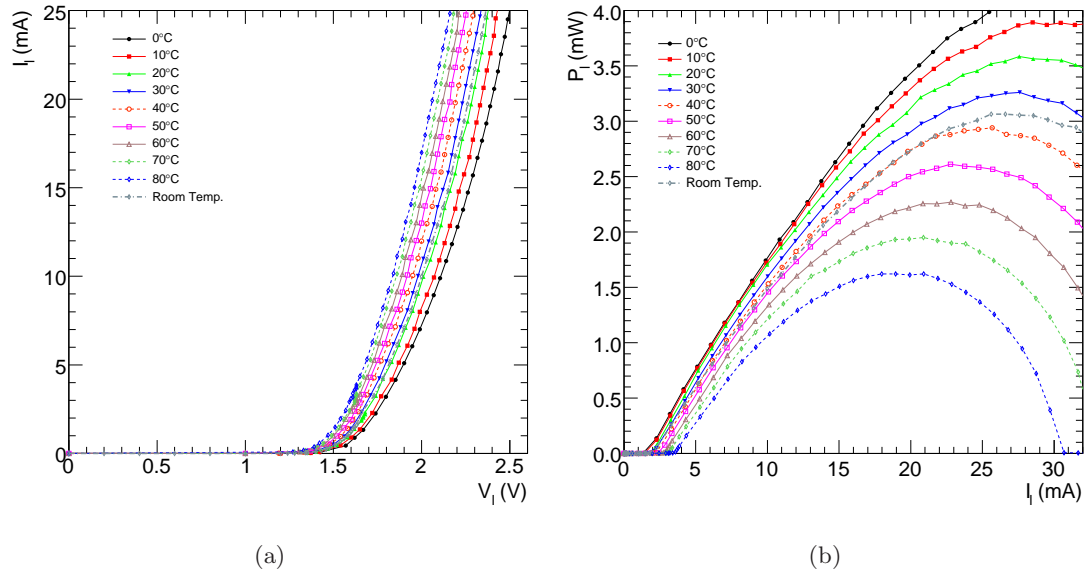


Figure 4.11: (a) The current through the VCSEL,  $I_l$  as a function of the voltage drop across the VCSEL,  $V_l$ , taken at various temperatures. (b) The optical output power produced by the VCSEL,  $P_l$ , as a function of  $I_l$ , again taken at various temperatures.

used for the experiments performed in this section is described in Appendix A.2.

#### 4.6.1 VCSEL Characteristics

To interpret the measurements made in the proceeding subsections it is important to fully understand the behaviour of the VCSEL independent of the optical link. Thus, prior to soldering the E2000 mounted VCSEL to the transmitter a simple circuit consisting of a variable voltage supply and resistor is used to drive the VCSEL. The supply voltage ( $V_s$ ) is altered and voltage drop across the VCSEL ( $V_l$ ) and resistor ( $V_R$ ) are both measured. The current through the VCSEL ( $I_l$ ) is calculated and a plot of  $I_l$  vs.  $V_l$  is constructed as shown in Figure 4.11(a). The optical output power of the VCSEL is also measured using a Noyes OPM4 optical power metre and used to construct a plot of  $P_l$  vs.  $I_l$  as shown in Figure 4.11(b). The measurements are repeated for a range of temperatures between 0°C and 80°C in 10°C steps.

Figure 4.11(a) shows the expected semi-conductor behaviour intrinsic to the working principle of the VCSEL. Initially no current flows through the VCSEL. As  $V_s$  is increased  $V_l$  increases and at some point a current begins to flow.  $I_l$  increases exponentially at

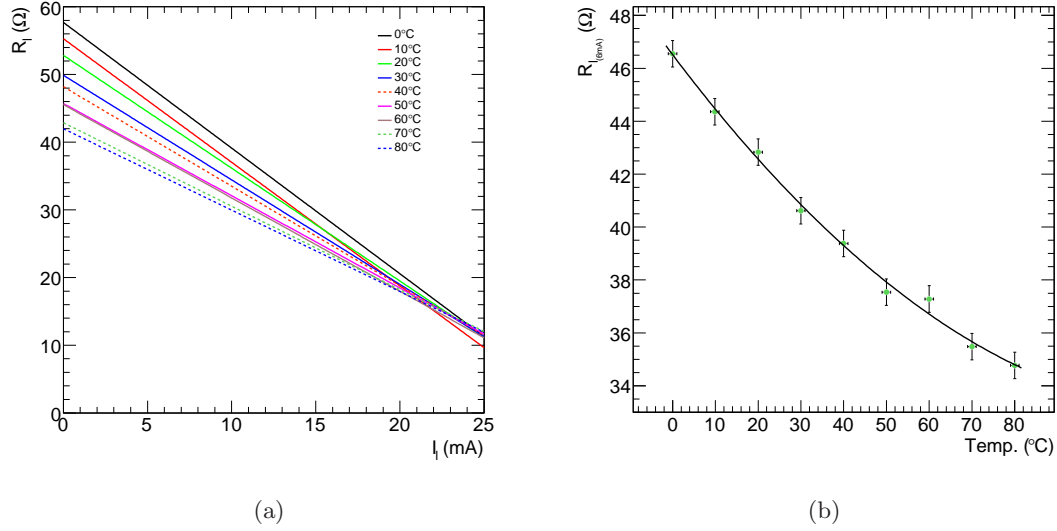


Figure 4.12: (a) The inverse of the gradient of the curves in Figure 4.11(a) indicating the resistance of the VCSEL,  $R_l$ . (b)  $R_l$  as a function of temperature.

first and then, above the threshold voltage the current behaves approximately linearly with  $V_l$ . The current corresponding to the threshold voltage is the threshold current,  $I_t$ . The current at a given  $V_l$  increases with temperature, and although at higher temperatures the VCSEL begins to lase at a lower  $V_l$ , the linear regime occurs higher up the exponential turn-on curve and consequently  $I_t$  increases with temperature. The inverse of the gradients of the curves in Figure 4.11(a) indicates the resistance of the VCSEL,  $R_l$  as shown in Figure 4.12(a) obtained by differentiating second-order polynomial fits to the  $I_l$  vs.  $V_l$  curves.  $R_l$  decreases as temperature increases as shown in Figure 4.12(b).

The power vs. current relationship further emphasises the behaviour seen in the  $I_l$  vs.  $V_l$  plot. Initially the optical output power increase is slow and linear with  $I_l$  between  $\sim 0$  mA and  $\sim 3$  mA. In this regime the output power is dominated by spontaneous emission. At these low currents the probability of stimulated emission is small and most of the photons are absorbed by the semiconductor. The effect is best seen by zooming in on the Figure 4.11(b) as shown in Figure 4.13(a). Increasing the current increases the number of photons generated via both spontaneous and stimulated processes. Eventually  $I_t$  is reached (between 1 mA and 3.5 mA) at which point the number of photons emitted and absorbed are equivalent. Above  $I_t$  stimulated emission dominates the op-

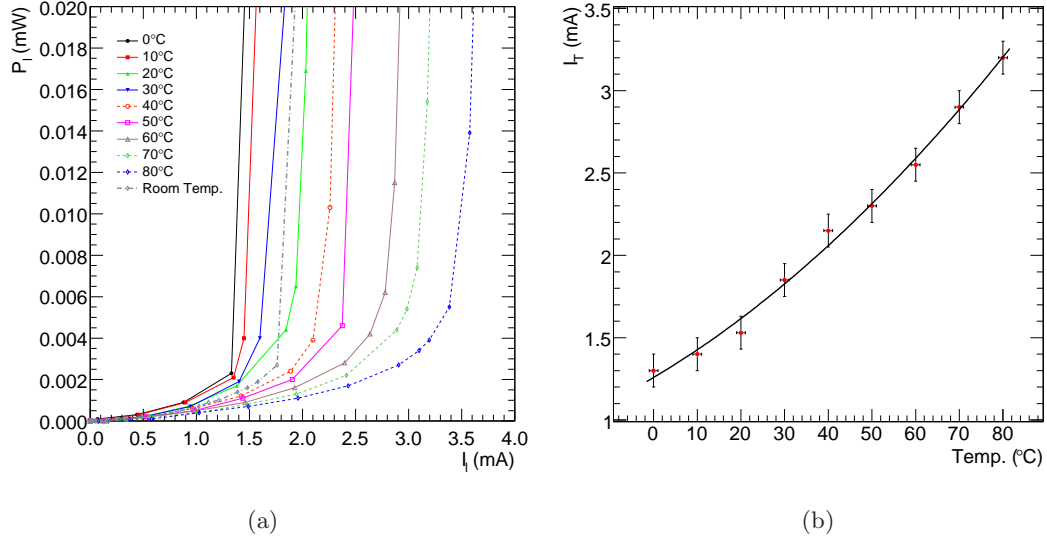


Figure 4.13: (a) A close up of Figure 4.11(b) illustrating the rapid increase in  $P_l$  when operating above the VCSEL threshold current,  $I_t$ . (b)  $I_t$  as a function of temperature with a second-order polynomial fit.

tical power which increases rapidly with  $I_l$  and enters a nearly linear region up to at least 10 mA. The output power then gradually saturates and even begins to turn over at very high  $I_l$ . The linear region begins at lower currents and extends to higher currents at lower temperatures. Conversely at higher temperatures the optical power saturates at far lower currents.  $I_t$  may be determined by extrapolating the linear portion of the stimulated-emission dominated region, which can be seen as the practically vertical region of Figure 4.13(a), down to where it intersects the current axis. A low  $I_t$  is an important laser feature and a large  $I_t$  causes problematic self-heating in the laser (see Section 4.7). Figure 4.13(b) shows the relationship between  $I_t$  and temperature, which is well described by a second-order polynomial, as shown by the solid black line.

The gradient of the  $P_l$  vs.  $I_l$  curve is known as the slope efficiency,  $s_l(I)$ , and represents the efficiency with which electrical modulation is converted to optical modulation as first mentioned in Section 4.4.1. The higher,  $s_l(I)$  the better. Here  $s_l(I)$  is used to describe the fibre-coupled slope efficiency and consequently includes losses in efficiency in the coupling of the VCSEL to the E2000 connector. Figure 4.14(a) shows  $s_l(I)$  as a function of  $I_l$  obtained by fitting the  $P_l$  vs.  $I_l$  curve at a given temperature with a sixth-

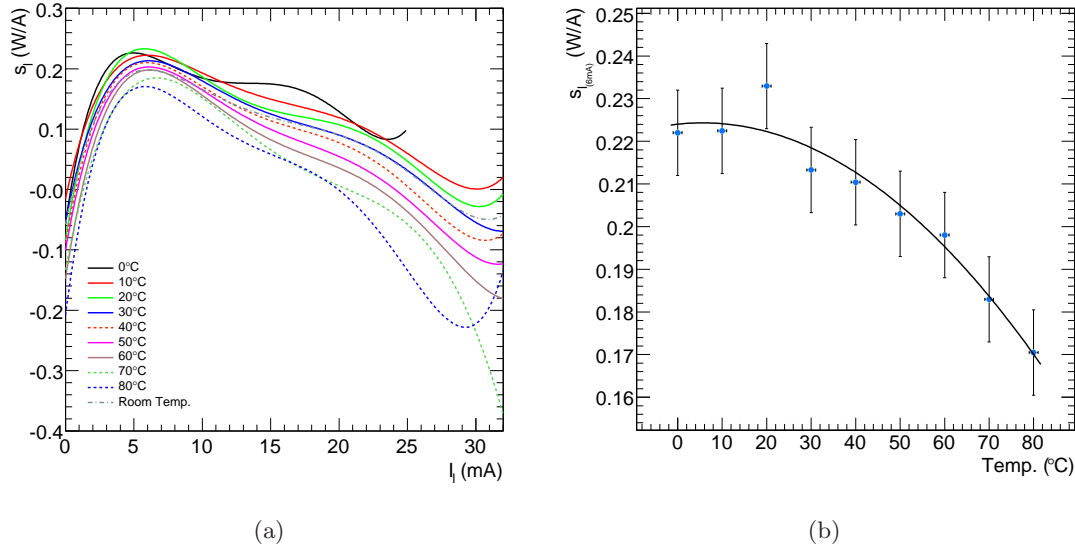


Figure 4.14: (a) The fibre coupled slope efficiency,  $s_l$  for various VCSEL temperatures as given by the gradient of the  $P_l$  vs.  $I_l$  curve obtained by differentiating a sixth order polynomial fit to Figure 4.11(b). (b)  $s_l$  as a function of temperature with a second-order polynomial fit.

order polynomial and differentiating the resulting function.  $s_l$  increases steeply with  $I_l$  and reaches a peak between  $\sim 0.15$  W/A and  $\sim 0.25$  W/A depending on temperature, consistent with the expected value of  $\sim 0.2$  W/A noted in Section 4.4.1. At high currents the function used to estimate  $s_l$  acts unpredictably due to the sixth-order polynomial fit used, however, in the current range of interest here (above  $I_t$  and below  $\sim 12$  mA)  $s_l$  is satisfactorily described. The slope efficiency at 6 mA as a function of temperature is shown in Figure 4.14(b) with a second-order polynomial fit. It is evident that an increase in temperature that changes  $s_l$  may be counteracted by altering  $I_b$ , although this clearly depends on the severity of the required change in  $s_l$ .

It should be noted that  $s_l(I)$  can also be expressed in terms of the external differential quantum efficiency,  $\eta_l$ , the ratio of the change in the number of emitted photons coupled in the fibre to the change in the number of injected electrons:

$$s_l(I) = \frac{\eta_l(I)hc}{q\lambda_o}, \quad (4.1)$$

where  $q$  is the charge of an electron and  $\lambda_o$  is the wavelength of light. The maximum slope efficiency occurs when  $\eta_l(I) = 1$  and corresponds to a value of 1.44 W/A for light

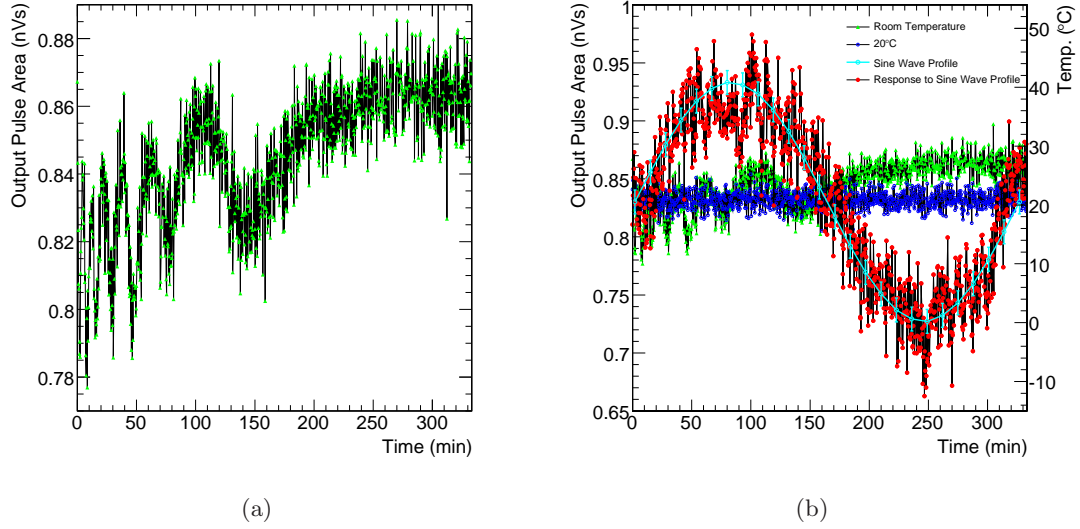


Figure 4.15: (a) The stability of the output pulse area given a constant input at room temperature. (b) The results of the stability measurement, again at room temperature (green), at a constant  $20^{\circ}\text{C}$  (blue), and as a the temperature is varied according to a sine-wave profile (red).

of wavelength 850 nm. For  $s_l=0.2\text{ W/A}$  (a reasonable estimate at room temperature when  $I_b=6\text{ mA}$ ) then  $\eta_l(6mA)=0.16$ , for  $\lambda_o=850\text{ nm}$ .

### 4.6.2 Stability

The IACT technique relies on an accurate estimation of the photon flux incident on a PMT from the area of the resulting pulse. It is therefore essential that the output pulse area from the optical link does not change radically over time given a steady input. To assess the long-term stability of the optical link the VCSEL is biased to 6 mA, a pulse of amplitude  $100\text{ mV}^4$  and FWHM 5 ns is input to the transmitter and the area of the output pulse is measured once every 20 s for 330 minutes. To minimise the contribution of the pedestal to measured area the Agilent Infinium MSO is configured to sample the pulse over a narrow, 15 ns, window centred on the pulse at a rate of 4 GSa/s.

The results of the stability test taken with the transmitter at room temperature are shown in Figure 4.15(a). The pulse area has a maximum deviation from the mean of

<sup>4</sup>Although the minimum pulse size that it is desirable to transmit within VERITAS is  $\sim 10\text{ mV}$  a typical Cherenkov pulse will have an amplitude of  $\sim 100\text{ mV}$  corresponding to  $\sim 10\text{ p.e.}$

6.0%. The long time variations are clearly larger than the baseline, short term variations that constitute the noise of the optical link (see Section 4.6.4 for more about noise). To investigate the larger than expected variations observed at room temperature the transmitter is placed in the environmental chamber and the stability of the output pulse area with the temperature held at 20° is measured. The result is shown in blue in Figure 4.15(b) along with the result at room temperature for comparison. The output pulse area varies from the mean by a maximum of only 3.0%, implying a strong dependence on temperature. The red points in Figure 4.15(b) show the stability of the output pulse area when the temperature is set according a sine-wave temperature profile that ranges from 0°C to 40°C. The programmed sine-wave profile is plotted in cyan and the temperature is shown on the right y-axis. The output pulse area is clearly correlated with the temperature, with a maximum deviation from the mean of 19.3%. As the temperature increases the output area also increases. Figure 4.11(b) indicates a decrease in VCSEL optical power  $P_l$  with an increase in temperature. However, this assumes a constant  $I_l$ . Figure 4.11(a) shows that at a given  $V_l$ , as supplied by the op-amp,  $I_l$  increases as the temperature increases. From Figure 4.11(b) it can be seen that operating at this higher  $I_l$  outweighs the intrinsic drop in  $P_l$  experienced by accessing the  $P_l$  vs.  $I_l$  curve at a higher temperature, as long as the VCSEL is not near saturation.

It is clear that variations in the temperature of the transmitter affect the stability of the optical link. Inside the VERITAS camera the temperature can vary from 0°C to 40°C in the course of a single evening and the output pulse area will be affected correspondingly. The issue of temperature compensation and the resulting long term stability is addressed further in Section 4.7.

### 4.6.3 Linearity

It is not only important that an input pulse of constant area is transmitted reliably over the optical link as investigated in the previous subsection but also that the area of the output pulse is related linearly to that of the input pulse over a large range of pulse sizes [118]. This *linearity* directly determines the useable dynamic range of the optical link. The noise introduced to a transmitted pulse by the optical link is related to the size of that transmitted pulse. As the pulse size is decreased the measured signal

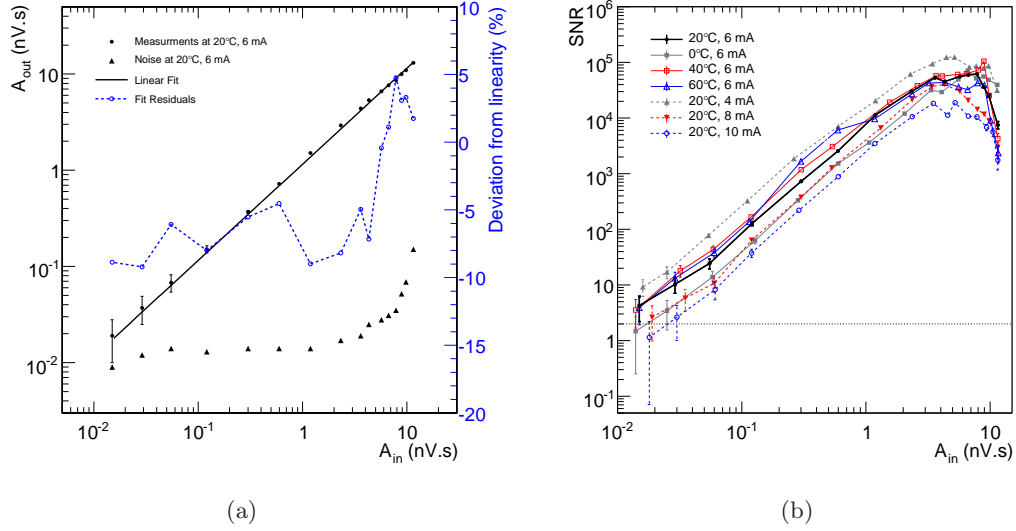


Figure 4.16: (a) The output pulse area,  $A_{out}$  and RMS noise in the output pulse area, as a function of the input pulse area,  $A_{in}$  with the transmitter at  $20^\circ\text{C}$  and  $I_b=6\text{ mA}$ . The data is fit with a linear relationship and the fit residuals are shown in blue corresponding the right-hand side y-axis. (b) The signal to noise ratio, SNR, as a function of the  $A_{in}$  at various transmitter temperatures and  $I_b$ .

approaches the level of fluctuations, or noise, in that signal. If the noise exceeds the signal the dynamic range is limited. It is therefore important that the amount of noise associated with a given pulse size at a given  $I_b$  and temperature is predictable and well understood and this is covered in Section 4.6.4.

Figure 4.16(a) shows the measured output pulse area,  $A_{out}$ , as a function of the measured input pulse area,  $A_{in}$ , in red with the transmitter at  $20^\circ\text{C}$ .  $A_{in}$  corresponds to a range of input amplitudes from 2 mV to 2.2 V all with FWHM 5 ns. The measured noise, given simply by the RMS in  $A_{out}$  is shown in the lower curve. During these measurements the Agilent Infinium MSO is configured to mimic the response of a VERITAS FADC channel, sampling the pulse at a rate of 500 MSa/s across a  $\sim 13$  ns integration window. The mean area measured by the MSO in the absence of a pulse on the input channel gives an indication of the combined MSO and pulse-generator pedestal included in the measured pulse area. The RMS of the pedestal area indicates the MSO and pulse generator noise included in the measured pulse area. The pedestal is subtracted from both  $A_{in}$  and  $A_{out}$  and the pedestal RMS is subtracted in quadrature from the measured

noise in the output pulse area.

The relationship between  $A_{in}$  and  $A_{out}$  is well described by a linear fit, as shown by the solid line in Figure 4.16(a), and is related to the *transducer power gain*,  $g_t$ , of the optical link, given by:

$$g_t = \frac{P_{out}}{P_{in}} = \frac{A_{out}^2}{A_{in}^2}, \quad (4.2)$$

where  $P_{in}$  and  $P_{out}$  are the electrical power available at the transmitter input and receiver output respectively. The available electrical power is proportional to the voltage squared, and therefore also the pulse area squared. Thus, the gradient of the linearity plot,  $m$ , is directly related to the *transducer power gain* of the optical link via  $g_t = m^2$ . The gradient of the linear fit in Figure 4.16(a)  $1.15 \pm 0.02$  leads to an average gain over the range of the fit of  $1.33 \pm 0.05$ .

The intrinsic properties of the laser are best explored by considering the *intrinsic gain*,  $g_i$ , defined as the *transducer power gain* of an amplifier-less optical link and given by:

$$g_i = g_l \cdot g_f \cdot g_d, \quad (4.3)$$

where  $g_l$ ,  $g_f$  and  $g_d$  are the VCSEL, fibre and photodiode gains respectively. To proceed it is first noted that electrical power is proportional to optical power squared. Then:

$$g_i = \left( \frac{P_l^2}{P_s} \right) \cdot \left( \frac{P_d^2}{P_l^2} \right) \cdot \left( \frac{P_{load}}{P_d^2} \right), \quad (4.4)$$

where  $P_s$  is the electrical power available at the VCSEL, and  $P_{load}$  is the electrical power supplied by the photodiode to the receiver load.  $P_s$  and  $P_{load}$  are related to  $P_{in}$  and  $P_{out}$  by the transmitter op-amp gain,  $g_{in}$ , and receiver op-amp gain,  $g_{out}$ .  $g_f$  may be expressed in terms of the optical transmission through the fibre,  $T_f$ :

$$P_d = P_l T_f, \quad (4.5)$$

measured to be -1.28 dB, or 75%, over 100 m of fibre. Then:

$$g_i = \left( \frac{P_l^2}{P_s} \right) \cdot T_f^2 \cdot \left( \frac{P_{load}}{P_d^2} \right). \quad (4.6)$$

The optical output power of the VCSEL,  $P_l$  is related to the current at the VCSEL,  $I_l$  via the fibre coupled slope efficiency,  $s_l$  and given by:

$$P_l = s_l I_l. \quad (4.7)$$

Similarly the current at the photodiode,  $I_d$  is related to the responsivity,  $r_d$  by the optical power at the photodiode,  $P_d$  and given by:

$$I_d = r_d P_d. \quad (4.8)$$

Then, returning to  $g_i$ :

$$g_i = \left( \frac{R_{load}}{R_s} \right) s_l^2 T_f^2 r_d^2 \quad (4.9)$$

where  $P_s = I_l R_s$  and  $P_{load} = I_d R_{load}$  have been substituted for  $P_s$  and  $P_{load}$  respectively.  $R_{load}$  is the impedance of the load at the receiver and  $R_s$  is the impedance of the transmitter driver circuit and, in this case, is approximately equivalent to the resistance of the VCSEL,  $R_l$ . The *transducer power gain* is then:

$$g_t = g_i \cdot g_s \cdot g_{load} = 10 \cdot \left( \frac{R_{load}}{R_l} \right) s_l^2 T_f^2 r_d^2. \quad (4.10)$$

Obtaining  $s_l$  from Figure 4.14(a) at 6 mA and 20°C leads to  $g_t = 1.4$ , which is roughly consistent with  $m^2$ . From here on the *transducer power gain* is referred to simply as the *gain*.

Referring again to Figure 4.16(a); the linear-fit residuals are shown in blue and correspond to the scale indicated on the second y-axis (again in blue). A maximum deviation from the linear fit of 11.9% is found. The input pulse amplitudes range from 2 mV to 2.2 V corresponding to a dynamic range of 1100 (although this is not the *useable* dynamic range), or as more commonly expressed, 61 dB, exceeding the specification noted in Section 4.3. Deviations of up to ~8% were reported in the optical link installed in the

Whipple-10 m telescope [49], although the dynamic range was limited to between 1 mV to 100 mV. The MAGIC system experienced deviations from linearity of up to  $\sim 15\%$  [142] across a dynamic range closer to that obtained here, from 1.5 mV to 940 mV.

The greatest deviations from linearity appear at the smallest input pulse amplitudes. Here the noise approaches the signal level, best visualised by considering SNR as a function of input pulse area as shown in Figure 4.16(b) for several temperatures and bias currents. The SNR is given by:

$$SNR = \frac{P_{out}}{P_{noise}} = \left( \frac{A_{out}}{A_{noise}} \right)^2, \quad (4.11)$$

where  $P_{noise}$  is the average noise power at the receiver output and  $A_{noise}$  is the corresponding RMS area. In RF electronics it is generally accepted that a signal is distinguishable from the associated noise if the SNR is at least 2. The SNR drops to below 2 for the smallest input pulse amplitudes at the low end of the temperature range and at the highest bias currents. The SNR is at least 2 across all temperatures and bias currents for input amplitudes between 7.5 mV and 2.2 V, corresponding to a *useable* dynamic range of 293, or 49 dB.

The *gain* of the optical link is expected to increase with temperature since, as noted in Section 4.6.2,  $A_{out}$  increases with temperature. Figure 4.17(a) shows the measured linearity with the transmitter held at 0°C, 20°C, 40°C and 60°C. Indeed  $m$  is seen to increase from 1.01 to 1.30, corresponding to an increase in *gain* from 1.02 to 1.69. The difference in  $m$  between 20°C and 40°C is approximately 20%, consistent with the 19% increase in  $A_{out}$  observed using the sine-wave temperature profile in the previous stability measurement. It should also be noted that the noise increases and as it will be seen in the proceeding noise analysis (see Section 4.6.4, this is expected and can be modelled reasonably easily. A similar behaviour is seen when increasing  $I_b$  whilst at constant temperature as shown in Figure 4.17(b), implying, as previously expected, that a decrease in bias current can be used to compensate for an increase in temperature.

Eq. 4.10 can be used to model this behaviour. Although  $R_{load}$  is a constant,  $R_l$  decreases as temperature increases as shown in Figure 4.12(b). The  $s_l$  also decreases as temperature increases as indicated by Figure 4.14(b), and  $s_l$  and  $R_l$  both depend on  $I_b$ . Therefore:

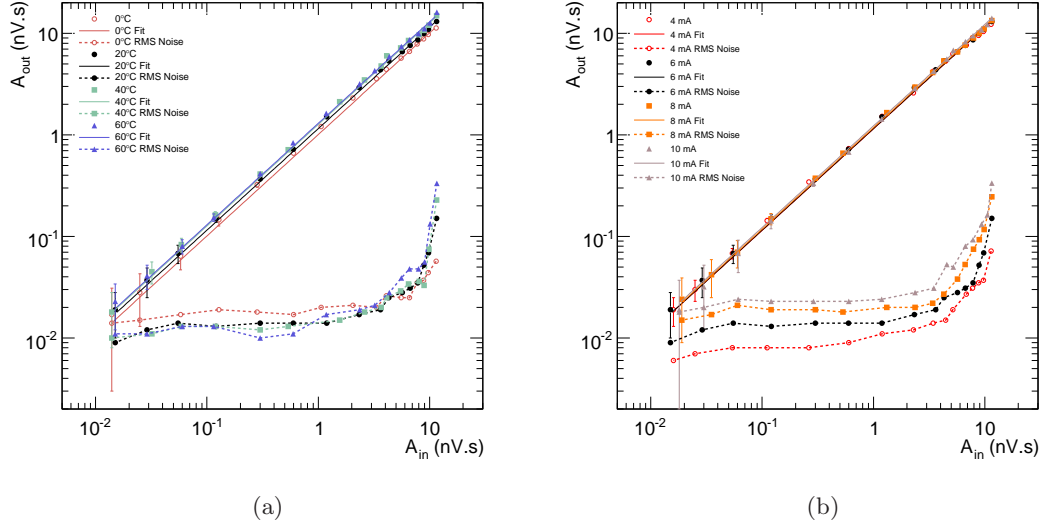


Figure 4.17: (a)  $A_{out}$  and the associated RMS noise as a function of  $A_{in}$  with the transmitter at various temperatures. (b)  $A_{out}$  and the associated RMS noise as a function of  $A_{in}$  with the transmitter operated at various values of  $I_b$ .

$$g_t(T, I_b) = \sigma_w \frac{s_l(T, I_b)^2}{R_l(T, I_b)}, \quad (4.12)$$

where  $\sigma_w$  will be referred to as the *gain parameter* and is a constant with units of  $A^2$  for a given optical link.

$g_t(T, I_b)$  is shown for constant  $I_b = 6mA$  in Figure 4.18(a) along with data points indicating the gradients of the linear-fits in Figure 4.17(a).  $g_t(T, I_b)$  at constant temperature is shown in Figure 4.17(b) along with data points indicating the gradients of the linear-fits in Figure 4.17(b). It is clear that the changes in  $R_l$  outweigh those in  $s_l$ , causing an increase in  $g_t$  with temperature and  $I_b$ . The variations in *gain* with temperature are more severe than those experienced when changing  $I_b$ , which is a consequence of operating the VCSEL in the linear regime of Figure 4.11(b).

#### 4.6.4 Noise Performance

A variety of phenomena cause signals to degrade as they progress through the fibre optical link. Signals attenuate due to VCSEL slope efficiency,  $s_l$ , fibre transmission,

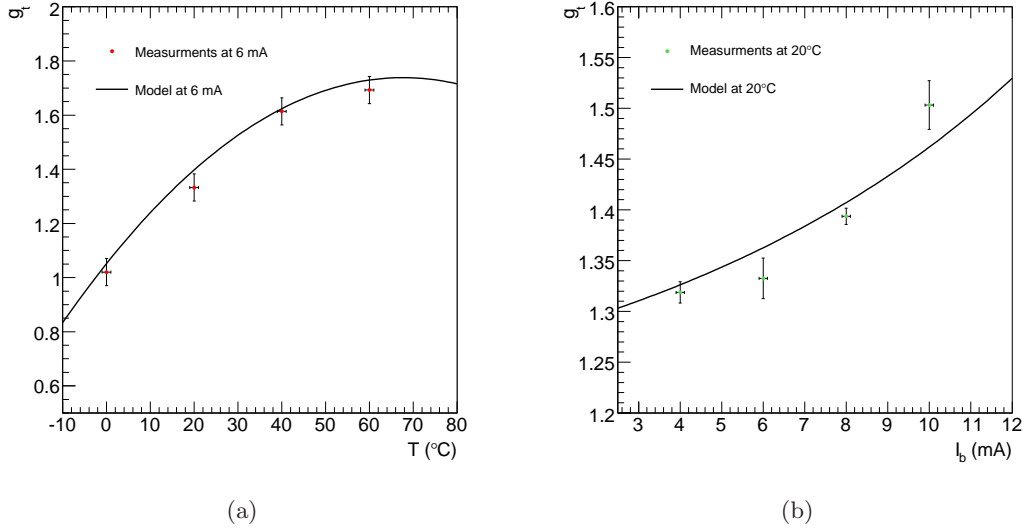


Figure 4.18: The gain obtained from Figure 4.17(a) (red data points) and the model prediction as a function of VCSEL temperature (solid line). The gain obtained from Figure 4.17(b) (green data points) and the model prediction as a function of  $I_b$  (solid line).

$T_f$  and the photodiode responsivity,  $r_d$ . Amplification at the receiver compensates for the signal attenuation, but does so at the cost of also amplifying the link noise. As the amplitude of the input signal is reduced the received power drops and eventually reaches the noise level. Noise is a random process and is therefore described adequately by the mean-squared value. The dominant sources of noise in a link are thermal noise, shot noise and relative intensity noise [152], which combine to give a total mean-square current noise of:

$$\begin{aligned}
 \langle I_{noise}^2 \rangle &= g_{out} \cdot (\langle I_{NTE}^2 \rangle + \langle I_{SN}^2 \rangle + \langle I_{RIN}^2 \rangle) \\
 &= g_{out} \cdot \frac{4k [2T + T_{e(-1)} + T_{e(10)}] f_{3dB}}{R_{load}} \\
 &\quad + g_{out} \cdot 2e [(I_b + I_s) s_l T_f r_d] f_{3dB} \\
 &\quad + g_{out} \cdot RIN [(I_b + I_s) s_l T_f r_d]^2 f_{3dB}. \tag{4.13}
 \end{aligned}$$

Where  $g_{out}$  is the gain of the second receiver op-amp (10) and  $\langle I_{NTE}^2 \rangle$ ,  $\langle I_{SN}^2 \rangle$  and  $\langle I_{RIN}^2 \rangle$  are the relative contributions of thermal noise current, shot noise current and relative intensity noise current respectively. The thermal noise current includes the noise

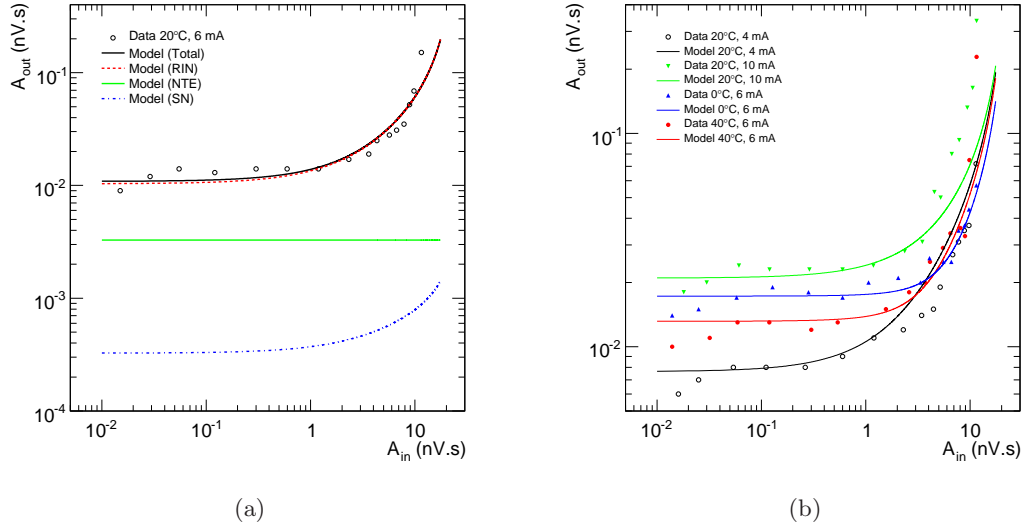


Figure 4.19: (a) The measured RMS noise in  $A_{out}$  as a function of  $A_{in}$  (hollow data points) at  $20^\circ$  and  $I_b=6$  mA and the corresponding model prediction from Eq. 4.13 (black). The contributions of RIN, NTE and SN to the model are shown in red, green and blue respectively. (b) The RMS noise in  $A_{out}$  for various values of temperature and  $I_b$  and the corresponding predictions from the noise model.

introduced by both op-amps at the receiver through the *effective temperatures*  $T_{e(-1)}$  and  $T_{e(10)}$ . RIN is the relative intensity noise as specified by the ZL60052 VCSEL data sheet as -120 dB/Hz and  $T$  is the temperature of the receiver. The full derivation of Eq. 4.13 along with a detailed explanation of the variables therein is given in Appendix B.  $\langle I_{noise}^2 \rangle$  is transformed to a corresponding RMS noise area at the receiver output,  $\sigma_{A_{out}}$ . Similarly the  $A_{in}$  is used to obtain  $I_s$ , and in doing so, a dependence on  $R_l$  is introduced. Again, the details of these transformations are contained in Appendix B.

The contributions of thermal, shot and relative intensity noise to the total noise are shown in Figure 4.19(a) along with the data collected at  $20^\circ\text{C}$  and 6 mA. The total noise is completely dominated by the RIN noise. This implies that the bias current should be kept low, and in future VCSELs with an improved RIN should be sourced.

Figure 4.19(b) shows the total noise for a variety of temperatures and values of  $I_b$  along with the data from Figure 4.17. The changes in noise due to temperature are less extreme than those due to changes in  $I_b$ . The model matches the data reasonably well

as temperature and  $I_b$  are varied. It should be noted that this simple model is not intended to parameterise the noise, but rather aid in the physical understanding of its origins. In this respect the model succeeds, and it can be seen that the predicted link noise is dominated by RIN noise from the VCSEL across the desired operational range of temperature and  $I_b$  as observed in the measurements.

#### 4.6.5 Frequency Response

The frequency response of the optical link to a sine wave input of 100 mV amplitude from the Rohde & Schwarz SMX Signal Generator is used to determine the electrical bandwidth of the system. The frequency of the input sine-wave is varied and the area of the input and output signal over a fixed integration window is measured and used to compute  $g_t$ . The *gain* is expressed in terms of decibels as  $G_t = 10 \cdot \log(g_t)$ . The electrical bandwidth,  $f_{-3dB}$  is defined as the frequency at which  $G_t$  drops by 3 dB from  $G_t$  at low frequencies.

The frequency response of the transmitter is shown in Figure 4.20(a) for a variety of bias currents at 20°. The frequency response of a VCSEL is expected to alter with  $I_b$  according to:

$$f_{relax} = \frac{\sqrt{\frac{I_b}{I_t} - 1}}{\sqrt{2\pi\tau_n\tau_p}} \quad (4.14)$$

where  $f_{relax}$  is the relaxation resonance frequency and refers to a peak in the frequency response of the VCSEL due to a resonance between the stimulated emission in the laser cavity and the injected carriers used to create that emission [145].  $\tau_n$  and  $\tau_p$  are the lifetimes of the injected carriers and cavity photons respectively. No shift in the frequency response of the transmitter is observed as  $I_b$  is varied, and the bandwidth of the transmitter is  $\sim 470$  MHz for all values of  $I_b$ . Substituting  $\tau_n = 1$  ns,  $\tau_p = 1$  ps and  $I_b = 3I_t$  into Eq. 4.14 results in  $f_{relax} = 17.8$  GHz, far above the bandwidth observed. It is therefore not the VCSEL that is limiting the frequency response of the transmitter but rather the OPA695 op-amps used in both the transmitter and receiver.

The frequency response of the transmitter at  $I_b = 6$  mA is also shown in red in Figure 4.20(b) along with the frequency response of the entire optical link connected with

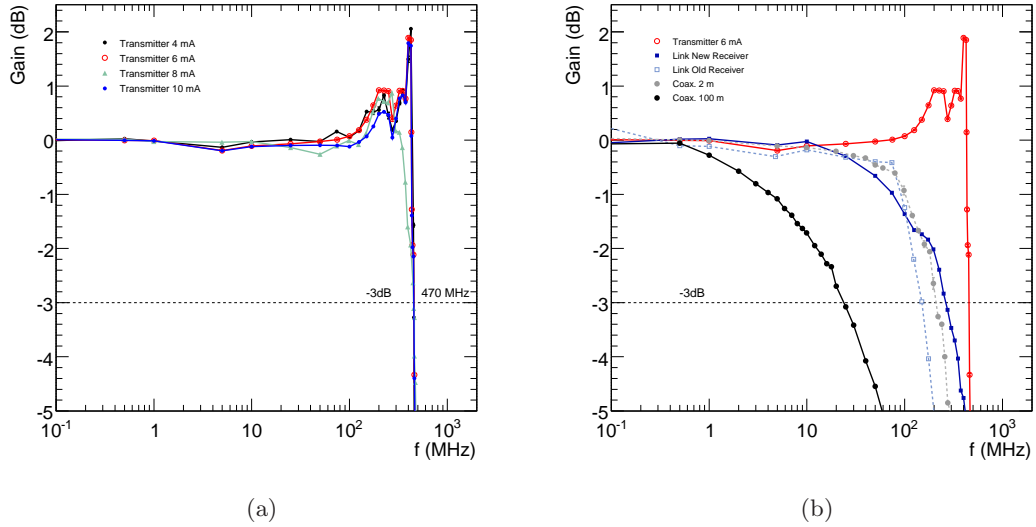


Figure 4.20: (a) The transmitter gain as a function of frequency from various values of  $I_b$ . (b) The frequency response of the transmitter (hollow red symbols) and entire optical link (filled blue symbols) at  $20^\circ\text{C}$  and  $I_b = 6\text{ mA}$ . Also included are the frequency response of the link using the original receiver (hollow blue symbols) and 2 m and 100 m of RG59 coaxial cable (grey and black symbols respectively).

$\sim 100\text{ m}$  of optical fibre shown in solid blue. The receiver significantly reduces the bandwidth of the optical link to  $\sim 250\text{ MHz}$ . The receiver includes two OPA695 op-amps, operated at gains of -1 and 10 respectively. Operating the second op-amp at a large gain is the dominant contribution to the loss of bandwidth. The bandwidth of the optical link connected to the receiver used in the original Whipple-10 m system is even lower at only  $\sim 150\text{ MHz}$ , as shown by the open, light blue squares in Figure 4.20(b). However, the bandwidth of the link easily surpasses that obtainable with 100 m of coaxial cable ( $\sim 25\text{ MHz}$ ), as shown in black, and even 2 m of coaxial cable ( $\sim 200\text{ MHz}$ ), as shown in grey.

For future UNDs and IACT arrays a bandwidth of at least 500 MHz is desirable. The transmitter approaches this benchmark, but a further iteration is needed to raise the link bandwidth. One possibility worth exploring is to reduce the gain of the receiver op-amp from 10 to 5 and increase the gain of the transmitter op-amp to 2. For VERITAS a link bandwidth of 250 MHz is acceptable and matches the specification in Section 4.3. The bandwidth exceeds that of the Whipple-10 m system ( $\sim 150\text{ MHz}$ ) and matches that of

the MAGIC system ( $\sim 250$  MHz)

#### 4.6.6 Transit Time

The transit time across the optical link connected with 100 m of fibre as a function of the transmitter temperature relative to that measured at  $20^\circ\text{C}$  is shown in Figure 4.21(a) for several values of  $I_b$ . As the temperature increases a linear increase in the transit time of  $4.0\pm 0.2$  ps/ $^\circ\text{C}$  is observed. The result is independent of  $I_b$ . Altering  $I_b$  to compensate for changes in the gain of the link due to variations in temperature will not affect the arrival times of pulses at the FADCs.

The relative transit time across the link as a function of fibre temperature is shown in blue in Figure 4.21(b). The variations are comparable to, and at low temperatures greater than, those due to altering the transmitter temperature. As the temperature increases the fibre expands and the transit time increases, although the relationship is not linear [60]. The variations in transit time over the optical link are an order of magnitude smaller than those experienced over the same length of coaxial cable, as shown by the black data points in Figure 4.21(b). The transit time across coaxial cable decreases as temperature increases by an average amount of 53.8 ps/ $^\circ\text{C}$ . The coaxial cable is constructed from an inner core carrying the signal within a dielectric surrounded by stranded cable acting as ground. As the temperature increases the core expands and the transit time increases. However, the strands also expand reducing the pressure on the dielectric, decreasing the capacitance between signal and ground and thereby decreasing the transit-time. The duality between core and strand expansion leads to non-linear variations in transit time .

#### 4.6.7 Distortion

The deviations from linearity noted in Section 4.6.3 distort a signal transmitted over the optical link. These distortions are present both in the shape and spectrum of the transmitted signal [38]. Figure 4.22(a) shows an input pulse of amplitude 100 mV, FWHM 6 ns and rise time,  $T_r$ , 1.8 ns before (green) and after (blue) transmission over the optical link connected with 100 m of fibre. After transmission the pulse FWHM is 6 ns and the  $T_r$  is  $\sim 3.2$  ns. The optical link creates a dispersion of  $\ll 1$  ns and increases

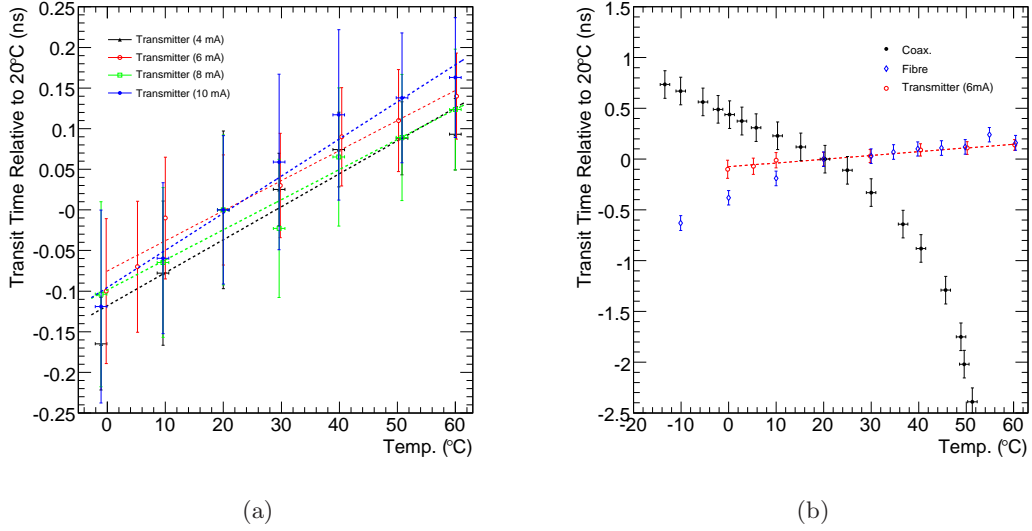


Figure 4.21: (a) The transit time across the optical link relative to that at 20° C as a function of transmitter temperature for several values of  $I_b$  including linear fits. (b) The transit time across 100 m of RG59 coaxial cable (black, filled symbols) and the optical link (blue, hollow symbols) as a function of coaxial cable and fibre temperature respectively. The result at 6 mA from (a) is also included (red hollow symbols) for comparison and again all measurements are relative to the transit time at 20° C.

the  $T_r$  by  $\sim 1.4$  ns. Assuming a Gaussian impulse function a  $T_r$  of  $\sim 1.4$  ns corresponds to a bandwidth of 243 MHz, consistent with that measured in Section 4.6.5. The result after transmission over 100 m of coaxial cable is also included in Figure 4.22(a) (red) and has a FWHM of 8.3 ns and a  $T_r$  of 4.3 ns. The pulses in Figure 4.22(a) have been normalised to an amplitude of 100 mV to compare the dispersion. The FWHM and  $T_r$  of the pulse after transmission over the optical link are unaffected by the temperature of the transmitter or fibre as shown in Figure 4.22(b), and similarly after transmission over coaxial cable.

The distortion introduced into the transmitted signal transfers power from the fundamental frequency to harmonic frequencies [72]. The amount of harmonic distortion may be assessed by inputting a sine wave to the optical link and comparing the resulting Fourier spectrum. Figure 4.23(a) shows the Fourier spectrum of a sine wave of fundamental frequency 10 MHz at the input to the transmitter (green) and output of the receiver (blue). The *Total Harmonic Distortion* (THD) in the signal is then given by

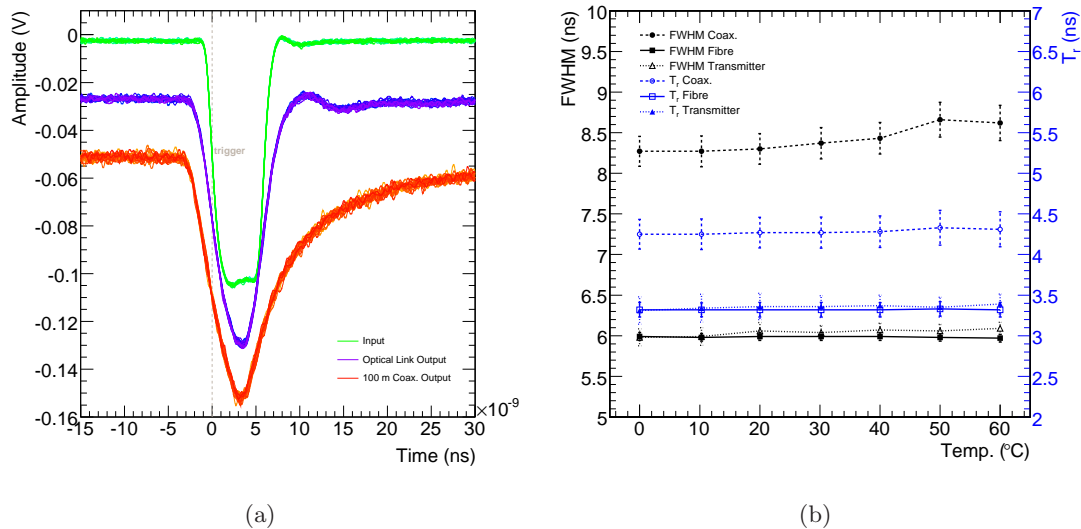


Figure 4.22: (a) The input (green) and output pulses after transmission over the optical link (blue) and 100 m of RG59 coaxial cable (red). The pulses are normalised and offset for easy comparison. (b) The FWHM (left y-axis) and  $T_r$  (right y-axis) of the green pulse shown in (a) after transmission over 100 m of RG59 coaxial cable and the optical link as a function of the coaxial cable, fibre and transmitter temperature.

the ratio of the total power in the harmonics to that in the fundamental:

$$THD = \left( \frac{\sum_{i=1}^n P_i}{P_0} \right). \quad (4.15)$$

The input is not a perfect sine wave and a fraction of the spectral power is already distributed amongst some higher harmonics. For the 10 MHz signal shown in Figure 4.23(a) the output strongly resembles the input, at least at the lower harmonics shown. Using an Anritsu MS261B Spectrum Analyzer, capable of measuring up to 2.2 GHz, the power in the fundamental and first 5 harmonics in both the input and output signal are measured and used to calculate the THD, taking into account the distortion in the input signal. Figure 4.23(b) shows the resulting power distributed to the first two harmonics due to transmission over the optical link. The THD is shown in blue, corresponding to the right y-axis. The THD at 10 MHz is 36.4 dB below the fundamental, or only

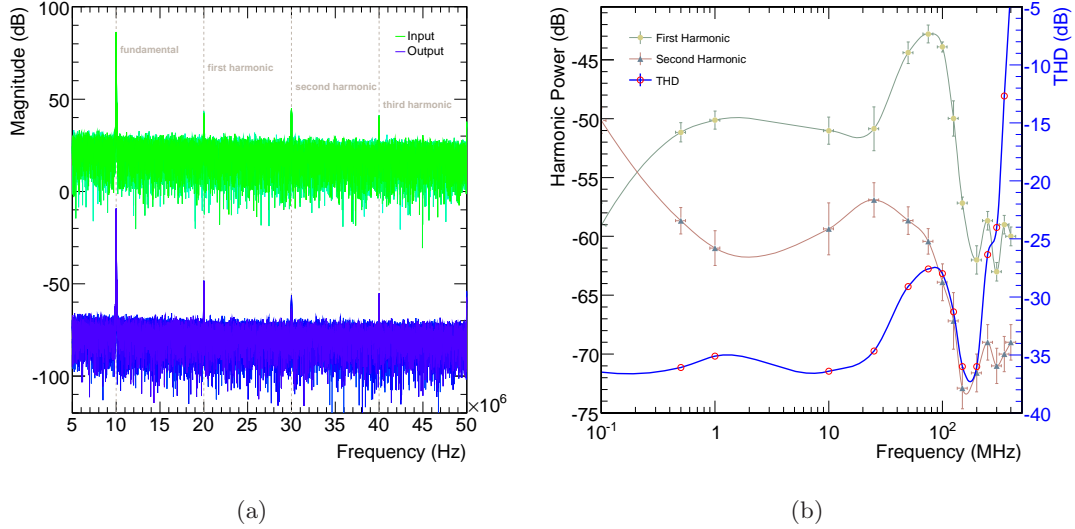


Figure 4.23: (a) The Fourier spectrum of a 10 MHz input signal (green) and the corresponding spectrum at the output of the optical link (blue). (b) The power of the first two harmonics at the output of the optical link as function of the fundamental frequency of the sine-wave input and the corresponding THD (blue line, red circles) as described in the text.

0.023 % of the fundamental. As the fundamental frequency exceeds the bandwidth of the optical link ( $\sim 250$  MHz, see Section 4.6.5), the spectral power of the fundamental drops sharply and the THD rapidly increases.

## 4.7 Temperature Compensation

The performance of the optical link is highly dependent on the temperature of the VCSEL. Even operating at room temperature it is not stable since the VCSEL junction gradually heats up due to the drive current (self-heating). In this section the bias current supplied to the VCSEL is altered in an attempt to stabilise the output over a given temperature range. To determine the value of  $I_b$  that must be set to maintain a constant link gain at a given temperature the area of the output pulse given a constant input pulse of amplitude 100 mV is measured as a function of temperature and  $I_b$ . The results are shown for 3 values of temperature in Figure 4.24(a) and in their entirety in Figure 4.24(b).

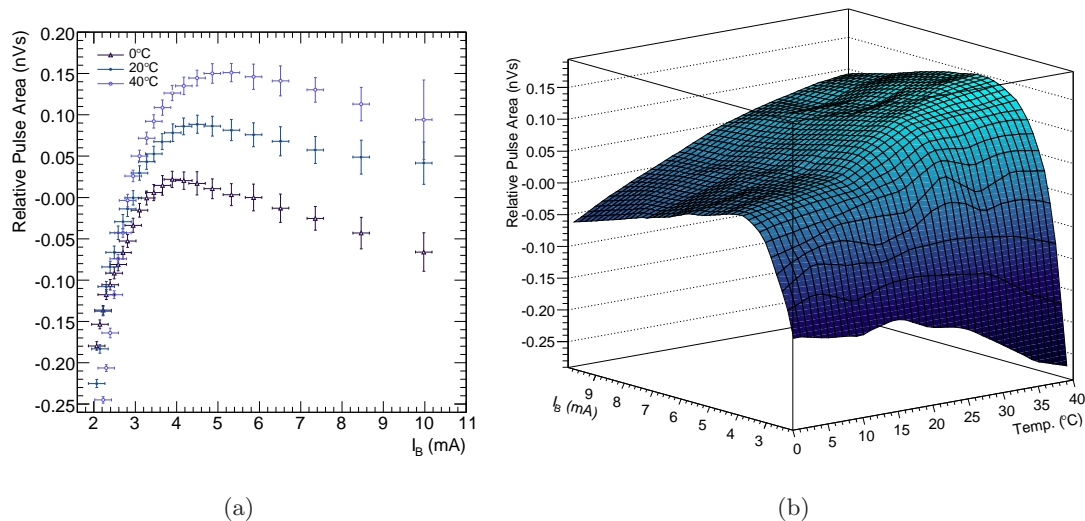


Figure 4.24: (a)  $A_{out}$  as a function of  $I_b$  at  $0^\circ\text{C}$  (hollow triangles),  $20^\circ\text{C}$  (filled circles) and  $40^\circ\text{C}$  (hollow circles). (b)  $A_{out}$  as a function of  $I_b$  and temperature.

The  $I_b$  required to maintain a gain equivalent to that at  $20^\circ\text{C}$  is shown in red in Figure 4.25(a). A requirement that  $I_b$  is greater than 4 mA is included to ensure the VCSEL is well above the lasing threshold at all temperatures. The filled red symbols indicate the  $I_b$  required to preserve the gain within 0.015 nVs ( $\sim 2\%$  for a 100 mV input pulse). The gain may only be maintained to this accuracy between  $14^\circ\text{C}$  and  $26^\circ\text{C}$ . Loosening the tolerance to 0.050 nVs ( $\sim 7\%$  for a 100 mV input pulse), as indicated by the open red symbols, increases the operational range to between  $14^\circ\text{C}$  and  $39^\circ\text{C}$ . The temperature in the VERITAS camera boxes may vary from  $0^\circ\text{C}$  and  $40^\circ\text{C}$  during normal operation. The accessible temperature range may be extended to between  $0^\circ\text{C}$  and  $40^\circ\text{C}$  by selecting a surface of constant gain equivalent to that at  $0^\circ\text{C}$  and removing the minimum  $I_b$  requirement as shown in blue in Figure 4.25(a). Again the open symbols indicate an accuracy of 0.050 nVs and the closed symbols, 0.015 nVs. The extension in temperature range is made possible by accessing the steep slope evident in the  $A_{out}$  vs.  $I_b$  curves to the far left of Figure 4.25(a). To access the full temperature range requires the VCSEL to be operated at low  $I_b$ , close to  $I_t$ . Whilst the specific VCSEL used here remains above  $I_t$  across the entire temperature range this may not be the case for all ZL60052 VCSELs.

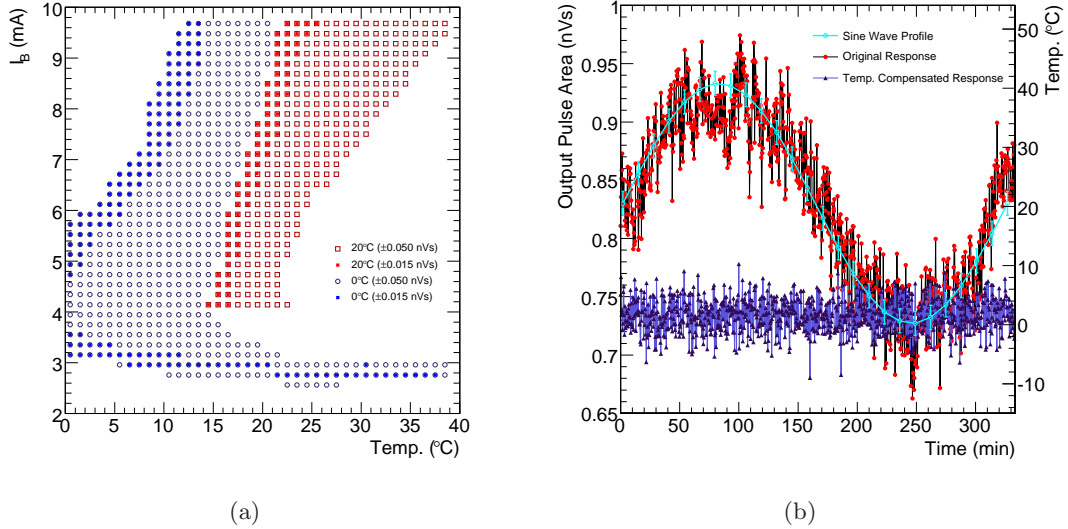


Figure 4.25: (a) The required  $I_b$  to maintain a constant gain to within 0.050 nVs (hollow symbols) and 0.015 nVs (filled symbols) of that at  $20^\circ\text{C}$  (red) and  $0^\circ\text{C}$  (blue). (b) The stability of  $A_{out}$  given a constant input pulse as the temperature is varied according to the sine-wave profile shown in cyan (right y-axis) with temperature compensation (blue) and without (red).

The DS1859 digital resistor chip not only controls  $I_b$ , but also monitors the temperature of the VCSEL. A lookup table corresponding to the desired  $I_b$  as a function of temperature following the filled blue symbols is programmed into the DS1859 over an I<sup>2</sup>C interface. The stability measurement made in Section 4.6.2 varying the temperature according to a sine-wave profile is repeated. The results are shown in blue in Figure 4.25(b) along with those obtained originally with no temperature compensation in red. The sine-wave temperature profile is shown in cyan and corresponds to the scale shown in the right y-axis.  $A_{out}$  appears stable despite the changes in temperature. The mean taken in 5 minute bins varies by only 2.2% inline with the expected 2%. A maximum deviation from the mean of 6% is experienced compared to 19% with no temperature compensation<sup>5</sup>.

As described in Section 4.4.2 the transmitter is designed to accommodate a VCSEL with

<sup>5</sup>This large deviation from the mean may be due to electronic noise introduced by the environmental chamber when changing temperature. This is also present in the results with no temperature compensation and, crucially, absent in the results taken at constant  $20^\circ\text{C}$ , where the environmental chamber needs to do relatively little work to maintain the temperature.

an onboard monitor-photodiode such as the ZL60002 [137]. A feedback loop within the MAX3740A adjusts  $I_b$  to compensate for changes in the optical output of the VCSEL based on the current at the monitor-photodiode. This offers an alternative method of temperature compensation. However, the response of the photodiode and feedback loop to the fast pulses associated with PMTs is uncertain. The MAX3740A is also capable of supplying digital pulses to the VCSEL via a differential input. The most reliable method of removing the temperature dependence in the case of VERITAS may be to continuously transmit calibration pulses of a known size at a low rate,  $\sim 1$  Hz, during normal data taking. The PMT pulses could then easily be calibrated offline using the ratio of the known area of the calibration pulse to that measured. The temperature of the camera could also be recorded in the data stream to aid offline calibration.

## 4.8 Conclusion

A coaxial cable read out scheme is unsuitable for the larger cameras desired for next generation IACT arrays. An optical system offers significantly lower dispersion and attenuation and higher bandwidth than a coaxial system. Additionally fibre is much less bulky than coaxial cables. For example in the MAGIC telescope 72 fibres are packed in a single cable of 16 mm, whereas a single RG59 coaxial cable has a diameter of 5 mm. Optical fibres are at least two orders of magnitude lighter than coaxial cables, which is important to keep the load (and consequently the inertia) of the telescope low. Furthermore there is no crosstalk between channels, signals travelling through optical fibres are immune to electromagnetic interference, and fibre optic cabling is immune to lightning strikes. It is known that lightning can and does strike the VERITAS cables. This leads to (sometimes catastrophic) physical damage.

A prototype optical link has been designed and constructed for the transmission of fast analogue pulses over optical fibre using VCSELs. The transmitter uses the novel concept of supplying the bias current to the VCSEL via a commercially available digital laser driver chip. The performance of the ZL60052 VCSELs exceeds expectations and the resonant peaks due to mode-hopping experienced with previous VCSELs are absent. The optical link exhibits good linearity (to within 12%) over a large dynamic range of 61 dB with an acceptable amount of pulse-shape distortion (the FWHM is distorted

by  $\ll 1$  ns and  $T_r$  is distorted by  $\sim 1.4$  ns) and harmonic distortion ( $< 30$  dB below the fundamental) across the entire bandwidth of  $\sim 250$  MHz, which is itself limited by the response of the receiver. The transmitter alone exhibits a significantly larger bandwidth of  $\sim 470$  MHz.

The gain of the link depends on the temperature of the transmitter. Whilst the area of the output pulse at constant temperature is stable, an increase of  $\sim 19\%$  in area occurs when increasing the temperature from  $20^\circ\text{C}$  to  $40^\circ\text{C}$ . The gain and the noise of the link are modelled effectively once the fibre-coupled slope efficiency and VCSEL resistance are measured as a function of bias current and temperature. The changes in link gain due to variations in the temperature of transmitter are successfully reduced to within 6% of the mean across the entire operating range of the VERITAS camera from  $0^\circ\text{C}$  to  $40^\circ\text{C}$  by automatically setting the bias current according to a pre-programmed lookup table.

There are still difficulties in working with VCSELs. This work, however, indicates that transmission over analogue optical link is a viable option for the read out of next generation IACT arrays and UNDs and offers several advantages over the equally viable alternative of digitising pulses in the camera. All PMT analogue signals are available in the DAQ building, which allows easy inspection for debugging purposes. In the case of IACTs, the camera is lighter since it contains less electronics and power supplies. This helps in controlling the camera oscillations and reduces the counterweight that has to be used. The telescope inertia is lower, which allows a fast telescope repositioning. Separating the trigger system and digitising electronics from the PMTs significantly reduces the pickup noise affecting the PMT signals. The trigger and digitisation system do not have constraints of weight, size and heat dissipation that can significantly increase the cost of the read out system.



## Chapter 5

# High-Speed Topological Triggering with FPGAs

---

The VERITAS pattern recognition trigger consists of a signal splitter (SS) crate to re-route pixels from the camera and a CAMAC crate of pattern selection trigger (PST) modules [33]. In this chapter the pattern recognition trigger is developed using FPGA technology. The resulting trigger design removes the PST crate from the system, performing all pattern decisions in the signal splitter crate. The design increases functionality, providing multiple, parallel, trigger decisions allowing the system to be scaled to much larger cameras. Prototypes of both SS input cards and output cards are produced and tested to evaluate performance and the cost efficiency of the design. The FPGA architecture allows future developments to take place with no further hardware investment. The feasibility of such a trigger for use in VERITAS and future IACTs is discussed.

### 5.1 Introduction

Each VERITAS camera consists of 499, 2.86 cm diameter PMTs. The innermost 463 camera pixels take part in the L2 trigger and are divided into 19 overlapping patches of

pixels. The first patch consists of 19 pixels at the centre of the camera (referred to from herein as  $P_0$ ), whilst the other 18 patches each span an elongated hexagon of 59 pixels. As described in detail in Section 3.4.2, pixels are copied and routed in these patches to the PST modules via the SSICs and SSOCs housed in a custom built crate. The patches of 59 are then copied and mapped to 5 overlapping hexagonal patches of 19 within the PST modules.

The signals within each patch of 19 are summed and input to a majority logic comparator to check if there are more than any 2, 3 or 4 signals present. The comparator decision is used to trigger a time-consuming memory look-up operation to determine if the pattern contains the required number of adjacent signals. The memory look-up decision is latched with a delayed version of the majority logic comparator signal to create a PST FLAGOUT, ensuring a jitter of  $<1$  ns relative to the inputs. The FLAGOUT signals from the PST modules are connected to a custom built OR module to produce the overall L2 trigger decision. The current PST forms a decision in 65 ns, during which time the input is unable to accept further CFD hit patterns. However, note that the other 18 PST modules are still ready to trigger.

In an IACT precise timing between trigger channels is desirable in order to reduce the telescope coincidence resolving time and hence lower the detector energy threshold. To achieve this within VERITAS each pixel channel is equipped with a custom-designed CFD with a trigger time which is independent of the input pulse height. The CFD output width, which corresponds to the coincidence resolving time between pixels, is programmable in 12 steps between 4 ns and 25 ns, a width of 10 ns was used as standard for telescope operations in 2006-2007. A 3-bit, 6 ns programmable delay is provided for each channel so as to correct for systematic differences in the relative signal paths due to cable length differences and the voltage-dependent PMT transit times.

Random fluctuations in the NSB and ion leakage within the PMTs results in a single pixel trigger rate of up to  $\sim 1$  MHz for a CFD threshold of  $\sim 50$  mv (4.5 p.e.). The L2 topological trigger reduces the system trigger rate to the manageable level by requiring  $k$  adjacent pixels out of  $n$  total pixels trigger within a time  $\tau$ , where  $k$  is a pre-programmed coincidence of 2, 3 or 4. The accidental trigger rate due to the NSB is then:

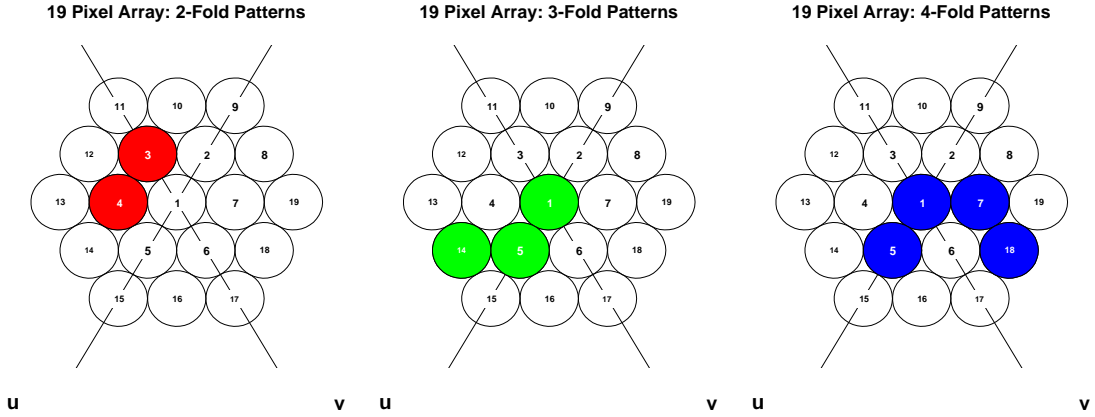


Figure 5.1: Examples of the 2, 3 and 4-fold patterns required to trigger the PST logic.

$$S_k = M_k f_{CFD}^k \tau^{k-1} L, \quad (5.1)$$

where  $M_k$  is the number of possible patterns,  $f_{CFD}$  is the single channel rate after applying the CFD threshold and  $L$  is the number of overlapping patches across the camera. In each VERITAS camera there are  $L = 91$  overlapping patches of 19 pixels. Each patch of 19 contains  $n_2 = 42$  2-fold patterns,  $n_3 = 111$  3-fold patterns, and  $n_4 = 308$  4-fold patterns. An example of each is shown in Figure 5.1. A single pixel rate of  $\sim 1$  MHz is reduced to a system rate of  $\sim 150$  kHz by imposing a 3 fold coincidence condition between adjacent pixels. The accidental coincidence rate between  $k$  adjacent pixels increases as  $f_{CFD}$  increases at a rate depending on  $k$ .  $S_k$  is lower than  $f_{CFD}$  until:

$$f_{CFD} = \left( \frac{1}{M_k \tau^{k-1} L} \right) (1/k), \quad (5.2)$$

at which point  $S_k$  becomes greater than  $f_{CFD}$ . For 2, 3 and 4-fold coincidences within VERITAS this occurs at  $\sim 50$  kHz,  $\sim 2$  MHz and  $\sim 7$  MHz respectively. As it will be shown in Section 5.5.3, this cross-over means that the maximum PST decision frequency limits the single pixel input frequency. For the current L2 system the PST logic requires  $\sim 65$  ns to make a decision, and therefore the output frequency is limited to  $\sim 15$  MHz. The maximum allowable single pixel rate for 3-fold coincidences is then  $\sim 2$  MHz. This in turn places a lower limit on the CFD threshold ( $< 30$  mV), although this limit is well below that currently set ( $\sim 45$  mV) to maintain a manageable array level data rate of

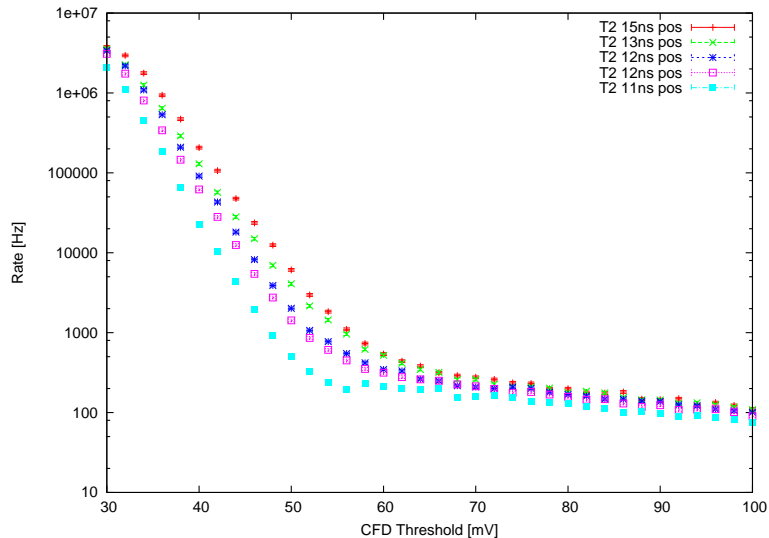


Figure 5.2: *VERITAS T2 bias curves for varying CFD output widths. The NSB is seen to decrease gradually as the CFD width decreases until a sudden drop occurs as the coincidence resolving time of the T2 L2 system is approached.*

~200-300 Hz.

The inputs to the PST modules are aligned in time by adding individually calculated lengths of wire-wrapping to every channel of the output stage of the SSOcs. In this way the inputs to the PST modules are aligned to within a maximum of 2.5 ns of each other.

The required overlap time between adjacent CFD hits at the PST corresponds to the coincidence resolving time of the L2 trigger system. This is determined by the combination of skew between the signals and minimum overlap requirement imposed by the PST comparator. The coincidence resolving time of the current L2 system is  $\sim 6$  ns for T1 and  $\sim 10$  ns for T2, T3 and T4 (due to the use of different comparators). Thus, whilst the coincidence resolving time between pixels may be reduced to the order of a typical Cherenkov pulse rise time convolved with the reflector response ( $\sim 5$  ns) by simply lowering the CFD output widths, the coincidence resolving of the telescope remains limited by that of the L2 trigger.

The effect of altering the CFD width on the VERITAS T2 3-fold trigger rate is shown in Figure 5.2 by the so-called *bias curve* first introduced for varying L2 multiplicities

in Figure 3.13(b). The NSB is seen to decrease gradually as the CFD width decreases until a sudden drop occurs as the coincidence resolving time of the T2 L2 system is approached.

The current VERITAS L2 PST is not scalable to future IACTs, where higher-density cameras and arrays of greater numbers of telescopes are desirable. Although an FPGA based solution was considered for use in the original PST modules this idea was abandoned due to the large jitter and routing uncertainty inherent to FPGA technology at the time. Recent improvements in FPGAs and the successful application of this technology to IACTs by the MAGIC collaboration [26; 131; 165] suggest that it is now timely to reconsider this option.

## 5.2 FPGA Basics

A FPGA is a semiconductor device containing programmable logic components known as *configurable logic blocks* (CLBs), and programmable interconnects. CLBs can be programmed to perform the function of basic logic gates such as AND, and OR, or more complex combinational functions such as decoders or simple mathematical functions. In most FPGAs the CLBs also include memory elements, which may be simple flip-flops or more complete blocks of memories. A hierarchy of programmable interconnects allows CLBs to be connected as needed. A typical CLB consists of a 6-input lookup table (LUT), and a flip-flop. The programmable interconnects and CLB are surrounded by input and output (I/O) blocks. Each of these provides individually selectable input, output, or bi-directional access to one of the general-purpose I/O pins on the exterior of the FPGA package. FPGAs are now available with up to  $\sim 800$  I/O pins. The I/O standard may be selected at design time, although not all FPGAs are capable of accepting and driving differential signals, and there are no FPGAs that can deal with negative differential signals such as the NECL used throughout VERITAS.

Over the past few years the density of the average FPGA has increased dramatically and the maximum number of gates in an FPGA now exceeds 500,000. Different manufacturers use different definitions to define gate count, and so this value is largely arbitrary, but whatever the definition, the price of an individual NAND or NOR is rapidly ap-

proaching zero. More relevant is the maximum clock speed. High performance FPGAs can perform at over 500 MHz and even up to 1 GHz in rare instances, whilst even average FPGAs reach 200 MHz. However, FPGAs are usually slower than their application specific integrated circuit (ASIC) counterparts, they cannot handle as complex a design, and draw more power. But their advantages include a shorter development time, the ability to re-program in the field, and lower non-recurring engineering costs [24].

There are several manufactures of FPGAs, and the leading competitors are Xilinx and Altera. In this work the Xilinx Spartan II, Spartan 3 and Virtex-4 FPGAs are used, although the Spartan 3 is not introduced until Chapter 6.

In order to program an FPGA a description of the hardware's structure and behaviour is first written in a high-level hardware description language. In this work Very High Speed Integrated Circuit Hardware Description Language (VHDL) is used [144]. The code is compiled and then placed and routed through the user specified FPGA package in software before downloading the resulting bit file prior to execution. Schematic capture is available for design entry, and this option is used in Chapter 6.

### 5.3 An FPGA Based Topological Trigger

The proposed FPGA based L2 design is shown in Figure 5.3. FPGAs are added to both the SSICs and the SSOCs in the SS crate. The PST Camac crate and the cumbersome ribbon cable interconnects that were described in Section 3.4.2.1 and shown in Figure 5.4(b) are completely removed from the design. The FPGAs on board the SSIC will allow the user to disable and enable channels and inject test pulses over an I<sup>2</sup>C interface in an identical manner to the current SSIC. The FPGAs on board the SSOCs must first align the 59 input signals and then perform the PST operations. In the current PST crate an OR module provides a NIM output if any of the PST are triggered. In the new system the OR module will contain a further FPGA to not only provide the logical OR of the 19 sets of 59 FLAGOUT signals, but also align the signals and mask patches from the trigger as desired by the user.

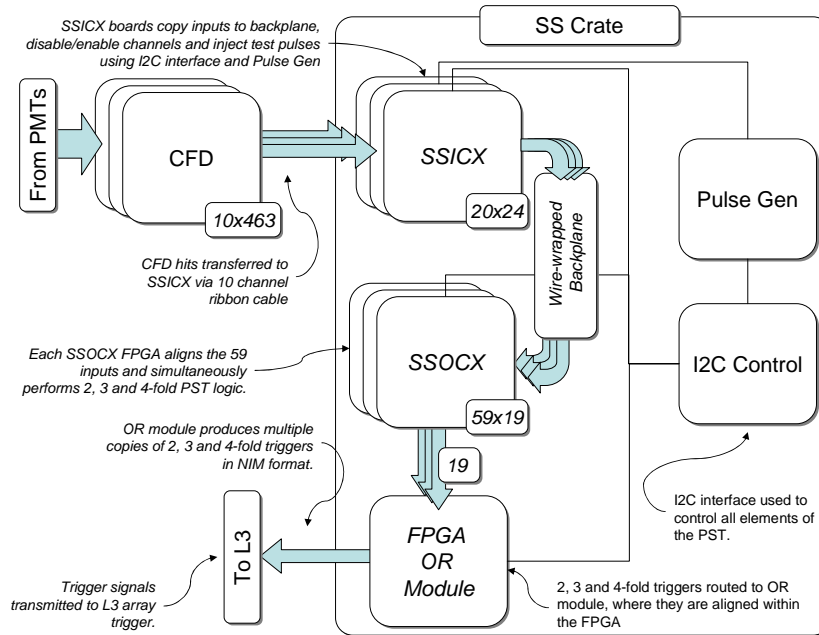


Figure 5.3: The control structure of the intended FPGA based PST system.

## 5.4 The Splitter Input Card with Spartan-II (SSICXv1)

The existing SSIC was adapted to include a Xilinx Spartan-II XC2S50 FPGA [189] as shown in Figure 5.4(a) to create the signal splitter input card with Xilinx (SSICXv1). The SSIC is not required to perform complex operations or signal alignment thus a low-end FPGA was initially chosen to reduce the production cost. The current SSIC costs  $\sim\pounds 100$ , whereas the SSICXv1 costs  $\sim\pounds 1800$  for a one-off prototype. However, the cost of the prototype is dominated by the design, layout and routing and is expected to reduce by a factor of ten when  $>10$  boards are needed. The FPGA cost is relatively low, and the Spartan-II offers  $\sim 70$  I/O pins for  $\sim \pounds 20$ .

### 5.4.1 SSICXv1 Design

The SSICXv1 accepts 20 differential NECL signals on two boxed, latched headers. The inputs are converted to single ended TTL signals, suitable for input to the Spartan-II FPGA, using MC10H125P level converters.

In order to prototype the trigger logic eventually intended for the SSOC with onboard

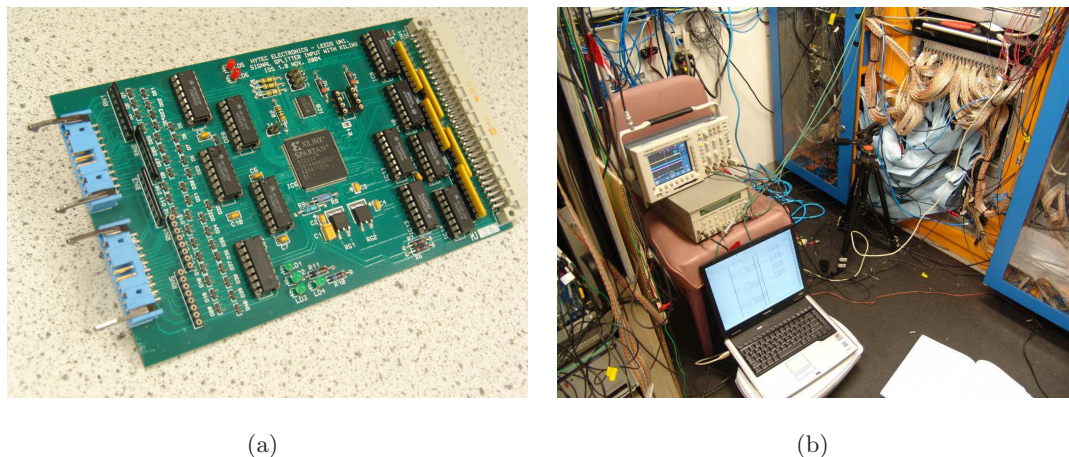


Figure 5.4: (a) The SSICXv1 with Spartan-II FPGA. (b) The test setup used to evaluate the onsite performance of the SSICXv1 in the VERITAS T1 electronics trailer. Note the current L2 system to the right. The FPGA implemented system will remove the lower PST crate and the bulky blue ribbon cables.

FPGA (SSOCX), the SSICXv1 was programmed not only to map input signals to the back plane of the SS crate, but also to perform 3-fold adjacent trigger recognition between the first 19 input signals.

The functionality of the original SSIC is implemented using a simple combinatorial method of disabling or enabling a given channel. Test pulses can be injected across all channels simultaneously via the backplane using an additional FPGA I/O pin. The I<sup>2</sup>C interface is equivalent to the original SSIC. The 20 signals are routed through the FPGA and output on a second set of 20 I/O pins. The signals are output as TTL, converted to NECL using MC10H124P chips, and output to the backplane.

The PST logic itself consists simply of layers of AND gates to assess each 3-fold adjacent pattern and then OR gates to assess if any of the patterns have occurred. This simple combinatorial architecture is possible due the thousands of available logic gates in the FPGA.

#### 5.4.2 SSICXv1 Performance

At the time of testing the SSICXv1 there was no efficient way of injecting 20 NECL input signals and monitoring both the NECL output signals and the resulting pattern

trigger decision in the laboratory in Leeds. Instead the prototype was tested onsite using the first VERITAS T1 telescope. The onsite test setup is shown in Figure 5.4(b). The SSICXv1 was inserted into the T1 L2 SS crate, replacing the first SSIC, which accepts the  $P0$  camera pixels.  $P0$  is identical in shape to those that overlap to form the elongated hexagonal patches of 59 in the current PST modules, and therefore searching for coincidences within this inner patch is an adequate indication of the trigger logic performance within the FPGA. To allow VERITAS to operate uninterrupted, it was necessary to perform both the PST logic within the SSICXv1 and simultaneously route the input signals to the back plane.

The SSICXv1 successfully routed signals to the back plane. A skew of around 0.81 ns was noted between channels. On average, over four of the original SSICs, a skew of 0.85 ns was noted between the 20 input channels. Although the SSIC and SSICXv1 introduce similar spreads into the transit times of input pulses, the SSICXv1 is faster than the SSIC, taking on average  $\sim 50$  ns to traverse the board as opposed to  $\sim 56$  ns. This difference misaligns the first 20 camera signals at the current SSOC outputs. Furthermore when the FPGA is programmed with the PST logic in addition to the feed-through operations, the transit times of the individual channels alters due to the FPGA routing. There is no onboard clock on the SSICXv1, so there is no reliable way to delay the input signals. A crude tap-delay, using LUTs, was attempted, but only achieved a resolution of between 1.8 ns and 3.0 ns, depending on the routing. With no accurate way of maintaining the alignment at the SSOC it was not possible to integrate the SSICXv1 into the current VERITAS L2 system.

The SSICXv1 PST logic was tested by injecting identical copies of pulses to the input channels using a pulse generator. Adjacent pixels resulted in a positive trigger decision and non-adjacent pixels did not. However, not all 111 combinations of 3-folds could be checked by hand, let alone all the combinations of pixels that should not result in a trigger. The minimum width of the three input pulses that resulted in a positive trigger decision determines the coincidence resolving time and depends on the skew between the adjacent channels in question. For the relatively few combinations checked this was around 10 ns. This large coincidence resolving time was attributed to the uncorrected skew between channels, worsened by differences in the internal FPGA routing, and the

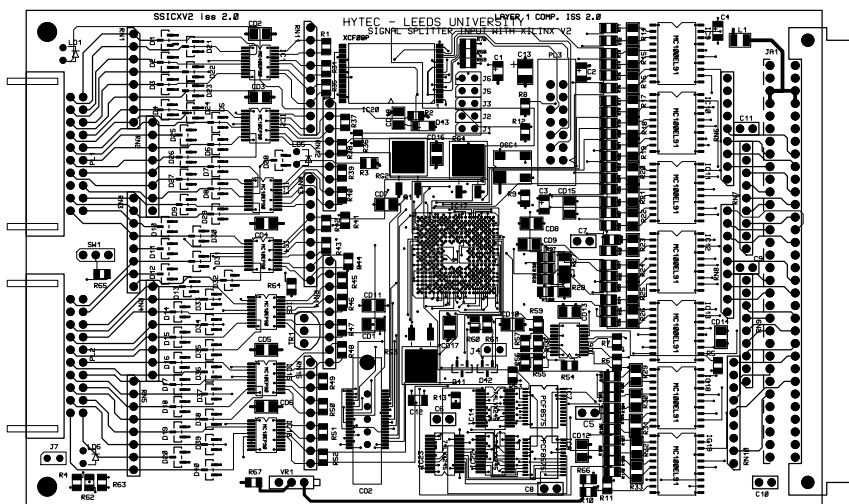


Figure 5.5: *The top layer of the PCB routing for the SSICXv2.*

use of the relatively slow switching speed ( $\sim 4$  ns for a 2.5 V swing) of the TTL signals. It became clear that in order to reduce the coincidence resolving time of the PST differential signalling and a high-speed clock were required.

## 5.5 The Splitter Input Card with Virtex-4 (SSICXv2)

To reduce the coincidence resolving time of the FPGA implemented PST and to match the timing of signals within the current SS crate, a second iteration of the SSICX, the SSICXv2, was designed and built. The Spartan-II FPGA was replaced with a Xilinx Virtex-4 XC4VLX15, capable of handling differential signals and high-clock speeds (of up to 500 MHz) needed to accurately delay and align the input signals. A fast oscillator was added to the circuit, and a high-density MICTOR connector was included to test the board in the laboratory using a new piece of equipment acquired after the onsite testing of the SSICXv1 - an Agilent 16903A Logic Analyser (LA).

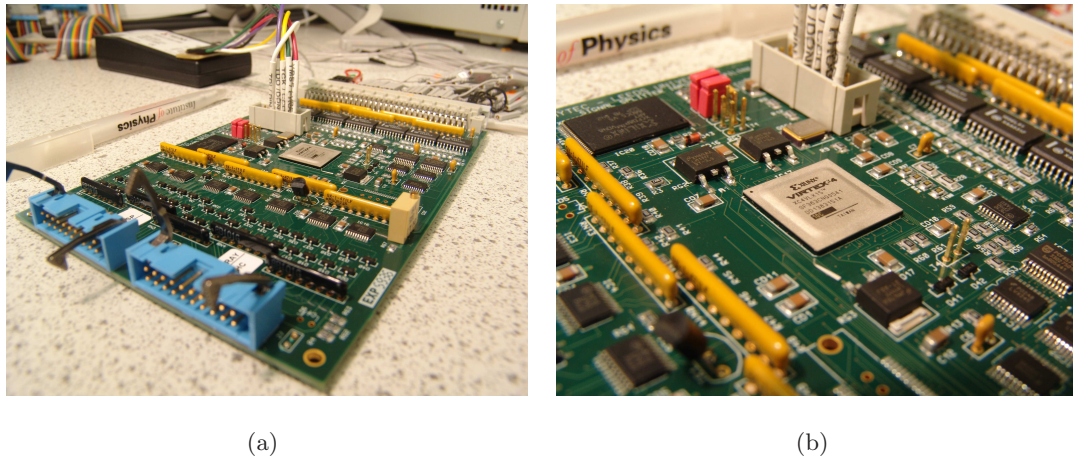


Figure 5.6: (a) The SSICXv2 with onboard Virtex-4 FPGA. (b) A close up of the Virtex-4 FPGA.

### 5.5.1 SSICXv2 Design and Implementation

The top layer of the PCB routing for the SSICXv2 is shown in Figure 5.5. As with the SSIC and the SSICXv1, the SSICXv2 accepts 20 differential NECL signal pairs in the form of two latched boxed headers with signals 1-10 on the upper header and signals 11-20 on the lower header. The NECL signals are converted to differential LVPECL by seven, three-channel, surface mounted MC10EP90 chips [138] which were also used in the DAT modules as will be described in Section 6.5.1. An eighth MC10EP90 chip is used to convert the two NECL external trigger pairs routed from the backplane. All 22 signal pair lines are then terminated with 100 Ohms as close to the FPGA as possible. The completed SSICXv2 is shown in Figure 5.6.

The 22 pairs of LVPECL signals are input to the Xilinx Virtex-4 XC4VLX15 SF363. The Virtex-4 provides 240 I/O pins and each pin forms one half of a differential I/O pair. There are also 20 signal enable lines (EN1-EN20) from two I<sup>2</sup>C (PCF8575) chips, and 4 external trigger enable lines input to FPGA I/O pins. It is desirable to eventually implement the I<sup>2</sup>C interface within the FPGA, removing the need for the 24 I/O line and the I<sup>2</sup>C chips. Consequently a copy of the I<sup>2</sup>C control signals, SCL and SDA are also input to the FPGA, and selectable with a simple jumper. Additional I/O pins are also used to drive LEDs. The 20 signals corresponding to the original NECL inputs from the front panel are output from the FPGA as LVPECL signals, which are converted back to NECL using seven, three-channel MC100EL91 chips. The NECL pairs are then output

to the backplane as in the normal SSIC. The result of the PST logic is also output from the FPGA in LVPECL form and made available in NECL form on both the backplane and on a simple pin header for debugging purposes.

The FPGA firmware is downloaded to a reprogrammable EEPROM using a JTAG connection inset on the board. A PROGRAM button loads the firmware from the EEPROM to the FPGA. On the SSICXv1 there was no reprogrammable EEPROM and consequently the FPGA had to be reprogrammed over the JTAG interface every time the power was cycled.

External examination of FPGA signals is done via a MICTOR header requiring 34 FPGA I/O pins and providing signals on a 38 way header output to an Agilent Logic Analyser equipped with Agilent B4655A FPGA Dynamic Probe Software.

A high-frequency, 50 MHz, onboard oscillator provides the Virtex-4 with a reference clock to accurately align the 20 input signals.

### 5.5.2 SSICXv2 FPGA Operations

In this subsection the methodology used to implement the feed-through and PST logic operations within the SSICXv2 FPGA are described.

The Virtex-4 contains *idelay* elements which may be used to delay the buffered input from an I/O pin by a fraction of a reference clock cycle. The 50 MHz clock is buffered onto a dedicated *low-skew* network within the FPGA and used to drive a digital clock manager (DCM)<sup>1</sup>. The DCM creates a 500 MHz clock based upon the 50 MHz input. This is in turn used to clock the *idelay* blocks allowing the input signals to be individually delayed with a resolution of  $\sim 78$  ps over a range of 2 ns. Note that when integrating the SSICXv2 into the current L2 system the input signals must all be delayed by around 6 ns. In this case the 50 MHz clock is used directly to drive the *idelay* blocks resulting in a resolution of 780 ps of an extended range of 10 ns.

In the tests done here the signals are delayed within the *idelay* blocks by a *fixed* phase-shift. The transit time of each signal through the SSICXv2 is measured and the required

---

<sup>1</sup>DCMs are used extensively in the development of the DAT modules and described in detail in Section 6.6.3

phase-shift computed and entered at compilation time to the *idelay* blocks. It is desirable that in the full FPGA based PST the signals become automatically aligned upon power-up to avoid measuring the transit time across each channel. This would also allow the system to cope with variations in transit time due to changes in cable lengths and replace damaged/malfunctioning boards without having to repeat measurements. The possibility of *variable*, or *dynamic* phase-shifting, is examined further in the context of the DAT modules in Section 6.9.

The PST logic used in the SSICXv1 and v2 is completely combinatorial. However, unlike the SSICXv1, the SSICXv2 simultaneously examines 2, 3 and 4 fold adjacency. The logical AND of every pair of input signals from adjacent pixels is examined and the logical OR of the 42 outputs are used to form the 2-fold adjacency trigger result. The output of each of the 2-fold AND gates is entered into a second set of AND gates with the neighbouring signals, the logical OR of the results then provides the 3-fold adjacency trigger. A further layer of AND gates and OR gates provides the 4-fold adjacency trigger. The design is entered into the Xilinx ISE software using VHDL, thereby avoiding the time consuming task of entering every gate individually in a schematic layout.

### 5.5.3 SSICXv2 Performance

As mentioned in the previous subsection the SSICXv2 is tested in the lab using the Agilent LA. The LA is used to inject 20 synchronous NECL inputs and a RACAL-DANA 1991 *nanosecond Universal Counter* monitors the resulting trigger rate.

In order to check that the PST recognises the correct patterns given a manageable input rate and a large overlap between the incoming signals, a simple C++ program is used to generate three ASCII files containing all possible 2, 3 and 4-fold coincidences. These are then loaded into the LA and used to generate 200 ns wide pulses which are input to the SSICXv2 at the rate of 2 Hz. As expected 42 2-folds, 111 3-folds and 308 4-folds were recorded. The process was repeated with ASCII files containing all possible 2, 3 and 4-fold patterns including those that should not generate triggers. The total number of all possible patterns is given simply by:

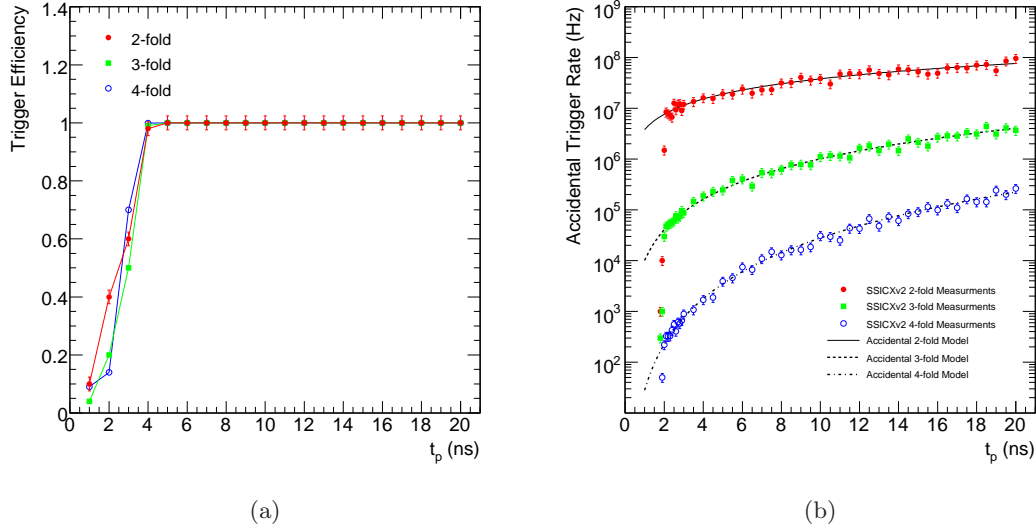


Figure 5.7: (a) The trigger efficiency of the SSICXv2 for all possible synchronous 2, 3 and 4-fold combinations as a function of the input pulse width. (b) The 2, 3 and 4-fold adjacency trigger rate of the SSICXv2 for random signals input independently on each channel at 1 MHz as a function of the input pulse width.

$$C = \frac{n!}{k!(n-k)!}, \quad (5.3)$$

where  $n$  is the number of pixels (19) and  $k$  is the multiplicity. For  $k = 2, 3, 4$  there are 171, 969 and 3876 possible combinations. The counter again indicated 42, 111, and 308 when inputting the 2, 3 and 4-fold patterns respectively and therefore the PST correctly identifies adjacent patterns and rejects all others.

To determine the coincidence resolving time of the SSICXv2 the trigger efficiency given synchronous inputs as a function of the input pulse width,  $t_p$ , is measured as shown in Figure 5.7(a). The synchronous inputs are again read from ASCII files containing all possible combinations,  $C$ . The trigger efficiency is defined as  $\epsilon = N(k)/T(k)$ , where  $N(k)$  is the number of recorded trigger events for a multiplicity  $k$  and  $T(k)$  is the total number of  $k$ -adjacent patterns. The trigger efficiency remains at 1 for all  $k$  until  $\sim 4$  ns when  $t_p$  drops below the coincidence resolving time,  $\tau_c$ , given by:

$$\tau_c = \Delta t + (t_r + t_f), \quad (5.4)$$

where  $\Delta t$  is the skew between the signals after alignment at the *idelay* block due to internal routing differences within the FPGA and  $t_r + t_f$  is the rise and fall time of the logic gates output signals.  $t_r + t_f$  indicates the minimum overlap required between the inputs of a logic gate within the FPGA to result in a NECL pulse at the SSICXv2 backplane and therefore includes the switching speed of the logic gate, the FPGA I/O pins and the converter chips.

$\Delta t$  may be separated from  $\tau_c$  by determining  $t_r + t_f$ . This may be done by measuring the accidental trigger rate due to random fluctuations in the NSB as a function of the CFD output width. Here this is achieved by inputting random pulses independently on each SSICXv2 channel at a rate of 1 MHz and measuring the resulting trigger rate as a function of pulse width,  $t_p$ , as shown in Figure 5.7(b). The calculated results from Eq. 5.1 for 2, 3 and 4-fold multiplicities are also included. Below  $\sim 2$  ns the trigger rate deviates from that expected, and below  $\sim 1.9$  ns disappears completely, and this is therefore  $t_r + t_f$ .

The frequency response of the SSICXv2 is shown in Figure 5.8(a), where all possible combinations,  $C$ , are again input via the LA and the trigger efficiency,  $\epsilon$ , is measured. The width of the input pulses is set to  $\tau_c = 4$  ns.  $\epsilon$  drops below 1 as the PST saturates at the maximum output frequency,  $f_{max}^{out}$ , and then rapidly drops towards zero. The maximum input frequency  $f_{max}^{in}$  depends on  $k$ , as shown by the vertical dashed lines added by eye in Figure 5.8(a), however,  $f_{max}^{out}$  is equivalent for all  $k$ , and determined by:

$$f_{max}^{out} = \frac{1}{\tau_c + t_{jitter}}, \quad (5.5)$$

where  $t_{jitter}$  is the peak-to-peak jitter in the trigger decision.  $t_{jitter}$  is measured to be  $\sim 2$  ns, and therefore for  $\tau_c = 4$  ns,  $f_{max}^{out} \approx 165$  MHz. Operating with CFD widths of 5 ns and 10 ns,  $f_{max}^{out}$  would be  $\sim 140$  MHz and  $\sim 80$  MHz respectively.

$f_{max}^{out}$  may also be determined by measuring the accidental trigger rate of the SSICXv2 as a function of the single pixel input rate, as shown in Figure 5.8(b), where the expected results from Eq. 5.1 have been included (obtained in a similar manner to Figure 5.7(b)). The output trigger rate behaves as predicted by Eq. 5.1 until  $f_{max}^{out} = 150$  MHz, where it saturates and drops rapidly as the trigger decision becomes latched *on*. Eq. 5.1 may then be used to obtain  $f_{max}^{in}$ , of  $\sim 3$  MHz,  $\sim 10$  MHz and  $\sim 17$  MHz for 2, 3 and 4-

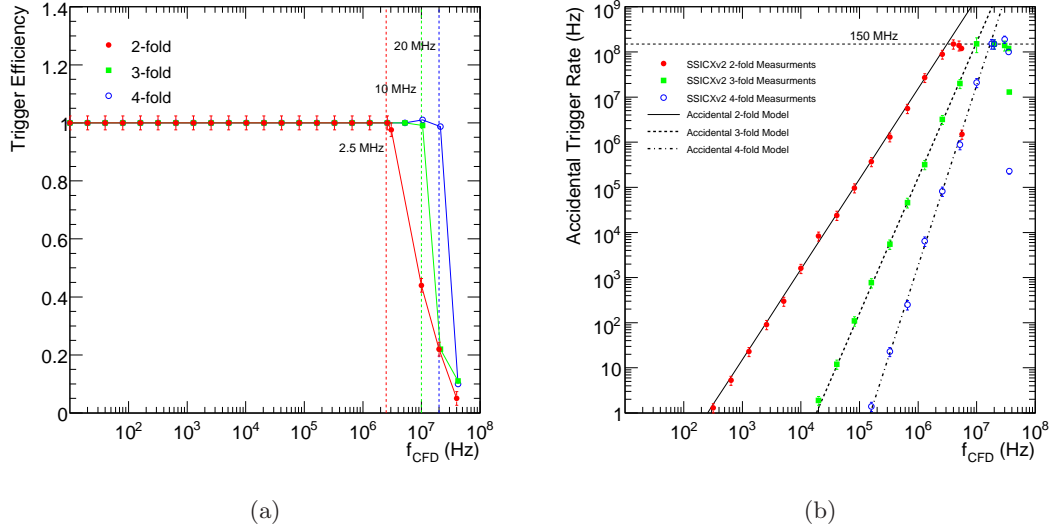


Figure 5.8: (a) The trigger efficiency of the SSICXv2 for all possible synchronous 2, 3 and 4-fold combinations as a function of the input pulse frequency. (b) The 2, 3 and 4-fold adjacency trigger rate of the SSICXv2 for random signals of width  $\tau_c$  input independently on each channel as a function of the input pulse frequency.

fold multiplicities respectively, which are consistent with the approximations made in Figure 5.8(a).

The maximum output frequency of the current PST is  $\sim 15$  MHz, determined by the PST decision time of  $\sim 65$  ns. From Eq. 5.1 an accidental coincidence rate of  $\sim 15$  MHz corresponds to a maximum single-pixel input rate,  $f_{max}^{in}$ , of  $\sim 2$  MHz for a 3-fold multiplicity. The ability to handle  $\times 5$  greater single pixel rate would allow the VERITAS CFD threshold to be reduced, and will be important in future IACTs where larger reflectors are desirable.

The average transit time of signals through the original SSIC was  $\sim 56$  ns, with a skew of 0.85 ns between channels. The average transit time of signals through the SSICXv1 was  $\sim 50$  ns, with a skew of 0.81 ns between channels. Although the skew experienced with the SSICXv1 was comparable to that obtained with the SSIC, the large difference in average transit time meant the SSICXv1 could not easily be integrated into the current L2 system. The skew between channels in the SSICXv2 is a mere 78 ps, due to the *idelay* blocks and 500 MHz clock. However the average transit time is  $\sim 48$  ns. To delay

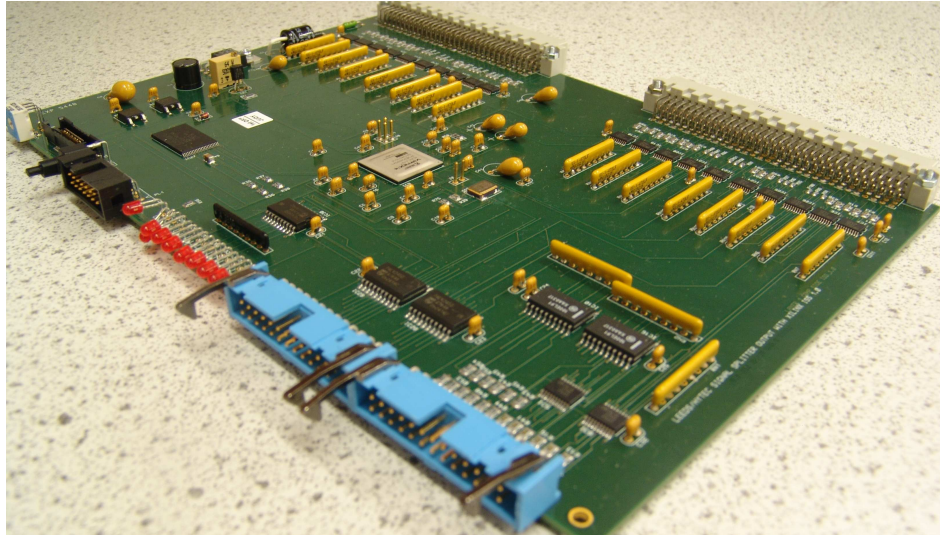


Figure 5.9: *The SSOCX prototype board. NECL signals are input on the backplane, converted to LVPECL and enter the Xilinx Virtex-4 FPGA at the center of the board. The resulting PST decision is output at the front of the SSOCX.*

the signals by the  $\sim 8$  ns required to integrate the SSICXv2 into the L2 trigger system, the 500 MHz clock is reduced to 50 MHz. The delay on each input may then be set over a range of 10 ns, but the resolution drops to 390 ps. The SSICXv2 is yet to be tested within VERITAS, but laboratory tests, that were not possible at the time of developing the SSICXv1, indicate that both the feed-through and PST logic will perform well.

## 5.6 The Signal Splitter Output Card with Virtex-4 (SSOCX)

Given the success of using the Virtex-4 FPGA in the SSIXv2, a version of the SSOC with an identical FPGA was designed and constructed. As shown in Figure 5.9, the SSOCX contains a single Virtex-4 FPGA with 59 differential PECL inputs originating from the 59 NECL signals on the back plane and converted using 20 MC100EL91 [139] chips.

The PST trigger logic consists of 5 copies of the 19 pixel logic used in the SSICXv2 with the input signals routed appropriately. Trigger decisions are output to the front panel. Unfortunately, due purely to the time constraints of this work, the SSOCX has not been fully evaluated. Initial tests show the PST logic used in the SSICXv2 also holds

for the SSOCX, however it is difficult to fully test the SSOCX as 59 NECL inputs are simultaneously required. The increase in routing differences within the FPGA in moving from a single patch of 19 to 5 patches of 19 will undoubtedly increase the coincidence resolving time, the exact amount will be best determined by onsite testing. It is also difficult to align the 59 signals using the *idelay* elements since the signals are no longer fed-through the FPGA. The interface to the MICTOR connector via the LA must be relied upon, and this will not be available onsite.

## 5.7 Conclusions

The advantages of using a  $k$ -fold adjacency PST within IACTs to reduce the effect of the NSB were established in Section 3.4. However, the current VERITAS L2 PST is not scalable to future IACTs, where higher-density cameras and arrays of greater numbers of telescopes are desirable. Accordingly development has begun on a high-speed topological trigger for the next generation of IACT arrays and UNDs. The design is based on the current VERITAS L2 system and aims to completely remove the PST CAMAC crate and reams of bulky ribbon cabling from the front of the SS Crate by replacing the SSIC and SSOC with alternatives containing Xilinx Virtex-4 FPGAs.

The SSICXv2 indicates that the FPGA based solution would reduce the coincidence resolving time to  $\sim 4$  ns from  $\sim 10$  ns at an increased single pixel rates from  $\sim 2$  MHz to 10 MHz. The improvements are due to the ability to delay input signals with a resolution of 78 ps and the lack of dead time associated with the combinatorial method chosen to implement the PST logic. The SSICXv2 also provides 2, 3, and 4-fold coincidences simultaneously, whereas the current system must be reprogrammed to change the trigger multiplicity.

Due simply to time constraints the high-speed FPGA trigger work in this thesis remains in the developmental stage and there are several key aspects that require future work. The SSOCX must be fully tested in-situ within VERITAS. The coincidence resolving time of the SSOCX should be measured to assess the effect of the additional routing on the skew between signals within the FPGA. If the SSOCX performs adequately the possibility of further trigger functionality should be explored and the power consump-

tion of the system assessed before a full prototype L2 trigger is constructed. When constructing the full FPGA based L2 system the output conversion on the SSICXv2 and input conversion on the SSOCX could be removed and either LVPECL or LVDS used through out the SS crate.

Several areas of further functionality are open to be explored. The simplest is a 5-fold multiplicity. Perhaps the most complicated is the transmission of the full camera trigger patterns from all telescopes to a central location where an additional FPGA trigger system assesses coincidences between the position of patches on adjacent telescopes.

There are also several alternative PST strategies that may improve the coincidence resolving time over that explored here. For example a synchronous, 2 ns step (500 MHz), design may reduce the susceptibility to the FPGA routing, or perhaps it is possible to perform the PST logic between all 59 pixels at once, rather than by dividing them into 5 overlapping patches. If the power consumption of the FPGAs in the tightly-packed SS crate becomes problematic the possibility of performing two or three patches of 59 within a single FPGA may not be unrealistic, although this would require an FPGA with a greater number of I/O pins.

The incredible flexibility offered by FPGAs means the system can, in principle, be expanded beyond a simple pattern trigger. For example the trigger may prove useful within VERITAS for the novel technique of detection of so called direct Cherenkov light from CRs [15; 79; 102; 103; 104].

Although a  $\sim 4$  ns resolving time is possible with the SSICXv2, the minimum useable coincidence resolving time of VERITAS is given by the rise time of the Cherenkov flash at the camera, which is  $\sim 5$  ns, dominated in VERITAS by the dispersion introduced by the Davis-Cotton reflector (see Section 2.3.5). A 50% reduction in the coincidence resolving time of the current T2, T3 and T4 L2 systems from 10 ns to 5 ns would reduce the accidental 3-fold L2 trigger rate due to the NSB by a factor of four, allowing the CFD threshold, and consequently, the energy threshold of the detector to be reduced. However, the coincidence resolving time of the VERITAS T1 L2 system is already  $\sim 6$  ns, and it may be possible to reduce those of T2, T3 and T4 by simply upgrading the comparator chips onboard the PST modules. It is therefore unlikely that VERITAS-4 will be retrofitted with this new system. However, VERITAS-4 is soon expected to expand

to VERITAS-7, requiring three more SS crates and PST CAMAC modules. In this case the move to an FPGA based PST would be feasible and timely. In the future high-speed FPGA based triggers will be essential to accommodate IACT cameras with  $\sim 2000$  pixels and arrays consisting of up to  $\sim 100$  telescopes, as is desired in CTA. Furthermore future IACTs are expected to be partly populated by larger (30 m) parabolic reflectors, which are not limited by the time-dispersion introduced by the Davis-Cotton design. In this case it may be desirable to lower the coincidence resolving time to  $\sim 2$  ns.

Kilometre scale UNDs will consist of  $\sim 10\,000$  detector elements. FPGAs offer the versatility to be reprogrammed remotely and are therefore suitable for a local, underwater, trigger. The high-speeds (up to 1 GHz) and high-density of I/O pins (up to  $\sim 800$ ) that are now available also lend FPGAs well to an off-shore trigger system.

## Chapter 6

# Parallel Distribution of Asynchronous Optical Signals

---

The experience gained in Chapter 4 with fibre optics and in Chapter 5 with FPGAs is combined in this chapter in the development of a dead-time free system for the parallel optical distribution of trigger signals, event numbers and housekeeping information within VERITAS. The Digital Asynchronous Transceiver (DAT) system consists of a transmitter (DAT-TX) and receiver (DAT-RX) implemented as VME modules relying on a parallel optical link (PAROLI) for the optical transmission of signals. The development of the DAT over several iterations of the modules is described and the timing performance of the modules is assessed including a detailed analysis of the jitter. Combinatorial logic functions are implemented in Xilinx Spartan-3 FPGAs, providing a versatile solution adaptable for use in future IACT arrays and UNDs. The DAT modules enable communication between the VERITAS telescopes and the central trigger system without limiting array performance, which is in turn the focus of Chapter 7. The system is also relevant to UNDs where it could be used, for example, to distribute reference signals along strings of OMs.

## 6.1 Introduction to the DAT

VERITAS uses a multi-level trigger system to reject fluctuations in background light whilst efficiently recording signals from  $\gamma$ -ray initiated air showers. Discriminated PMT signals are passed to a PST at each telescope [33] resulting in a CR trigger rate at high telescope pointing elevations of  $\sim 150$  Hz for a discriminator threshold of  $\sim 6$ -7 pe. These decisions are then passed to a central array trigger requiring a multiple telescope coincidence. The array trigger requires the distribution of multiple, fast, digital pulses between telescopes. A versatile solution is essential as not only fast, narrow, trigger signals but also variable width event numbers and long calibration flags must be transmitted.

The data from each camera pixel is digitised into 2 ns slices by custom built 500 MHz FADC boards [35]. Upon receiving an array trigger signal the FADC buffers are read out. The trigger signals require nanosecond accuracy to trigger the read out of the FADC modules from the correct point in the buffers. The FADC read out time has a direct effect on the telescope dead time and energy threshold, so it is important to minimise the read out window around the data pulse. A large amount of jitter in the trigger signal would require a large read out window, increasing the system dead time and the detector energy threshold. In VERITAS the FADC read out window is typically set to 24 samples, or 48 ns.

In this chapter a Digital Asynchronous Transceiver (DAT) developed by the author at the University of Leeds in collaboration with Hytec Electronics Ltd. primarily for signal distribution within VERITAS is discussed. The single width, 6U high VME modules denoted DAT-TX and DAT-RX are separated by up to 150 m and linked by fibre optic interconnects between telescopes. Fibre is lighter and less bulky than coaxial cable of the equivalent length and is not susceptible to electromagnetic interference or cross talk, as detailed in Section 4.1.

A prototype pair of DAT modules (DAT-V1) produced in 2004 is shown to perform poorly before a second improved prototype pair (DAT-V2), designed and built in October 2005, is shown to meet the required timing performance [180]. The modules were tested in depth before a further four pairs were produced, tested and installed on the first two VERITAS telescopes between January and May of 2006 [176]. A final batch of

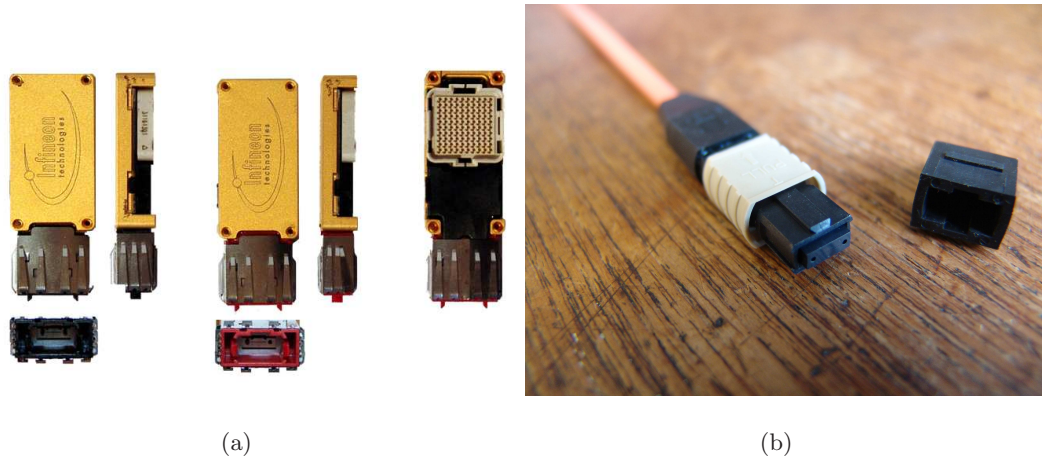


Figure 6.1: (a) A female MPO 12 channel fibre optic connector. (b) The PAROLI 2<sup>®</sup> transmitter (red neck) and receiver (black neck).

modules (DAT-V3) with minor design changes are described and were deployed across the remaining VERITAS telescopes in September 2006.

## 6.2 Specification

The DAT-TX must accept differential NECL inputs via both an IDC header and twin-axial Lemo connectors before presenting them in an identical form at the DAT-RX outputs. Ideally the solution should exceed the current trigger requirements, and be adaptable for future developments both within IACT arrays and UNDs.

To minimise the FADC read out window within VERITAS it is desirable to maintain the trigger timing to the level of one FADC sample. The array trigger signal distributed by the DAT modules is based upon telescope level triggers also transmitted over DAT modules and received centrally. The array trigger itself has an RMS jitter of  $\sim 1$  ns, so to keep the total RMS jitter of the array trigger signal below one FADC sample, each channel of a DAT module should have  $< 1$  ns RMS jitter. The array trigger system uses a PDM to compensate for the differences in timing introduced by the difference in arrival time of the shower front at the telescopes depending on the observation direction. This method requires the array system signals to traverse a path of predictable duration. Therefore a maximum channel-to-channel skew of 2 ns within the DAT modules

is desired.

For versatility, the DAT must transport asynchronous pulses of varying width at an undefined frequency such that the same system can be used to distribute housekeeping information<sup>1</sup>. The system should be dead time free to remove the possibility of missing incoming pulses whilst the data is being transmitted.

To maintain signal integrity and avoid any lightning induced power surges a 62.5/125  $\mu\text{m}$  core fibre optic interconnect is used to transport signals over the distance of at least 150 m between telescopes. A ruggedised, 62.5/125  $\mu\text{m}$  core 12 channel MPO pre-terminated cable as shown in Figure 6.1(a) is used to connect the modules in the lab. The conversion of electrical signals to optical signals is achieved using the Infineon 1.25 Gbit/s parallel optical link (PAROLI 2<sup>®</sup> [96] consisting of a small form factor, 12 channel, 850 nm VCSEL driven transmitter (PAROLI-TX) and PIN diode array based receiver (PAROLI-RX), as shown in Figure 6.1(b). Further details about the cabling scheme and PAROLI can be found in Appendix C.

The PAROLI-TX contains a channel alerter circuit that switches the respective data channel output off if the input duty cycle (DC%) permanently exceeds 57% (switching range 57% min. - 65% max.). The minimum alerter response time is 1  $\mu\text{s}$  with a constant high input. Thus the asynchronous variable width and variable rate input data signals *cannot* be sent to the PAROLI directly, they must first be modulated to the DC% requirement in a recoverable manner.

### 6.3 The Principle of Exclusive OR Encoding

To meet the DC% condition imposed by the PAROLI, data entering the DAT-TX is encoded using a 25 MHz clock via exclusive OR (XOR) gates as shown in Figure 6.2. An input pulse ( $A$ ) and the 25 MHz clock ( $B$ ) enter an XOR gate at the DAT-RX. The result ( $C$ ), produced according to the rules in Table 6.1, satisfies the operating conditions of the PAROLI-TX and is correctly transmitted to the PAROLI-RX. The clock is also transmitted over the PAROLI ( $B'$ ) and enters a second XOR gate with received encoded

---

<sup>1</sup>In the case of VERITAS the width is of the order of tens of nanoseconds to milliseconds at frequencies of the order of Hz up to a few MHz.

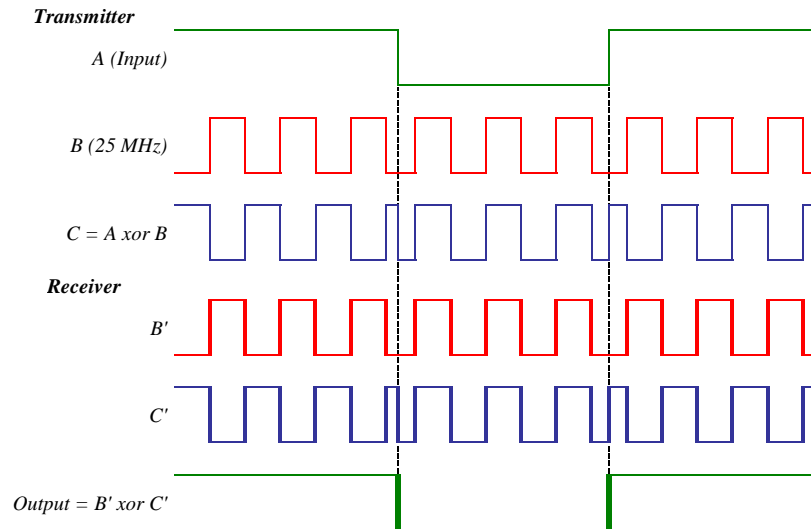


Figure 6.2: Using an XOR gate to encode data to satisfy the operating conditions of the PAROLI at the DAT-TX before recovering the original signal at the DAT-RX.

Table 6.1: The functionality of an XOR gate. Inputs  $A$  and  $B$  produce the output  $C$ .

A	B	C
0	0	0
0	1	1
1	0	1
1	1	0

data ( $C'$ ) at the DAT-RX. The result is a recovered version of the input data at the receiver. Correct data recovery requires the encoded data to be aligned accurately with the clock at the receiver to the sub-nanosecond level. Additionally the signals leaving the PAROLI-RX must have similar DC%, rise time, and fall time as those entering PAROLI-TX. In DAT-V1 the XOR encoding takes place via dedicated discrete logic chips, whereas in the later iterations the encoding is embedded in FPGAs.

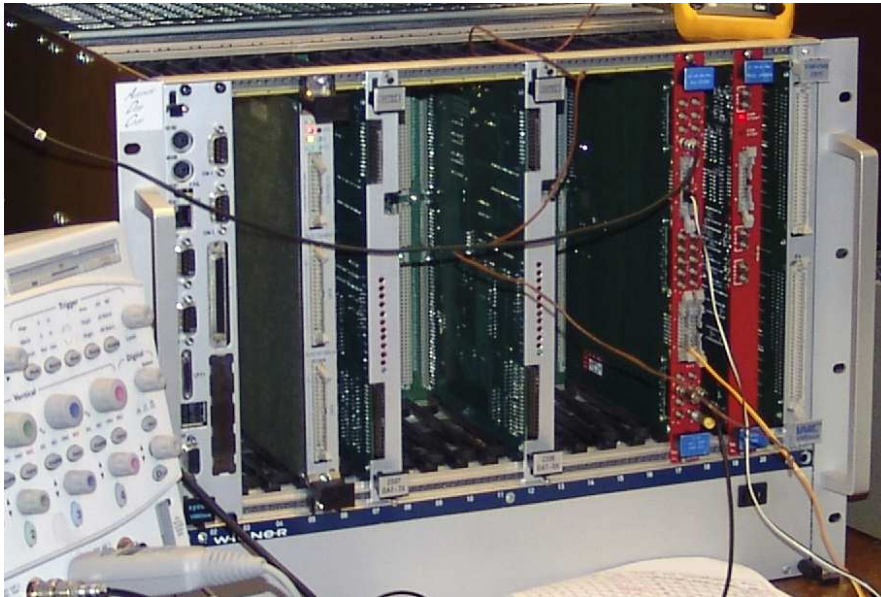


Figure 6.3: *The DAT -V1 VME modules (centre) seated in a CERN V430 VME crate.*

## 6.4 The Beginning Stages of the DAT

Here the first attempt at the DAT, the DAT-V1, is briefly described and the timing performance assessed. The DAT-V1 consists of two 6U high, single width VME modules, as shown in Figure 6.3. Signals are input in differential NECL form at the DAT-TX, XOR encoded with an onboard 25 MHz clock using discrete logic chips and transmitted to the DAT-RX along with a copy of the clock over the PAROLI. The DAT-RX then repeats the XOR procedure to recover the data which are output, again in differential NECL form. A wire interconnect to the DAT-RX is provided in addition to the optical link and the onboard clock may be disabled and an external clock selected over VME interface, implemented in a Xilinx Spartan-XL FPGA[184].

### 6.4.1 Design and Implementation

The DAT-TX accepts 11 differential NECL input signals from a 34-way header on the front panel with the positive half of the channel 0 input signal on the bottom right pin. An external clock NECL input and 4 spare NECL inputs are also provided. All 16 signals are then converted to TTL. The 4 spare TTL signals are input directly to

the FPGA, and the external clock signal may be selected over VME as an alternative to the onboard oscillator. The 11 TTL data signals pass through a piece of logic which attempts to alter their DC% to nearly 50% using the clock and XOR gates. These signals and the clock are then converted to LVDS and sent to the PAROLI-TX and a 26-way header where pins 1 to 22 carry the 11 encoded data outputs and pins 23 and 24 carry the clock. When powered on the DAT-TX will operate in a default state requiring no intervention from the VME interface to transmit incoming data over the differential LVDS 26-way header when connected to the DAT-RX via a simple 26-way twisted pair ribbon cable. To use the fibre optic link the cable is removed and the PAROLI-TX is attached via a custom daughter board (DB) mounted on a dual in line (DIL) socket. The PAROLI-RX is connected to the DAT-RX in a similar fashion and connected to the PAROLI-TX with a 12 channel MPO ribbon cable. The PAROLI-TX is then enabled over the VME interface.

At the DAT-RX the 11 encoded data signals and clock signal are input from the PAROLI-RX or the LVDS 26-way header and converted to TTL. The TTL encoded data signals each go to a piece of logic, which attempts to recover their timing using XOR gates and the TTL clock signal. The recovered data signals are converted to NECL and output to the front panel on a 34-way header, with the positive half of the channel 0 input signal on the bottom right pin.

Both modules are equipped with a set of VME registers in A16 (short addressing). The register set comprises an ID register, showing FF7F, indicating manufacturer and type, offset from the base address by +00h; a Model Code register, showing 2337 decimal (TX), 2338 decimal (RX), offset by +02h; and a Control and Status Register (CSR) through which the unit is controlled and its status observed, offset by +04h. For a complete explanation see the Hytec Technical Manuals [124; 125]. An onboard jumper selects the address mode of each module. When the jumper is in place the VME base address of a module is set with four additional jumpers. If the unit is used in a CERN specification V430 crate with JUAX (the centre 30-way DIN connector) with geographical addressing, removing the address mode jumper allows the module's base address to be set automatically in A16 space.

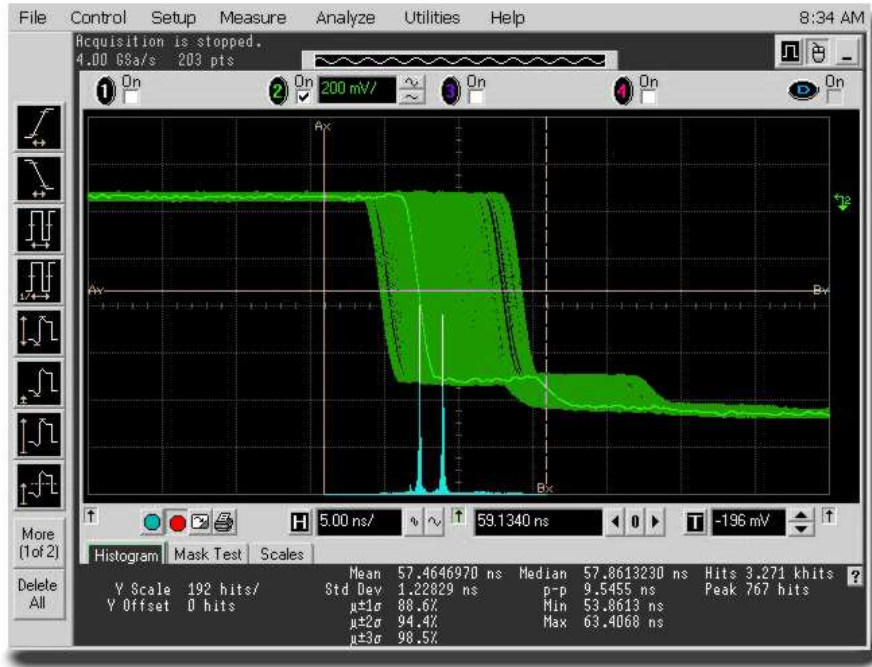


Figure 6.4: Distribution of arrival times for a 1 MHz, 200 ns wide pulse at the DAT-RX channel 3 output relative to the input.

### 6.4.2 Performance and Limitations

Using the test setup described in Appendix D, the variation in the arrival time of the falling edge of pulses at the DAT-RX output relative to that at the DAT-TX input is measured to give an indication of the jitter for that channel. Figure 6.4 shows the jitter distribution for a 1 MHz, 200 ns wide signal input on channel 3 using a 2 m long fibre optic link.

The distribution of  $n$  arrival times on channel  $i$  has an RMS of  $rms_{Tar_i}$  and a peak-to-peak (p-p) value of  $pp_{Tar_i}$ . The distribution in Figure 6.4 has a  $pp_{Tar_3} = 9.5$  ns and  $rms_{Tar_3} = 1.2$  ns for  $n = 3$  kHits. Table 6.2 shows the arrival times and jitter values for each of the 11 channels. A mean RMS of  $\overline{rms}_{Tar} = 1.09 \pm 0.04$  ns and a mean p-p value of  $\overline{pp}_{Tar} = 9.10 \pm 0.25$  ns are noted. The skew, given by the range in average arrival times between all 11 channels is  $2.16 \pm 1.52$  ns. The worst case skew is 11.82 ns. This is given by the difference between the maximum arrival time  $T_{ar_i}^{max}$  on the channel with the maximum average arrival time and the minimum arrival time,  $T_{ar_i}^{min}$  on the channel with the minimum average arrival time.

The performance of DAT-V1 fails to meet the required specification of  $\leq 1$  ns RMS jitter, 2 ns p-p jitter, and 2 ns skew. The jitter distributions are not Gaussian and, as it will be seen in Section 6.7.1, the nature of the distribution is important in diagnosing the performance.

The measurements presented are taken using a 2 m ribbon-fibre link. The large jitter and skew is also present when using the wire LVDS interconnect. Disabling the clock over VME removes all trace of jitter from the output pulses using both the LVDS wire interconnect and PAROLI link. The jitter in this case is under 100 ps RMS and 300 ps peak-to-peak. The skew at the output remains at 2.16 ns, but the uncertainty drops to 400 ps. Only short fast pulses can be used in this scenario otherwise the PAROLI becomes disabled. Using an external clock does not remove the large jitter. However, if the external clock and input data are run at the same frequency and phase shifted to ensure that their edges never coincide, the jitter is significantly reduced to the level produced with the clock disabled. Thus, the jitter is caused when edges of the clock and data approach each other at the exclusive OR gates in the transmitter and receiver. When the 25 MHz oscillator is replaced with a 5 MHz oscillator the frequency of jitter reduces accordingly by a factor of 5. The range remains unchanged.

Jitter occurring when a data edge approaches a clock edge during encoding or recovery does so on a range related to the rise and fall times of signals and the switching response time of the XOR gates. The effect is large due to the relatively slow switching of the single-ended TTL standard.

The following conclusions are drawn:

- The PAROLI provides the timing performance required for the VERITAS trigger chain but requires data to be encoded before transmission.
- Discrete logic implemented XOR gates successfully encode and decode the data but a large amount of jitter is introduced into an input pulse by the DAT-V1 and the skew between output channels becomes large when taking into account the uncertainty in the arrival time of each channel due to the jitter.
- The jitter is reduced significantly if the clock and data edges never approach each

Table 6.2: Channel by channel performance of the DAT-V1 over a 2 m fibre optic link.

Channel $i$	Mean Ar. Time $T_{ar_i}$ (ns)	RMS $rms_{T_{ar_i}}$ (ns)	p-p $pp_{T_{ar_i}}$ (ns)	Entries $n$ (kHits)	Min. $T_{ar_i}^{min}$ (ns)	Max. $T_{ar_i}^{max}$ (ns)
0	56.390	1.039	7.909	61	52.588	60.497
1	57.182	1.187	9.727	9.5	53.497	63.225
2	57.664	1.181	9.636	6.0	53.952	63.588
3	57.465	1.228	9.546	3.3	53.861	63.407
4	58.350	0.968	9.727	6.2	54.316	64.043
5	58.314	1.275	9.727	11	54.497	64.225
6	58.546	1.104	10.00	6.2	54.407	64.407
7	58.252	1.140	9.091	2.5	54.225	63.316
8	57.599	0.745	7.818	6.3	53.497	61.317
9	57.611	1.104	8.091	7.1	53.861	61.952
10	57.839	1.063	8.818	5.1	54.043	62.861

other. However, due to the asynchronous nature of the data input to the DAT, the clock and data edges will coincide.

- The jitter occurring when the clock and data edges coincide is dominated by the response of the XOR chips to changing inputs and the relatively slow rise and fall times associated with the TTL signal standard.

## 6.5 Developing the DAT

In this section the development of the DAT through two further iterations (DAT-V2 and DAT-V3) is described. Whilst the DAT-V2 represents a major leap from the original design, the DAT-V3 incorporates only small changes to the design of the DAT-V2. Both iterations again consist of two, 6U high, single width VME modules denoted DAT-TX and DAT-RX. Geographical addressing is used to assign the modules with slot-dependent

addresses automatically upon placement within a VME crate. Control and monitoring takes place via a VME interface embedded into an onboard Xilinx Spartan-3 XC3S50 FPGA [195]. Further information on the Xilinx Spartan-3 XC3S50 can be found in Appendix C.2.1.

In an attempt to circumvent the inherent jitter characteristics associated with the discrete XOR chips on the DAT-V1 all combinatorial logic operations are performed within the onboard FPGA. This approach accommodates rapid design change to optimise the boards for additional applications and the possibility of a PAROLI without rigorous input signal demands. Implementing such a design serves as a test of FPGA combinatorial performance at the sub-nanosecond level and, as the gate array is a pre-requisite to the implementation of the VME interface, this also offers an economically favourable solution. Details of the FPGA design can be found in Section 6.6.

Twin-axial differential Lemo connectors are added as an alternative to the 26-way IDC header. The wire-interconnect IDC header is removed from the front panel and set back onto the main PCB and the number and functions of the LEDs is changed. A debug header is included on the boards as an important diagnostic tool for the FPGAs.

In total five pairs of DAT-V2 modules were produced. The first pair remains in Leeds whilst the other four are installed on VERITAS telescope 1 and 2 as described in Section 6.8. Eight pairs of DAT-V3 modules were produced and four were installed within VERITAS telescopes 3 and 4 (T3 and T4) whilst the remaining four offer an onsite redundancy of 50% in case of accidental damage or technical faults.

### 6.5.1 The Second Iteration of the DAT

The prototype pair of DAT-V2 modules are shown in Figure 6.5 whilst Figure 6.6 indicates the data flow through the modules. Differential NECL data enters the front of the DAT-TX via either a 26-way IDC header or eleven twin-axial Lemo connectors, selectable over a VME interface. Surface mounted three-channel MC10EP90 [138] chips convert the NECL signals into LVPECL suitable for input to the FPGA [67; 183]. Retaining a differential signal standard improves signal integrity, but requires twice as many FPGA input pins. The 25 MHz clock is provided by an onboard TTL oscillator.

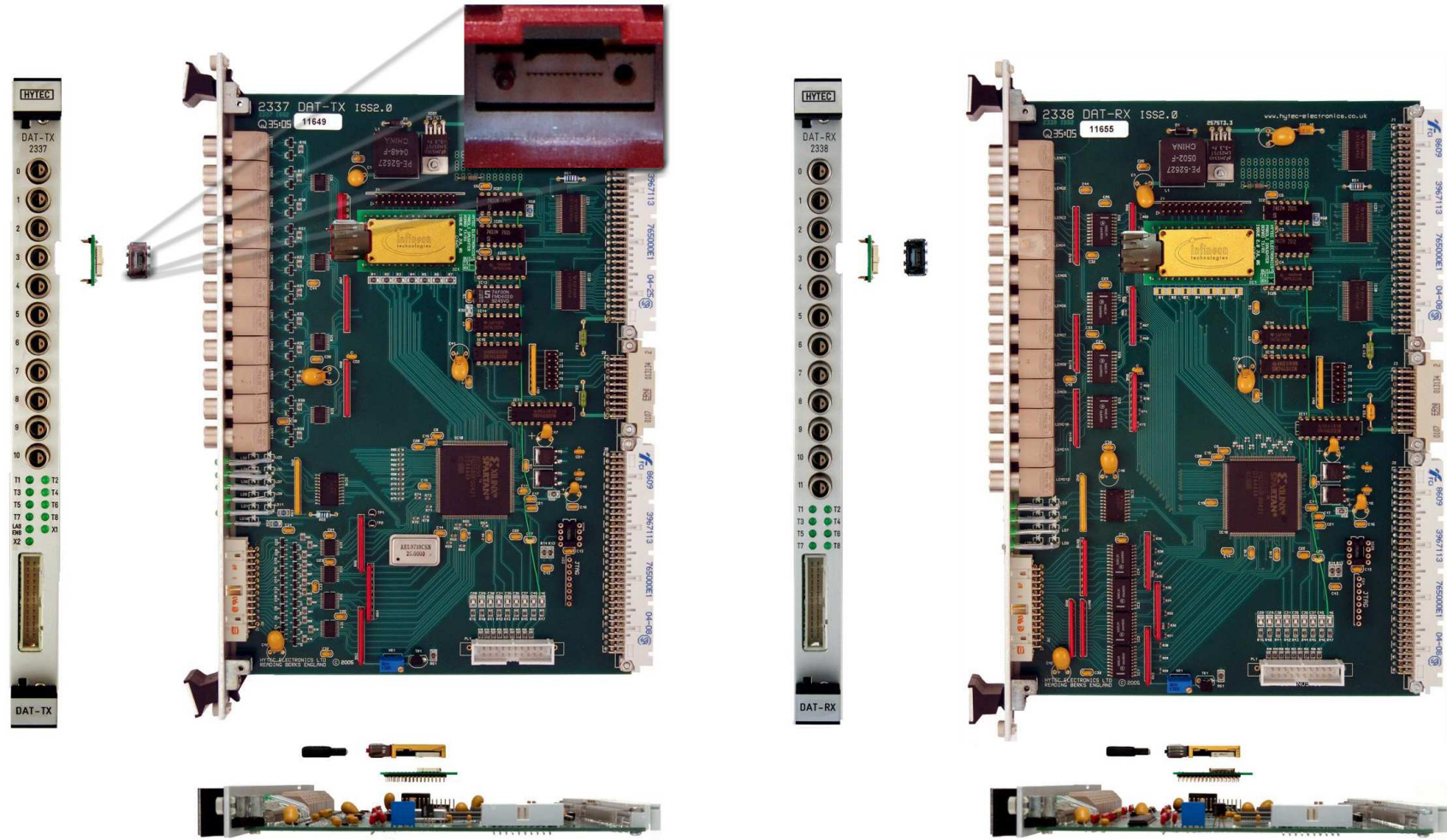


Figure 6.5: The first DAT-V2 pair, transmitter on the left, receiver on the right. The twin-axial Lemo connector inputs and outputs can be seen on the TX and RX front panels respectively. The TX main PCB board houses an onboard 25 MHz oscillator (left, lower central silver box). The bottom figures show how the PAROLI attaches via a DB and DIL socket. A close up of the Infineon PAROLI 2<sup>®</sup> [96] is inset showing the individual laser channels.

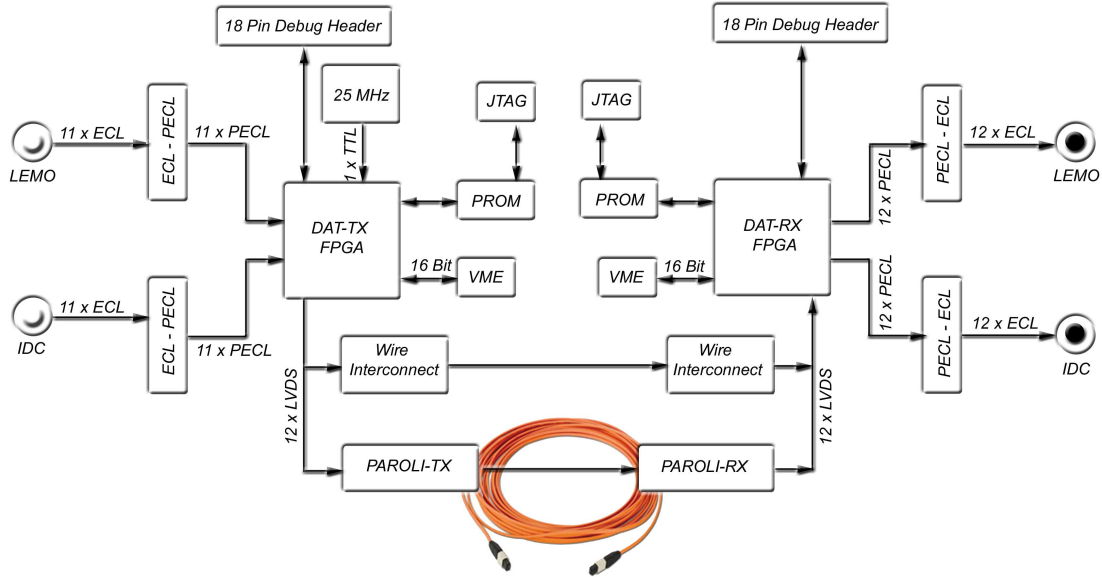


Figure 6.6: Functional diagram of the DAT modules depicting the data flow from transmitter to receiver including signal standards.

The XOR encoded data and clock are output from the FPGA in LVDS form [188] and input to the PAROLI-TX, which, as in the DAT-V1 modules, attaches to a DB. This configuration allows the PAROLI to be replaced with a future device by simply redesigning the DB for around £50. A male MPO terminated 12 channel fibre optic cable is plugged directly into the PAROLI-TX and connected to the PAROLI-RX on the DAT-RX. The PAROLI-RX converts the incoming optical signals back to LVDS. As in DAT-V1 there is also a 26-way wire interconnect option available to communicate between DAT modules intended for system debugging. This option must be activated over the VME interface. The LVDS signals are sent to the DAT-RX Xilinx Spartan 3 FPGA where recovery of the data takes place.

The recovered data lines are output from the FPGA as LVPECL and converted with three channel MC100EL91 [139] chips to NECL. The eleven data signals and clock signal are presented on the front panel to both twin-axial Lemo connectors and a 26-way IDC header.

A debug port to the lower rear of both boards allows nine single-ended I/O lines to be brought into or out of the FPGA for diagnostic purposes. The choice of input and

output on these pins and exact signal standard are limited by the FPGA banking rules. The Spartan-3 consists of eight banks of pins as described in Appendix C.2.1. Whilst it is possible to mix input signal standards of varying common-mode voltage to a bank, it is not possible to mix output standards of varying common-mode voltage [67]. Due to the pinning budget imposed by the use of differential data lines the connections of the debug port to the FPGA serve a dual purpose. They are also used to drive eight front panel LEDs, selected during normal operation over the VME interface by enabling a latch external to the FPGA. The transmitter also contains three further LEDs driven by dedicated FPGA pins. Two are utilised by the VME interface and the third indicates that the PAROLI-TX is connected to the board.

Upon power-up the FPGA on each module is programmed from a socket mounted Atmel AT17LV512 EEPROM [20] via jumper selection. In the absence of a PROM programming may take place via a JTAG header [168]. This setup provides the most versatile programming architecture, allowing the user to reprogram the FPGA at will during development over the JTAG connection [190].

Assuming the VME crate in which a given DAT module is placed generates slot-based, or geographical, addresses, the module is automatically assigned a base address given by Equation 6.1. If no geographical addressing is present, the module's base address may be set by the three jumpers directly below the PROM/JTAG selection jumper located on the center-right of the boards as shown in Figure 6.5.

$$\text{Hex}(\text{BaseAd}) = \text{Hex}(\text{Dec}(\text{SlotNumber})) \times \text{Hex}(800) \quad (6.1)$$

### 6.5.2 The Third Iteration of the DAT

The PAROLI on DAT-V2 is attached to the PCB via a DB and was held in place via the pluggable BGA mounted connector. The DB was mounted on a low profile DIL socket such that the total width of the module did not exceed a single VME slot. As a result the PAROLI sat very close to the main PCB directly behind the front panel Lemo connectors. A notch in the front panel approximately 1 cm wide and 0.25 cm deep allowed the fibre optic cable to be attached even if another VME module was present in the adjacent slot. The geometry however, caused the cable to incur a small bend

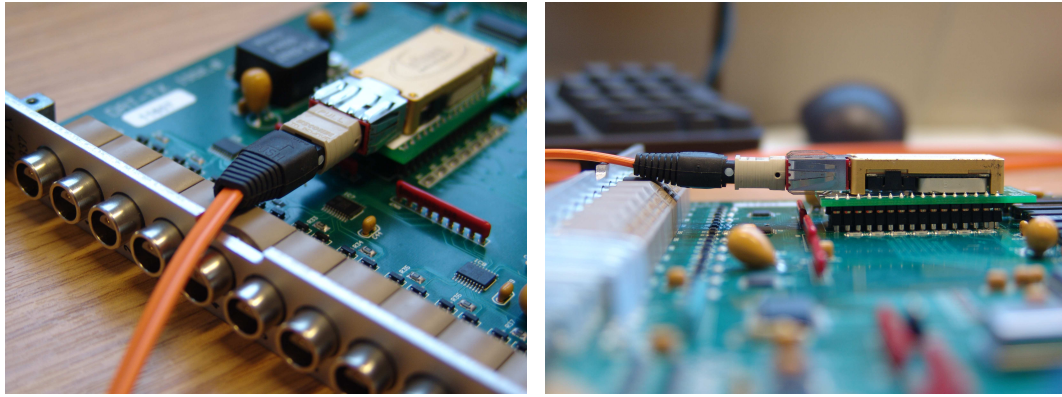


Figure 6.7: *The DAT-V2 boards with MPO terminated cable connected causing the PAROLI to become unseated from the DB. The large black rubber bend-protection on the fibre seen here was removed by Sachsenkabel in a batch of custom made cables.*

radius as illustrated in Figure 6.7. In turn the PAROLI was forced slightly from the DB causing channels 5 and 6 (counting from 0) to become unreliable on long time scales.

Custom cables from Sachsenkabel without the large black plastic bend protection are used onsite with the DAT-V2 modules to mitigate the problem. The DAT-V3 design includes alterations to secure the PAROLI to the DB with 4 small screws. The DIL socket is moved towards the back of the PCB and the Lemo connectors are spaced to allow a deep narrow notch to be cut into the front panel directly in front of the PAROLI as shown in Figure 6.8. Additional DBs with screws for the PAROLIs were retrofitted to the DAT-V2 boards.

During the initial DAT-V2 development stage a 300 mV oscillation on the 3.3 V supply line was noticed. In addition the 3.3 V line was incurring a larger load than expected [178] and was reduced to around 2.8 V when the PAROLI was activated and the FPGA was clocking fast signals. The 3.3 V supply originates from the 12 V VME backplane reduced via a chopper circuit. A replacement regulator with a higher current tolerance was fitted to the chopper circuit and the inductor and capacitor at the regulator's output stage were replaced appropriately. The resulting voltage was 3.3 V with an acceptable<sup>2</sup> oscillation of 100 mV. The alterations to the chopper circuit were included in the DAT-V3 design.

<sup>2</sup>The FPGA can tolerate  $\pm 150$  mV according to [195].

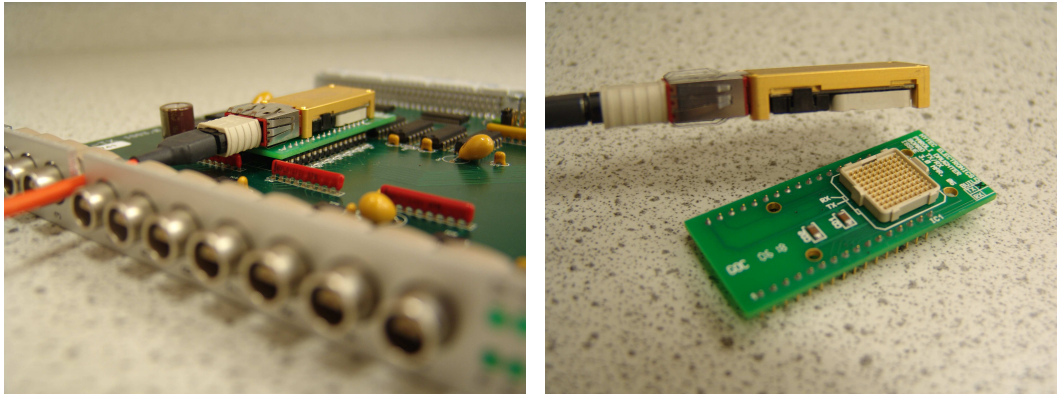


Figure 6.8: *The modified front panel and DB design for the DAT-V3 modules with rubber bend-protection on the fibre removed by Sachsenkabel.*

In DAT-V2 the 16 MHz VME system clock is input via a make-shift wire connection to the debug header for use within the FPGA. In DAT-V3 the VME system clock is routed across the PCB from the backplane to a dedicated FPGA pin.

## 6.6 FPGA Design

The FPGA design for the DAT-V2 is a combination of VHDL programs and schematic layouts implemented with the Xilinx ISE software tools [187]. The top-level of a design consists of a schematic representation, Figure 6.9 shows an example from DAT-RX. VHDL code is written and converted to a *'black-box'* which can be inserted into the top-level schematic. The design is mapped onto the specific FPGA model using the desired pinning specified in a constraints file. The mapped design is routed through the FPGA taking into account user specified timing constraints before uploading to the PROM or JTAG header. In the proceeding section the FPGA design is broken down into several major elements, shown here in bold. The VME interface, a standard use for FPGAs, is dealt with briefly. Combinatorial operations are discussed in detail including the importance of data to clock alignment at the receiver. In turn, knowledge of the digital clock manager is required and the issue of a guaranteed receiver clock is addressed.

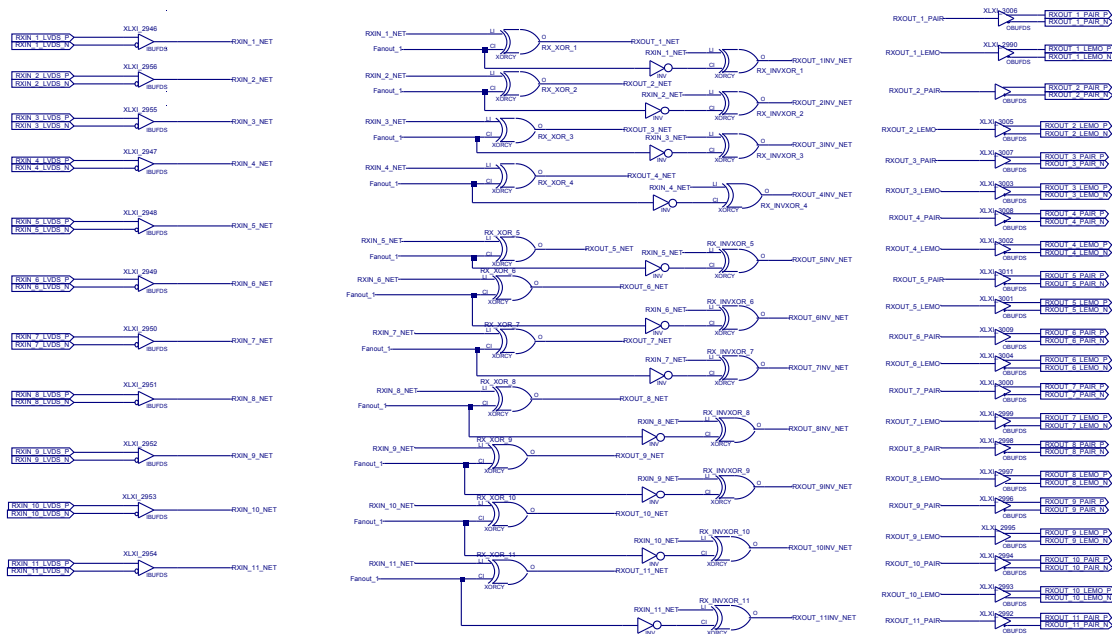


Figure 6.9: ISE schematic of the XOR decoding, see Section 6.6.2. Signals are buffered onto the FPGA (left), routed to XOR gates and combined with a fanned out clock (fanout1) and inverted clock from a DCM.). Signals are input to DDRFFs (not shown) and output from the FPGA (right).

### 6.6.1 VME Interface

As in DAT-V1 the embedded VME interface and register set provide 16 bit access to three registers. The first two registers, offset from the module base address by +00h and +02h, read the module model (0xFF7F) number and ID (2337 for TX, 2338 for RX). The third Control and Status Register (CSR) is offset from the base address by +04h and allows the user to enable or disable various features, such as input settings and laser functionality, and read back the status of the module, described more fully in Appendix G.2.

### 6.6.2 Combinatorial Operations

At the DAT-TX the 22 differential LVPECL signals from both the twin-axial and IDC inputs are buffered onto the FPGA. Each input is selected individually over the VME via multiplexers within the gate array. The 25 MHz clock is input via a dedicated clock-

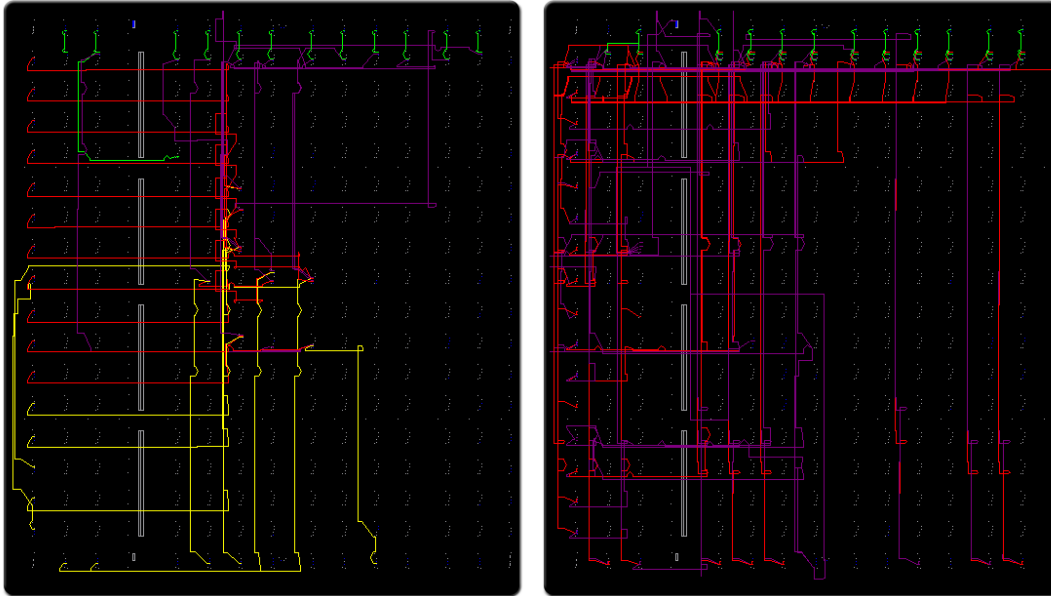


Figure 6.10: *FPGA data routing. Left(TX): Inputs from the Lemo connectors (Red) and IDC header (Yellow) routed to multiplexers and then XOR gates (Purple) before traversing identical path lengths to the LVDS outputs (Green). Right(RX): LVDS inputs (Green) routed to nearby XOR gates. The XOR gate outputs (Red and Purple) are routed via similar path lengths to DDRFFs.*

buffer to a low skew network on the FPGA and fanned out 12 times via a DCM to maintain DC%. Each of the fanned out clocks enters an XOR gate with a corresponding data line. The twelfth clock enters an XOR gate with ground to again maintain DC% and transit time. The eleven encoded data lines and clock encoded with ground are buffered to differential output pins on the FPGA. To minimise skew of the signal lines once encoded the XOR gates are placed very close to the FPGA output buffers, as shown in Figure 6.10(left).

The Mentor Graphics software Model Sim Xilinx Edition-III is used in conjunction with ISE to simulate signal delays due to routing through the FPGA design. Such simulations indicate that each of the 12 signals transit for 0.304 ns with zero skew between them, once encoded. Figure 6.11 shows the resulting LVDS FPGA output waveforms from a simulation of the DAT-TX in which all input data lines are tied to ground. The skew between output lines is 160 ps. Since the encoded lines are synchronous the skew is due entirely to the fanned out clock lines. Due to automatic routing, the clock skew was initially on the order of 1 ns. By individually assessing each clock path this was

reduced by a factor of five. Figure 6.12(left) shows the exact path each clock fan-out takes through the FPGA.

As will be presented in Section 6.7.3, the DC% of the DAT-TX output signals shift away from 50% depending on the channel and the input state of the data. This edge sensitivity is addressed by inverting the signals at four points in the schematic design forcing the rising and falling edges of the signals to take similar paths when routed through the FPGA.

At the DAT-RX the differential clock is buffered to the DCM. Figure 6.12(right) shows the clock routing through the DAT-RX FPGA. Feedback into the DCM facilitates a phase shift between the input and output with a resolution of 156 ps for a 25 MHz clock, described in detail in Section 6.6.3. The phase shifted clock is fanned out and entered, along with the 11 data lines, to XOR gates. To correctly recover the original input data the clock must be accurately aligned with the encoded data [159]. Furthermore the skew between encoded data lines must be such that for a single phase shift the clock is aligned with all 11 encoded data lines.

There are only two DCMs available in the Spartan-3 XC3S50 , negating the possibility of providing alignment on a channel to channel basis. Attempts were made to delay the encoded data lines individually using custom built, LUT based *tap* delays [135; 194], but did not provide the required resolution. Instead the receiver XOR gates are positioned very close to the input buffers to minimise the skew between encoded data channels, see Figure 6.10(right). Simulated transit time between input buffer and corresponding XOR gate is 0.174 ns for all channels.

Due to the DC% dependence on the state of the input data, it is not possible to phase shift the clock to a point where the input is accurately reproduced for both *high* and *low* input states. The technique applied in the DAT-TX FPGA of inverting the signal at various points along the data path to maintain a 50% DC% cannot be used for DAT-RX since the signals are decoded before they are output from the FPGA. Instead the clock is phase shifted to a position where the output accurately represents the input during a *low* state. During a *high* state the output shows sharp spikes down to the *low* state. Thus for an input to DAT-TX as shown in Figure 6.13 the result (A) is obtained. An inverted copy of the phase shifted clock is XOR combined with a second copy of the data

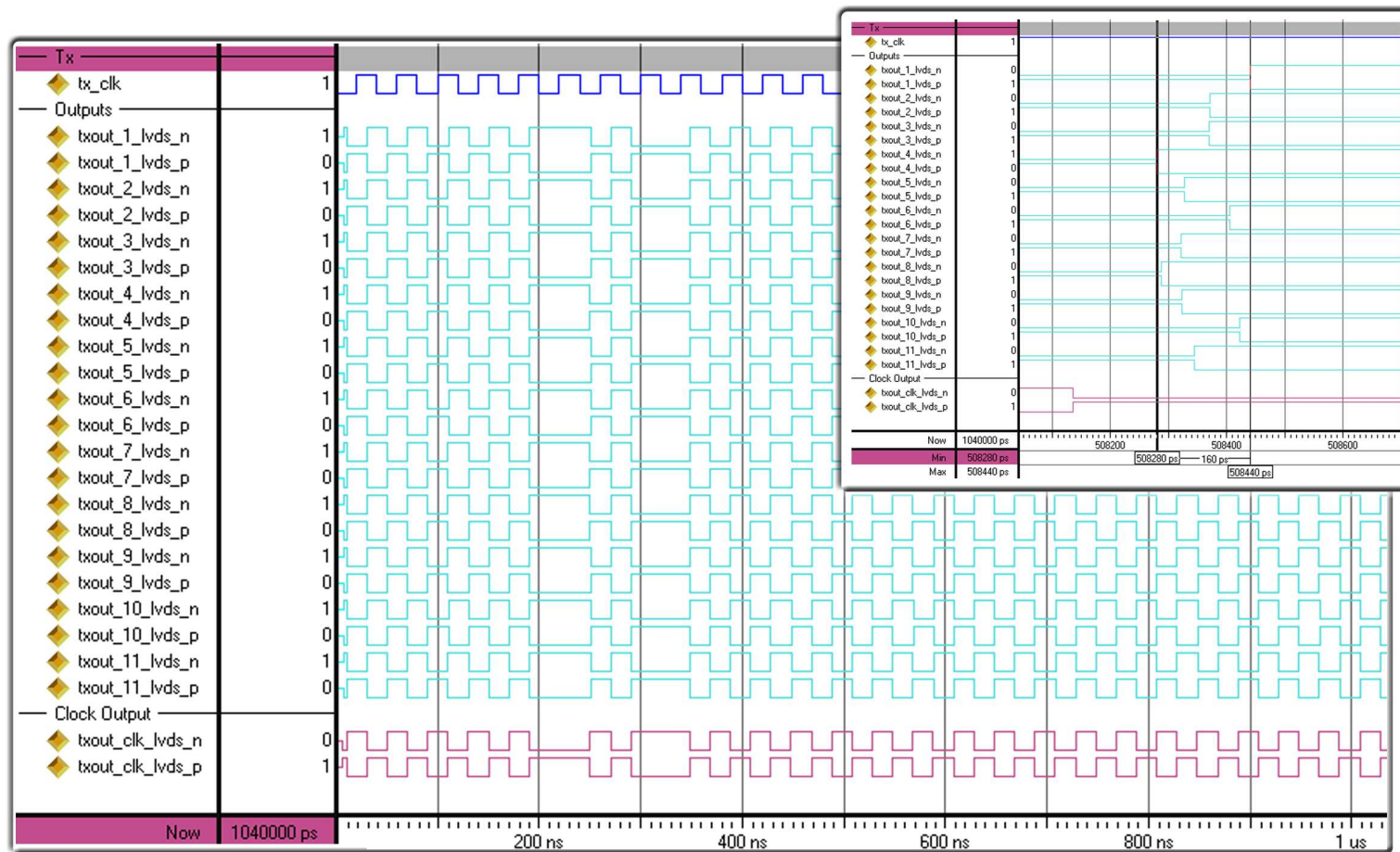


Figure 6.11: DAT-TX FPGA output waveforms from a simulation in which all input data lines are tied to GND. The upper-most waveform shows the clock used as stimulus. The irregularities in the outputs between 190 ns and 350 ns are due to the DMC locking onto the input clock too early. Inset is a close-up showing the skew on the outputs to be 160 ps due entirely to clock skew.

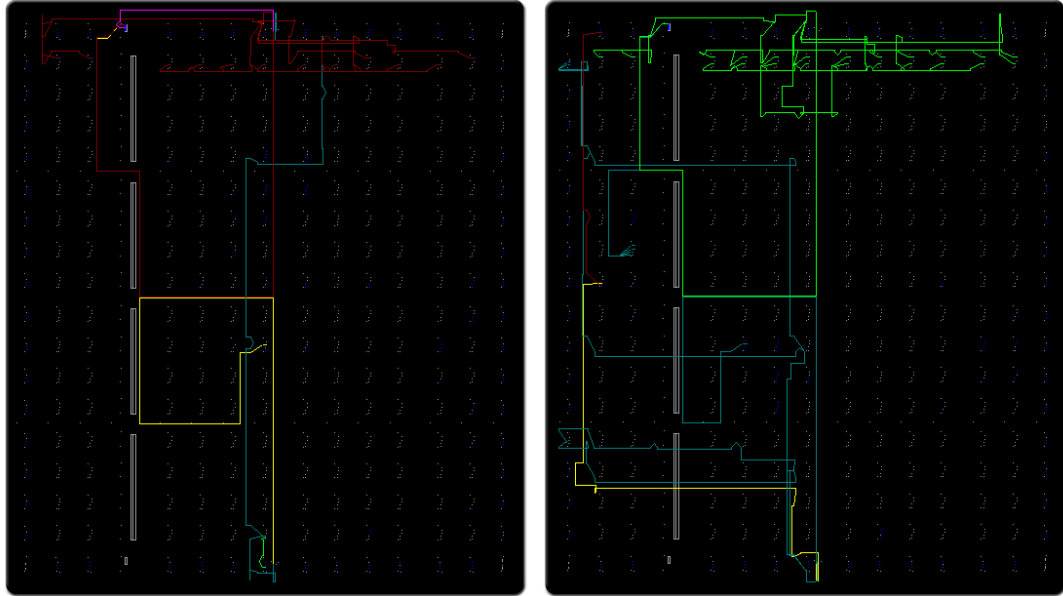


Figure 6.12: *FPGA clock routing. Left(TX): The clock is input (Green), inverted (Dark Cyan), routed to a DCM (Yellow) and then to a buffer (Magenta) before being fanned out (Dark Red). Right(RX): The clock is input (Dark Red), inverted (Yellow), routed to a DCM (Dark Cyan) and fanned out (Green).*

to produce the result (B). The results (A) and (B) are used to clock a dual data rate flip-flop (DDRFF) at the output stage to reproduce the data, (Q); where the behaviour of the flip-flop is given by the simple rules in Table 6.3 [191]. The routing of these signals is shown in Figure 6.10(right) in red, A, and purple, B. In Section 6.7.1 the effect of DC% distortion on the recovered state of the data is addressed.

Table 6.3: *Given inputs (A) and (B) the flip-flop, as configured for the DAT receiver, will produce output (Q). It is only sensitive to rising edges ( $\uparrow$ ). An irrelevant state is represented by 'X'.*

A	B	Q
$\uparrow$	X	1
$\downarrow$	X	Q
X	$\uparrow$	0
X	$\downarrow$	Q

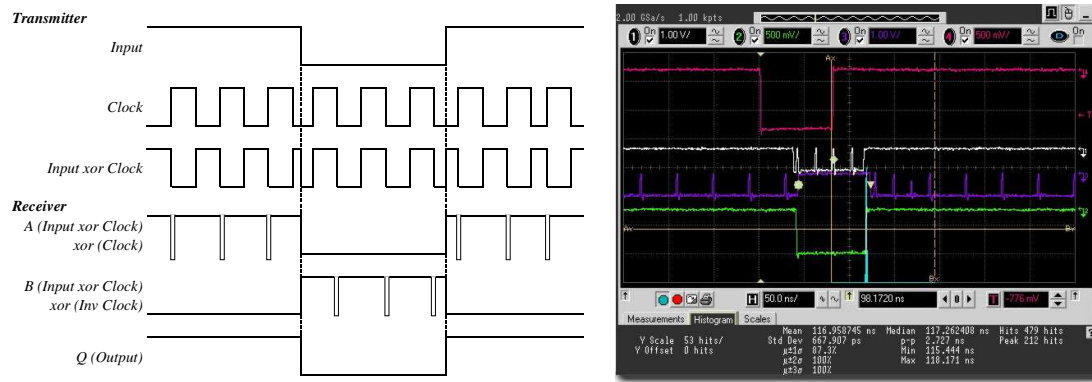


Figure 6.13: Response of the DDRFF. An input pulse (Right: top trace, magenta) encoded with the 25 MHz clock at the transmitter experiences glitches at the receiver during the data high state when decoded with the clock, (A) (Right: third trace, purple), and during the data low state when decoded with the inverted clock (B) (Right: second trace, white). The DDRFF takes (A) and (B) as input and results in (Q) (Right: fourth trace, green). (Note the DDRFF inputs are inverted in the image on the right due to the polarity of the oscilloscope probes).

### 6.6.3 The Digital Clock Manager

As shown in Figure 6.14 (and described in [185]) Digital Clock Managers (DCMs) can multiply or divide the incoming clock frequency, eliminate clock skew and optionally phase shift the clock outputs to delay the incoming clock by a fraction of the clock period.

In the DAT-TX a DCM is used to fanout the input clock signal twelve times with minimal skew. The DCM achieves this via a Delay-Locked Loop (DLL) that compensates for the delay on the routing network by monitoring an output clock, CLK0. The DLL unit effectively eliminates the delay from the external clock input to the individual clock loads (the XOR gates) within the device.

In the DAT-RX a DCM is again used to de-skew the clock fanout signals, however here the DLL is further exploited to provide a fixed phase shift between CLKIN and CLK0 as shown in Figure 6.15. The amount by which the clock is phase shifted is controlled by the PHASE\_SHIFT attribute specified at design time and set during the FPGA configuration process. The application cannot change the value during run time<sup>3</sup>. The

<sup>3</sup>In Section 6.9 the possibility of using a dynamic phase shift to alter the value at run time is

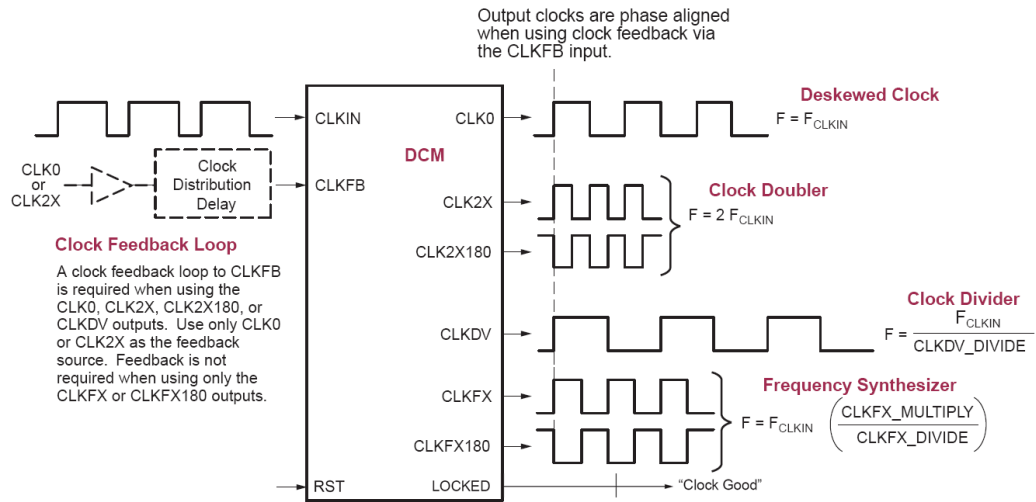


Figure 6.14: *Capabilities of the Spartan-3 DCM, adapted from [185]. The DCM CLKIN input produces the in phase CLK0 output of identical frequency via feedback to the CLKFB pin. Also available are double frequency (CLK2X), 180° phase shifted (CLK180, CLK2X180), lower frequency (CLKDV) and higher frequency (CLKFX) clocks.*

value of PHASE\_SHIFT is an integer between -255 and +255 and results in a phase shift of:

$$T_P = \frac{P}{256} \cdot T_{CLKIN}, \quad (6.2)$$

where  $P$  represents the value of PHASE\_SHIFT and  $T_{CLKIN}$  is the time period of the incoming clock. The 25 MHz oscillator used in the DAT modules results in a phase shift resolution of 156 ps.

The DCM's LOCKED output pin indicates when the enabled DCM functions have locked to the CLKIN input. In the DAT-TX this occurs when the edges of the input clock line up with the edges from the feedback clock and in the DAT-RX when the design specified phase shift has been reached. The status of the DCM LOCKED pin is reflected by a front panel LED on both the DAT-TX and DAT-RX. The LOCKED output is *low* immediately after the FPGA finishes its configuration process and is *low* whenever the DCM RST input pin is asserted *high*. After configuration, the DCM always attempts to lock, whether the CLKIN signal is valid or not. If the input clock is not yet stable, the

---

investigated.

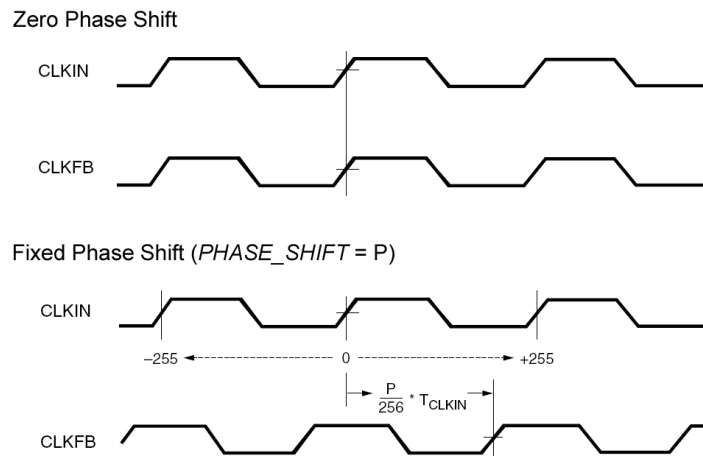


Figure 6.15: Illustration of the DCM fixed phase shift attribute. With no phase shift the rising edges of *CLKIN* and *CLKFB* are aligned. A fixed phase shift creates a delay between *CLKIN* and *CLKFB* directly related to the phase at the fanout point of the clock to the XOR gates in the *DAT*.

FPGA circuit should continuously pulse the *RST* input until the *CLKIN* input stabilises. This issue is addressed in Section 6.6.4. The DCM output clocks are not valid until the *LOCKED* pin becomes *high* and before that time can exhibit glitches, spikes, or other spurious behaviour. The DCM will take a maximum of 2.88 ms to assert *LOCKED high* after receiving a *RST* pulse in the presence of a valid 25 MHz input clock .

The DLL unit of the DCM requires an input clock frequency of between 24 MHz and  $\sim 167$  MHz with no more than  $\pm 0.87$  ns period jitter <sup>4</sup>. The resulting output will incur an additional period jitter of  $\pm 100$  ps .

#### 6.6.4 A Guaranteed Receiver Clock

For correct operation a DCM must receive a constant monotonic input clock. The onboard oscillator ensures this is always the case for the transmitter, but the receiver relies on the incoming 25 MHz clock from the transmitter to regulate the DCM. In this architecture, if the *DAT-RX* is configured at run time before *DAT-TX*, the DCM will experience a period during which no 25 MHz clock is present. Under such conditions the

<sup>4</sup>Period Jitter is the worst-case deviation from the average clock period of all clock cycles in a collection of over 100 000 clock periods sampled.

DCM behaviour will become unpredictable. In order to prevent this the receiver DCM clock input is continuously sampled with a VHDL implemented frequency monitor. If the frequency of the incoming clock is not between 20 MHz and 30 MHz, the DCM is sent a reset signal, RST. This process is clocked by the 16 MHz VME system clock present on the crate backplane originating from the controller CPU. The reset pulse is one clock cycle long meeting the DCM specified requirements of  $>2$  ns. The DCM continues to reset until a steady 25 MHz input is found, at which point the DCM locks, the LOCKED pin is asserted *high* (indicated by an LED on the front panel) and the output clock is correctly phase shifted. The DCM reset circuit is shown in Figure 6.16.

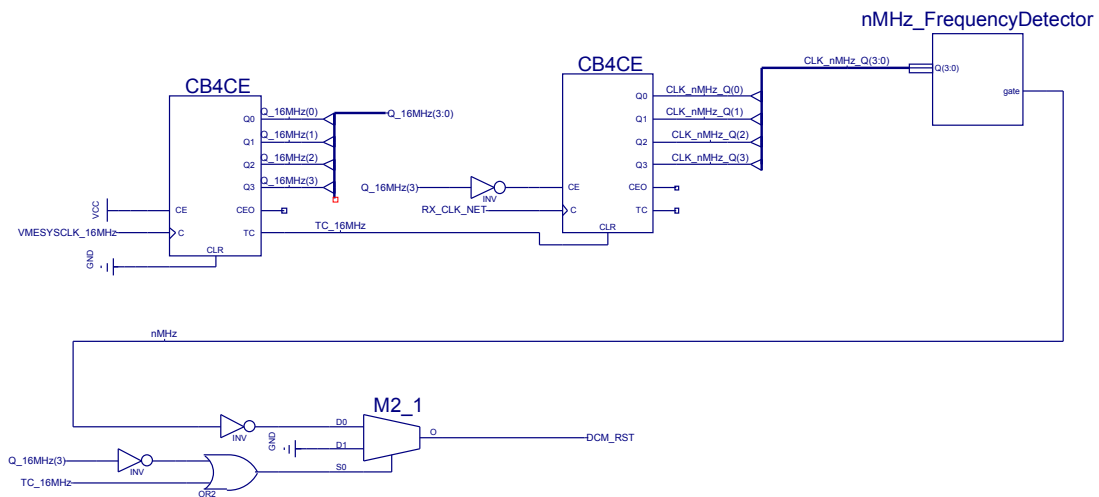


Figure 6.16: *The DCM reset circuit.*

## 6.7 Performance

In this section the timing attributes of the prototype DAT-V2 modules are presented in detail before the performance of the other DAT-V2 and DAT-V3 modules are summarised. The distortion introduced by the DAT modules into an input pulse is considered using the test setup described in Appendix D by examining: the jitter in arrival time of the falling edge of a pulse relative to that at the input; the variation in the pulse width at the output; the channel-to-channel jitter and both the long and short term stability. The components of the jitter are described and the total jitter is analysed

using the dual-Dirac model.

### 6.7.1 Components of Jitter

In Section 6.4.2 the jitter in the arrival time of an input pulse at the output was considered for the DAT-V1. It was quickly established that the timing performance did not meet the specification and no further measurements were required to qualify the device. In the case of DAT-V2 the timing is examined in more detail in an attempt to explain the origin of any jitter.

The term *jitter* simply refers to the uncertainty of a data edge in time. There are several methods of measuring the jitter. The chosen method here is to use the Agilent MSO to record the arrival time of the edge many times and add these values to a histogram. The jitter distribution consists of two principle components, random jitter,  $RJ$ , and deterministic jitter,  $DJ$ . In this work the dual-Dirac model, described in Section 6.7.2, is used to determine  $RJ$  and  $DJ$ .

Random jitter is uncorrelated<sup>5</sup> and unbounded, and thus, given long enough, will have an unlimited peak-to-peak value. For this reason  $RJ$  is measured in terms of an RMS value. The Probability Distribution Function (PDF) of random jitter is always Gaussian in distribution.  $RJ$  is often caused by thermal noise in decision circuits and oscillator phase noise [198].

Deterministic jitter is bounded and always measured in terms of a peak-to-peak value. Although the distribution of deterministic jitter can be very unpredictable the likely causes and characteristics of the individual sub-components of measured deterministic jitter are not, assuming they can be separated. The sub-components of deterministic jitter consist of DC% Distortion (DCD), Data Dependent Jitter (DDJ), and Periodic Jitter (PJ) as shown in Figure 6.17 [76]. In the case of the DAT a further deterministic component is introduced by the use of the DDRFF. The components of jitter and their relationship to the results obtained with the DAT modules are explained in Appendix E.

---

<sup>5</sup>Jitter correlation refers to the relationship of the jitter with the data or any of the system clocks. If the jitter is independent of all system clocks and data lines, it is uncorrelated [73].

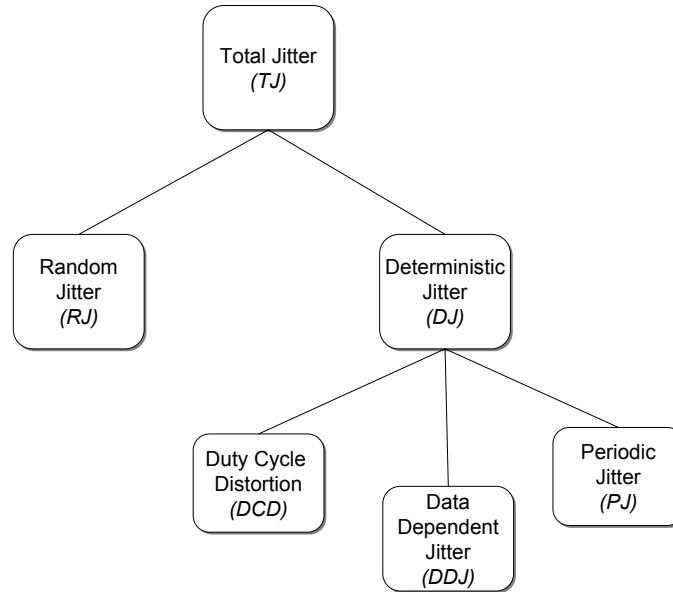


Figure 6.17: *The components of jitter. Total jitter consists of random and deterministic jitter. Deterministic jitter is made up of DC% distortion, data dependent jitter, and periodic jitter.*

## 6.7.2 The Dual Dirac Model

The jitter distributions obtained in the evaluation of the DAT timing performance are not Gaussian, instead they contain contributions from both  $RJ$  and  $DJ$ , as described in Section 6.7.1. Here a method of isolating  $RJ$  and  $DJ$  from the measured jitter and extrapolating to obtain a total jitter is described. The dual-Dirac model is a Gaussian approximation to the outer edges of the jitter distribution displaced by  $DJ(\delta\delta)$  [3]. Using such an approach deterministic and random jitter may be separated from the recorded distribution and used to predict a total jitter for the industry standard Bit Error Ratio (BER) of  $10^{-12}$  [126]<sup>6</sup>.

The measured jitter distribution can be described by:

$$J(x) = RJ(x) * DJ(x) \quad (6.3)$$

with

<sup>6</sup>It is not practical to measure the jitter distribution directly to such a high BER. For example, a BER of  $10^{-7}$  required 12hr 40min of acquisition at 4 GSa/s with a 1 MHz input, see Section 6.7.7.

$$RJ(x) = \frac{1}{\sqrt{2\pi}\sigma} \exp\left[-\frac{x^2}{2\sigma^2}\right]. \quad (6.4)$$

Then:

$$J(x) = \frac{1}{\sqrt{2\pi}\sigma} \int DJ(x') \exp\left[-\frac{(x-x')^2}{2\sigma^2}\right] dx'. \quad (6.5)$$

For bounded  $DJ(x)$  the asymptotic behavior of  $J(x)$  is the same as that of a Gaussian displaced by  $\mu$ :

$$\lim_{x \rightarrow \infty} J(x) = A \exp\left[-\frac{(x-\mu)^2}{2\sigma^2}\right]. \quad (6.6)$$

In the dual-Dirac model two delta functions displaced by  $\mu_L$  and  $\mu_R$  in  $x$  respectively are convolved with a Gaussian under the above assumption to give:

$$\begin{aligned} J(x) &= [\delta(x - \mu_L) + \delta(x - \mu_R)] * \exp\left[-\frac{x^2}{2\sigma^2}\right] \\ &= \exp\left[-\frac{(x - \mu_L)^2}{2\sigma^2}\right] + \exp\left[-\frac{(x - \mu_R)^2}{2\sigma^2}\right], \end{aligned} \quad (6.7)$$

as shown in Figure 6.18.

The  $BER(x)$  is given by the probability for a logic transition fluctuating across the sampling point,  $x$ . Setting aside the dual-Dirac model and assuming the probability density function is a single Gaussian, then  $BER(x)$  for the positive side of the Gaussian distribution is given by:

$$\begin{aligned} BER(x) &= \int_x^\infty J(x') dx' \\ &= \frac{1}{\sqrt{2\pi}\sigma} \int_x^\infty \exp\left[-\frac{(x-\mu)^2}{2\sigma^2}\right] dx'. \end{aligned} \quad (6.8)$$

It is possible to relate the BER to the quantity,  $Q$ , a multiple of the standard deviation of the Gaussian offset by  $\mu$  and given by:

$$Q = \frac{x - \mu}{\sigma}. \quad (6.9)$$

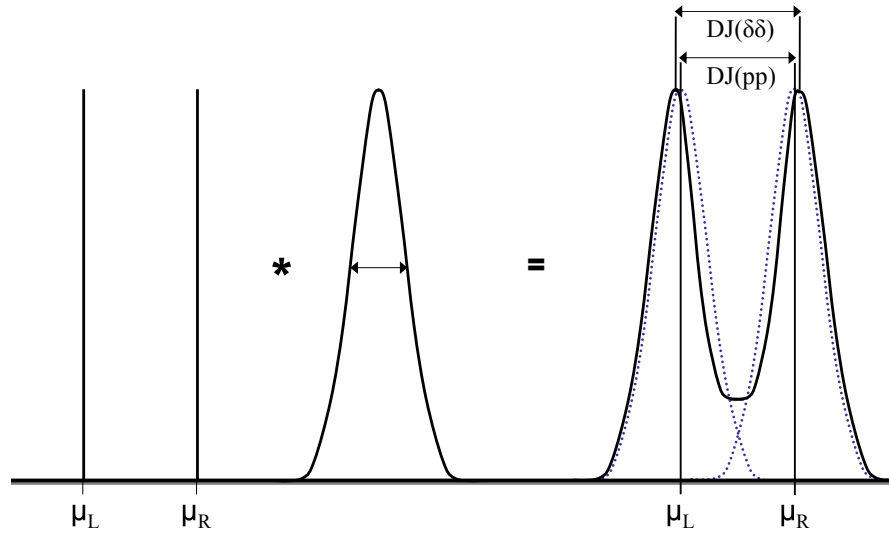


Figure 6.18: *The dual-Dirac model.*

Substituting  $Q$  into Eq. 6.8 produces:

$$BER(Q) = \frac{1}{\sqrt{2\pi}} \int_Q^\infty \exp\left[-\frac{Q'^2}{2}\right] dQ'. \quad (6.10)$$

Now consider the complementary error function in the most general form:

$$erfc(x) = \frac{2}{\sqrt{\pi}} \int_x^\infty \exp -t^2 dt, \quad (6.11)$$

easily re-written as:

$$erfc\left(\frac{Q}{\sqrt{2}}\right) = \sqrt{\frac{2}{\pi}} \int_Q^\infty \exp\left[-\frac{Q'^2}{2}\right] dQ' \quad (6.12)$$

and substituted into Eq. 6.10:

$$BER(Q) = \frac{1}{2} erfc\left(\frac{Q}{\sqrt{2}}\right). \quad (6.13)$$

A  $BER$  of  $1 \times 10^{-12}$  is found to correspond to  $Q = 7.0$  [126]. Restated: the probability of an event arriving outside the range of  $\pm 7\sigma$  is  $1 \times 10^{-12}$ , for a purely Gaussian

jitter distribution. Returning to the dual-Dirac model the distribution consists of two Gaussians and the deterministic jitter must be included in the estimate of total jitter:

$$TJ_{BER} = DJ(\delta\delta) + 2QRJ, \quad (6.14)$$

where the deterministic jitter is given by the peak-to-peak separation,  $DJ_{\delta\delta}$ , of the Gaussian peaks and RJ is the average standard deviation of these peaks<sup>7</sup>. In reality the situation is often more complicated, and distributions other than pure delta functions must be used to model the measured PDF. In the case of the DAT a large amount of *grass* is found in the jitter distribution. The low statistics of this *grass* are unsuitable for fitting with a Gaussian at the outer edges. Instead the two most prominent edges in the distribution are fitted and an average RMS for RJ extracted.  $DJ_{\delta\delta}$  is given by the peak-to-peak value of the measured PDF. This approximation will include a small amount of RJ in the determination of DJ, but as Eq. 6.14 shows, errors in DJ are relatively unimportant compared to those in RJ.

The validity of this method is tested in two trials. The Agilent MSO is set to average the waveform over a number of acquisitions, the resulting jitter distribution averages out the deterministic jitter leaving only random jitter. The RMS of this distribution is consistent with the RJ derived from the dual-Dirac method. Secondly the dual-Dirac model is used to estimate TJ for a BER of  $10^{-7}$  and compared to the peak-to-peak value of the measured jitter distribution for the same BER (see Section 6.7.7). Again the two are found to be consistent.

### 6.7.3 Duty Cycle Distortion

There is an observed deviation from 50% in the DC% of the encoded data signals leaving the DAT-TX FPGA and arriving at the receiver. As described in Appendix E.1 such distortions lead to DCD jitter in a recovered data pulse. The deviation from 50% is found to be dependent on the state of the input data. Measurements of DC% in the encoded data stream are shown for both the input data held *low* and *high* in Figure 6.19 for

---

<sup>7</sup>Note that the true DJ,  $DJ(pp)$ , given by the separation in time of the delta functions is only equivalent to the measured DJ,  $DJ(\delta\delta)$ , if the convolution results in no overlap between Gaussians. Usually  $DJ(\delta\delta)$  is less than  $DJ(pp)$ . The true DJ is irrelevant to the calculation of total jitter.

the final DAT-V2 FPGA code. Readings were taken with both 2 m and 60 m long fibre interconnects using input pulses of a 0.8 ns rise and fall time. The input pulses originate from the Agilent 81110A pulse-generator, which creates NIM pulses then converted to ECL using the CAEN ModV538A converter. The errors presented do not include the intrinsic uncertainty in the Agilent MSO trigger, which is a nominal 20 ps.

As noted in Section 6.6.2 the DCD dependence on input data state leads to undesirable consequences when decoding the data. Consider the clock arriving at the DAT-RX with  $DC\% = 50 - A$ . The encoded data must also have  $DC\% = 50 - A$  whilst data is *low* to result in a correctly recovered *low* level. If the encoded data has a  $DC\% = 50 + B$  when the data is high, the recovered data *high* state will contain glitches down to the *low* state at 25 MHz. The width of the glitches will be approximately  $\frac{|A-B|}{100} \times T_p$ , where  $T_p$  is the time period of the clock (40 ns). The situations resulting in no glitches correspond to  $A = B$ , indicated by the dotted line in Figure 6.19(b). For example a 49% DC% clock and 49% encoded data signal for data low and 51% for data high, align to correctly recover the *low* state and the *high* state.

The DC% of both the clock and encoded data during a *low* state is constrained to approximately 50% by the DAT-TX FPGA DCM. The variation between the DC% with input data *low* to *high*, is minimised by inverting the signal at stages throughout the FPGA design. The effect of the PCB routing, PAROLI and optical fibre on the DC% is minimal, and stable over different fibre lengths. The resulting DC% variation is not symmetric about 50%, but the glitch width during the input data *high* state is minimised. The narrow glitches are successfully removed with the aid of DDRFFs as described in Section 6.6.2.

Without constraining the DC% of the clock and encoded data within the DAT-TX FPGA the DC% of an encoded data leaving the DAT-TX is 49.3% for input data low, and 48.5% for data *high* and 50.1% for the clock line, resulting in misalignment glitches at the receiver (once the clock is phase-shifted to within 150 ps of the data) of 320 ps for data *low*, and 560 ps for data *high*.

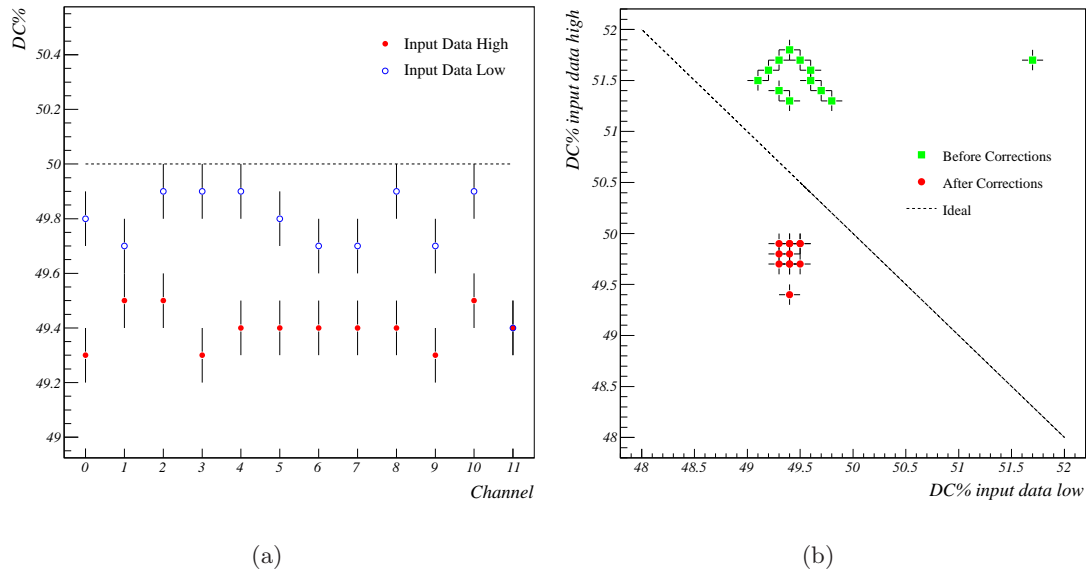


Figure 6.19: (a) The DC% dependence of the encoded clock on the input state of the data at the DAT-RX FPGA input over 60 m of fibre, (b) The DC% when the input data is held high against DC% when the input data is held low.

#### 6.7.4 Skew and Jitter in the Arrival Time

A 200 ns wide, 1 MHz, signal is input to the DAT. The arrival time of the falling edge at the output is measured relative to the falling edge at the input, which is used to trigger the Agilent MSO. A jitter histogram is built up of around 20k events as shown in Figure 6.20 and analysed using the dual-Dirac model to estimate  $TJ(10^{-12})$ . An example of the jitter distribution in arrival times is shown in Figure 6.21 for channel 9 of the DAT-V2 prototype pair connected with 2 m of optical fibre. The analysis results for all channels are shown in Table 6.4. The errors in  $TJ(10^{-12})$  are given simply by:  $\delta TJ = \sqrt{(14\delta RJ)^2 + \delta DJ^2}$ , where  $\delta RJ$  is given by the combination of uncertainties in the standard deviations of the Gaussian fits and  $\delta DJ$  is given by twice the bin width. Also included are the 95% confidence range, showing that on average, over all channels, 95% of pulses arrive within a range of  $0.745 \pm 0.232$  ns over 2 m of fibre and  $0.769 \pm 0.262$  ns over 60 m of fibre, where the errors represent the spread of the results, not the accuracy in determining the mean.

The full set of results and jitter histograms for this pair are available in Appendix F. The mean total jitter for a BER of  $10^{-12}$  is  $2.66 \pm 0.17$  ns over 2 m and  $2.73 \pm 0.17$  ns

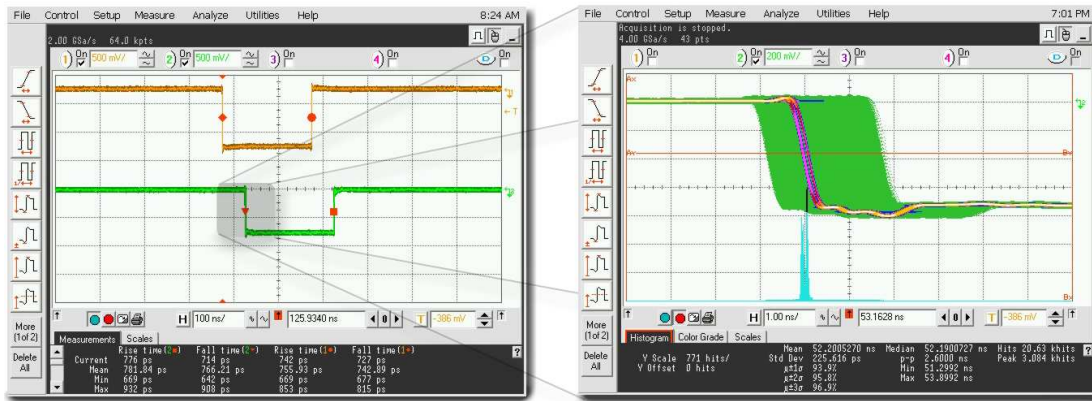


Figure 6.20: An example of the jitter distribution in arrival times from a 1 MHz, 200 ns wide input pulse over 2 m of fibre optic cable.

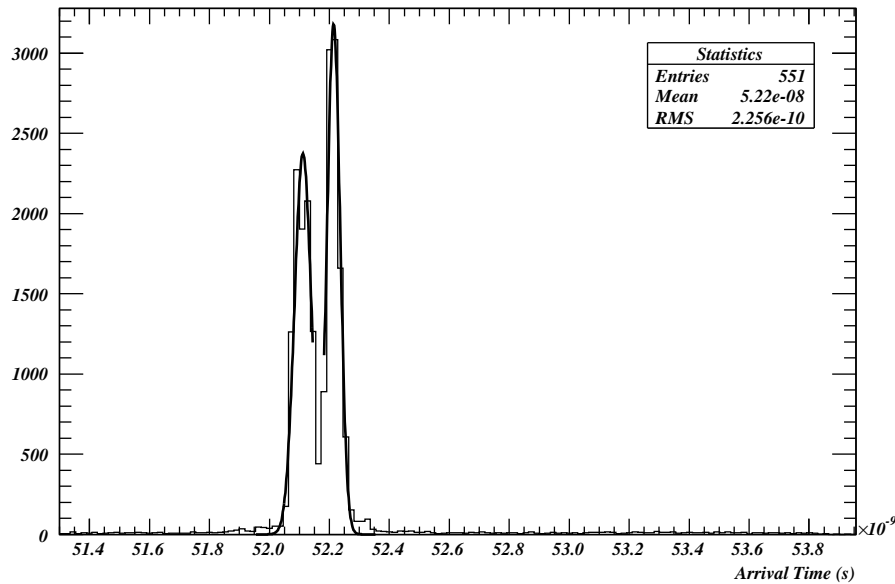


Figure 6.21:  $T_{ar}$  histograms with dual-Dirac fits for channel 9 of the prototype pair of DAT-V2 modules connected with 2 m of fibre.

over 60 m.

The skew computed from the average arrival times is  $1.71 \pm 0.17$  ns over 2 m of fibre and  $1.80 \pm 0.17$  ns over 60 m of fibre. The differences in average values for arrival time, jitter and skew between 2 m and 60 m are consistent with the short term variability of the modules noted in Section 6.7.7.

Table 6.4: *Arrival times for the 11 data channels of the prototype pair of DAT-V2 modules connected with 2 m of fibre.*

Channel	$T_{ar}$	p-p	RMS	RJ	DJ	TJ	$\delta$ TJ	95%
	(ns)	(ns)	(ns)	(ps)	(ns)	(ns)	(ps)	(ns)
0	53.1	2.49	0.209	27.3	2.28	2.67	36.6	1.07
1	51.9	2.29	0.211	36.1	2.01	2.53	40.0	9.09
2	51.4	2.40	0.186	30.1	2.17	2.60	37.3	4.36
3	52.2	2.47	0.213	29.0	2.25	2.66	36.6	5.09
4	52.6	2.18	0.168	28.4	1.96	2.37	36.6	4.55
5	52.6	2.18	0.196	49.0	1.80	2.50	40.6	8.18
6	52.2	2.42	0.197	24.9	2.23	2.58	36.5	5.27
7	52.3	2.51	0.253	32.0	2.26	2.72	37.2	1.00
8	52.2	2.64	0.226	24.9	2.44	2.80	36.6	9.27
9	51.7	2.80	0.220	22.5	2.62	2.95	37.2	6.91
10	52.8	2.66	0.217	38.6	2.35	2.91	37.2	8.55

### 6.7.5 Pulse Width Distortion

The distortion in the pulse width is best examined by considering the jitter of the recorded pulse width relative to the mean pulse width. The falling edge of the 1 MHz, 200 ns wide signal is used to trigger the oscilloscope and a jitter distribution for each DAT channel constructed at the rising edge of the same pulse. The mean of the distribution is the average pulse width at the DAT-RX output. The dual-Dirac approach is again taken to obtain TJ( $10^{-12}$ ), and the results are shown in Table 6.5.

The jitter in the pulse width measurements are the convolution of the arrival time jitter on both the falling and rising edges of the data and are therefore effected by the input pulse width. Since the clock period is 40 ns, if the falling edge of a 200 ns pulse (or any multiple of 40 ns) comes in close proximity to a clock edge during the encoding stage so does the adjacent rising edge. Thus every time there is an interaction between a falling

Table 6.5: *Pulse width measurements for the 11 data channels of the prototype DAT-V2 pair over 2 m of fibre*

Channel	$T_{pw}$ ( <i>ns</i> )	p-p ( <i>ns</i> )	RMS ( <i>ns</i> )	RJ ( <i>ps</i> )	DJ ( <i>ns</i> )	TJ ( <i>ns</i> )	$\delta$ TJ ( <i>ps</i> )
0	198.67	2.95	0.370	25.5	2.75	3.11	37.6
1	198.76	2.51	0.357	26.1	2.31	2.68	40.1
2	199.05	2.96	0.325	26.5	2.76	3.14	36.4
3	198.64	3.29	0.330	30.6	3.05	3.49	38.2
4	198.87	2.62	0.311	26.0	2.42	2.79	36.5
5	198.72	2.71	0.310	29.4	2.48	2.90	36.7
6	198.86	3.25	0.365	29.1	3.03	3.44	41.8
7	199.00	2.89	0.429	27.3	2.68	3.07	38.3
8	198.92	3.09	0.366	21.2	2.92	3.23	39.1
9	199.12	3.33	0.370	22.0	3.16	3.47	47.6
10	198.40	3.24	0.327	25.5	3.04	3.40	37.2

edge and a rising (falling) edge there is also an interaction between a rising edge and another rising (falling) edge. The pulse width varies according to DCD induced jitter on a scale related to the difference in rise and fall times as described in Appendix E.1.

In the case of a 190 ns wide pulse (or any non-multiple of 20 ns) if one edge is close to a clock transition the other edge is not, directly causing the pulse width to vary. The amount by which it varies depends on both the proximity and the nature of the edges. In this case the jitter distribution looks very similar to the case for a 200 ns wide input pulse. Since the transitions occur with a different frequency the distribution must be sufficiently sampled to obtain the same jitter result.

If an input pulse of 180 ns (or non-multiple of 40 ns) is used then when a falling data edge is near a falling (rising) clock edge, the corresponding rising data edge is near a rising (falling) clock edge. In this case the pulse width variations begin to cancel at the data edges. Again, all possibilities will still occur given time, but with a different

probability. The jitter occurs over the same range as above, but does so around a single large peak.

The total jitter in pulse width is independent of the input pulse width, but the nature of the jitter distribution is not. Different jitter 'modes' become active as the pulse width is varied altering the most probable resulting pulse width. The varying speed of the rising to falling edge of the pre-encoded and recovered data through the FPGA leads to DCD and systematically narrows the pulse width. Appendix F contains the pulse width distributions for Table 6.5 and the results over 60 m. Over 2 m the average TJ( $10^{-12}$ ) in the pulse width was  $3.16 \pm 0.28$  ns and  $3.15 \pm 0.30$  ns over 60 m.

### 6.7.6 Channel-to-Channel Jitter

Within VERITAS the L3 array trigger transmitted over the DAT modules is used to trigger the telescope read out. Directly following the L3 trigger a serial event number, also transmitted over the DAT modules is recorded by the telescopes. Thus the arrival time of a pulse on one DAT channel is used to trigger the read out of the pulse on another DAT channel. It is therefore important to understand how the arrival time of pulses on one DAT channel relates to those on another, this relationship is referred to here as the channel-to-channel jitter. To measure the channel-to-channel jitter the falling edge of the DAT output on channel 2 is used to trigger the oscilloscope and the jitter on the falling edge of the other 10 DAT output channels is measured. The exercise is repeated relative to channel 8. The expected jitter may be predicted from the quadrature addition of the jitter on the individual channels, however this assumption over-estimates the jitter. It follows that if the deterministic jitter on the trigger channel is in phase with the deterministic jitter on the measured channel the resulting distribution will consist only of RJ. Whilst the observed distributions do contain one very large peak there are smaller peaks offset from this peak.

For synchronous inputs the proximity of the clock to data edges at the encoding stage should be similar for all channels and the DDJ contribution to the total jitter due to clock-data edge proximity described in Appendix E.2 should be absent. Any DDJ remaining is due to the skew between data lines and the clock skew before and after encoding. The distribution still contains peaks due to DCD, PJ and jitter due to the

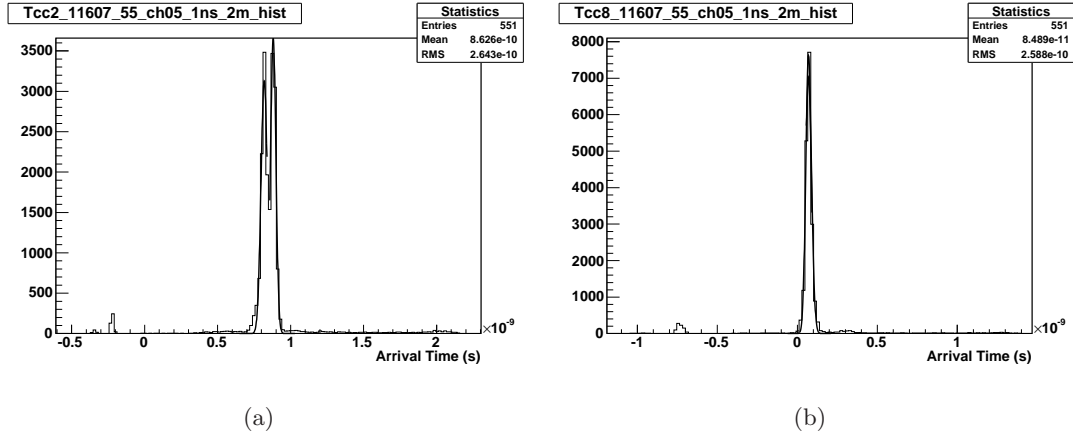


Figure 6.22:  $T_{cc}$  of channel 5 of the DAT-V2 prototype modules relative to channel 2, (a), and 8, (b).

DDRFF.

Table 6.6 shows the results over 2 m of fibre relative to channel 2. The results over 60 m relative to channel 2, and over 2 m and 60 m relative to channel 8 can be found in Appendix F. The difference in jitter when the fibre length was varied from 2 m to 60 m is negligible. The average total jitter for a BER of  $10^{-12}$  relative to channel 2 is  $2.83 \pm 0.37$  ns and  $2.98 \pm 0.34$  ns relative to channel 8 over 2 m and  $2.88 \pm 0.42$  ns and  $2.96 \pm 0.41$  ns over 60 m respectively. The total channel-to-channel jitter is less than the quadrature addition of the jitter in arrival time of the two channels, and therefore there is some phase correlation between channels. In fact, the total jitter is of the same order as the total arrival time jitter, which implies the outermost jitter peaks are due to events that are unlikely to occur at the same time on two channels. The largest peaks in the distribution are due to DDJ and in the case of channel-to-channel jitter these peaks may overlap to create a single larger peak when in phase, and a smaller peak much early and/or later in time when directly out of phase. Figure 6.22(a) shows the distribution for channel 5 relative to channel 2 and Figure 6.22(b) shows the distribution for channel 5 relative to channel 8. Whilst channel 5 appears to be in phase with channel 2, there appears to be a large phase difference between channel 5 and channel 8.

Table 6.6: *Arrival time measurements relative to channel 2 for the other 10 data channels over 2 m of fibre.*

Channel	$T_{cc2}$	p-p	RMS	RJ	DJ	TJ	$\delta$ TJ
	(ns)	(ns)	(ns)	(ps)	(ns)	(ns)	(ps)
0	1.45	3.04	0.315	20.3	2.88	3.17	38.6
1	0.200	1.98	0.190	17.7	1.84	2.10	37.9
3	0.447	2.82	0.247	22.1	2.65	2.97	39.2
4	0.871	2.87	0.230	28.8	2.65	3.06	39.3
5	0.863	2.89	0.264	20.6	2.76	3.02	37.6
6	0.556	2.89	0.250	16.3	2.76	2.99	36.8
7	0.538	2.31	0.236	15.6	2.19	2.41	40.3
8	0.471	2.42	0.203	17.6	2.29	2.53	37.8
9	0.004	2.62	0.193	29.9	2.39	2.81	36.2
10	1.14	3.13	0.271	20.3	2.97	3.26	40.6

### 6.7.7 Stability

The short-term stability of the prototype DAT-V2 modules is monitored by making arrival time measurements on channels 2 and 8 in 2 minute intervals (data is acquired on each channel for 1 minute) for 50 minutes over 60 m of fibre. The average arrival time is stable at  $345.295 \pm 0.003$  ns for channel 2 and  $345.421 \pm 0.003$  ns for channel 8 with a range of only picoseconds, as shown in Figure 6.23(a).

The p-p jitter is predicted to increase gradually as RJ expands the tails of the distribution, however, as seen in previous sections, RJ is of the order 20 ps, and the fluctuations between measurements in the p-p jitter, are of the order of 200 ps, as shown in Figure 6.23(b). It is unlikely the p-p jitter would vary by this much over a 1 minute sample due purely to RJ. Examining the distribution of p-p jitter more closely, a tail of smaller values building up to the large peak can be seen for both channels. This is believed to be due to deterministic jitter. Although DJ is bounded and does not expand with time,

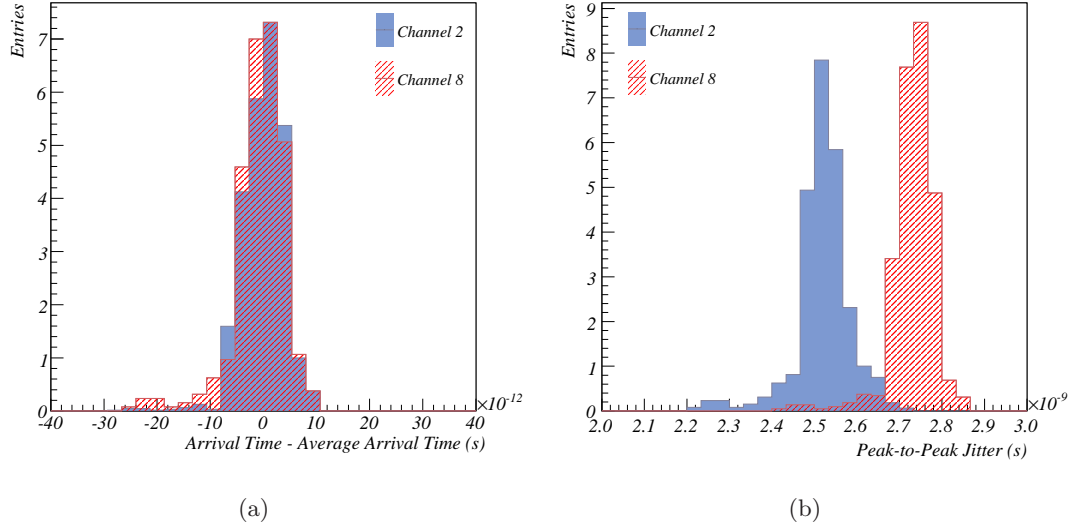


Figure 6.23: *Distribution of arrival times (a), and p-p jitter (b), for 25 measurements spaced equally across 50 minutes for channels 2 (solid blue) and 8 (hatched red) of the DAT-V2 modules.*

a certain number of samples are initially required for DJ to reach its finite limit. If this limit is not reached in 1 minute, variations between measurements will be observed. This is further evidenced by the sharp cut-off in values to the right of the distribution. The temperature of both the modules within the VME crate and the fibre are monitored during the test and both gradually decrease with time as shown in Figure 6.24(a). The average crate temperature was  $21.6 \pm 0.2$  °C and the average fibre temperature is  $21.0 \pm 0.2$  °C. Temperature and p-p and jitter are uncorrelated as shown in Figure 6.24(b), at least over the minimal temperature gradient experienced here. As noted in Section 4.6.6 the average transit time across the fibre will increase with temperature, but only by  $\sim 10$  ps per °C. Furthermore this small variation will affect the encoded data and clock lines equally, and therefore should not increase the jitter.

To assess the long term stability of the modules the arrival time of a pulse at the DAT-RX output is measured continuously over 12 hours and added to a jitter distribution as shown in Figure 6.25. The average arrival time is  $344.2 \pm 1.3$  ns, consistent with the average of the short term variability.  $TJ(10^{-12})$  is then  $2.61 \pm 0.04$  ns, which is consistent with the  $2.56 \pm 0.04$  ns obtained in Section 6.7.4. The jitter therefore evolves as predicted by the dual-Dirac model, and short-term fluctuations average out to produce a predictable,

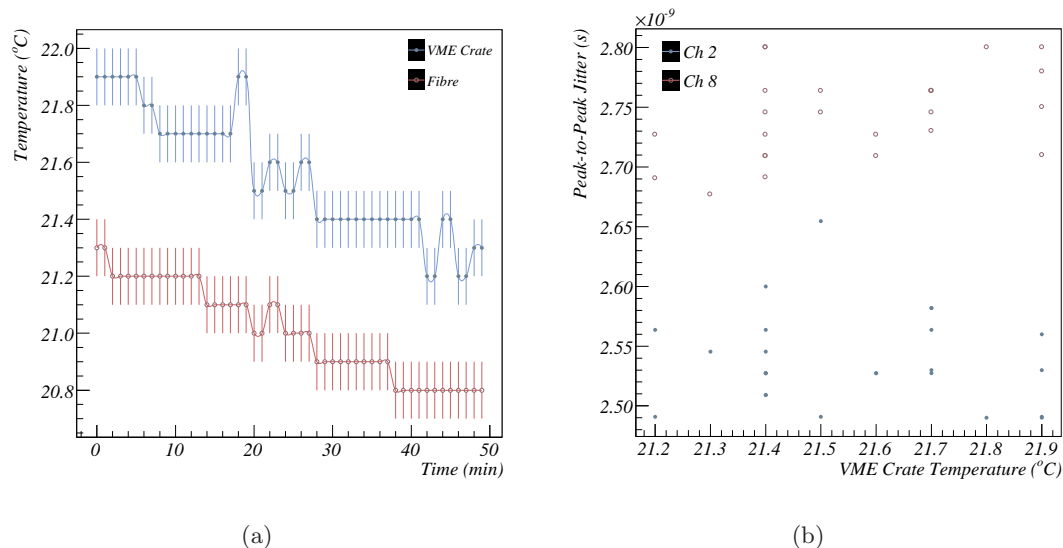


Figure 6.24: (a) Temperature of the VME crate, (filled blue), and fibre-optic cable, (hollow red), as varies over the 50 minute short-term stability test duration. (b) Peak-to-peak jitter as a function of VME crate temperature showing a lack of correlation for both channel 2 (filled blue) and channel 8 (hollow red).

stable long-term behaviour.

### 6.7.8 Results for the Remaining DAT Pairs

The measurements performed in Section 6.7.4 were repeated on several channels of the other four DAT-V2 pairs over 60 m of fibre. The results were consistent with those from the prototype pair of DAT-V2 modules.

When programmed with the same FPGA design as used in DAT-V2, the DAT-V3 modules show glitches on the recovered data lines indicative of misalignment. The combination of the new DB design and termination scheme alters the DC% and skew of the signal lines enough to miss-align the clock and encoded data at the DAT-RX FPGA input. As such each pair of DAT-V3 modules requires a different FPGA program to align the outputs. Once aligned, all channels were verified to be clear of noise and the jitter in the arrival times on several channels was measured and again found to be consistent with those from the prototype pair of DAT-V2 modules.

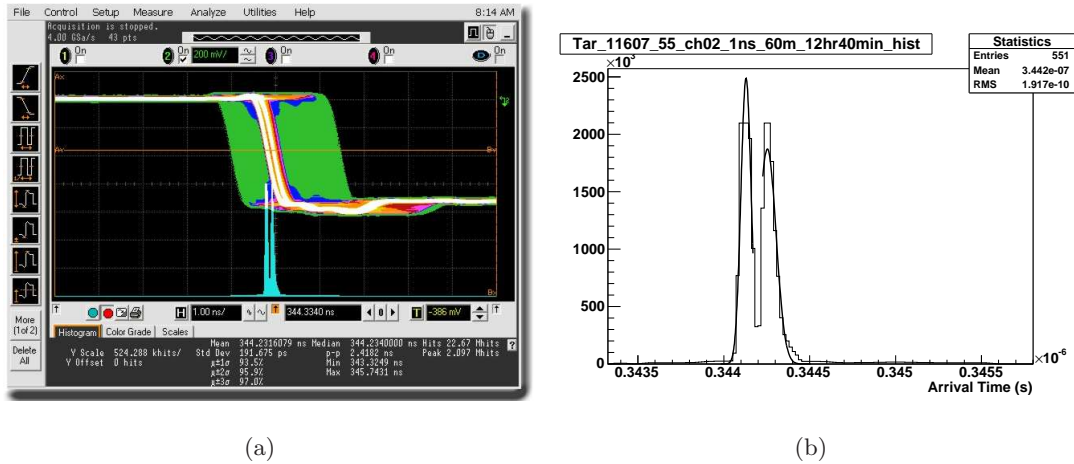


Figure 6.25: Long term stability of the DAT modules as captured by the oscilloscope, (a), and added to a histogram, (b).

## 6.8 The Integration of the DAT within VERITAS

Four DAT-V2 modules were installed in the first two VERITAS telescopes in 2006. Individual lengths of fibre laid between telescopes were connected to the DAT modules in T1 and T2 via patch panels and E2000 fanout cables as shown in Figure 6.26. During laboratory tests a 12 channel MPO terminated ribbon cable was used to connect the modules. Each of the fibres in the ribbon cable was constrained to be of near identical length by the manufacturing process. However, onsite the fibres routed to the E2000 patch panels were of different lengths and exhibited differences in transit times of up to  $5.3 \pm 0.1$  ns [176]. Careful channel-mapping was required to account for the skew and align 8 of the possible 11 channels in each pair of modules. In September 2006 150 m pairs of 12 channel MPO terminated armoured fibre ribbon cables were laid between the central trailer and the four telescopes, thereby alleviating the problem encountered with the E2000 patch panels and fibre skew. Four pairs of DAT-V3 modules were installed between the central trailer and the remaining two telescopes bringing the array into full operation. The installation of the DAT modules within VERITAS is described further in Appendix G.1 and the on-site performance of the DAT modules is measured over a long period of time by the successful acquisition of stereo data as discussed in Chapter 7. Onsite software is required to control and monitor the DAT modules over the FPGA

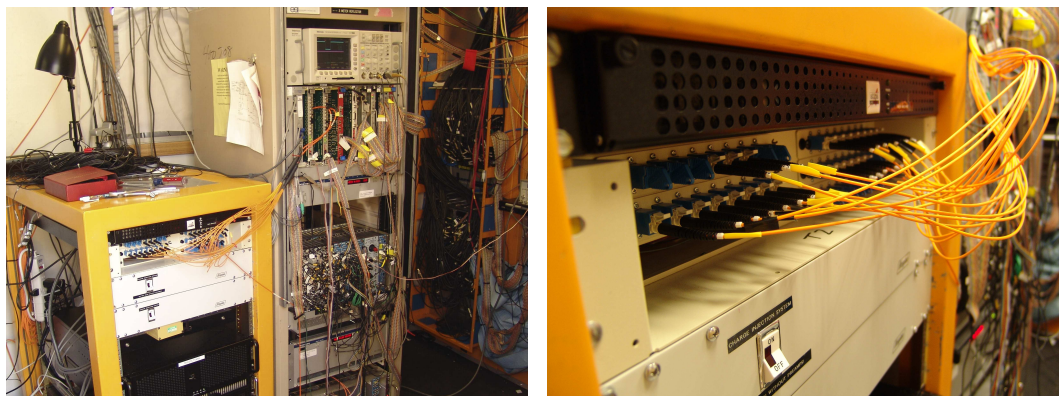


Figure 6.26: *Onsite installation of the DAT-V2 modules in the VERITAS T1 trailer using an E2000 patch panel to connect the DATs to T2 via individual fibres and E2000 to MPO fanout cables.*

implemented VME interface. The software is integrated into the VDAQ structure. Under normal operating conditions when a VME crate is powered up, a DAT shutdown procedure is run as a daemonised process to set the inputs to either IDC header or twin-axial Lemo connector on a channel-to-channel basis and disable the PAROLI-TX lasers making the modules safe and extending the lifespan of the PAROLIs. When the VERITAS array control software, used during observing to control the telescope subsystems and monitor data recording, issues a 'start-night' command VDAQ initiates the DATs in all four telescopes and the central trailer. Similarly at the close of observing VDAQ will receive an 'end-night' command and shut-down the DAT modules. During development work a utility program, 'DAT\_Diagnostic', provides the user with the ability to change and monitor all CSR bits with a user friendly interface. Further details about the DAT software can be found in Appendix G.2.

## 6.9 Dynamic Phase Shift

The value of the DAT-RX DCM PHASE\_SHIFT attribute set at design time provides a fixed phase shift to align the clock with the eleven data lines. The amount of skew between the eleven data lines on different DAT modules varies. Although a single value of the phase shift was found such that all channels on all pairs of DAT-V2 modules align, the DATs must be used in their tested pairs. That is, it can not be guaran-

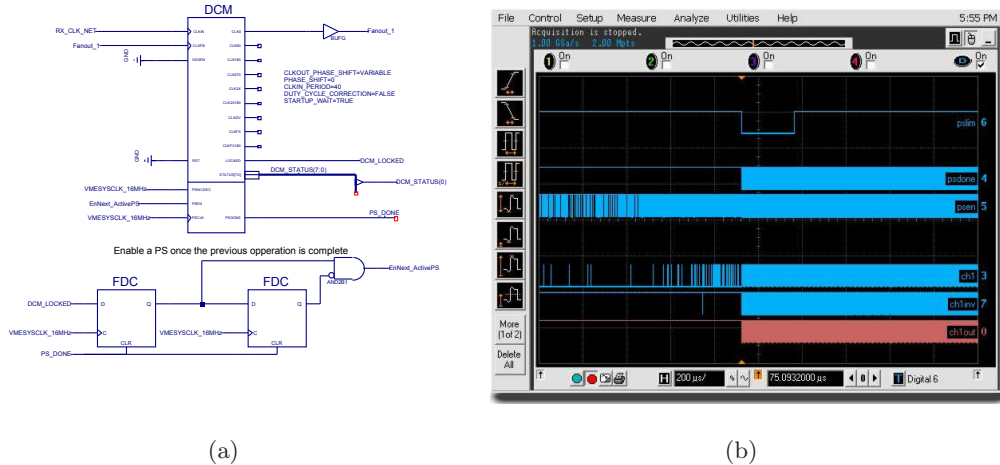


Figure 6.27: (a) The DAT-RX DCM setup to dynamically alter the phase relationship between *Fanout\_1* and *RX\_CLK\_NET*. *PHASE\_SHIFT* is incremented from 0 to +255. Short pulses enabling the a phase shift increment (*EnNext\_ActivePS*) are clocked by the 16 MHz clock also used to clock the DCM and *PSINDEC* correctly satisfying the operating conditions of the DCM. (b) The resulting relationship between the value of *PHASE\_SHIFT* and the DAT-RX channel 1 output obtained using the Agilent MSO's digital inputs. *STATUS(0)* (*PSLIM*, upper trace) is low during the phase-shift operations.

teed that a transmitter from one pair will work with the receiver from another pair. To address this issue the possibility of using a dynamic phase-shift was briefly investigated. In this scenario the DCM is connected as shown in Figure 6.27(a). When *PSINDEC* is *high* the *PHASE\_SHIFT* is incremented, when it is *low* *PHASE\_SHIFT* is decremented. *PHASE\_SHIFT* may range from 0 to +255. *PSEN* enables dynamic phase shift, when *low* the DCM remains at the current phase shift. The process is clocked by the 16 MHz VME clock input to *PSCLK*, and *PSDONE* goes *high* for one clock cycle after *PHASE\_SHIFT* is incremented or decremented. *STATUS(0)* is normally *low*, switching *high* when *PHASE\_SHIFT* reaches +255. *PSINDEC* and *PSEN* must only assert a signal *high* for one *PSCLK* cycle then wait until *PSDONE* goes *high* before requesting the next phase shift.

In the simple example shown in Figure 6.27(a) *PSINDEC* is connected to the 16 MHz clock. Figures 6.27(b), 6.28(a) and 6.28(b) show the resulting behaviour on three different timescales. When the FPGA is configured *STATUS(0)* (*PSLIM* in the figures)

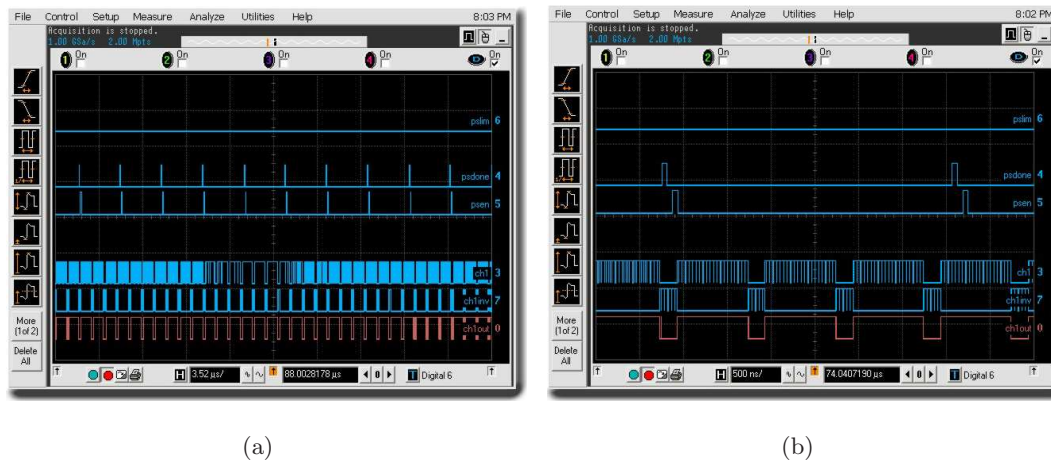


Figure 6.28: (a) Figure 6.29(b) on a smaller time-scale, here the individual PSEN and PSDONE operations can be seen and window in which the output becomes valid is seen. Ch1 is the clock XOR'd with the encoded data on channel 1, ch1inv is the inverted clock XOR'd with the data, and ch1out is the DDRFF output. (b) The centre of the dynamic phase-shift alignment window. After a PSDONE pulse, PSEN pulses high and the DCM output is phase-shifted to correctly recover the data at the DDRFF output.

is asserted *low*. The DCM phase shifts from 0 to +255 waiting for the DCM to lock between each transition. When +255 is reached STATUS(0) goes *high* and remains there. By appropriately adjusting the timescale a phase-shift window during which the output is correctly recovered is observed.

To evolve this basic experiment for use within the DATs, the DCM must phase-shift the clock until the output is correctly recovered and then stop. How to determine this point is not trivial. A simple idea is to take the logical AND of the clock and the first encoded data channel. To do this the input data at the DAT-TX must be held *low*. There is no guarantee that just because the clock is aligned with the first data channel that it will be aligned for all data channels, that is, the clock is not centred in the phase-shift alignment window. It is not possible to take the AND of all 11 channels and the clock and expect the result to be zero due to skew and routing errors.

## 6.10 Conclusions

Fast digital trigger and event number distribution is achieved within VERITAS using FPGA based DAT modules. The modules incorporate PAROLI fibre optic interconnects to protect against lightning induced power surges associated with coaxial cabling and to minimise channel-to-channel skew and jitter. The DC% operating restriction imposed by the PAROLI-TX laser-safety circuit is successfully satisfied using FPGA implemented XOR gate encoding. This combinatorial method of encoding and decoding the data results in a dead time free system, and helps to minimise the dead time of the VERITAS array as a whole. Implementing the combinatorial operations within Xilinx Spartan 3 FPGAs provides a versatile and adaptable solution suitable for future IACTs and UNDs.

The performance of the DAT-V2 modules exceeds the requirements of the current VERITAS trigger chain. However, the FPGA code and methodology have proven complicated due to the accuracy required to align the clock with encoded data at the receiver. In DAT-V3 modules the combination of the new DB design and termination scheme alters the DC% and skew of the signal lines sufficiently to create glitches in the recovered data lines. Consequently each pair of DAT-V3 modules requires a different FPGA program to align the outputs. If the alignment in the DAT-V2 or DAT-V3 modules is not correct at the sub-nanosecond level a given channel will produce spurious noise at either the clock frequency (25 MHz) or double the clock frequency (50 MHz). These pulses have a width corresponding directly to the misalignment of the clock and encoded data signal and a minimum width of around 2 ns, the signal switching time at the FPGA output stage. Spurious pulses do not occur at all if a channel is aligned. In practice a fibre-ribbon cable must be used to connect the DAT modules to ensure that the 12 fibres are of identical length. The resulting jitter introduced into an input pulse is dominated by DJ and well described by the dual-Dirac model. The DJ can be explained by considering the physical scenarios leading to the individual contributions of DCDJ, DDJ, PJ and DDRFFJ, although the individual components can not be isolated in the measured distribution. The DJ is dominated by DCDJ, verified by measuring the DC% of signals at the DAT-TX output and DAT-RX input and DDJ occurring as the clock and data edges approach each other during encoding and then as the clock and encoded data edges approach each other during decoding. The distribution of jitter introduced

into the width of a transmitted pulse depends on the ratio of the original pulse width to the clock period, but the range over which the jitter occurs does not. The channel-to-channel jitter can be larger than the average jitter in the arrival time if the jitter distributions on the two channels in question are out of phase, but significantly smaller if the distributions appear in phase, where the phase refers to the relationship between data and clock edge at the DAT-TX and encoded data and clock edge at the DAT-RX. Over 60 m of optical fibre for a BER of  $10^{-12}$  an average total jitter of  $2.73 \pm 0.17$  ns ( $0.769 \pm 0.262$  ns at the 95% confidence level) is introduced into the arrival time of the leading edge of a pulse and the pulse width jitters by  $3.15 \pm 0.30$  ns. The average channel-to-channel jitter is  $2.88 \pm 0.42$  ns and  $2.96 \pm 0.41$  ns relative to channels 2 and 8 respectively.

Although the total jitter in the arrival time is relatively large, this is for a BER of  $10^{-12}$ , which for normal operation may be too strict a criterion<sup>8</sup>. The total jitter in arrival time with 95% confidence is crucially less than 1 ns, facilitating the accurate transmission of VERITAS array trigger pulses. Consequently trigger signals arrive at the FADC modules accurately enough to allow the determination of the position of the data in the buffers to within one FADC sample (2 ns), as described in Sections 6.1 and 6.2. The skew between output channels from the average arrival times is  $1.6 \pm 0.4$  ns (at the 95% confidence level), small enough to integrate into the VERITAS trigger chain without affecting the pre-programmed delays within the array trigger system which compensate for the relative movement of the telescopes.

Laboratory tests showed no correlation between variations in either circuit board temperature and the transit time and jitter of pulses. On site the modules are cooled by fan trays to maintain an approximately constant temperature and therefore the narrow range of temperatures examined in the laboratory is sufficient. The temperature of the fibre-optic cable running between telescopes will experience more significant variations in temperature than measured in the laboratory. The dependence of transit time on fibre temperature is equivalent to that determined in Section 4.6.6. The use of 12-channel fibre-ribbon cable ensures that the transit times down both the clock and encoded data channels are affected equally by any temperature variations and thus the jitter is un-

---

<sup>8</sup>Operating at a nominal L3 rate of  $\sim 200$  Hz it would take 159 years of constant (24 hr/day) DAT operation before a pulse arrived outside this window.

affected by fibre temperature. The load stability and the effect of instabilities in the power supply have not been measured and this should certainly be examined in any future work.

Since the system introduces no dead time the minimum pulse width that can accurately be transmitted is limited by the signal switching speed and the system jitter. The minimum transmittable pulse width at  $\text{BER}=10^{-12}$  is around 5 ns. This is also the time gap required between consecutive pulses and therefore the maximum transmittable data rate is 200 Mbps.

The four telescope VERITAS array has been successfully operating with 8 pairs of DAT modules since March 2007. However whilst the performance of the DAT-V2 modules onsite has been reliable, the DAT-V3 modules are not as stable, typically requiring user intervention around once per month. This would be inconvenient for a larger array of telescopes and completely unacceptable for a UND. The focus of future work would be to improve the reliability of the modules and reduce the need for such accurate data to clock alignment. That said, the DAT is the only dead time free multi-channel parallel optical distribution system in the world capable of transmitting signals over such a wide range of DC%*s* and frequencies. Furthermore the DAT modules are at least one order of magnitude cheaper than purchasing many copies of a single-channel commercial solution. This versatile technology could be adopted for future IACT arrays such as CTA and other applications such as triggers for particle physics experiments or clock distribution within UN*D*s.



## Chapter 7

# Benefits of Stereoscopic Observations with a Hardware Array Trigger

---

The development of new technology for the transmission of analogue signals over optical fibre and high-speed triggering described in Chapters 4 and 5, with VCSELs and FPGAs respectively, was combined in Chapter 6 to successfully design, develop and deploy a system for the optical distribution of trigger signals, event numbers and housekeeping information within VERITAS. The DAT modules enable the use of multiple telescopes connected with a hardware array trigger. In this chapter observations of the VHE  $\gamma$ -ray standard candle, the Crab Nebula, are used to assess the benefits of operating several telescopes in stereo. Observations with a single telescope are compared to those taken with two telescopes using both software and hardware implemented array triggers. Finally, the first observations of the Crab Nebula with three VERITAS telescopes are presented.

## 7.1 Introduction

In this chapter observations of the Crab Nebula taken during the commissioning stages of VERITAS between January 2006 and March 2007 are used to compare the performance of single and multiple telescopes. Monte Carlo simulations play a key role in the analysis chain and are included to verify the analysis procedure. It is shown that using multiple telescopes reduces the detector energy threshold, increases the sensitivity and improves the angular resolution. Focus is given to the intrinsic improvements resulting directly from the use of a hardware implemented array trigger and therefore no optimisation of the data analysis procedure or energy reconstruction and spectral analysis is attempted.

Two data analysis packages are used in this work. The first, EventDisplay, was written at the University of Leeds as the Prototype and then the first and second VERITAS telescopes (T1 and T2) came online. EventDisplay was used following the acquisition of data from T1 and T2 prior to the implementation of the hardware array trigger. The ability to analyse software stereo data, obtained by GPS time-matching events from individual telescope runs, is included in EventDisplay. As the hardware array trigger came online so did the official collaboration analysis package, VEGAS (VERITAS Gamma-ray Analysis Suite). VEGAS is specifically designed to analyse data from multiple telescopes connected with a hardware array trigger. The ability to analyse single telescope data is included, but not software stereo data. Therefore VEGAS is used to analyse the two and three telescope hardware stereo data and EventDisplay is used to analyse software stereo data. Both packages are used to analyse single telescope data and the results compared to verify their consistency.

## 7.2 The Crab Nebula

At a distance of approximately 2000 parsecs and known to be the remnant of a supernova observed in 1054 AD, the Crab SNR is an archetypical plerion and is exceptionally well studied across the entire extent of the accessible spectrum (see Figure 7.1). The Crab Nebula was discovered in VHE  $\gamma$ -rays in 1989 by the Whipple collaboration [173] and has been independently detected by many high-energy experiments including HEGRA [119], CAT [39], CANGAROO, H.E.S.S. [13] and MAGIC [120]. The Whipple 10 m

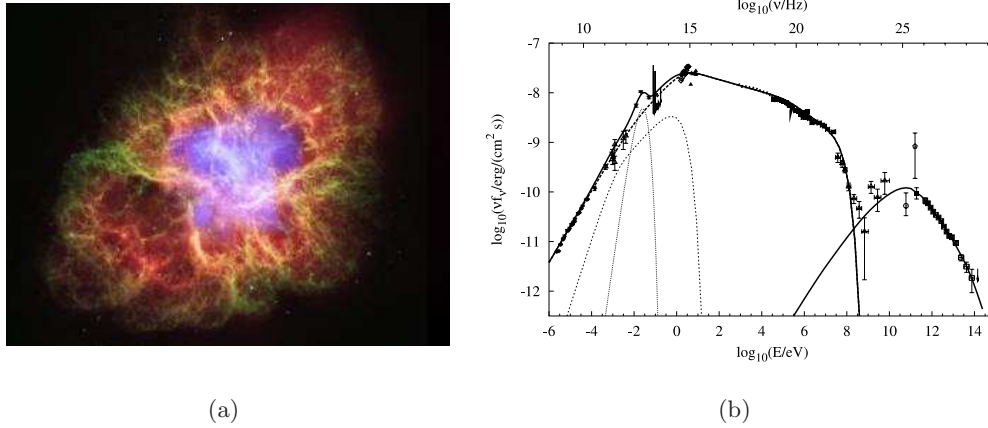


Figure 7.1: (a) Composite image of the Crab Nebula combining data from Chandra, Hubble and Spitzer indicating emission in X-rays (blue-purple), optical (green) and infrared (red) wavebands. (b) The Crab Nebula spectrum over a wide range of energies from a variety of measurements. Taken from [9].

telescope reached a level of 5-6  $\sigma$  on the Crab in one hour with a  $\gamma$ -ray rate of  $\sim 3$   $\gamma$ /min. Emission models of VHE  $\gamma$ -rays from the Crab Nebula are based on a simple Inverse Compton-synchrotron model. The radio to X-ray emission can be explained by synchrotron radiation from relativistic electrons in the pulsar wind shocks. In this scenario GeV - TeV photons are produced by IC scattering of these electrons with soft ambient photons (see Chapter 1). The Crab Nebula is regarded as a standard candle in VHE  $\gamma$ -ray astronomy due to its steady emission from 300 GeV to 3 TeV and well established flux and spectrum. It is therefore an ideal calibration source for telescopes, used during both the commissioning/engineering phase and throughout regular observations to understand the instrument and optimise the analysis.

### 7.3 Observations

Observations of the Crab Nebula were taken with VERITAS during the engineering stage between January 2006 and March 2007. Data with the VERITAS T1 telescope were taken in January 2006. As the size of the Crab nebula is small compared to the VERITAS PSF, it may be treated as a point source for this analysis. During this period data from T2 were also taken and is suitable for use in a software array trigger analysis.

In Pairs mode the source is observed at the centre of the camera for a dedicated amount of time (28 minutes in the observations used here); this is the *on* region. The telescope is then repositioned to track a patch of empty sky 30 sidereal minutes later in right ascension and data is recorded for another 28 minutes. This *off* region data thus covers the same zenith angle range as the *on* region to ensure a equivalent telescope response. Four, 28 minute T1 and T2 Pairs are used in this analysis. Two and three telescope hardware array trigger data were taken in Wobble mode between October 2006 and March 2007. In Wobble mode the target is offset from the centre of the FoV by  $\pm 0.3^\circ$  or  $\pm 0.5^\circ$  in declination or right ascension and a data run is taken. Typically a second run is also taken with the target offset in the orthogonal direction and the data are analysed together. Wobble mode increases the detector duty cycle, but the source is not at the centre of the FoV and the sensitivity is consequently reduced. Two telescope hardware array trigger data were taken over four 28 minute Wobble runs offset by  $0.3^\circ$  East, West, North and South respectively. Three telescope hardware array trigger data were taken similarly, but with a  $0.5^\circ$  offset and an individual run duration of 20 minutes. Each data run is matched to an accompanying laser run from the same night of observations for calibration purposes (see Section 7.5). Only data runs taken in *good* weather conditions are selected. Figure 7.2 shows the effect of *bad* weather on the trigger rate; it is straight forward to recognise and reject those data runs.

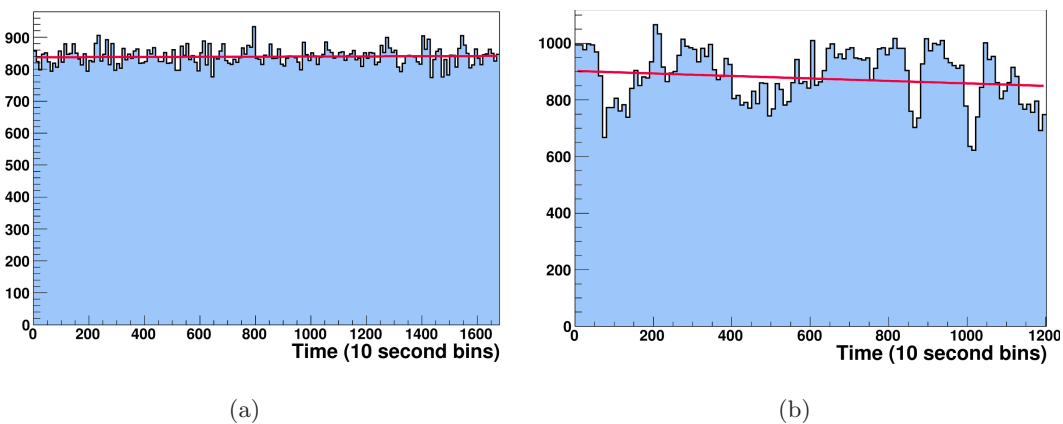


Figure 7.2: Array trigger rate (*y*-axis - Hz) for a Crab Nebula data run taken during good (a) and bad (b) weather. In the case of bad weather, the trigger rate varies as clouds pass across the FoV, and such a run is excluded. The red line is used to guide the eye; for this small data set runs were rejected by visual inspection.

The energy threshold of VERITAS is related to the CFD threshold of the telescopes in the array. The CFDs remove pulses below the threshold level on a pixel-by-pixel basis and are used to reject signals due to the NSB as described in Section 3.4.1. Pulses from CR and  $\gamma$ -ray associated events are also removed below the CFD threshold. Figure 7.3 shows the system trigger rate as a function of CFD threshold, or so-called *bias curves*, for telescopes in several trigger configurations. In each configuration the L2 PST multiplicity is set to three and the array trigger coincidence window in the two and three telescope curves is set to 100 ns. In each set of data a smooth power law dependence gives way to a rapidly increasing trigger rate at the lower CFD thresholds where fluctuations in the NSB dominate over the CR background. The CFD threshold is set to maintain a manageable system trigger rate of  $< 350\text{Hz}$  corresponding to an acceptable dead time of  $< 10\%$ .

When operating with a single telescope, as shown in black for T1, red for T2 and cyan for T3, a threshold of 70 mV (or 6.7 p.e.) is used to constrain the trigger rate to 300 Hz and corresponds to a dead time of 6%. The bias curves for each telescope are taken during the same evening, but at different times.

Operating with a software array trigger requires that multiple telescopes record data independently. The CFD threshold is therefore the same as for a single telescope. No improvement in energy threshold is obtained. Furthermore the amount of data that must be recorded by the array doubles and the dead time is detrimentally affected.

The shift to a hardware implemented array trigger removes events that do not illuminate multiple telescopes within the coincidence window and allows the telescopes to operate at the reduced CFD threshold of 50 mV (or 4.5 p.e.). The energy threshold of the detector is therefore reduced. The system trigger rate of T1 and T2 operating in stereo is shown in the blue data points in Figure 7.3. Since each stereo event contains twice the data the system trigger rate is constrained to a lower value than in the case of a single telescope (175 Hz in this instance). Note that the exact trigger rate at the normal operating CFD threshold will vary on a nightly basis due to the random nature of the NSB. Typical variations are from 100 Hz to 300 Hz. Adding a third telescope to the array and operating with a 2/3 telescope coincidence, as shown in green in Figure 7.3, does not reduce the system trigger rate, and therefore the energy threshold in this configuration

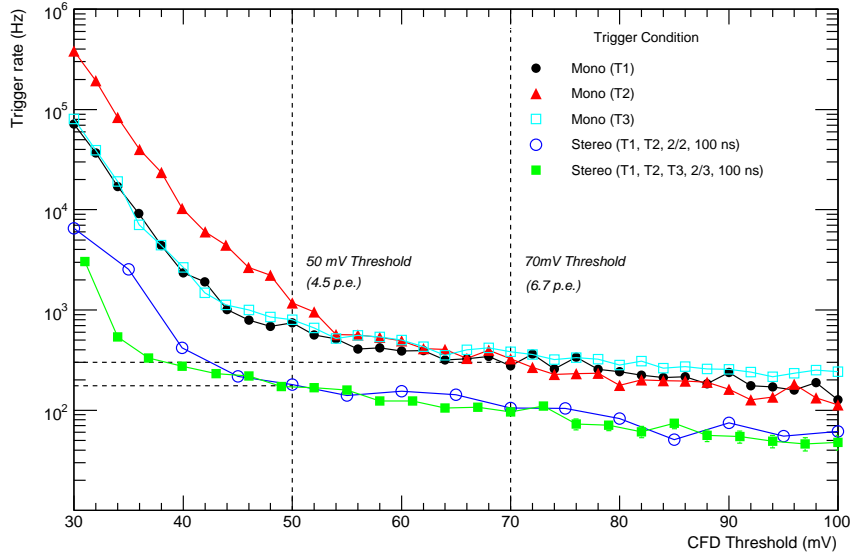


Figure 7.3: Bias curves taken with  $T1$ ,  $T2$  and  $T3$  operating independently,  $T1$  and  $T2$  connected with a hardware array trigger requiring both telescopes to trigger within a 100 ns coincidence window, and  $T1$ ,  $T2$  and  $T3$  connected with a hardware array trigger requiring two of the three telescopes to trigger within a 100 ns coincidence window.

is approximately the same as in the two telescope case. The differences between the two and three telescope bias curves are due to fluctuations in the NSB and differences in the telescopes as these data were taken at very different times. An array trigger condition of 3/3 or 3/4 telescopes would allow a further reduction in the CFD threshold, as would the implementation of the zero suppression scheme described in Section 3.5.

As described in Section 3.4.3 the array trigger system uses the PDM to compensate for the differences in timing introduced by the difference in arrival time of the shower front at the telescopes depending on the observation direction. Figure 7.4 shows the three telescope array trigger rate as a function of the array trigger coincidence window. The stability of the system trigger rate down to at least 10 ns implies that the PDM modules are programmed with the correct delays and that the DAT modules in all three telescopes are operating correctly. A large jitter in the DAT modules would cause the system trigger rate to drop and a misaligned DAT channel would cause the rate to vary wildly. Below 10 ns the combined effects of curvature in the shower front, the Davies-Cotton reflector time-spread and the uncertainty in the pulse transit time through the

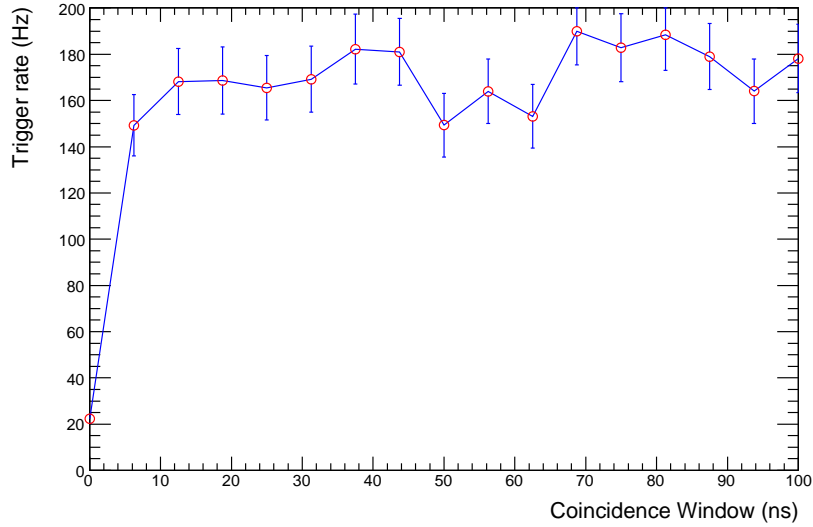


Figure 7.4: *System trigger rate as a function of the array trigger coincidence window. The approximately constant rate down to  $\sim 10$  ns indicates that the DAT modules and PDM are working correctly.*

PMTs, cabling, L1, L2, DAT modules and PDM in each telescope causes the system trigger rate to drop rapidly. In the stereo observations used here, taken during the engineering phase of the array trigger, the coincidence window is set to 100 ns.

## 7.4 Simulations

Monte Carlo simulations of  $\gamma$ -ray and proton-initiated EASs are used to produce a data set of events with known energy and direction [122]. By passing these events through a detector simulation and then the analysis chain the detector response to  $\gamma$ -rays and CRs is assessed. EASs are simulated using the CORSIKA air shower simulation package [80] assuming a US Standard Atmosphere. Within CORSIKA EM interactions were modelled using EGS v4, HE interactions were modelled using QGSJet II and low-energy interactions were modelled by FLUKA 2006.3. The low-high transition took place at 500 GeV and the observation level was set to 1270 m a.s.l. Using inputs such as spectral index, energy range and particle type, CORSIKA produces, for each simulated event, the distribution of Cherenkov photons on the ground (see Section 2.2.2).

The response of the VERITAS array is simulated using the GrISUDet4 package which takes the Cherenkov photons striking the telescope mirror and uses ray-tracing to propagate the photons back to the camera. Quantum-efficiency and PMT response functions are used to generate a simulated camera output. This output is read by the trigger simulation which determines whether the telescope, and subsequently the array, has triggered. Simulated FADC traces are produced and the results saved in the same format as is a real data run, so that they can be analysed in an equivalent way. The efficiency of the  $\gamma$ -ray selection cuts (see Section 7.8) and the accuracy of the energy and directional reconstruction may then be assessed via comparison to the original simulation inputs. The GrISUDet4 settings were chosen to match the characteristics of VERITAS during the observing period, these included the d.c. to single pe ratio, the pedestal value, and the CFD threshold.

In this work results from simulations are compared to those obtained from the analysis of real single telescope data to justify their use in the MSW and MSL calculations (which are described in Section 7.8.3). Proton induced EASs are simulated with a spectral index of  $-2.7$  between 30 GeV and 30 TeV whilst  $\gamma$ -ray air showers are simulated with a spectral index of  $-2.5$  (chosen to be close to that of the measured Crab Nebula) between 50 GeV and 10 TeV.  $\gamma$ -ray showers are simulated at zenith angles of  $0^\circ$ ,  $20^\circ$ ,  $30^\circ$ ,  $40^\circ$  and  $50^\circ$  in order to calculate lookup tables for MSL and MSW. Approximately  $1.6 \times 10^6$   $\gamma$ -rays are simulated, whilst  $7.5 \times 10^7$  protons are required as these do not trigger the array as frequently. For both  $\gamma$ -ray and proton initiated air showers, the core location of each shower is randomised and resampled ten times in order to improve statistics.

## 7.5 Telescope Calibration

Telescope calibration is divided into absolute calibration and relative calibration, which are described in Sections 3.6.1 and Section 3.6.2 respectively. Absolute calibration is concerned with understanding the signal size produced by a single pe such that the detector response and the energy scale can be accurately modelled in Monte Carlo simulations. The distribution of charges for a single channel from a p.e. laser run is shown in Figure 3.15(a), where the HV is set at higher than normal operating values so that the single photoelectron peak can be easily seen. Extrapolating to normal operating

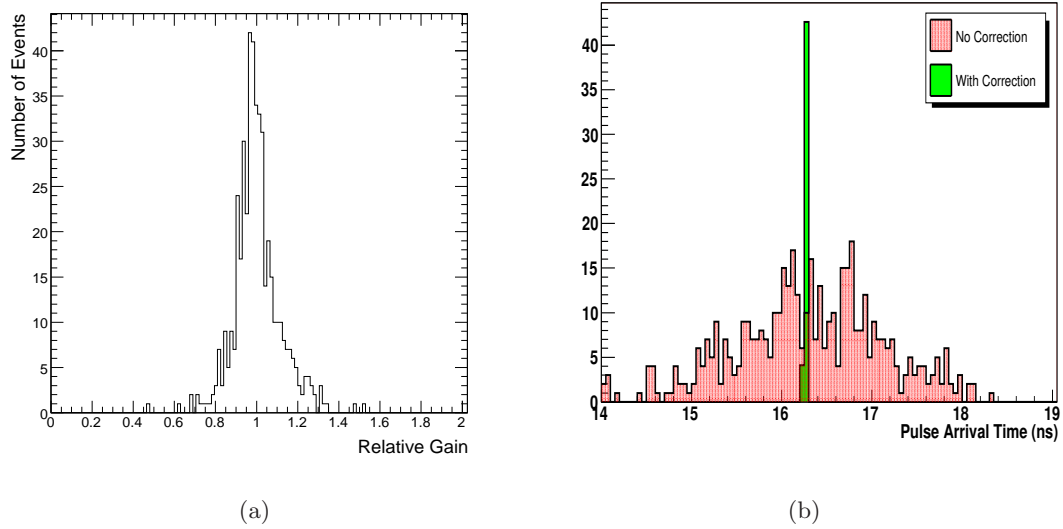


Figure 7.5: (a) The distribution of the mean relative gains for all channels of T1 from the laser run used for mono observations in this analysis. (b) The average trace arrival time over all channels is displayed by the red distribution. After application of the  $T_{offset}$  correction, the re-calculated green distribution is tight and located at the mean of the original uncorrected distribution, from [41].

voltages yields 5.3 d.c./p.e.[91].

Relative calibration is essential to ensure a uniform response across the face of the camera and involves removing the FADC injected pedestal and equalising the PMT pulse heights and pulse arrival times using a dedicated laser-calibration run. The pedestal values and pedestal standard deviations for each FADC channel are determined on a run by run basis from artificially triggered FADC samples. The pedestal standard deviation, referred to as  $pedvar$ , is a measure of the noise in a given channel. The optimum pedestal integration window is discussed in [41]. A dedicated laser run allows the relative gains of the PMTs and the relative arrival time of pulses at the FADCs to be equalised across the camera. The relative gains for each PMT of T1 for a given laser run are shown in Figure 7.5(a). The arrival time of a single FADC event, referred to as  $T_{zero}$ , is defined as the time on the falling edge at which the trace reaches half of its maximum value after subtraction of the pedestal baseline. The relative differences in transit time between channels, due to differences in cable length, HV and electronic delays on the FADC boards, are corrected for using the  $T_{offset}$  calculation.  $T_{offset}$  is the difference between

the arrival time of an event at a given channel and the average arrival time of the event across the camera averaged over many events, see Figure 7.5(b).

## 7.6 Image Reconstruction

To calculate the energy and direction of incident  $\gamma$ -rays the amount of Cherenkov light and the orientation of the image recorded in the camera must be accurately parameterised. Prior to parameterisation relative calibration information is applied to the camera in a process known as *Pixel Cleaning* and an algorithm is used to isolate images over the surrounding background light in the camera, *Image Cleaning*.

### 7.6.1 Pixel Cleaning

To calculate the amount of residual light incident on each pixel the FADC trace in each channel is integrated over a pre-defined window. Corrections are made to the start of the integration window using the  $T_{offset}$  calculations, ensuring that all traces are integrated in an equivalent manner. Once the charge has been integrated, the pedestal baseline is subtracted. What remains represents the amount of light deposited in that pixel, however the representation is not uniform across the camera due to the uneven gain distribution. This is remedied by applying relative gain corrections to the charge calculated for each pixel.

Before image cleaning in Pairs mode it is necessary to compensate for differences in the sky brightness of the *on* and *off* fields. Different noise levels in the opposing fields can introduce a bias in the number and nature of the images recorded in the *on* and *off* regions. A software trigger threshold is applied, rejecting signals below the measured charge of the  $n_{th}$  brightest pixel, where  $n$  is the number of pixels required by the PST. This reduces the trigger rate of both the *on* and *off* runs. The *pedvar* of each PMT in the *on* and *off* fields are then compared. Gaussian noise is artificially added, offline, in quadrature to the less noisy PMT signal until the *pedvar* of both signals match. Adding this *padding* to less noisy pixels raises events above the software trigger threshold so that they contribute to the effective trigger rate.

## 7.6.2 Image Cleaning

A two-pass cleaning algorithm is applied to the pixel-cleaned image to ensure that all pixels which contain a significant amount of Cherenkov light are retained whilst those pixels dominated by background light are excluded. In the first pass, any pixel whose charge exceeds the product of its *pedvar* and some fixed threshold, referred to as the *Picture Threshold*, passes the cleaning algorithm. In the second pass any pixel which is adjacent to a pixel which passed the first criterion, and whose charge exceeds the product of its *pedvar* and some lower fixed threshold, referred to as the *Boundary Threshold*, passes the cleaning algorithm. Pixels which pass the first criterion are referred to as *Picture Tubes*, whereas pixels which pass the second criterion are referred to as *Boundary Tubes*, both are regarded as *Image Tubes*. The charge of all other tubes is set to zero. An example of an image before and after cleaning is shown in Figure 7.6. Any isolated pixels which can skew the parameterisation are removed. In this work the *Picture Threshold* is set to  $5 \times \textit{pedvar}$  and the *Boundary Threshold* is set to  $3 \times \textit{pedvar}$ . An alternative approach to cleaning [32], identifies image patches, called islands, which are surrounded by pixels with no significant signal.

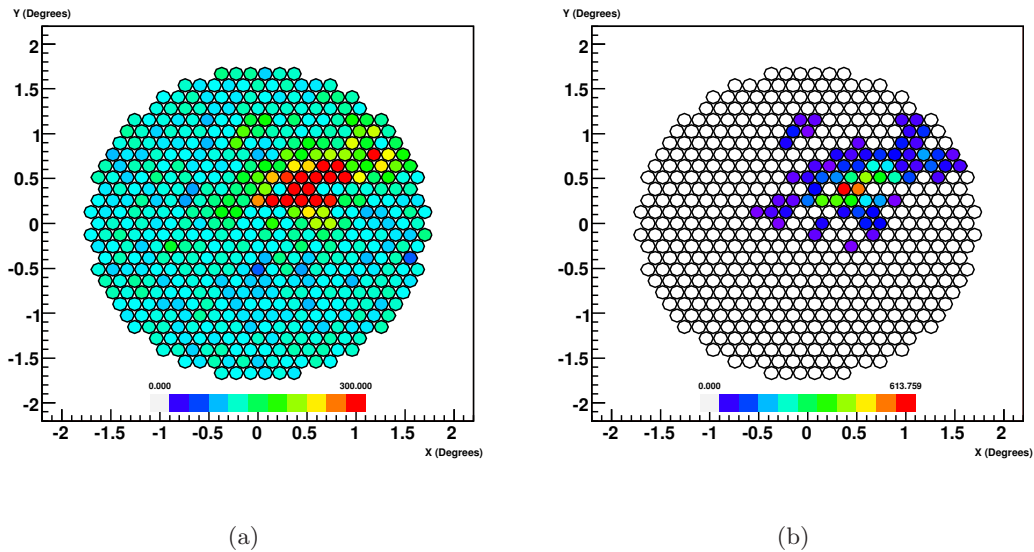


Figure 7.6: *The image of a CR in the VERITAS T1 camera (a) before and (b) after cleaning. Taken from [41].*

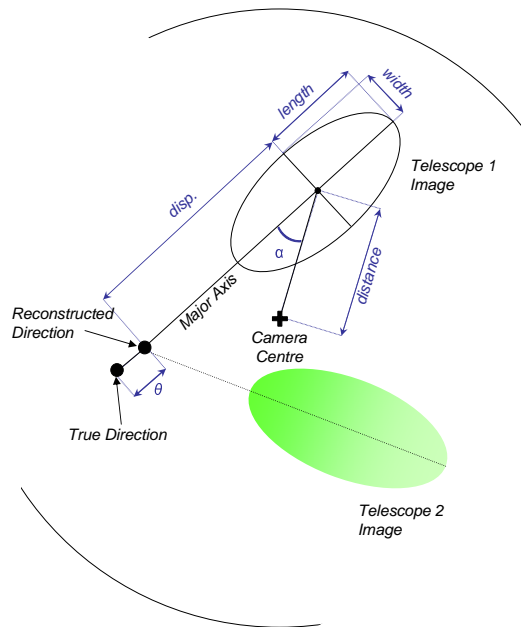


Figure 7.7: Geometric definition of the parameters used to describe the image of a Cherenkov shower in the focal plane of an IACT.

### 7.6.3 Parameterisation

As introduced in Section 2.3.3 an image formed in an IACT camera by a  $\gamma$ -ray may be distinguished from that due to a CR, once cleaned, through the use of the Hillas parameters [84]. The Cherenkov light intensity distribution for  $\gamma$ -ray induced showers in the camera is, to a first approximation, elliptical. This ellipse can be characterised by parameters which can be written in terms of moments of the light intensity distribution. The parameters correspond to position, orientation, shape and brightness of the image in the camera. The Hillas parameters (and those defined subsequently) of interest in this work are described in Table 7.1 and shown graphically in Figure 7.7. The distribution of *alpha*, *distance*, *length* and *width* for T1 observations of the Crab Nebula are shown in Figure 7.8 and agree well with the predictions from Monte Carlo simulations.

## 7.7 Shower Reconstruction

The reconstruction of an EAS from the Cherenkov light distribution in an IACT leads to both the energy and direction of the progenitor particle. This work is primarily concerned with the directional reconstruction.

<i>length</i>	RMS spread of light along the major axis of the image, a measure of the vertical development of the cascade.
<i>width</i>	RMS spread of light along the minor axis of the image; a measure of the lateral development of the cascade.
<i>distance</i>	Distance from the centroid of the image to the centre of the FoV.
<i>size</i>	Sum of the number of counts in all of the tubes; corresponding to the total light content of the image.
<i>length/size</i>	The ratio of the parameters <i>length</i> and <i>size</i> .
<i>alpha</i>	Angle between the major axis of the ellipse and a line joining the centroid of the ellipse to the centre of the FoV.
<i>disp.</i>	Angular distance between the image centroid and the reconstructed source position.
$\theta$	Angular distance between the reconstructed source position and the true source position.

Table 7.1: *The image parameters used in this analysis including those originally defined by Hillas[84] and those introduced to reconstruct the source location in the FoV by Lessard [112] (see Section 7.7).*

In single telescope data analysis the source location is assumed to lie along the major image axis. The angular distance from the image centroid to the source location, *disp.* can be calculated according to Lessard, [112]. However, the ability to reconstruct showers with a single telescope is hampered by the inherent uncertainty in determining which side of the camera the shower originated in. As the stereoscopic technique requires more than one camera to be triggered by the Cherenkov light from the same shower, the directional reconstruction can make use of viewing the shower from different angles simultaneously to avoid this problem. By intersecting the major axes of the ellipses from the different cameras an accurate determination of the shower direction can be achieved (Figure 7.9(a)). The stereoscopic approach also allows the determination of the core location on the ground as shown in Figure 7.9(b). The distance from a telescope to the reconstructed core location on the ground is known as the impact parameter. The impact parameter proves far more powerful than with the *disp.* method. Accurate de-

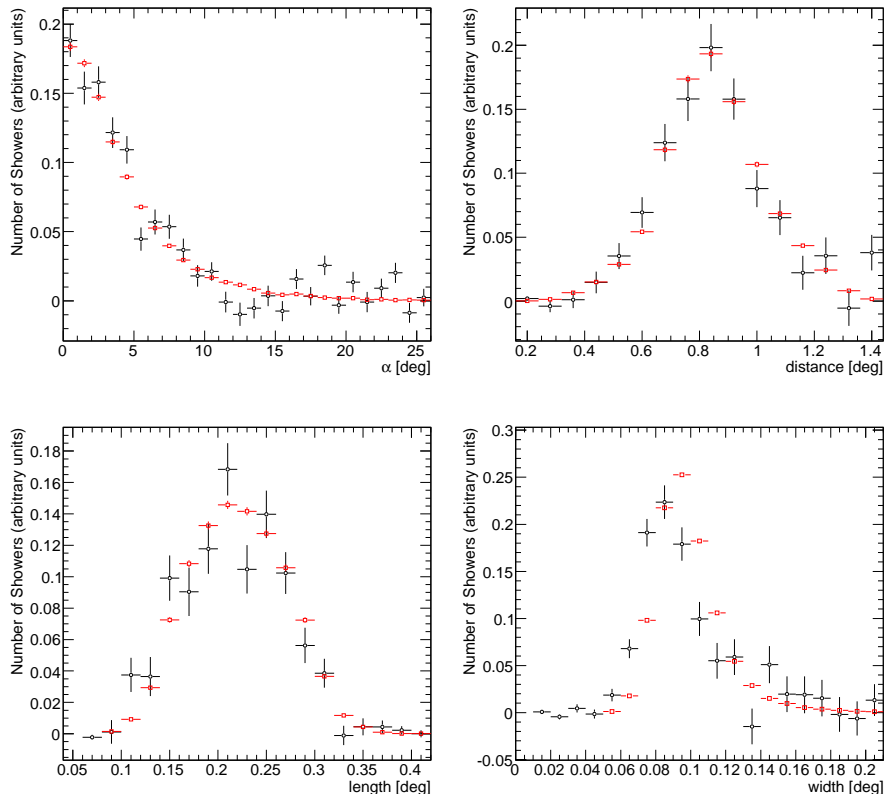


Figure 7.8: Image parameter distributions obtained from real data taken with T1 (black) compared to those predicted from Monte Carlo simulations (red). The distributions show the difference between the image parameters from an on source run and those derived from an off source run and have been normalised to the total number of showers.

termination of the impact parameter leads to knowledge of the position of the telescopes within the Cherenkov light pool (see Figure 2.7), which in turn improves the energy reconstruction. Furthermore the impact parameter can be used in conjunction with Monte Carlo simulations of EASs to provide a powerful background rejection technique (see Section 7.8.3).

The shower source location in the FoV is the point with the minimum perpendicular distance to each image axis, weighted with the image *size*. If more than two images are available, a source location is computed for each pair of image axes, weighted by angular separation and averaged. Pairs of images with a large angular separation are closer to being orthogonal which provides a better geometrical reconstruction than pairs of images with a small angular separation which are more parallel. As described in Section 7.8.1

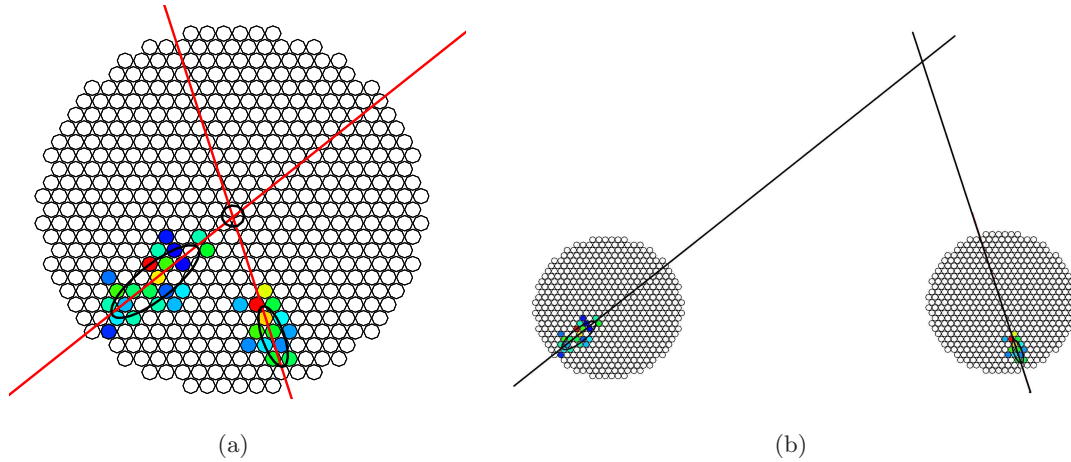


Figure 7.9: (a) Simple source location reconstruction using intersection of axes. The Cherenkov images of the same shower as seen by two telescopes are overlaid on one camera. (b) Simple core location reconstruction using intersection of axes. Taken from [41].

a cut is placed on the angle between pairs of images to reject parallel events that would otherwise be poorly reconstructed.

## 7.8 $\gamma$ -Ray Selection

Images due to background events must be removed from the cleaned, parameterised data in order to correctly isolate EASs initiated by  $\gamma$ -rays and reconstruct the energy and direction of the primary. The rejection of background events is achieved by applying cuts to the image parameters. The selection cuts which retain the maximum number of  $\gamma$ -rays whilst rejecting the maximum amount of background events are determined via Monte Carlo simulation and then optimised for point-source studies each observing season using data from the Crab Nebula. For the purposes of this work the standard VERITAS cuts have been used. These are defined for single telescope and stereo observations here.

### 7.8.1 Quality Cuts

Quality cuts are applied to the total image brightness (*size*) and number of tubes contributing to the cleaned image (*nTubes*) in each camera to reject poorly reconstructed events at the expense of a higher energy threshold (see Table 7.2). Events with large

impact parameters suffer truncation at the edge of the camera. It is impossible to accurately reconstruct the direction of such showers. The effect of truncation of images by the camera edge is reduced by a cut on the angular *distance* of the centre of gravity of images from the centre of the camera, which is related to the distance of the shower core position on the ground. The VERITAS standard quality cuts used in this work, and shown in Table 7.2, are the same for single and multiple telescope observations. The distribution of the *distance* parameter obtained from observations with T1 (before cuts) is compared to predictions from Monte Carlo simulations in Figure 7.8.

Parameter	Min.	Max.
<i>size</i> (d.c.)	400	-
<i>nTubes</i>	5	-
<i>distance(deg)</i>	0.05	1.3

Table 7.2: *Quality cuts used to reject poorly reconstructed events in both single and multiple telescope observations. There is no upper limit on the size or nTubes.*

When observing with multiple telescopes an additional quality cut is used to reject pairs of images with an angle of under  $10^\circ$  between them. Such events are poorly reconstructed. The effect of this cut can be seen in the reconstructed core locations of showers on the ground as shown in Figure 7.10 for a two telescope Wobble run on the left and a three telescope Wobble run, on the right. The contours indicate regions of high density, included to highlight the position of the telescopes. The effect of the cut to remove parallel images reduces the number of showers in the two telescope data creating a lobe structure and reducing the effective area of the detector.

### 7.8.2 Single Telescope Observations: *Standard Selection Cuts*

Due to the purely electromagnetic nature of  $\gamma$ -ray initiated air showers,  $\gamma$ -ray Cherenkov images are expected to be more compact than CR images and can be preferentially selected by applying cuts on the *length* and *width* parameters.

Showers originating from a point source, such as the Crab Nebula, will be orientated with their major axes pointing back to the position of the source at the centre of the

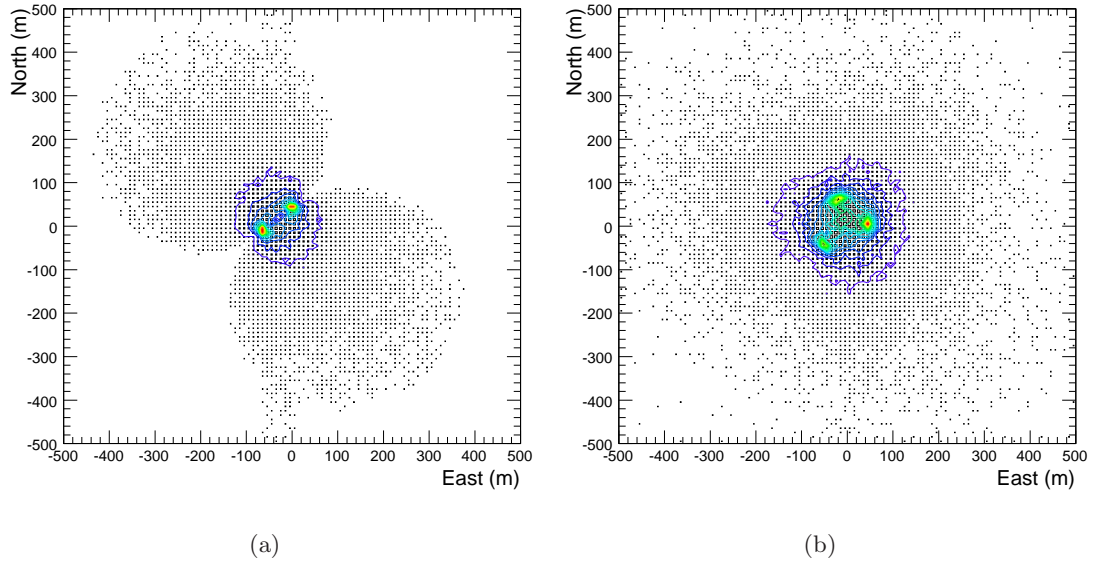


Figure 7.10: *The reconstructed core locations of showers on the ground for (a) a two telescope Wobble run and (b) a three telescope Wobble run, both with a hardware array trigger. The contours indicate regions of high density, included to highlight the position of the telescopes. The effect of the cut to remove parallel images, that are otherwise poorly reconstructed, reduces the number of showers in the two telescope data creating a lobe structure.*

Parameter	Min.	Max.
$length(deg)$	0.125	0.318
$width(deg)$	0.058	0.120
$\alpha(deg)$	-	7
$length/size (deg/d.c.)$	-	0.0002

Table 7.3: *The non-optimised single telescope selection cuts used in this work.*

camera. When observing with a single telescope an additional cut on the parameter  $\alpha$ , describing the orientation of the image in the camera, can therefore be used to isolate  $\gamma$ -ray candidates.

The ratio of the image  $length$  to its total  $size$  (where  $size$  is the integrated charge over all PMT signals in the image) is used to discriminate  $\gamma$ -rays from the otherwise overwhelming background of local muons (see Section 2.3.9.4) which generate short arcs in the camera with a constant  $size$  per unit arc length. The  $\gamma$ -ray selection cuts used for

single telescope observations within this work are shown in Table 7.3.

### 7.8.3 Stereo Observations: *Scaled Cuts*

The amount of light recorded in an image of a shower is strongly dependent on the distance to the shower core. There is, therefore, a disparity between whether a fainter image implies a lower energy primary, or simply a more distant impact point. A set of *scaled cuts*, introduced in [47], addresses this problem by comparing the *width* and *length* parameters of the images from the data to those from a set of simulations. *Scaled cuts* are most appropriate for stereoscopic observations, where an accurate measurement of the impact parameter can be obtained. A large number of  $\gamma$ -rays are simulated at several discrete zenith angles, and their images are then parameterised to obtain *width* and *length* as a function of *size* and impact parameter. A scaled width (SW) is then calculated as the ratio of the image *width* in the data to the average width in simulations, as a function of *size* and impact parameter, and similarly for the scaled length (SL). The SW and SL from multiple telescopes can be weighted with the *size* of the image and combined to obtain the Mean Scaled Width (MSW) and Length (MSL).

Parameter	Min.	Max.
<i>MSW</i>	0.04	1.2
<i>MSL</i>	0.04	1.3
$\theta^2(\text{deg}^2)$	-	0.04

Table 7.4: *The non-optimised scaled  $\gamma$ -ray selection cuts used in this work for stereo-data analysis.*

When observing with multiple telescopes the  $\alpha$  constraint is replaced with a cut on  $\theta^2$ , the squared angular difference between the source and the reconstructed shower direction. Such a cut is only used in determining the number of  $\gamma$ -rays from the source direction (1-dimensional analysis), and is not required in the creation of a sky-map (2-dimensional analysis). Table 7.4 shows the cuts used for stereo analysis.

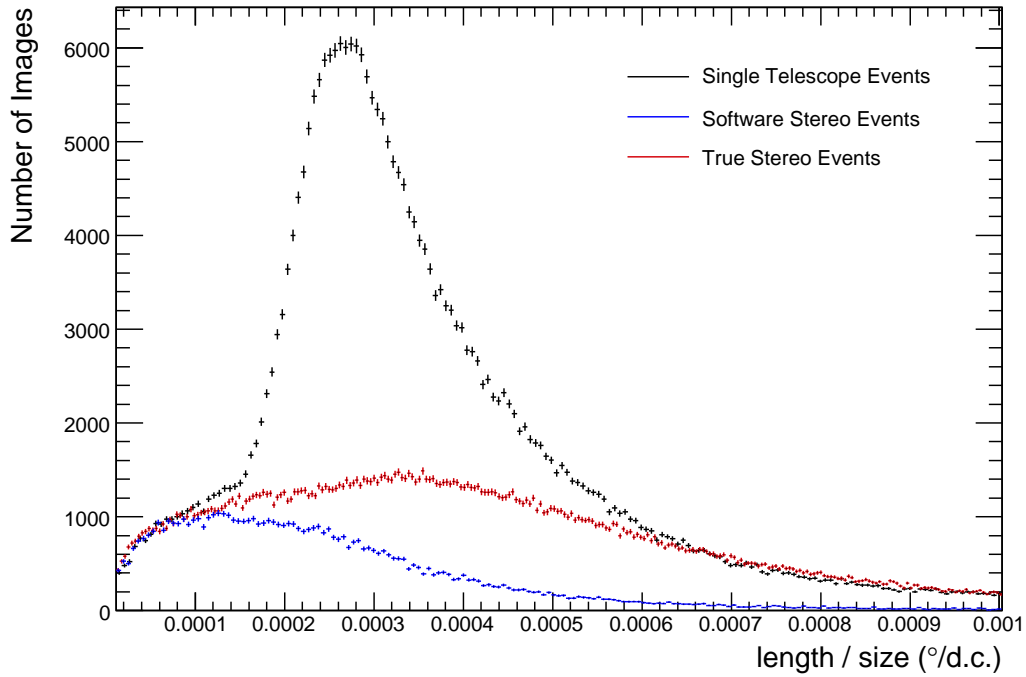


Figure 7.11: *The length/size distributions for parameterised data before cuts. The black points are recorded by T1 operating as a single telescope. The blue points are data recorded by T1 with a coincident event in T2 (software stereo) and the red points are true stereo data from T1 and T2.*

#### 7.8.4 Local Muons

As noted in Section 7.8.2 a *length/size* cut is required to remove local muons from the data when observing with a single telescope. The images formed by local muons have a characteristic *length* to *size* ratio similar to the small images formed by low energy  $\gamma$ -rays. Thus by implementing a *length/size* cut, not only muons, but also low energy  $\gamma$ -rays are removed from the data thereby increasing the detector energy threshold and lowering the sensitivity. However, local muons typically only illuminate a single telescope and a *length/size* cut is no longer required when multiple telescopes are available, even when operating with a software implemented array trigger.

The *length/size* distribution for monoscopic observations of the Crab Nebula with T1 before selection cuts is shown in black in Figure 7.11. A cut above 0.0002 is required to remove the peak due to the local muons. The blue data points indicate the *length/size*

distribution for T1 events with a corresponding image in T2 (software stereo) whilst the distribution for true stereo observations is shown in red. The distributions have been normalised to the area at the left associated with  $\gamma$ -rays. The peak due to local muons is almost completely removed from the stereo data stream when operating with either a soft or hard array trigger, although the shape of the *length/size* distribution for the soft stereoscopic data may indicate a loss of  $\gamma$ -rays due to the large coincidence window or a trigger bias between telescopes T1 and T2.

## 7.9 Background Estimation and Signal Extraction

To assess the presence of a signal in an observed region on the sky, the expected background in that region must be estimated. The method of background estimation depends on the observing mode. Here the Pairs and Wobble modes are considered. Both rely upon background estimation from observing a dark region of the sky close to the candidate source. A comparison of most of the available background estimation methods can be found in [28]. As noted in Section 2.3.6 the number of excess  $\gamma$ -ray events is given by:  $N_\gamma = N_{on} - \kappa N_{off}$ , where  $N_{on}$  and  $N_{off}$  are the number of counts in the source and background regions respectively and  $\kappa$  is a normalisation factor. In general  $\kappa$  depends on the acceptance of  $\gamma$ -ray like showers,  $\eta_\gamma$ , in each region. This in turn depends on the position in the camera, the size of the region, the zenith angle of observation and the exposure time. Once the background is estimated and subtracted from the *on* source data, the statistical significance of the extracted signal and the  $\gamma$ -ray detection rate are determined.

### 7.9.1 Single Telescope Observations

Data collected with the VERITAS T1 telescope was taken in Pairs mode as outlined in Section 7.3. When observing in Pairs mode a candidate source is observed at the centre of the FoV for a time  $T_{on}$ . This is the *on* region and after calibration, cleaning and parameterisation and  $\gamma$ -ray selection, results in  $N_{on}$ . The telescope is then repositioned 30 sidereal minutes in right ascension and observed for a time  $T_{off}$ . This is the *off* region and is passed through the same analysis procedure as the *on* run. In Pairs mode

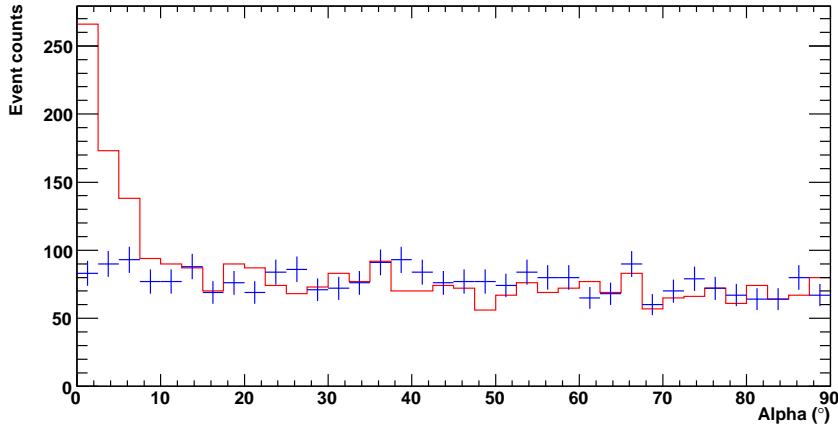


Figure 7.12: *Single telescope  $\alpha$  distribution resulting from analysis with Event Display (Red: on-source, Blue: off-source).*

the *off* region is taken at the same zenith angle as the *on* region to ensure an equivalent telescope response. Thus  $\kappa$  is given simply by the ratio of  $T_{on}$  to  $T_{off}$ . Here both source and background are observed for 28 minutes.

As described in Section 7.8.2 images due to  $\gamma$ -rays will be oriented with their major axes pointing back to the position of the source at the centre of the camera. When observing with a single telescope the image parameter  $\alpha$ , describing the orientation of the image in the camera, can therefore be used to isolate  $\gamma$ -ray candidates. Figure 7.12 shows the distribution of  $\alpha$  for parameterised images in the *on* (red) and *off* (blue) runs after the quality and selection cuts described in Sections 7.8.2 and 7.8.3 respectively as analysed using EventDisplay<sup>1</sup>.

In this simple, one-dimensional, analysis the source is assumed to be point like and located at the centre of the FoV. Images with a small value of  $\alpha$  are considered to be consistent with having originated from the source location whilst those with a large value of  $\alpha$  are not. The excess in *on* source counts observed in Figure 7.12 at small  $\alpha$  angles indicates the presence of a point source of  $\gamma$ -rays, whilst at larger angles the flat distribution is indicative of the isotropic CR background. The similarity between the *on* and *off* source data at large values of  $\alpha$  suggests that the *off* field provides an adequate estimate of the background in the source region. A cut in  $\alpha$  of  $7^\circ$  is applied to

<sup>1</sup>The  $\alpha$  distribution resulting from VEGAS is found to be similar and, as will be shown, yields comparable results.

both the *on* and *off* distributions to isolate events attributed to the source and estimate the background in the source region. The statistical reliability of the excess number of events,  $N_\gamma$ , in the *on* source data over the *off* source data in this region is then assessed using Equation 17 in Li & Ma [113]:

$$S = \sqrt{2} \left( N_{on} \ln \left[ \frac{1 + \kappa}{\kappa} \left( \frac{N_{on}}{N_{on} + N_{off}} \right) \right] + N_{off} \ln \left[ (1 + \kappa) \left( \frac{N_{off}}{N_{on} + N_{off}} \right) \right] \right)^{\frac{1}{2}}. \quad (7.1)$$

Where the significance of a detection is given in units of standard deviation, and it is assumed that the fluctuations in background are Gaussian distributed (proved true in Section 7.9.2). The significance of the single telescope observations of the Crab Nebula using this 1D method is found to be  $11.1 \sigma$  ( $8.1 \sigma/\sqrt{hr}$ ) using VEGAS and  $11.7 \sigma$  ( $8.5 \sigma/\sqrt{hr}$ ) using Eventdisplay. The  $\gamma$ -ray detection rate was determined to be  $2.76 \pm 0.25 \gamma/min$  and  $3.16 \pm 0.27 \gamma/min$  respectively. These results are in reasonable agreement with each other and with the previously published result of  $\sim 10 \sigma/\sqrt{hr}$  [91], bearing in mind the limited size of the data set and the lack of cut optimisation in this work.

A 2D analysis may also be applied to single telescope observations. The  $\gamma$ -ray source location is assumed to lie along the shower axis at an angular distance *disp* from the image centroid. Where *disp* must be inferred from the shape of the single observed image following [112] and detailed in, amongst others, [58]. A sky map is produced for both the *on* and *off* fields by constructing a 2D histogram of the reconstructed arrival direction with respect to the centre of the camera. Errors in reconstructing both the image axis and *disp* are accounted for by convolving with a Gaussian smoothing function with a standard deviation given by the telescope PSF. Two possible arrival directions are obtained for every event, each of which is on the major axis of the shower image, separated from the centroid by the calculated parameter, *disp*. In creating a 2D map of the detected events, the origin of each event is assigned to both possible directions in the hope that one will have an excess as the event origins are superimposed. The significance in each bin is then assessed using Equation 7.1 resulting in a 2D significance map such as those shown in Figure 7.13 for the Crab Nebula as analysed by EventDisplay (left) and VEGAS (right). The peak in significance is located at the camera centre, verifying the pointing accuracy of the telescope. The maximum significance agrees well both between

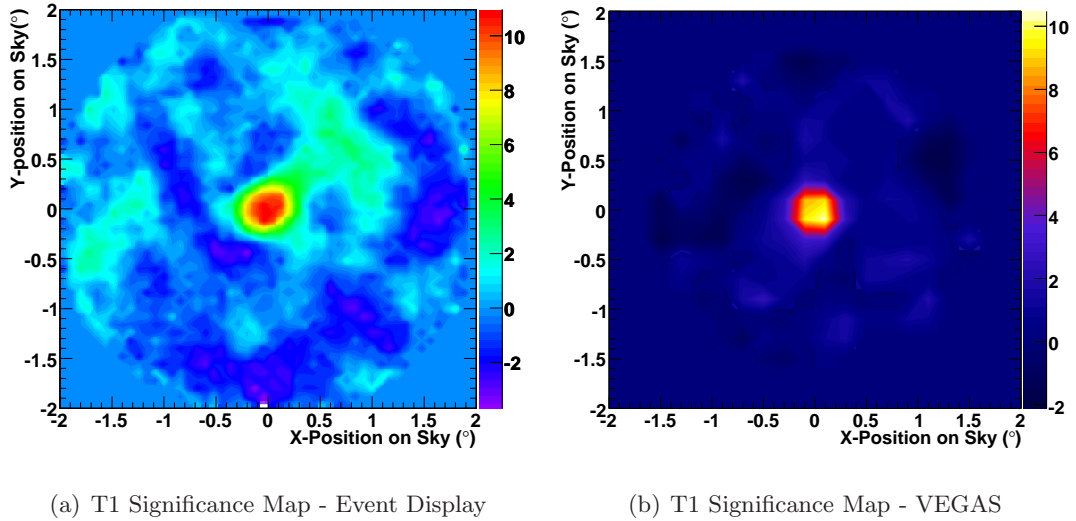


Figure 7.13: *Significance maps obtained from a 2D analysis of the same single telescope data runs in Pairs mode (112 min on-source) taken on the Crab Nebula.*

analysis packages and with the 1D,  $\alpha$ , analysis. Note that for a single telescope the width of the peak in significance, representing the angular resolution (since the Crab Nebula is a point source), is dominated by the accuracy of the directional reconstruction rather than the PSF of the telescope.

## 7.9.2 Software Stereo Observations

The observations of the Crab Nebula taken with T1 in Pairs mode and analysed in the previous section were simultaneously taken with T2. A set of software stereo runs was created by GPS time-matching events from both telescopes. Events seen by both telescopes within  $10 \mu\text{s}$  were retained whilst all others were removed. The relatively large coincidence window was chosen to account for inaccuracy between the GPS timing systems of the two telescopes and the geometry of the EAS.

The software-stereo *on/off* Pairs may be analysed in a similar way to true stereo Pairs using EventDisplay. The direction of the primary particle is determined by the intersection point of the major axes of the images of the coincident events when overlaid in camera plane as shown in Figure 7.9(a). The parameter  $\theta$  represents the angular difference between this reconstructed shower position and the true source position as shown in Figure 7.7. In Pairs mode the true source position is simply the centre of the

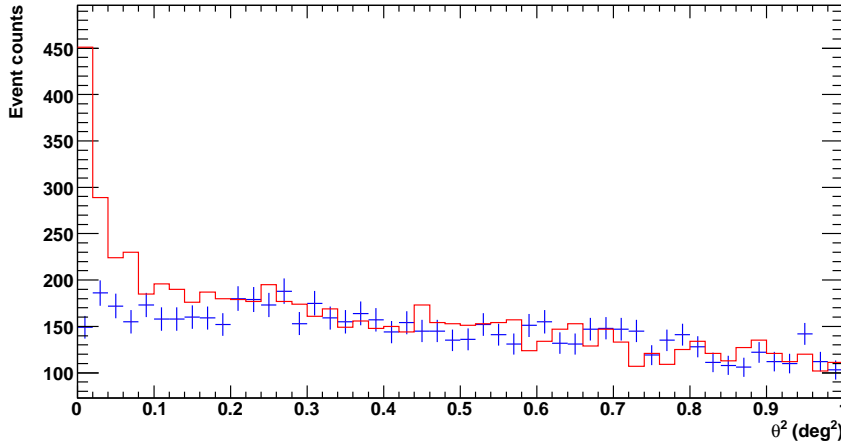
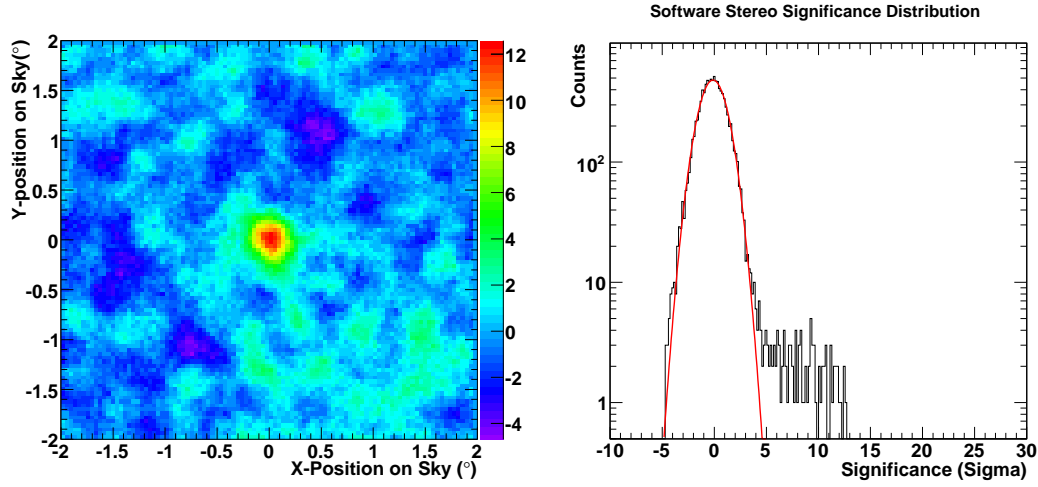


Figure 7.14: *Software Stereo  $\theta^2$  distribution (Red: on-source, Blue: off-source) obtained using a 1D analysis following observations in Pairs mode.*

camera. Events with a small  $\theta$ , originating close to the camera centre, are attributed to the source whereas those at large  $\theta$  are due to the isotropic CR background. To ensure a constant solid angle on the sky per bin this distribution is typically expressed in terms of  $\theta^2$  as shown in Figure 7.14. As with  $\alpha$  in the case of single telescope analysis a strong excess is seen near zero in the *on* source data whilst the *off* source data is isotropic. A cut of  $0.04 \text{ deg}^2$  in  $\theta^2$  is applied to both the *on* and *off* data leaving 740 *on* and 342 *off* events in the region directly surrounding the source corresponding to a rate of  $3.59 \pm 0.29 \text{ } \gamma/\text{min}$  and statistical significance of  $12.6 \sigma$ , or  $9.2 \sigma/\sqrt{hr}$  as calculated by Equation 7.1. The width of the excess distribution in  $\theta^2$  can be used to study the extension of a source when compared to the PSF of the detector. In the case of a point source the width of the distribution indicates the angular resolution of the detector, dominated by the PSF of the telescopes for stereo data, and found here to be  $\sim 0.22^\circ$  (68% of the width of the  $\alpha$  distribution assuming a Gaussian fit).

Given the arrival directions of every event in both the *on* and *off* fields the excess and corresponding statistical significance may be calculated for every point on the sky in a 2D analysis resulting in the map shown in Figure 7.15(a), again smoothed with a 2D Gaussian. The maximum significance is  $13.02 \sigma$  and it is clear that no other sources of VHE  $\gamma$ -rays are present in the FoV other than the Crab Nebula. The distribution of the significances in the 2D map is shown in Figure 7.15(b), where the presence of



(a) Software Stereo Significance Map

(b) Software Stereo Significance Distribution

Figure 7.15: *Significance map and corresponding distribution obtained from a 2D analysis of two telescope data taken in Pairs mode and operating with a software array trigger (112 min on-source).*

the Crab Nebula is indicated by the excess above  $5\sigma$ . Fluctuations in the background are Gaussian and centred around zero, confirming the assumption made when using Equation 7.1 and verified using the fitted curve between  $-5$  and  $5\sigma$  shown in red.

There is an improvement in sensitivity over that obtained with a single telescope of around 14% (for single telescope analysis with Event Display). The improvement is due to the lack of local muons in the data negating the need for a *length/size* cut and the improved angular resolution resulting in more events being reconstructed close to the true source position. There are several possible reasons why the sensitivity is not better:

- The lack of optimisation of cuts on this stereo data set may have a larger effect than on the single telescope data from the same set.
- In order to keep the dead time at a manageable level the individual telescope trigger thresholds are the same as in the single telescope analysis (70 mV). Whilst each telescope is individually triggering at  $\sim 250$  Hz, the effective trigger rate after GPS time matching is a mere  $\sim 25$  Hz. This implies a high energy threshold and a small collection area.
- The additional cut on the relative orientation of the images in camera to reject

parallel events is required in two-telescope stereo analysis and further reduces the effective area.

- The pointing of one or both of the telescopes may be slightly off. As the angular resolution increases with stereo reconstruction the detector response becomes more sensitive to errors in the pointing. An error in the pointing of T1 may not have been noticed in the single telescope analysis, where the angular resolution is dominated by the reconstruction algorithm.
- T2 was in the early engineering stages when this data was taken, and there were known problems with the alignment of the mirrors. Thus the response of T2 may be significantly lower than that of T1.

### 7.9.3 True Stereo Observations - 2 Telescopes

Observations of the Crab Nebula taken with T1 and T2 operating in hardware stereo were taken with both telescopes in a relative state of maturity, having operated stably and consistently over a period of months. The array trigger required both telescopes to form a local trigger within a coincidence window of 100 ns. The resulting data runs were analysed with the fully working official array analysis package, VEGAS, and show great improvements over both single telescope and software stereo observations.

In true stereoscopic observations, where accurate shower core and shower source location lead to a more accurate background estimation, Wobble observations can be used, in which the target is offset from the centre of the FoV by  $\pm 0.3^\circ$  or  $\pm 0.5^\circ$  in declination or right ascension. Wobble mode increases the detector duty cycle, but the source is not at the centre of the FoV and the sensitivity is consequently reduced since the acceptance,  $\eta_\gamma$ , drops away when moving outwards from the camera centre. For stereoscopic operations the trade-off is acceptable (acceptance decreases by  $\sim 10\%$  whilst exposure increases by 100%) . For the observations of the Crab Nebula taken in Wobble mode in this work the background is estimated in two independent ways in a 1D and 2D manner.

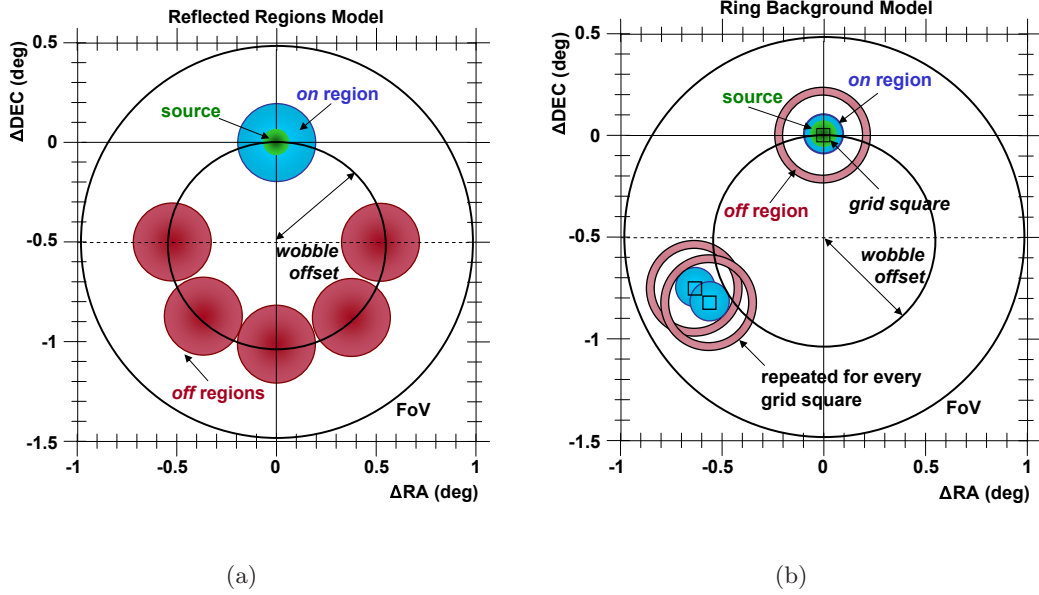


Figure 7.16: Schematic illustration of (a) the reflected region background model in which the background is estimated from multiple regions around the camera centre and (b) the Ring Background Model in which the signal in a given bin (grid square) is calculated from the on region whilst the background from the off region centred on the bin.

### 7.9.3.1 1D - The Reflected Region Model

In the reflected region background model the locations of the background fields are selected at equivalent radii to the Wobble offset from the centre of the camera as shown in Figure 7.16(a). Each background region is of an equivalent size to the *on* region and, as the acceptance is radially symmetric and the exposure times of the *on* and *off* regions are equivalent,  $\kappa$  only depends on the number of reflected regions chosen,  $N$ , and is given by  $\kappa = 1/N$ . For a Wobble offset of  $0.3^\circ$  used here, four background regions are taken resulting in  $\kappa = 0.25$ . A 1D analysis may then be performed by simply constructing an  $\theta^2$  distribution for the *on* and *off* source regions as shown in Figure 7.17.

As was the case with the software stereo observations a cut of  $0.04 \text{ deg}^2$  is placed in  $\theta^2$  reducing the data to 595 counts *on* source and 481 *off* source. The significance of the excess is calculated using Equation 7.1. A rate of  $4.23 \pm 0.17 \text{ } \gamma/\text{min}$  and a significance of  $25.5 \sigma$ , or  $18.7 \sigma/\sqrt{hr}$  is found. The distribution is significantly narrower than for the software stereo analysis and yields an angular resolution of  $\sim 0.14^\circ$  (68% of the width

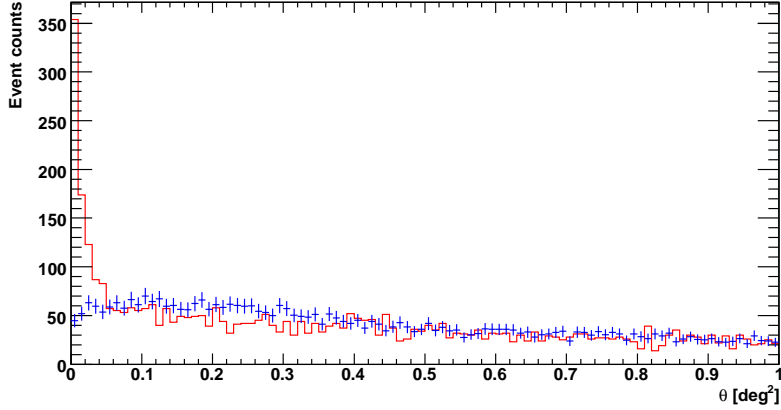


Figure 7.17:  $\theta^2$  distribution for stereo observations in Wobble mode with T1 and T2 connected with a hardware array trigger and analysed using the reflected region background estimation model (Red: on-source, Blue: off-source).

of the  $\theta^2$  distribution assuming a Gaussian fit). A vast difference in detector sensitivity when moving from a software to a hardware array trigger is evident. The increase is due to several factors:

- The reduction in data rate afforded by the hardware array trigger allows the individual telescope trigger thresholds to be reduced from 70 mV to 50 mV without increasing the system dead time. The system trigger rate is then  $\sim 250$  Hz (for the runs used here), ten times that obtained from a soft stereo approach. It follows directly that decreasing the trigger threshold also reduces the energy threshold of the detector. Since the spectrum of VHE  $\gamma$ -rays from the Crab Nebula is a decreasing power law in energy, the number of additional  $\gamma$ -rays observed then increases dramatically as lower energies become accessible.
- The improvement in angular resolution over that obtained with software stereo analysis indicates the telescopes have improved in pointing and focus between the respective data taking periods. This increased angular resolution results in more events from the Crab Nebula surviving the  $\theta^2$  cut.

Since the *on* and *off* source fields are in the same FoV, it is not trivial to calculate the excess in events at every point in the FoV and move from a 1D analysis to a 2D sky

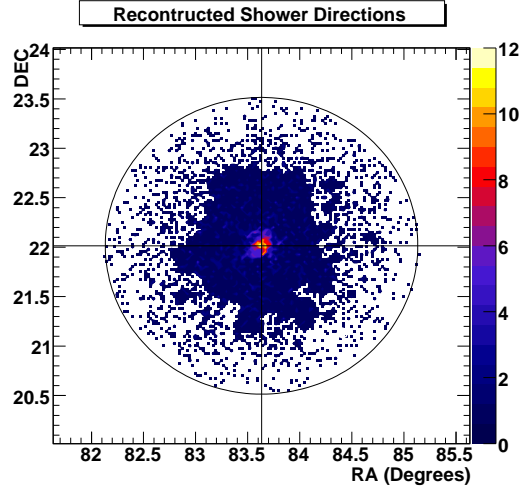


Figure 7.18: *Two-dimensional map of the reconstructed arrival directions of all events after  $\gamma$ -ray selection cuts for observations of the Crab Nebula with T1 and T2 operating with a hardware implemented array trigger.*

map as it was for stereo Pairs observations. In this work the ring background model is used to do so.

### 7.9.3.2 Ring Background Model

The first step in a 2D analysis is to construct a sky map of the arrival directions of every event in the FoV regardless of whether they are source or background as shown in Figure 7.18 where the data is placed in  $0.025^\circ \times 0.025^\circ$  bins. The data set consists of four Wobble runs offset in complementary directions such that, when superimposed, the source position is placed at the centre of the FoV.

In the ring background model the signal in each bin in the FoV is given by the number of counts within a circle of radius  $0.2^\circ$ . The background is estimated from an annulus placed around this circular signal bin of inner radius  $0.5^\circ$  and outer radius  $0.8^\circ$ . An exclusion region is placed around the true source position from which no background is taken. The process is repeated for every bin in the FoV leading to the signal and background maps shown in Figure 7.19.

The RBM is not straightforward as the acceptance across the annulus, or ring, is not constant and therefore neither is  $\kappa$ . An acceptance function must be derived and used

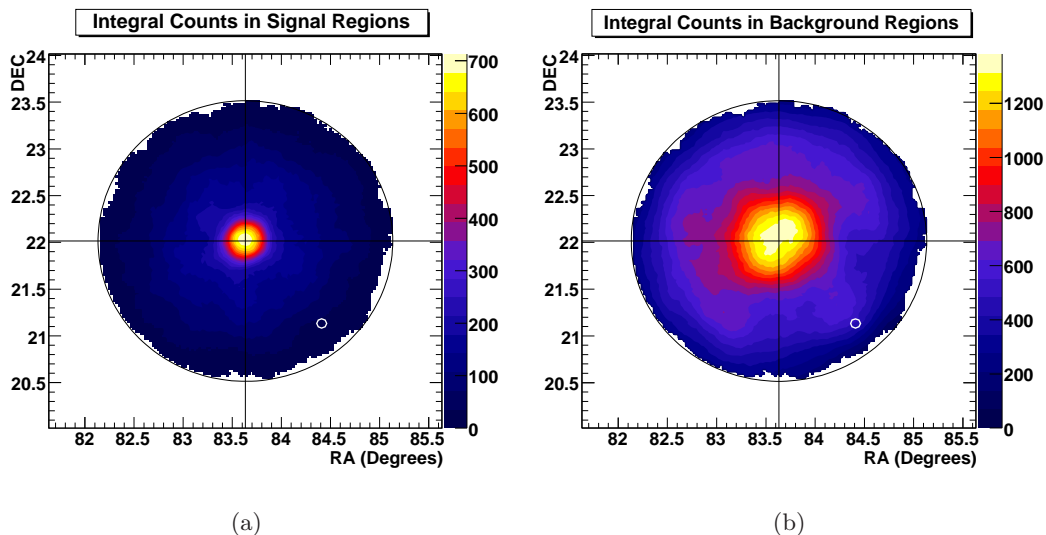


Figure 7.19: *Integrated signal (a) and background (b) maps resulting from the RBM applied to the map of reconstructed shower directions shown in Figure 7.18 for two telescopes connected in hardware stereo.*

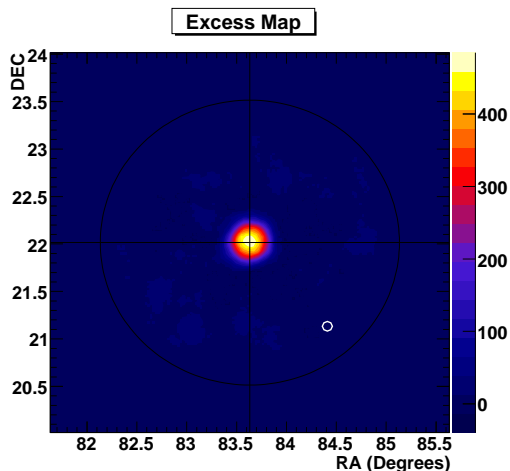
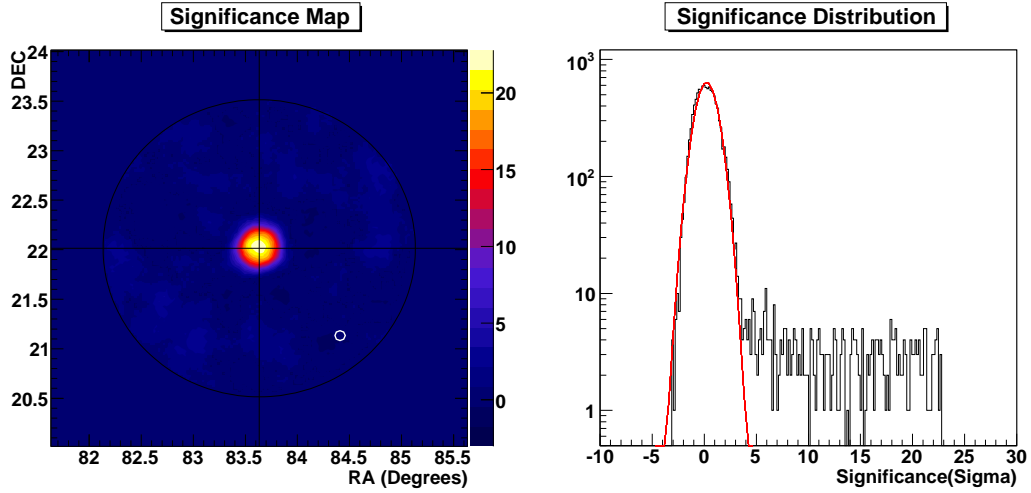


Figure 7.20: *Excess map obtained from difference between the determined signal and background in every grid square used in the RBM for two telescopes connected in hardware stereo.*

to calculate a 2D  $\kappa$  map as described in [41]. This may then be used to scale the background allowing the excess counts in each bin to be determined and resulting in the 2D map shown in Figure 7.20. The significance map and distribution are then found as before and shown in Figure 7.21. The RBM yields 771 *on* counts and 1315 *off* counts in the region below  $\theta^2 = 0.04 \text{ deg}^2$  corresponding to a rate of  $4.32 \pm 0.19 \gamma/\text{min}$  and 22.8



(a) Hardware Stereo Significance Map

(b) Hardware Stereo Significance Distribution

Figure 7.21: *Significance map and corresponding distribution obtained from a 2D analysis of two telescope data taken in Wobble mode and operating with a hardware array trigger (112 min Wobble).*

$\sigma$  ( $16.7 \sigma/\sqrt{hr}$ ). This result is consistent with the simple 1D reflected region model, which does not rely on the complicated extraction of the acceptance function.

#### 7.9.4 True Stereo Observations - 3 Telescopes

The reflected region and ring background models were applied to data taken with the first three VERITAS telescopes connected via the DATs to the hardware array trigger. The array required at least two telescopes of the available three to trigger within a 100 ns coincidence window. Observations were again taken in Wobble mode, but with an offset of  $0.5^\circ$ . Additionally the run duration was reduced from 28 min (112 min total exposure for 4 runs) to 20 min (80 min total exposure for 4 runs). The resulting  $\theta^2$  plot is shown in Figure 7.22 and yields a rate of  $7.50 \pm 0.22 \gamma/\text{min}$ . A total of 703 *on* counts and 812 *off* counts corresponding to a significance of  $34.5 \sigma$ , or  $29.9 \sigma/\sqrt{hr}$  is found. The distribution is narrower still than for the two telescope stereo analysis and leads to an angular resolution of  $\sim 0.1^\circ$  (68% of the width of the  $\theta^2$  distribution assuming a Gaussian fit). The RBM retains 821 *on* counts and 1061 *off* counts in the region below  $\theta^2 = 0.04 \text{ deg}^2$  corresponding to a rate of  $7.96 \pm 0.26 \gamma/\text{min}$  and  $30.2 \sigma$  ( $26.1 \sigma/\sqrt{hr}$ ).

Whilst no cut optimisation is done here, it is clear that this improved angular resolution would facilitate a reduction in the  $\theta^2$  cut to below  $0.04 \text{ deg}^2$ , resulting in an increase in the sensitivity. The significance map and distribution are shown in Figure 7.23. Furthermore, with three telescopes it is no longer necessary to remove parallel images as it was with two telescopes and the effective area increases in a corresponding manner, increasing the sensitivity of the array.

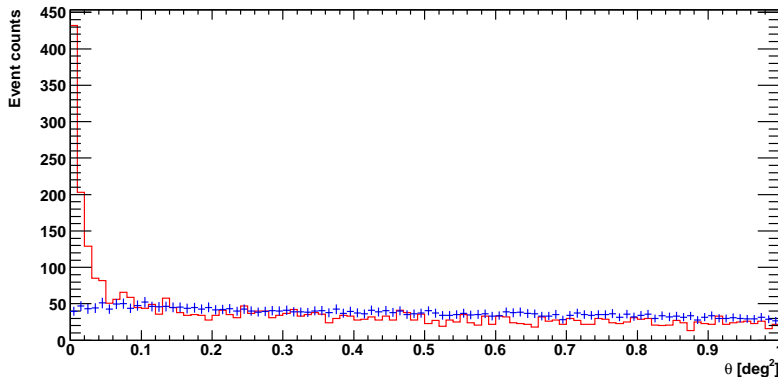


Figure 7.22:  $\theta^2$  distribution for three-telescope observations in Wobble mode with T1, T2 and T3 connected with a hardware array trigger (requiring any 2/3 telescopes to trigger) and analysed using the reflected region background estimation model (Red: on-source, Blue: off-source).

## 7.10 Summary and Conclusions

The single telescope, software and hardware stereo results are summarised in Table 7.5. There is a clear gain in the sensitivity associated with operating multiple telescopes with a hardware array trigger made possible, in part, by the successful operation of the DAT modules developed in Chapter 7. The energy threshold of the detector is decreased and the angular resolution improved, making it possible to probe more distant sources and map the morphology of extended sources at ever decreasing energies to overlap with space-based HE  $\gamma$ -ray detectors such as GLAST.

The energy threshold of the detector before cuts is directly related to the CFD trigger threshold of the individual telescopes. In order to maintain a manageable dead time the CFD threshold of a single telescope, or multiple telescopes operating with a software

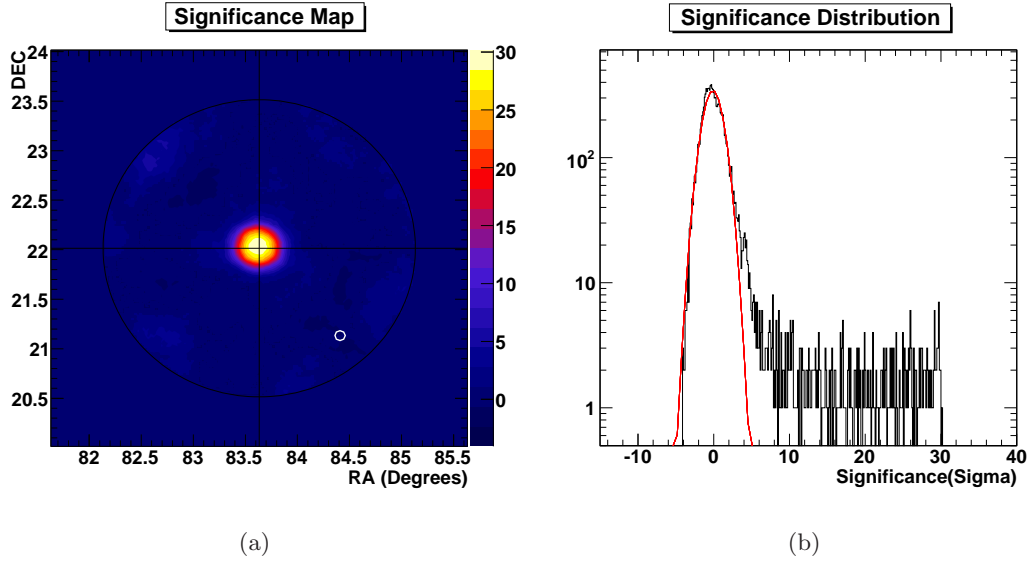


Figure 7.23: *Significance map and corresponding distribution obtained from a 2D analysis of three telescope data taken in Wobble mode and operating with a hardware array trigger (80 min Wobble).*

Config.	Analysis	Obs. Mode	T (min)	On	Off	Significance		Rate $\gamma/min$
						$\sigma$	$\sigma/\sqrt{hr}$	
Single	ED	On/Off	112	556	247	11.047	8.09	$2.76\pm 0.25$
Single	V	On/Off	112	649	354	11.669	8.54	$3.16\pm 0.27$
Soft. (2)	ED	On/Off	112	740	342	12.587	9.21	$3.59\pm 0.29$
Hard. (2)	V RR	Wobble ( $0.3^\circ$ )	112	595	481	25.503	18.67	$4.23\pm 0.17$
Hard. (2)	V RBM	Wobble ( $0.3^\circ$ )	112	771	1315	22.781	16.67	$4.32\pm 0.19$
Hard. (3)	V RR	Wobble ( $0.5^\circ$ )	80	703	812	34.470	29.85	$7.50\pm 0.22$
Hard. (3)	V RBM	Wobble ( $0.5^\circ$ )	80	821	1061	30.155	26.11	$7.96\pm 0.26$

Table 7.5: *Analysis results for all Crab Nebula observations in this work*

array trigger, is set to 70 mV. With a hardware array trigger the threshold can be reduced to 50 mV without increasing the system dead time as illustrated in Figure 7.3. The dead time is increased further when operating with a software array trigger due to the large GPS coincidence window required ( $10 \mu s$  as opposed to 100 ns with a

hardware array trigger). The reduction in energy threshold is a key aim for current and next generation IACTs. Whilst the Whipple 10 m telescope reached  $\sim 350$  GeV, the current generation detectors operating in stereo extend the range to 100 GeV and even below. An increasing population of AGN appear on the  $\gamma$ -ray horizon as the energy threshold of IACTs is reduced and larger redshifts are probed. By studying the spectra of these extragalactic objects over a larger range of energies and redshifts the exact nature of the extragalactic background light may be determined.

Lowering the energy threshold by reducing the CFD threshold also rapidly increases the number of  $\gamma$ -rays detected from the source. The number of events due to the CR background increases even more rapidly, but can be well isolated due to the improved angular resolution associated with multiple telescopes. This is an advantage over the alternative approach to lowering the energy threshold by using a larger single telescope (although larger reflectors are required to probe levels substantially lower than 100 GeV).

Local muons are almost completely removed when operating with either a software or hardware implemented array trigger. Removing local muons from the data negates the need for a *length/size* cut that also rejects  $\gamma$ -rays with a similar *length/size* to that of muons. Such events are typically of lower energy and removing the *length/size* cut further decreases the energy threshold of the detector.

The effective area of a single telescope to  $\gamma$ -rays is comparable to that of two telescopes operating with either a software or hardware array trigger. This is, in part, due to the stereo constraint rejecting coincident images formed at under  $10^\circ$  to each other that would otherwise be poorly reconstructed. This cut is not required for three telescopes, where parallel images in two telescopes are, in general, accompanied by a non-parallel image in the third. There is, therefore, a large increase in sensitivity when moving from a two telescope array to a three telescope array with the same trigger multiplicity requirement.

As the number of telescopes increases the angular resolution of the detector improves, more events are correctly isolated as originating from the source and the sensitivity increases. The improvement in sensitivity allows observations to be taken in Wobble mode, doubling the detector duty-cycle at the acceptable cost of using a less sensitive part of the camera. An increased angular resolution allows the morphology of extended

objects such as galactic SNR to be mapped, an important goal in identifying which regions of such objects are potential sites of CR acceleration. Better sensitivity improves the ability of IACTs to perform surveys, where only a limited exposure on each sky region is attainable, such as that performed on the inner part of the galactic plane by H.E.S.S. which yielded numerous previously undetected sources of VHE  $\gamma$ -rays [14]. Increased sensitivity also allows the investigation of highly-variable AGN on time scales of just a few minutes.

Proposed designs for future IACTs such as CTA all involve arrays of telescopes. The question of whether to use a hardware array trigger becomes non-trivial in such cases where 30-100 telescopes are contemplated. Expensive single channel communication systems incurring dead time, such as those available commercially, or as used in H.E.S.S., may be un-scalable to larger arrays. The accuracy of GPS time stamping and the read out capacity of the DAQ system would need to be improved substantially if a software trigger were instead chosen. The DAT modules are a potentially cost effective solution to enable a hardware implemented array trigger in such future detectors.



## Chapter 8

# Conclusions and Outlook

---

As motivated in Chapter 1 new technology is required for the next generation of IACTs and UNDs. In this thesis the transmission of fast analogue pulses over optical fibre, the implementation of high-speed trigger logic within FPGAs, and the parallel distribution of asynchronous optical signals are developed in this context.

VHE  $\gamma$ -ray astronomy has progressed rapidly over the past decade, driven largely by the work of the H.E.S.S., MAGIC and VERITAS collaborations. These third generation IACTs are advancing our understanding of the origin of galactic CRs and the nature of their progenitors. However, the technique has not yet reached the fundamental limits of its sensitivity and at least two large scale IACT arrays, AGIS and CTA, are planned for the coming decade. Conversely UNDs are in their infancy, and although the detection of a single neutrino signal from a known source of VHE  $\gamma$ -rays would confirm beyond reasonable doubt the existence of hadronic acceleration, as expected in objects such as the SNR RXJ17-13, this is, at the moment, a distant dream. The "*casual*" astroparticle physicist should, however, not be disheartened by this. As Figure 8.1 shows, the progress made in  $\gamma$ -ray and VHE  $\gamma$ -ray astronomy echoes that made in X-rays, and one might therefore hope that  $\nu$  astronomy may do the same, perhaps starting from the point tentatively placed at 2015. It is highly likely that the number of  $\gamma$ -ray sources will increase in the coming two years with the advent of GLAST, and that the number of

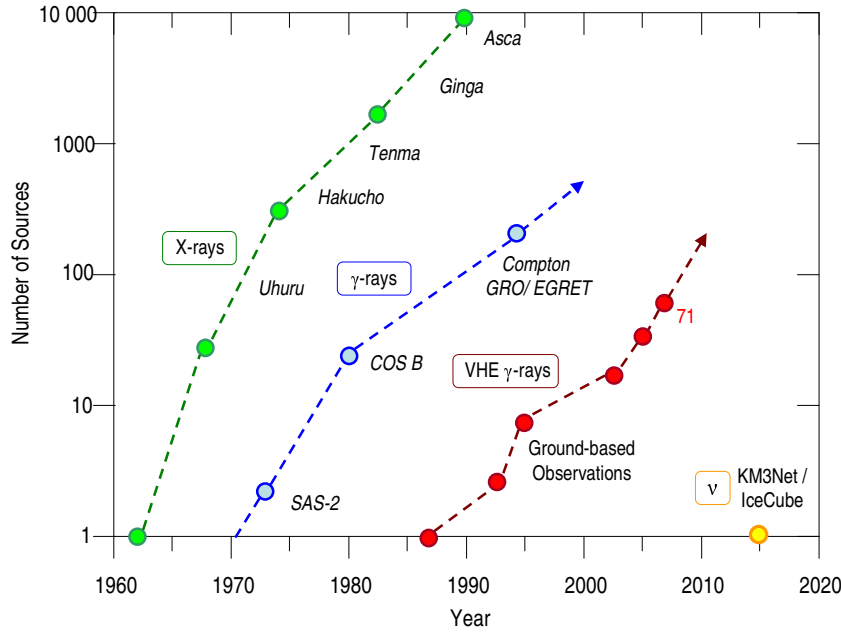


Figure 8.1: *Kifune Plot: The total number of sources detected as a function of time for X-ray,  $\gamma$ -ray and VHE  $\gamma$ -ray astronomy. A point has been added at 2015 to indicate when UNDs will reach the required sensitivity to begin detecting expected astrophysical sources of neutrinos.*

VHE  $\gamma$ -ray sources will increase as VERITAS begins to produce results and then as H.E.S.S. Phase II and MAGIC II come on-line.

For the next generations of IACTs and UNDs to reach maximum performance at the lowest feasible cost whilst maintaining reliability, new technology is required. Commercial components are rarely suitable for use in areas such as the detector read out, triggering, and the distribution of clock and trigger signals, due to the inflated cost and physical demands of the working environments.

In Chapter 4 the use of VCSELs for the transmission of fast analogue signals over optical fibre was explored as an alternative to the current VERITAS coaxial read out scheme. During the development of similar schemes for use in the Whipple 10-m telescope and the MAGIC telescope sporadic variations in the VCSEL light output attributed to laser mode-hopping were noted. The effect was minimised in the MAGIC system by rejecting the worst affected VCSELs in a batch prior to installation in the telescope. The ZL60052 VCSELs used in this thesis exhibited no mode-hopping. Therefore one need not budget

---

for VCSELs of this type to be routinely rejected when costing a new read out scheme. The prototype optical link developed in this work exhibits good linearity (to within 12%) over a large dynamic range of 61 dB with an acceptable amount of pulse-shape distortion (the FWHM is distorted by  $\ll 1$  ns and  $T_r$  is distorted by 1.4 ns) and harmonic distortion ( $< 30$  dB below the fundamental) across the entire bandwidth of  $\sim 250$  MHz, which is itself limited by the response of the receiver. The transmitter alone exhibits a significantly larger bandwidth of  $\sim 470$  MHz. Changes in link gain due to variations in the temperature of the transmitter are successfully reduced to within 6% of the mean across the entire operating range of the VERITAS camera, from  $0^\circ\text{C}$  to  $40^\circ\text{C}$ , by automatically setting the bias current according to a pre-programmed lookup table contained in a chip on the optical transmitter.

The PMT pulses of FWHM  $< 5$  ns,  $T_r \sim 2$  ns are distorted by the coaxial cable and arrive at the electronics trailer of a VERITAS telescope with FWHM  $< 11$  ns,  $T_r \sim 4$  ns. Pulses are read out across a 48 ns window, corresponding to 24 FADC samples. Implementing the analogue optical read out scheme described here would allow the FADC integration window to be shortened to at least 40 ns. In turn less noise would be integrated into the signal and the energy threshold of the detector would drop in accordance with Eq. 2.8. The amount of data to read out would also drop and the dead time of the telescope would be reduced correspondingly. Since decreasing the dead time is equivalent to increasing the observation time, the energy threshold and sensitivity of the array would be further improved.

Further work is required to improve the bandwidth of the optical link to the desired level of at least 500 MHz [40]. Alternative methods of temperature compensation should also be explored and the system extended and tested on an existing IACT array such as VERITAS in parallel with the current read out scheme.

There are still difficulties in working with VCSELs, however, the results presented in Chapter 4 lend credence to the transmission over analogue optical link as an equally viable solution for the read out of next generation IACT arrays and UNDs to the alternative of digitising pulses in the camera, or under the sea. The gain-to-cost ratio of replacing the current coaxial scheme within VERITAS is not high enough to justify a camera retrofit. However, the VERITAS camera boxes have been designed to allow an

---

expansion in camera size and it would be feasible to implement an analogue fibre read out scheme for these outer pixels.

The use of high-speed triggering within IACTs is essential to efficiently reject fluctuations in background light whilst retaining images due to Cherenkov events. The VERITAS L2 trigger system requires the camera signals to be mapped into overlapping patches via the SS crate prior to examining each patch for adjacent CFD triggers in the PST modules. This cumbersome system requires two full crates of electronics and labour intensive wiring per telescope to individually map the signals within the SS crate. Individual lengths of wire must then be added to each channel to align the signals to within 2 ns. The performance of this simple solution is sufficient for VERITAS, and the individual delays are adjustable onsite by users without expert knowledge. However, such a system is not suitable for future IACTs where the number of pixels will increase four-fold or more. In Chapter 5 an alternative method of implementing a PST within FPGAs was examined. The new design aims to completely remove the CAMAC crate and bulky ribbon cabling from the front of the SS Crate by replacing the SS input and output cards with alternatives containing Xilinx Virtex-4 FPGAs. The prototype work completed for this thesis indicates that an FPGA solution would reduce the coincidence resolving time to  $\sim 4$  ns from  $\sim 10$  ns. Furthermore the design is robust up to input rates of 150 MHz, whereas the current system is not guaranteed to function beyond  $\sim 15$  MHz. The improvements are mainly due to recent advances in FPGA design which allow one to delay input signals with a resolution of 78 ps and the lack of dead time associated with the combinatorial method chosen to implement the PST logic.

Due simply to time constraints the high-speed FPGA trigger work in this thesis remains in the developmental stage and there are several key aspects that require future work. The SSOCX must be fully tested with larger numbers of inputs, and an in-situ test must be performed with VERITAS. If successful the possibility of further trigger functionality should be explored, such as examining 5-fold coincidences at lower thresholds, and the power consumption of the system assessed before a full prototype L2 trigger is constructed.

The gains in replacing the current VERITAS PST with such an FPGA based system are minimal. However, any expansion of the VERITAS array to include more telescopes

---

would require more SS crates and PST CAMAC modules. In this case the move to an FPGA based PST would be feasible and timely. For a future system such as CTA an FPGA based pattern trigger system is expected and work has been done within the MAGIC and H.E.S.S. collaborations on similar solutions to that examined here.

The incredible flexibility offered by FPGAs means the system can, in principle, be expanded past a simple pattern trigger. For example the trigger may prove useful within VERITAS for the novel technique of measurement of so-called "direct Cherenkov" light from heavy-hadronic CRs.

The advantages of transporting signals over optical fibre observed in Chapter 4 were again exploited in Chapter 6 in the development of the DAT modules. The conversion of electrical signals to optical signals is achieved using the PAROLI modules, which impose a DC% condition on the input data met by XOR encoding and decoding signals within Xilinx Spartan 3 FPGAs. Four pairs of DAT-V2 and four pairs of DAT-V3 are currently used within VERITAS for the distribution of fast trigger signals, event numbers and housekeeping information. The versatility provided by implementing combinatorial operations within FPGAs has proven vital to the continued working of the DATs allowing channels to be remapped to accommodate on-going changes to the cabling system within the array.

The performance of the DAT modules exceeds the requirements of the current VERITAS trigger chain, allowing the FADC read out window to be minimised around the pulse to within a single sample (2 ns). Furthermore, by using a combinatorial encoding scheme the dead time associated with sequential design is avoided, helping to minimise the dead time of the trigger chain as a whole.

The development of the DAT has not been straightforward and work is on-going to produce a further iteration of the modules with a higher tolerance to changes in the propagation delay and DC% of the encoded signal and clock lines. Despite the limitations of the DAT modules they still offer significant benefits in performance, number of channels, physical size, and cost over commercial solutions. They also exceed the performance of the single channel system used by H.E.S.S., that relies on pulse-width encoding and consequently incurs a dead time.

The strength of the DAT modules lies in their ability to transmit signals over an ex-

---

tremely large range of pulse widths ( $>1$  s, down to  $\sim 5$  ns) and data rates ( $\sim$ bps to  $\sim 200$  Mbps). In addition signals with a DC% of  $\sim 50\%$  can be transmitted at  $\geq 1$  MHz to 1.25 GHz by disabling the encoding and decoding within the FPGAs. This specification makes the modules suitable not just for VERITAS, but also for future IACTs and UNDs. The DAT modules are also of interest to a unique application of IACTs for intensity interferometry . The signals from the central pixel of two IACT cameras are digitised locally at each telescope and then processed to assess the correlation of light from distant stars, requiring the accurate distribution of a high-speed clock to both telescopes from a central location. Alternatively the signals are digitised in a central location allowing a real-time FPGA-implemented correlator to be used. In this scenario the single channel analogue optical link could be used to transport the PMT signals from each telescope to the central location. The application of the technology developed in this thesis to intensity interferometry is described in [52].

The DAT modules enable the use of multiple telescopes connected with a hardware array trigger and therefore their utility is perhaps best judged by studying the performance and stability of the array trigger. In Chapter 7 observations of the Crab Nebula were used to assess the benefits of operating several telescopes in stereo. Observations with a single telescope were compared to those taken with two telescopes using both a software and a hardware implemented array trigger, before the first observations of the Crab Nebula with three VERITAS telescopes were presented.

The energy threshold of the detector is affected by the CFD threshold of the telescopes within the array. The CFD threshold can be lowered to 50 mV from 70 mV when operating with a hardware implemented array trigger without increasing the system dead time. Local muons are almost completely removed when operating with either a software or a hardware implemented array trigger, negating the need for a *length/size* cut that also rejects  $\gamma$ -rays with a similar *length/size* to muons and further decreasing the energy threshold of the detector. The effective area of a single telescope to  $\gamma$ -rays is comparable to that of two telescopes operating with either a software or a hardware array trigger, however there is a large increase in effective area, and correspondingly in sensitivity, when using three telescopes with a two-telescope array trigger multiplicity requirement. As the number of telescopes increases, the angular resolution of the detec-

---

tor improves, more events are correctly isolated as originating from the source and the sensitivity increases. The improvement in sensitivity allows observations to be taken in Wobble mode, doubling the detector duty-cycle at the acceptable cost of using a less sensitive part of the camera. An increased angular resolution will allow the morphology of extended objects such as galactic SNR to be mapped with VERITAS, an important goal in identifying which regions of such objects are potential sites of CR acceleration.

It is clear that over the next decade future generations of IACTs and UNDs will require new technology to meet the physical size, cost and performance targets suggested by extrapolation of the Kifune plot. The relatively accessible environment of VERITAS has been used in this work to successfully prototype new technology suitable for both IACTs and UNDs. It has also been found that such technology is of interest for intensity interferometry and direct Cherenkov detection.

The development of new technology is not entirely predictable. As VCSELs become more stable and FPGAs become faster, performance increases can be gained at a lower cost. Although the exact technology used within IACTs and UNDs in the coming years will almost certainly deviate from that developed here, it is reasonable to assume that VCSELs, fibre optics and FPGAs will play a significant role in CTA and KM3NeT. These state of the art detectors will push the boundaries of the now established field of ground-based VHE  $\gamma$ -ray astronomy and hopefully provide the first unambiguous signal of hadronic acceleration through the detection of astrophysical neutrinos.

---

# Appendices

---

## Appendix A

# Technical Details of the Optical Link Test Setup and Equipment

---

In this appendix the test setup used for the bias current scan test used in Section 4.5 and the equipment used in the performance testing of the prototype analogue optical link in Section 4.6 are described.

### A.1 The Bias Current Scan Test Setup

The equipment used in the bias current scan test is shown in Figure A.1. Input pulses with amplitude 940 mV and FWHM 2.6 ns are generated by a pulse generator at a rate of 40 kHz and attenuated to produce a 10 mV pulse with a slightly degraded FWHM of 2.7 ns. A signal splitter routes three copies of the signal to identical transmitters that each hold a single VCSEL. A small rubber washer is fitted to the VCSEL and the transmitter is attached to the top of the receiver as shown in the lower part of Figure A.1, thereby coupling the VCSEL directly to the photodiode. The output signals of the receiver boards are fed to a Tektronix 3054B, 4-channel, 4 GSa/s digital oscilloscope with a bandwidth of 500 MHz. An additional copy of the input pulse from the signal splitter is sent directly to channel 4 of the oscilloscope for constant monitoring. The

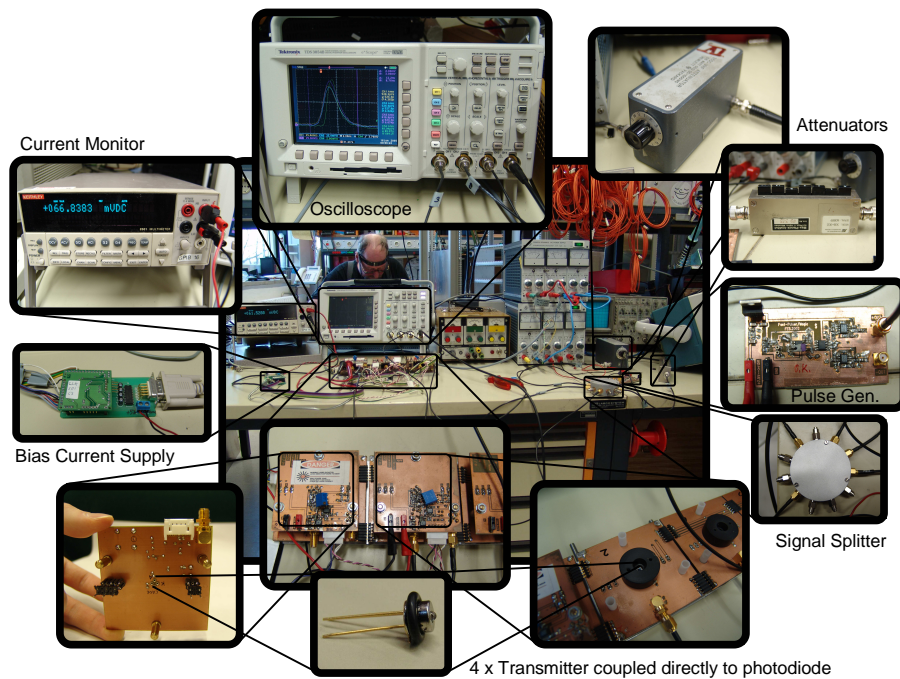


Figure A.1: *The bias current scan test setup.*

pulses are digitized at a rate of 1 GSa/s and the area under the pulses measured and relayed to a PC running Lab View over a GPIB interface. The bias current applied to the VCSELs is adjusted by a digital potentiometer that can be controlled by the serial port of the PC through a custom built microcontroller (courtesy of MPI Munich and visible to the left of Figure A.1). A Keithley picoammeter is used to monitor the bias current and is also controlled by the PC through a GPIB connection. The bias current scan test is then run automatically using Lab View on 3 VCSELs simultaneously. The measured areas and bias currents are stored together with a time stamp in ASCII format.

The performance of the test setup was established by feeding identical copies of the input pulse directly into the four oscilloscope channels. The RMS in the measured pulse area was seen to vary by up to 20% between channels. In order to reduce this dependence a pedestal measurement for each channel was taken before each bias current scan by attenuating the input pulse by 100 dB (such that it was of practically zero amplitude) and measuring the resulting area every 5 s for 10 minutes. The pedestal was then



Figure A.2: *The optical link test setup.*

subtracted from the measured pulse area. In this way the variations between the RMS of an input pulse, fed directly into the four oscilloscope channels, was reduced to  $\sim 5\%$ . The fluctuations in the measured area of the transmitted pulse were at least three times larger than this intrinsic noise and therefore the bias current scan test results are an accurate reflection of the VCSEL behaviour.

## A.2 Optical Link Test Setup and Equipment

The equipment used to evaluate the performance of the optical link is shown in Figure A.2. The single-channel transmitter is placed in the Design Environment Limited BS55-40 programmable environmental chamber with an accessible temperature range of  $-40^\circ$  to  $+200^\circ$  shown to the left of the picture. The transmitter is connected to the receiver by the 100 m reel of orange optical fibre. The output of the receiver is input to the Agilent Infiniium 54832D 1 GHz, 4 GSa/s Mixed-Signal Oscilloscope (MSO) shown in the centre of the picture. The PMT-like signal is produced by an Agilent 81110A 330 MHz Pulse-/Pattern Generator located above the MSO in the picture) and input

via BNC cable to the transmitter. A copy of the signal is also used to trigger the MSO. When measuring the frequency response the pulse-generator is replaced with a Rohde & Schwarz SMX Signal Generator 100 k-1000 MHz (directly above the pattern-generator). A PC running a C++ program is used to communicate with the DS1859 over I<sup>2</sup>C interface via a USB to I<sup>2</sup>C controller.

## Appendix B

# Details of the Analogue Fibre Noise Calculations

---

As described in Chapter 4 the dominant sources of noise in a fibre optic link are thermal noise, shot noise and relative intensity noise. Here these contributions to the total noise are assessed and used to derive Eq. 4.13.

### B.1 Thermal Noise

Thermal noise, also known as Johnson or Nyquist noise, originates within the photodiode's load resistor,  $R_{load}$ . Electrons within any resistor never remain stationary, because of their thermal energy, they continually move, even with no voltage applied. The electron motion is random, so the net flow of charge could be toward one electrode or the other at any instant. A randomly varying thermal noise current,  $I_{NT}$ , with an average value of zero is induced in  $R_{load}$ . The presence of thermal noise can be modelled by an ideal noiseless resistor, with resistance  $R_{load}$ , in parallel with a current source generating mean-square current:

$$\langle I_{NT}^2 \rangle = \frac{4kTf_{3dB}}{R_{load}}, \quad (\text{B.1})$$

where  $k$  is the Boltzmann constant ( $1.38 \times 10^{-23}$  J/K),  $T$  is the absolute temperature of the receiver and  $f_{3bB}$  is the electrical bandwidth of the optical link, taken to be 500 MHz here, although this is rather too large, as shown in Section 4.6.5. The thermal noise spectrum is uniform over all frequencies of interest here (white noise).

## B.2 Shot Noise

The discrete nature of electrons causes a signal disturbance called shot noise. When an electrical current is established via a series of independent, random charge carrier transits then a noise like current is superimposed on the average current. The current in the photodiode at the receiver in an optical link arises from a series of independent random events due to the statistical arrival of photons on the diode. Incoming optical signals generate discrete charge carriers. Each carrier contributes a single pulse to the total current. Consequently there is a shot noise current,  $I_{NS}(t)$ , superimposed on the average photodetector current,  $\langle I_d \rangle$ :

$$I_d(t) = \langle I_d \rangle + I_{NS}(t), \quad (\text{B.2})$$

where  $\langle I_{NS} \rangle = 0$ . The shot noise can then be represented by an equivalent circuit consisting of a single current source, and the mean-square shot noise current is:

$$\langle I_{SN}^2 \rangle = 2e \langle I_d \rangle f_{3bB}, \quad (\text{B.3})$$

where  $e$  is the magnitude of the charge on an electron. The shot noise spectrum is uniform over all frequencies of interest. As with thermal noise, shot noise current depends on the system bandwidth, not on the location of the band. However, unlike thermal noise, shot noise increases with the average photodetector current, and therefore the amplitude of the input signal.

## B.3 Relative Intensity Noise

Random fluctuations in the VCSEL output occur even when the driving current is constant. The relative-intensity noise (RIN) describes the amount of noise emitted by

the VCSEL. An average optical power,  $\langle P_l \rangle$ , emitted by the VCSEL results in an average current at the photo diode of  $\langle I_d \rangle$ , which is converted to a voltage at the output by the receiver circuit. The average value of the square of the noise current at the photodiode is:

$$\langle I_{RIN}^2 \rangle = RIN \langle I_d \rangle^2 f_{3bB} = RIN (\langle P_l \rangle T_f r_d)^2 f_{3bB}, \quad (\text{B.4})$$

where  $RIN$  is a measure of the average noise power normalised to the bandwidth, given by the VCSEL data sheet as -120 dB/Hz.

### B.3.1 Electronic Amplifier Noise

In an ideal situation the OPA695 op-amps at the receiver would multiply the power contained in both the signal and noise by the amplifier gain. Unfortunately real amplifiers not only multiply the input noise, but also introduce noise of their own. The presence of electronic amplifier noise can be modelled by adding an *effective temperature*,  $T_e$ , to the thermal noise.  $T_e$  is available from the OPA695 datasheet and depends on the amplifier gain. Then the thermal noise, including the electronic amplifier noise is:

$$\langle I_{NTE}^2 \rangle = \frac{4k(T + T_e)f_{3bB}}{R_{load}}, \quad (\text{B.5})$$

The first receiver op-amp is operated at a gain of -1 and has a corresponding *effective temperature* of  $T_{e(-1)}$ . The second OPA695 is operated at a gain of 10 and has a corresponding *effective temperature* of  $T_{e(10)}$ .

## B.4 Noise Analysis

Following Eq. B.4 the RIN noise of the optical link is given by:

$$\langle I_{RIN}^2 \rangle = RIN ((I_b + I_s) s_l T_f r_d)^2 f_{3dB}. \quad (\text{B.6})$$

The total thermal noise at the receiver, including the electronic amplifier noise is:

$$\langle I_{NTE}^2 \rangle = \frac{4k(2T_{RX} + T_{e(-1)} + T_{e(10)})f_{3dB}}{R_{load}}. \quad (\text{B.7})$$

and the shot noise is given by:

$$\langle I_{SN}^2 \rangle = 2e((I_b + I_s)s_l T_f r_d) f_{3bB}. \quad (\text{B.8})$$

Then the total mean noise current at the receiver, including the gain of the second OPA695 op-amp,  $g_{out}$ , is:

$$\begin{aligned} \langle I_{noise}^2 \rangle &= g_{out} \cdot (\langle I_{NTE}^2 \rangle + \langle I_{SN}^2 \rangle + \langle I_{RIN}^2 \rangle) \\ &= g_{out} \cdot \frac{4k [2T + T_{e(-1)} + T_{e(10)}] f_{3dB}}{R_{load}} \\ &\quad + g_{out} \cdot 2e [(I_b + I_s)s_l T_f r_d] f_{3bB} \\ &\quad + g_{out} \cdot RIN [(I_b + I_s)s_l T_f r_d]^2 f_{3dB}. \end{aligned} \quad (\text{B.9})$$

The mean square current is then converted to an RMS voltage by:

$$\sqrt{\langle I_{noise}^2 \rangle} = \frac{\sqrt{\langle V_{noise}^2 \rangle}}{R_{load}} \quad (\text{B.10})$$

The corresponding RMS output area,  $\sigma_{A_{out}}$  is then given by:

$$\sigma_{A_{out}} = \int_{t1}^{t2} \sqrt{\langle V_{noise}^2 \rangle} dt \quad (\text{B.11})$$

where  $t2 - t1$  is the size of the integration window. Similarly the area of the input pulse,  $A_{in}$ , creates an associated current  $I_s$  according to:

$$A_{in} = \int_{t1}^{t2} \frac{V_l}{R_l} dt. \quad (\text{B.12})$$

## Appendix C

# Details of the Commercial Hardware used in the DAT

---

In this appendix the parallel optical link (PAROLI), the MPO fibre-optic cabling system and the Xilinx Spartan 3 FPGA used in the development of the DAT modules in Chapter 6 are described.

### C.1 The Parallel Optical Link

There are several parallel optical link devices commercially available from companies such as Agilent [4], Picolight [146; 147], Zarlink [196], and Infineon [96]. All devices are similar in nature. The number of channels, data rate, price and the packaging differ slightly, but the timing specifications, connector and the operating principle remain the same. All devices contain VCSELs and qualify as Class 1M lasers.

The choice was made in 2004 to use the Infineon PAROLI 2<sup>®</sup> [96] for the DAT, competitively priced at under \$800 per pair. After initial timing performance tests using Infineon demonstration boards C.1(a) 16 PAROLI 2<sup>®</sup> pairs were purchased for the VERITAS 4 array. The 100 pin pluggable socket for the PAROLI is ball gate array (BGA) mounted onto a daughter board (DB) and connects to the DAT PCB via a dual-in-line

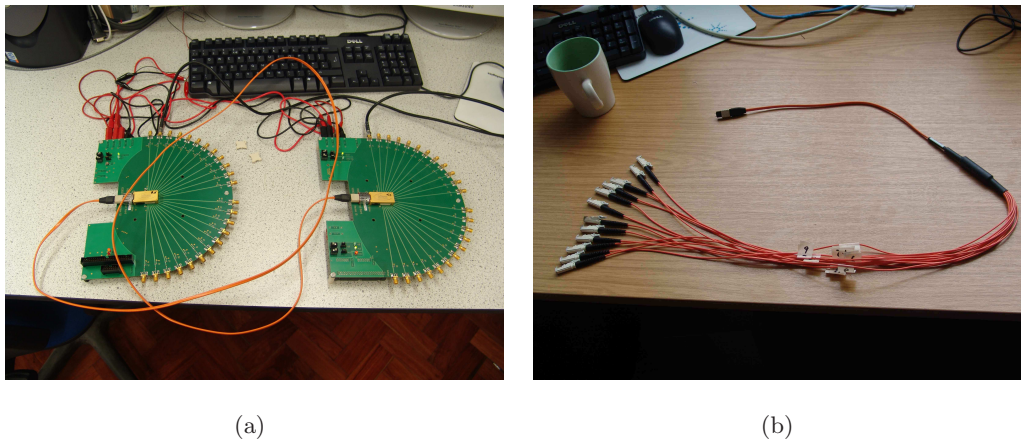


Figure C.1: (a) Demonstration boards for the Infineon PAROLI 2<sup>®</sup> with 2 m 12 channel fibre interconnect (see Section C.2). Differential LVDS signals are input to the transmitter (right) via 12 pairs of SMA connectors then recovered and output in the same form at the receiver (left). The PAROLI devices require 3.3 V and are configurable via onboard jumpers and switches. (b) 12 channel MPO to E2000 fanout cable.

(DIL) socket. In this way other parallel link devices may be used in the future at the relatively low cost ( $\sim$ £50 a piece) of producing new DBs.

The PAROLI 2<sup>®</sup> is a parallel optical link for high-speed data transmission optimized for 62.5  $\mu$  m multimode graded index fibre with MPO optical port connectors. A complete PAROLI link consists of a transmitter module, a 12-channel fibre optic cable, and a receiver module pluggable via 100 gold-over-nickel pin (10x10), ultra low profile, BGA socket standing at 4 mm in mated conditions.

The 3.3 V transmitter module converts parallel electrical input signals via a laser driver and an 850 nm VCSEL diode array into parallel optical output signals. All input data signals are multi-standard differential signals (LVDS, LVPECL and CML) selectable by the supply voltage input  $V_{IN}$ .

The PAROLI receiver module converts parallel optical input signals into parallel electrical output signals. Signal detect outputs (SD1 active *high* and -SD12 active *low*) show whether an optical signal is present at data input 1 and/or 12. The signal detect circuit can be disabled permanently generating an active level at signal detect outputs.

The transmission delay of the PAROLI system is at a maximum 1 ns for the transmitter,

1 ns for the receiver and approximately 5 ns per metre for the fibre optic cable. The quoted channel to channel skew is 100 ps for the transmitter and the receiver [96]. A skew of around 200 ps was measured across all channels using the demo boards, which includes pulse generator, cable, demo-board, PAROLI-TX and PAROLI-RX skew. The jitter is dependent on the input data and for a 1 MHz 50% DC% input pulse was Gaussian with an RMS of around 50 ps depending on the channel.

## C.2 The MPO Cabling System

The MPO fibre optic system provides high-density small form factor ferrule bearing spring loaded connector to link between 4 and 24 fibres. A 12 channel connector and fibre is used for the PAROLI. MPO pre-termination saves time and reduces the possibility of damage to the fragile optical tails and the risk of dirt getting into the fibre couplers.

Ruggedised, 62.5/125  $\mu\text{m}$  core, indoor 12 channel MPO pre-terminated cables are used for lab testing the DAT modules. Onsite two MPO setups were tested with the DAT. In first case individual fibres were laid between telescopes 1 and 2, terminated with individual E2000 connectors via patch-panels at each telescope. MPO fan-out cables were used to connect the PAROLI modules to the patch panels, see Figure C.1(b). Following the problems described in Section 6.8 and Appendix G 150 m long weather and rodent-proof pre-terminated MPO cables were laid between telescopes and connected to the PAROLI modules with 4 m indoor MPO cables (identical to those used for lab testing) via a simple adapter clip. In this way the short MPO cable is unplugged constantly from the DAT modules during installation, testing and operation not the longer, more expensive, outdoor cable. The later system was used to connect the DAT modules in the full VERITAS array. The standard loss incurred through the introduction of an MPO connector is  $\leq 0.75$  dB. The cables are quoted as experiencing 0.2 db losses in transmission during temperature cycling ( $-40^{\circ}\text{C}$  to  $+75^{\circ}\text{C}$ ) and long time (96 hr) high temperature ( $+75^{\circ}\text{C}$ ). The temperature at the VERITAS base camp site ranges from  $0^{\circ}\text{C}$  in winter to  $40^{\circ}\text{C}$  in summer [1].

### C.2.1 The Spartan-3 FPGA

The Spartan-3 XC3S50 in a PQ208 (quad flat-pack) package [195] as shown in Figure C.2 is chosen for use in the DAT-V2 and DAT-V3 modules. This FPGA offers increased functionality, resources and performance over the Spartan XL [184] used in DAT-V1 modules and is essential for extending the simple VME interface to include the combinatorial logic required for encoding and decoding the data. The XC3S50 provides 50K gates, 72K of block RAM, two DCMs (see Section 6.6.3) and 124 user I/O ports, allowing a maximum of 56 differential I/O pairs. The DAT-V2 requires 24 I/O differential pairs. The Spartan-3 family extends to XC3S5000 with 5M gates and 344 differential I/O pairs. The Spartan-3 family architecture consists of five fundamental programmable functional elements [148]. Configurable Logic Blocks (CLBs) contain RAM-based Look-Up Tables (LUTs) [193] to implement logic and storage elements that can be used as flip-flops or latches. CLBs can be programmed to perform a wide variety of logical functions as well as to store data. Input/Output (I/O) Blocks (IOBs) control the flow of data between the I/O pins and the internal logic of the device. Each IOB supports bidirectional data flow plus 3-state operation. Twenty-six different signal standards, including eight high-performance differential standards, are available. Double Data-Rate (DDR) registers are included. Block RAM provides data storage in the form of 18-Kbit dual-port blocks [192]. Multiplier blocks accept two 18-bit binary numbers as inputs and calculate the product [186]. DCM blocks provide self-calibrating, fully digital solutions for distributing, delaying, multiplying, dividing, and phase shifting clock signals

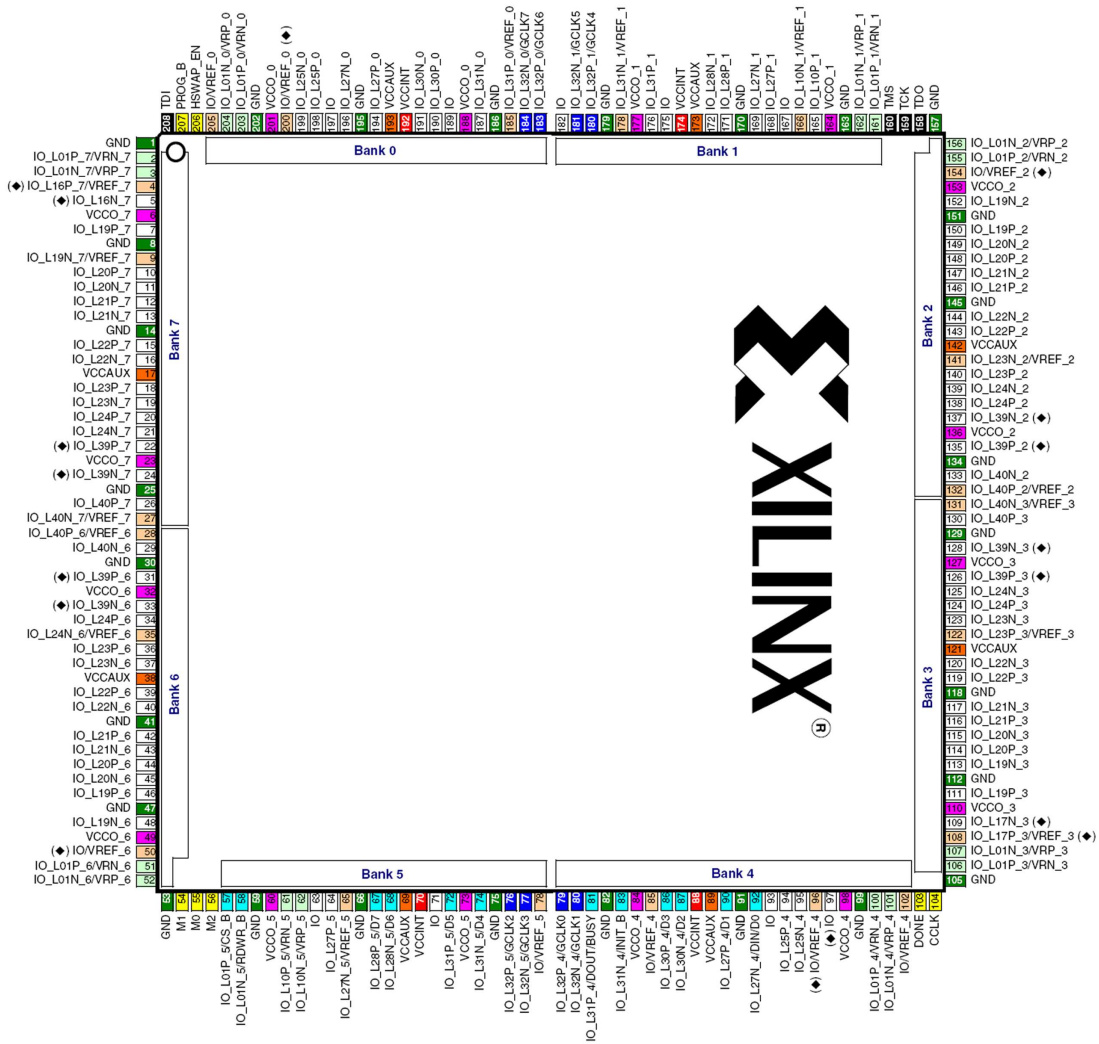


Figure C.2: The pinning of the Spartan-3 XC3S50 FPGA in the PQ208 package. The colour coding indicates pin functionality, which includes: I/O (White), GCLK: Global clock buffer inputs (Blue), VREF: I/O input voltage (Pink), VCCO: I/O output voltage (Magenta), VCCAUX: Aux. voltage, +2.5 V (Orange), VCCINT: Internal core voltage, +1.2 V (Red), GND:Ground (Green), JTAG: Configuration interface (Black). For full details see [195, pg. 138].



## Appendix D

# Details of the DAT Test Setup

---

The test setup to measure the distribution of jitter on a given DAT channel is shown in Figure D.1 and consists of a pulse generator, VME crate, DAT modules, and oscilloscope.

The DAT modules are placed in the CERN V430 VME crate shown to the right of the figure. The modules are controlled over ssh using the DAT software described in Appendix G.2 via the VME two-unit-wide CPU located in the first slot of the crate over ssh. The Agilent 81110A 330 MHz Pulse-/Pattern Generator to the top right of the figure is used to generate NIM test pulses of the desired width and frequency (typically 200 ns and 1 MHz). One copy of the test signal is input to channel 1 of the Agilent Infiniium 54832D 1 GHz, 4 GSa/s MSO. A second copy of the test signal is converted to differential NECL using a CAEN VME NIM-ECL-NIM converter and then input to the DAT-TX. The DAT-TX and DAT-RX are connected with either 2 m or 60 m of MPO terminated 12 channel fibre. The differential NECL signal at the DAT-RX output is converted back to NIM and then input into another channel of the MSO.

There are three trigger scenarios used in assessing the performance of the DAT modules. In measuring the distribution of arrival times (see Section 6.7.4) the MSO is set to trigger on falling edge of the input pulse and a histogram of the falling edge of the output pulse is created. In measuring the distortion in the pulse width (see Section 6.7.5) the MSO is set to trigger on falling edge of the output pulse and a histogram of the next rising

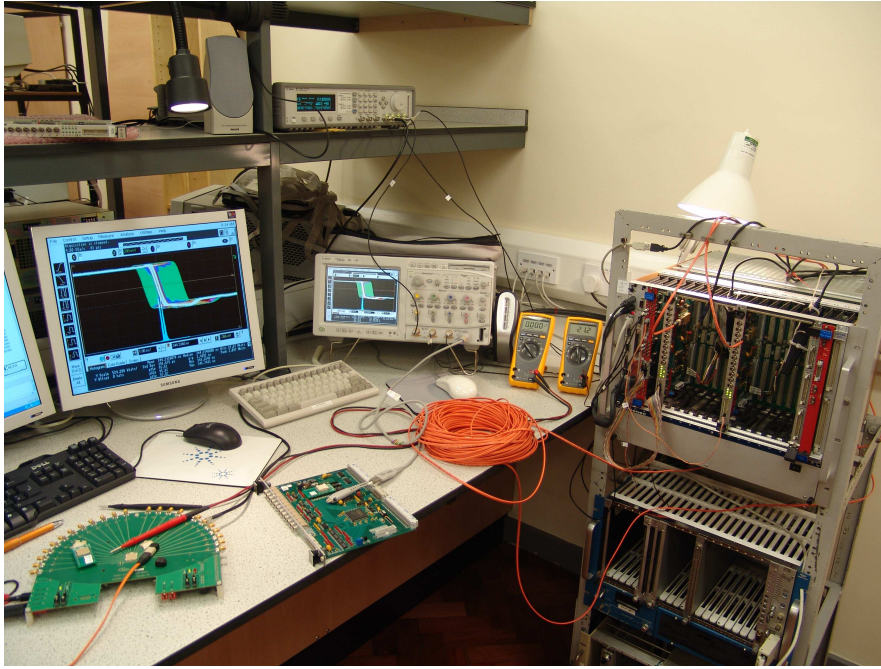


Figure D.1: *The test setup used to evaluate the performance of the DAT modules.*

edge of the output pulse is created. In measuring the channel-to-channel jitter (see Section 6.7.6) the channel 1 input is removed from the MSO, converted to NECL and input to another channel of the DAT-TX. The corresponding output at the DAT-RX is converted to NIM and input to an additional MSO channel. The falling edge is then used to trigger the MSO and a histogram of the falling edge of the other DAT output channel is created.

The differential probe shown in the centre of the picture is used to diagnose problems by probing the data and clock paths at various points within the DAT modules.

The DAT modules are reprogrammed during testing over JTAG using a PC and a Xilinx Platform USB-JTAG programmer.

## Appendix E

# The Components of Jitter

---

In this appendix the components of deterministic jitter introduced in Section 6.7.1 and shown in Figure 6.17 are described in relation to the jitter distributions observed with the DAT modules.

### E.1 Duty Cycle Distortion (DCD) Jitter

Duty Cycle Distortion (DCD) may be caused by asymmetry between the rising and falling edges of a signal or a variation in the threshold voltage of a device in the signal path. If either effect is time variable DCD jitter will occur as a function of the varying slew rate of the signal's edge transitions.

Oscillations due to noise on the common-mode voltage line can propagate to a device's threshold level leading to DCD jitter in the time domain. With a positive shift in the threshold level the resultant signal will have less than 50% duty cycle. If the threshold level is shifted negatively, the signal will have greater than 50% DC%. In the case of the DAT the ECL-PECL converters, TX FPGA, PAROLI-TX, PAROLI-RX, RX FPGA, and PECL-ECL converters are all possible sources of threshold induced DCD jitter.

DCD may also be caused by the varying response of a device to rising and falling edges. In the DAT such edge-sensitivity is observed in the encoded data lines leaving the TX

FPGA, where rising and falling edges undergo different transit times due to routing through the FPGA. Such a distortion causes a difference between the duty cycles of the clock and encoded data resulting in a glitch when decoding the data, as illustrated in Figure 6.13.

Alternatively if DCD occurs in the data line before encoding, or in the edges of the encoded signal corresponding to the data, then the distortion will propagate to the recovered data as DCD jitter. Since the input data is not a clock signal but rather a pulse, the result is best thought of as a distortion in the recovered data pulse width, as discussed in Section 6.7.5.

## E.2 Data Dependent Jitter (DDJ)

Data Dependent Jitter (DDJ), sometimes known as Inter-Symbol Interference (ISI), is the result of limited signal edge speeds at high data rates. In the case of the DAT DDJ is a direct consequence of the asynchronous relationship between clock and data. As the clock and data edges approach each other in time errors during both the encoding and decoding occur. Several cases are considered in Figures E.1 and E.2 and described below for a falling data edge.

**(A)** If the data edge occurs far from any clock edges it will result in an encoded edge with equivalent timing. If the clock is *low* a falling (rising) edge on the data will result in a falling (rising) edge in the encoded signal. If the clock is *high* a falling (rising) edge on the data will result in a rising (falling) edge in the encoded signal. This edge will be decoded correctly.

**(B)** If the rising clock edge occurs after, but close to, the falling data edge then the encoded data signal has time to drop below the required low-threshold. But before the encoded signal can reach a completely low state, the rising edge of the clock occurs sending the encoded signal back up towards the high-threshold. The encoded signal is low for less time than it would have been if the falling edge had reached the true low value before beginning to rise, thus the data edge is encoded earlier than it should have been. The situation becomes complicated when the signal is decoded. At the falling edge in the encoded signal corresponding to the original rising edge in the clock the recovered

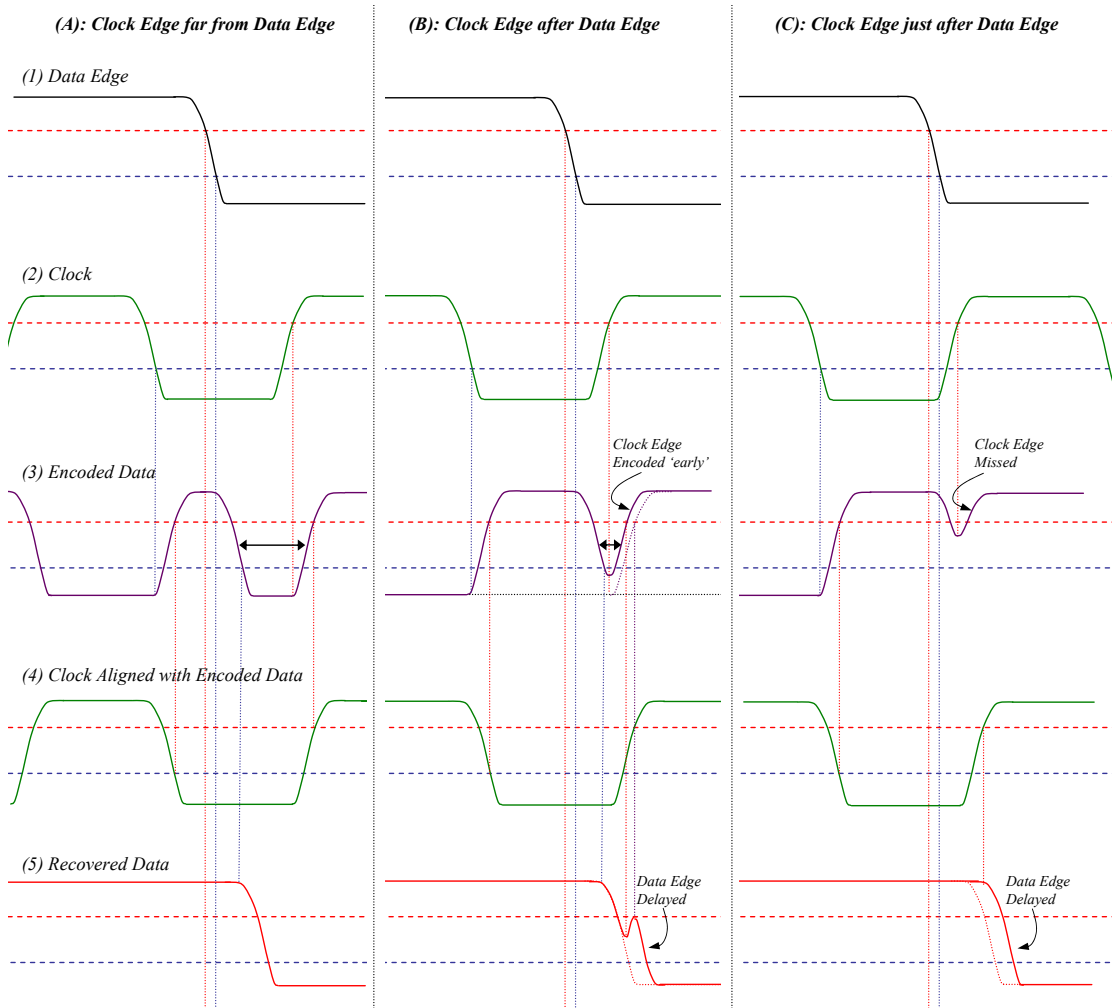


Figure E.1: The encoding and decoding of a falling data edge for several possible clock-to-data alignments at the transmitter. A data edge is correctly recovered if it is encoded far from a clock edge (A). However, as the data edge approaches a clock edge it is recovered later than expected (B) until at the edge is not encoded at all and the recovery takes place at the next available clock edge (C).

data correctly remains *high*. However at the point when the falling edge in the encoded signal reaches the low-threshold the recovered data will begin to switch low. This is a mistake, which is usually corrected very quickly as soon as the rising clock edge crosses the high-threshold <sup>1</sup>. If the rising edge in the encoded signal corresponding the data edge is detected by the recovered data whilst the signal is still rising from the previous mistake, it will begin to fall again before reaching a completely high state. This time the edge falls past the low-threshold creating a recovered data edge, later than otherwise expected.

(C) If a rising clock edge occurs just after the data edge the falling data edge will cause the encoded signal to begin falling towards a low-threshold. If a rising clock edge occurs before the low-threshold is reached, the encoded signal will begin to rise without first switching *low*. When the signal is decoded the falling data edge is incorrectly recovered at the clock edge, later than is correct.

(D), (E) If a clock edge instead occurs just before the data edge then using similar arguments that explain (B) and (C), the recovered data arrives earlier than expected.

(F) If the data edge perfectly coincides with a clock edge there is no edge at the point of encoding. This scenario results in a decoded data edge at the correct time.

Similar scenarios occur for both data edges when a rising or falling clock edge arrives just before or after the data edge. A falling edge interacting near a rising edge will create a different delay than a falling edge occurring near another falling edge due to differences in rise and fall times. The net result is a DDJ with many components and a magnitude related to the worst case signal slew speed in the design. Some scenarios may be more likely than others and create peaks in the DDJ distribution.

## E.3 Periodic Jitter (PJ)

Periodic Jitter (PJ) is usually the result of a cross-coupling, otherwise know as cross-talk, and can be either correlated or uncorrelated. Uncorrelated PJ could be caused

---

<sup>1</sup>This behaviour is caused by the gap between the low-threshold and high-threshold and difference between rise and fall times of the encoded signal, clock and receiver clock, and is thus linked to DCD induced jitter.

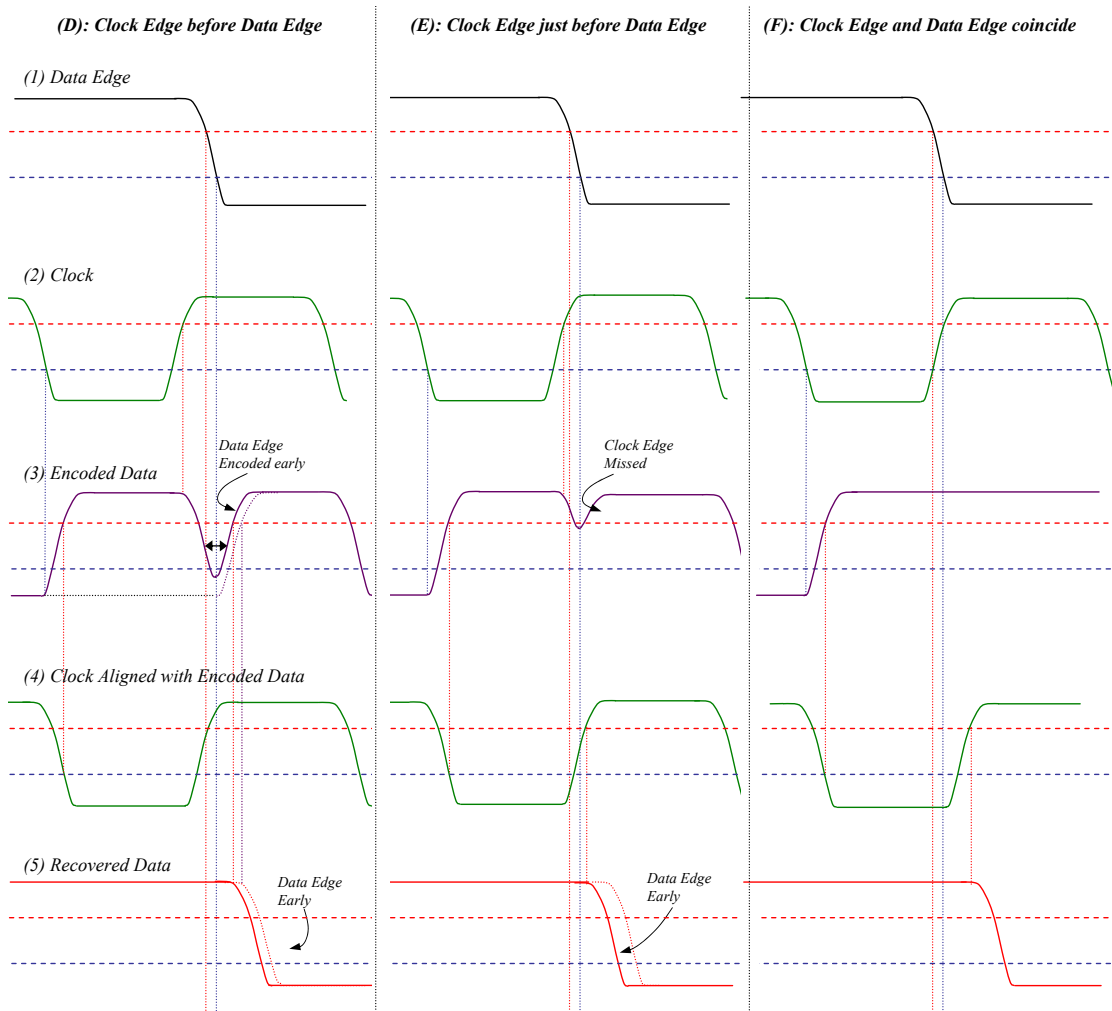


Figure E.2: The encoding and decoding of a falling data edge for several more clock-to-data alignments at the transmitter continued from Figure E.2. The data edge is correctly recovered if it perfectly coincides with a clock edge (D), but as the data edge moves past the clock edge it is recovered earlier than expected (E) and (F).

by a switching power supply coupling into the signal lines. Correlated PJ occurs when simultaneous signals on adjacent lines affect the arrival time of the edges on one of the lines. In the case of differential signals the two traces of one signal line are exactly equal and opposite and the traces are routed closely together. In this case the coupling between the two halves of the signal is symmetrical [36]. However, a net effect can occur if one half of a differential pair is coupled to one half of an adjacent pair.

When two PCB traces are placed close together the current flowing down one (aggressor) induces a current in the other trace (victim). The electric field causes a current in the victim trace that flows both backwards and forwards. A single electron at a point along the aggressor trace will repel electrons in the victim trace in both directions away from that point. This is known as capacitive coupling. The aggressor trace also generates a magnetic field, which in turn induces a current backwards in the victim trace. This is known as inductive coupling. Both coupling effects can result in unwanted currents in a signal trace which will manifest themselves as noise in the voltage domain [34]. As shown for DDJ any amplitude variations in voltage can propagate to the time domain if they occur near signal edges.

A further effect from the coupled electric field between two signal lines is possible. When a trace is far away from its neighbours, a signal propagating down the line has some electric field lines going only through the PCB and some field lines going partly through the air (fringe field lines), see Figure E.3 (a), when adjacent lines are close enough the field lines will interact, Figure E.3 (b) and (c) [31].

When the aggressor and victim carry the same bit both lines have the same voltage, and few fringe-field lines exist in the air above the traces, most flowing to the return plane through the bulk material. When the aggressor line is in the opposite state from the victim line a large fringe field exists between the lines. The higher the fraction of field lines from the victim line to the return path in the air the lower the effective dielectric constant of the PCB. A change in the effective dielectric constant changes the delay of the signal on the victim line. When the aggressor has the same bit pattern as the victim, the effective dielectric constant is higher, the propagation speed is lower, and the delay is longer. When the aggressors have the opposite bit pattern from that of the victim line, the effective dielectric constant is lower, the propagation speed is higher, and the

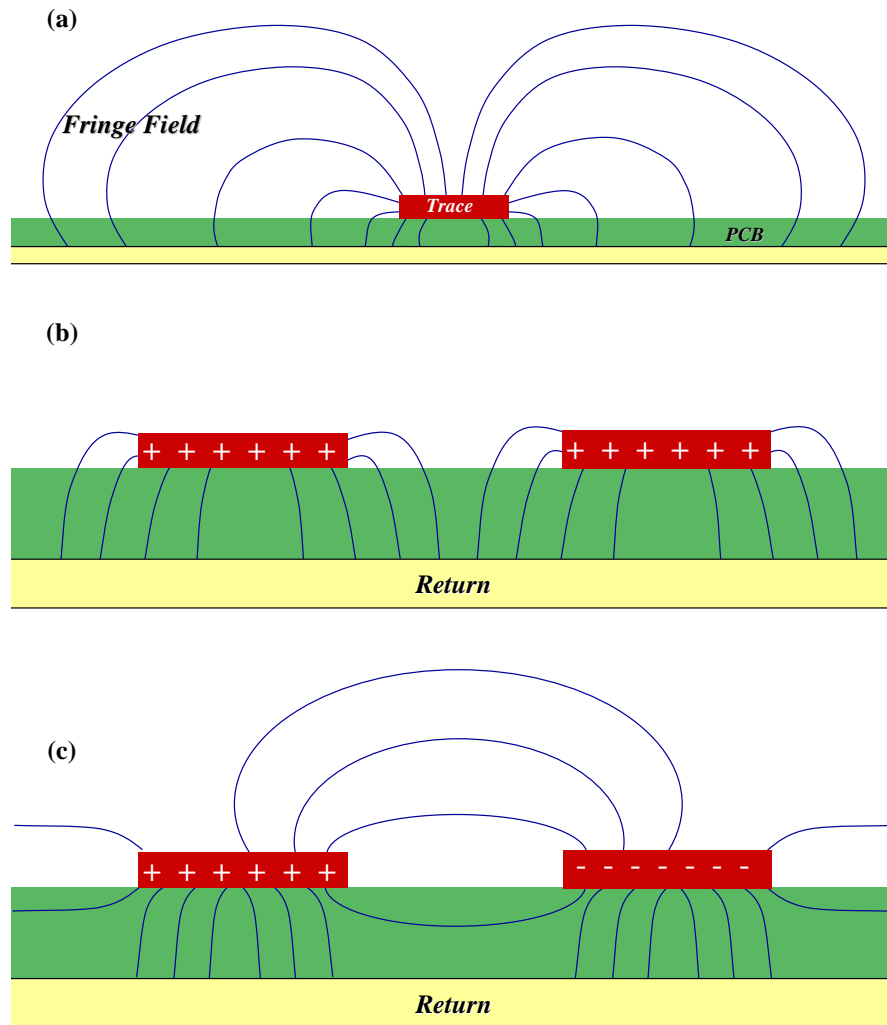


Figure E.3: *Scenarios for the possible occurrence of crosstalk induced jitter. (a) A single PCB trace far from neighbours. (b) A PCB trace and neighbour in the vicinity, with the same bit pattern. (c) A PCB trace and neighbour in the vicinity, with opposite bit pattern.*

time delay on the victim line is shorter.

## E.4 Dual-Data-Rate Flip-Flop Jitter (DDRFFJ)

If the two input signal lines to a DDRFF are mis-aligned the output will jitter by an amount equal to the misalignment. The misalignment is constrained to approximately the slew speed of the input signals. If the misalignment were greater then the glitches would propagate to the DDRFF output.



# Appendix F

## Further DAT Results

---

In this appendix further results from the DAT as described in Section 6.4.2 are presented.

The following are included for the prototype DAT-V2 pair:

Table F.1: Arrival Times, 60 m of Fibre.

Table F.2: Pulse Width Distortion, 60 m of Fibre.

Table F.3: Channel-to-Channel Jitter Relative to Channel 2, 60 m of Fibre.

Table F.4: Channel-to-Channel Jitter Relative to Channel 8, 2 m of Fibre.

Table F.5: Channel-to-Channel Jitter Relative to Channel 8, 60 m of Fibre.

Figure F.1: Arrival Times, 2 m of Fibre.

Figure F.2: Arrival Times, 60 m of Fibre.

Figure F.3: Pulse Width Distortion, 2 m of Fibre.

Figure F.4: Pulse Width Distortion, 60 m of Fibre.

Figure F.5: Channel-to-Channel Jitter Relative to Channel 2, 2 m of Fibre.

Figure F.6: Channel-to-Channel Jitter Relative to Channel 2, 60 m of Fibre.

Figure F.7: Channel-to-Channel Jitter Relative to Channel 8, 2 m of Fibre.

Figure F.8: Channel-to-Channel Jitter Relative to Channel 8, 60 m of Fibre.

Table F.1: **Arrival Times, 60 m of Fibre.**

Channel	$T_{ar}$	p-p	RMS	RJ	DJ	TJ	$\delta TJ$	95%
	( <i>ns</i> )	( <i>ns</i> )	( <i>ns</i> )	( <i>ps</i> )	( <i>ns</i> )	( <i>ns</i> )	( <i>ps</i> )	( <i>ns</i> )
0	345.97	2.71	0.221	28.8	2.49	2.90	3.66	1.18
1	344.75	2.38	0.215	28.6	2.16	2.57	3.72	0.964
2	344.24	2.33	0.180	35.5	2.05	2.56	3.72	0.509
3	345.01	2.53	0.219	55.0	2.11	2.88	5.09	0.618
4	345.39	2.22	0.165	32.9	1.96	2.43	3.69	0.418
5	345.32	2.38	0.201	45.0	2.03	2.67	3.71	0.709
6	345.06	2.49	0.193	25.6	2.29	2.66	3.66	0.546
7	345.09	2.64	0.269	24.6	2.45	2.80	3.65	1.22
8	344.51	2.62	0.215	26.8	2.41	2.79	3.65	0.800
9	344.47	2.71	0.223	23.2	2.53	2.86	3.65	0.673
10	345.55	2.66	0.219	34.5	2.39	2.88	3.67	0.818

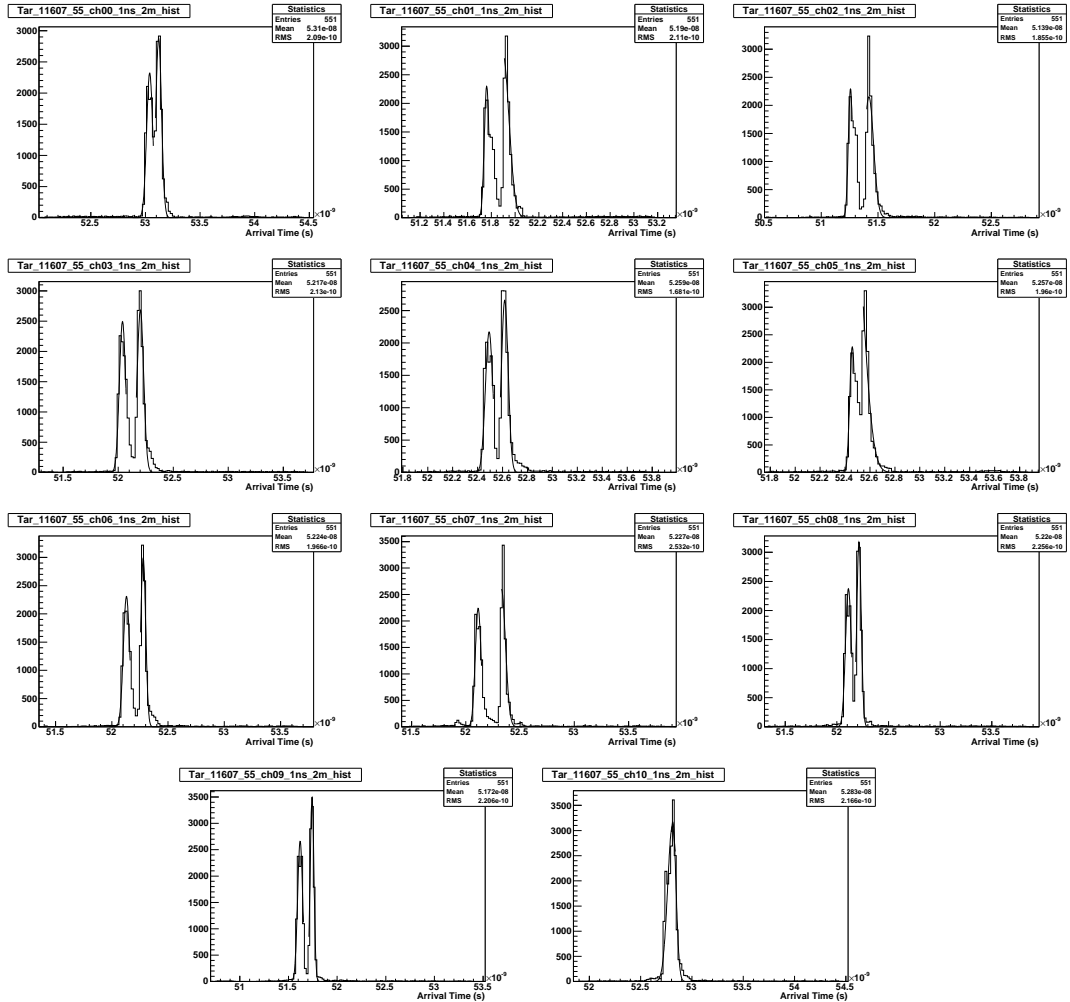


Figure F.1: Arrival Times, 2 m of Fibre.

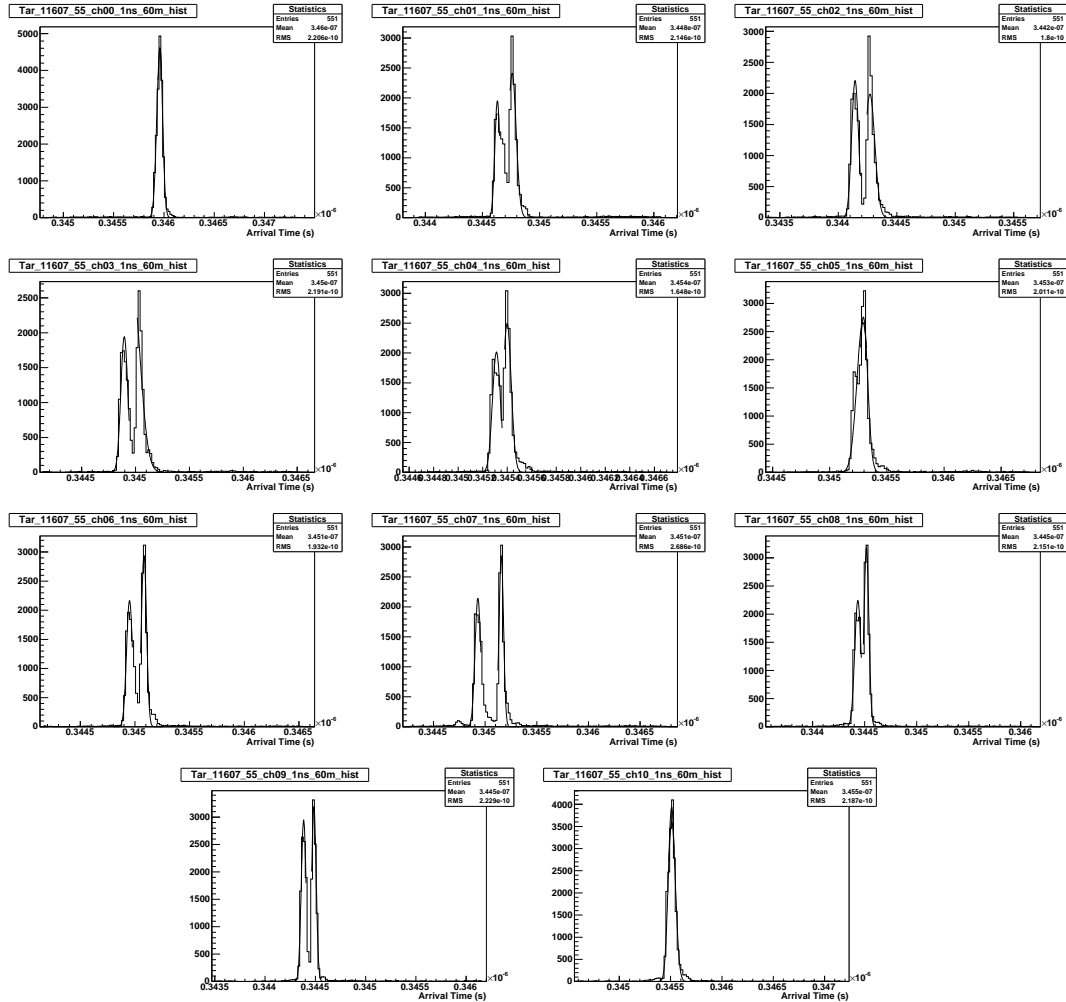


Figure F.2: Arrival Times, 60 m of Fibre.

Table F.2: **Pulse Width Distortion, 60 m of Fibre.**

Channel	$T_{pw}$ ( <i>ns</i> )	p-p ( <i>ns</i> )	RMS ( <i>ns</i> )	RJ ( <i>ps</i> )	DJ ( <i>ns</i> )	TJ ( <i>ns</i> )	$\delta$ TJ ( <i>ps</i> )
0	198.69	3.45	0.375	20.3	3.30	3.59	37.8
1	198.79	2.85	0.333	19.4	2.70	2.98	40.3
2	199.08	2.82	0.271	22.6	2.64	2.96	36.9
3	198.67	3.07	0.309	22.2	2.90	3.22	38.8
4	198.89	2.73	0.276	20.4	2.57	2.86	36.6
5	198.73	2.75	0.285	21.5	2.58	2.89	36.2
6	198.88	3.15	0.319	20.6	2.99	3.28	43.1
7	198.99	2.69	0.388	20.7	2.53	2.83	38.7
8	198.92	2.84	0.318	18.1	2.70	2.95	50.3
9	199.15	3.51	0.321	17.7	3.37	3.62	39.2
10	198.42	3.31	0.312	19.8	3.15	3.44	40.4

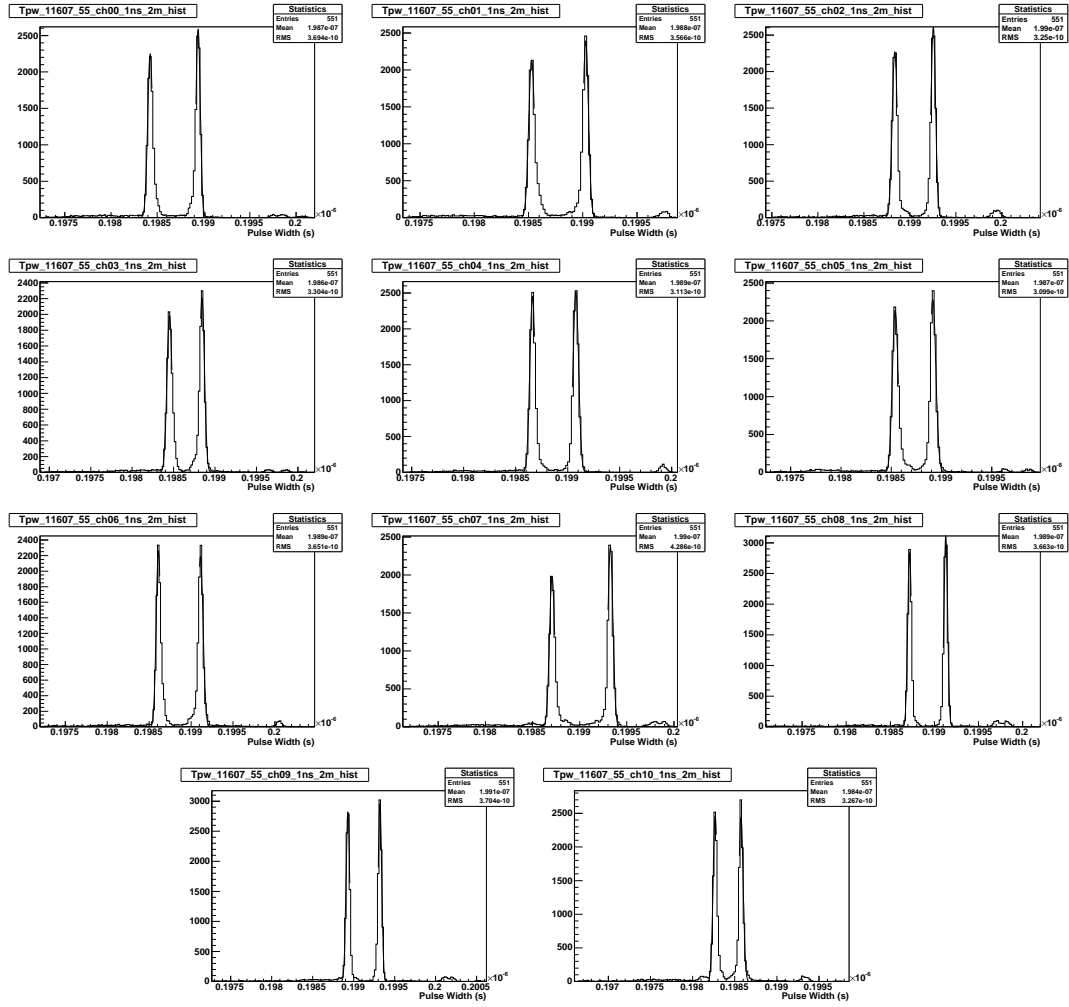


Figure F.3: Pulse Width Distortion, 2 m of Fibre.

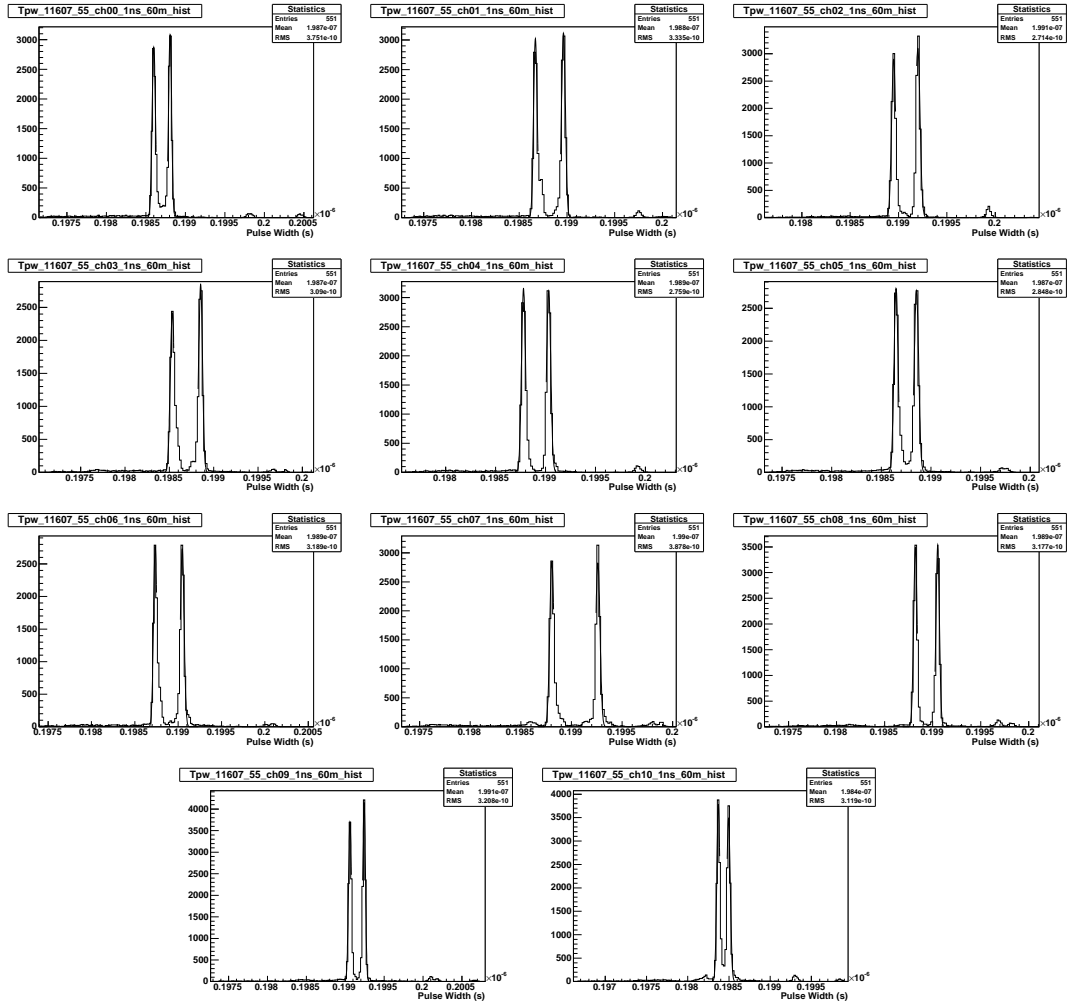


Figure F.4: Pulse Width Distortion, 60 m of Fibre.

---

Table F.3: Channel-to-Channel Jitter Relative to Channel 2, 60 m of Fibre.

Channel	$T_{cc2}$	p-p	RMS	RJ	DJ	TJ	$\delta$ TJ
	( <i>ns</i> )	( <i>ns</i> )	( <i>ns</i> )	( <i>ps</i> )	( <i>ns</i> )	( <i>ns</i> )	( <i>ps</i> )
0	1.44	3.57	0.352	22.7	3.39	3.71	38.3
1	0.173	2.18	0.212	18.4	2.04	2.30	40.1
3	0.442	2.66	0.264	23.3	2.47	2.81	41.6
4	0.837	2.67	0.241	29.5	2.44	2.86	39.0
5	0.757	2.91	0.280	20.4	2.75	3.04	39.8
6	0.504	2.84	0.261	16.4	2.71	2.94	41.5
7	0.513	2.31	0.259	15.7	2.19	2.41	40.0
8	0.471	2.42	0.203	17.1	2.29	2.53	38.3
9	-0.135	2.67	0.189	26.3	2.47	2.84	36.8
10	0.969	3.18	0.273	19.4	3.03	3.31	40.6

---

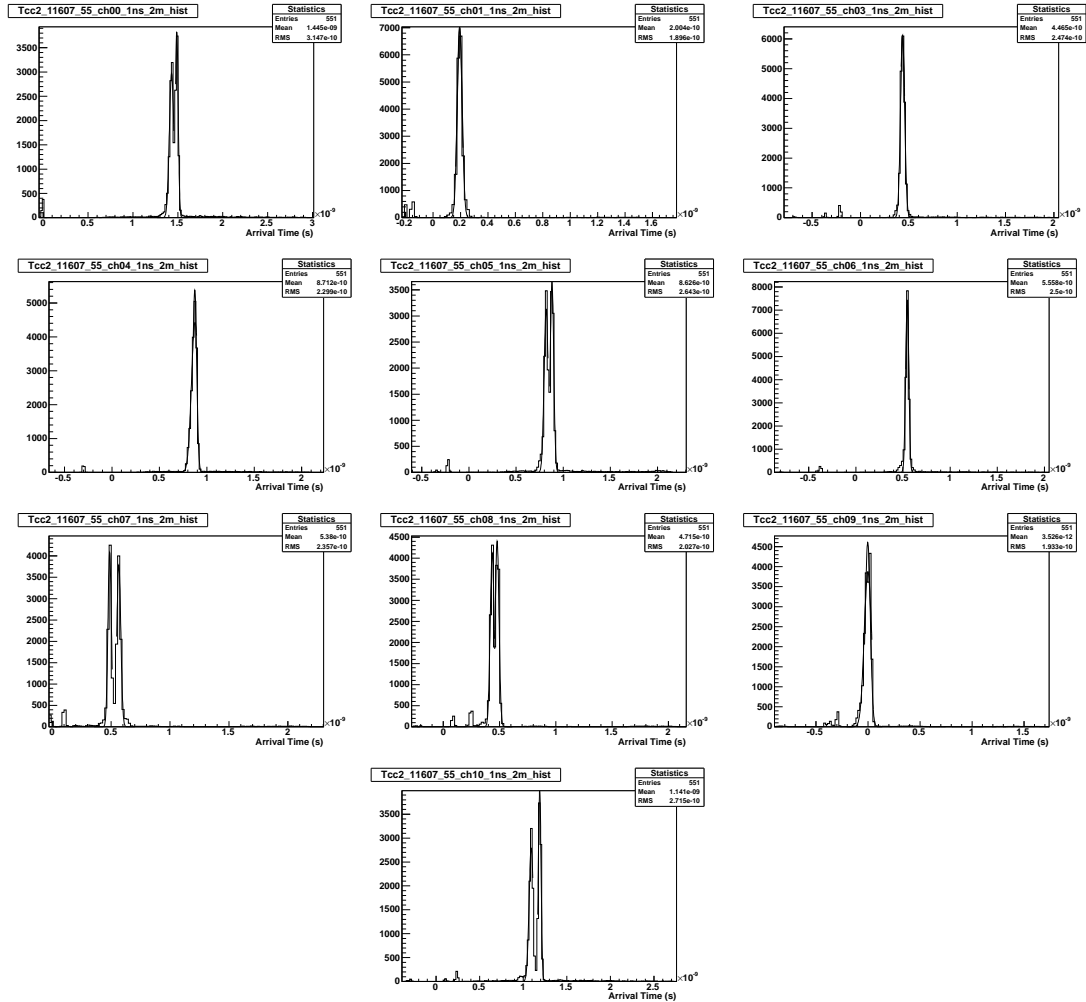


Figure F.5: Channel-to-Channel Jitter Relative to Channel 2, 2 m of Fibre.

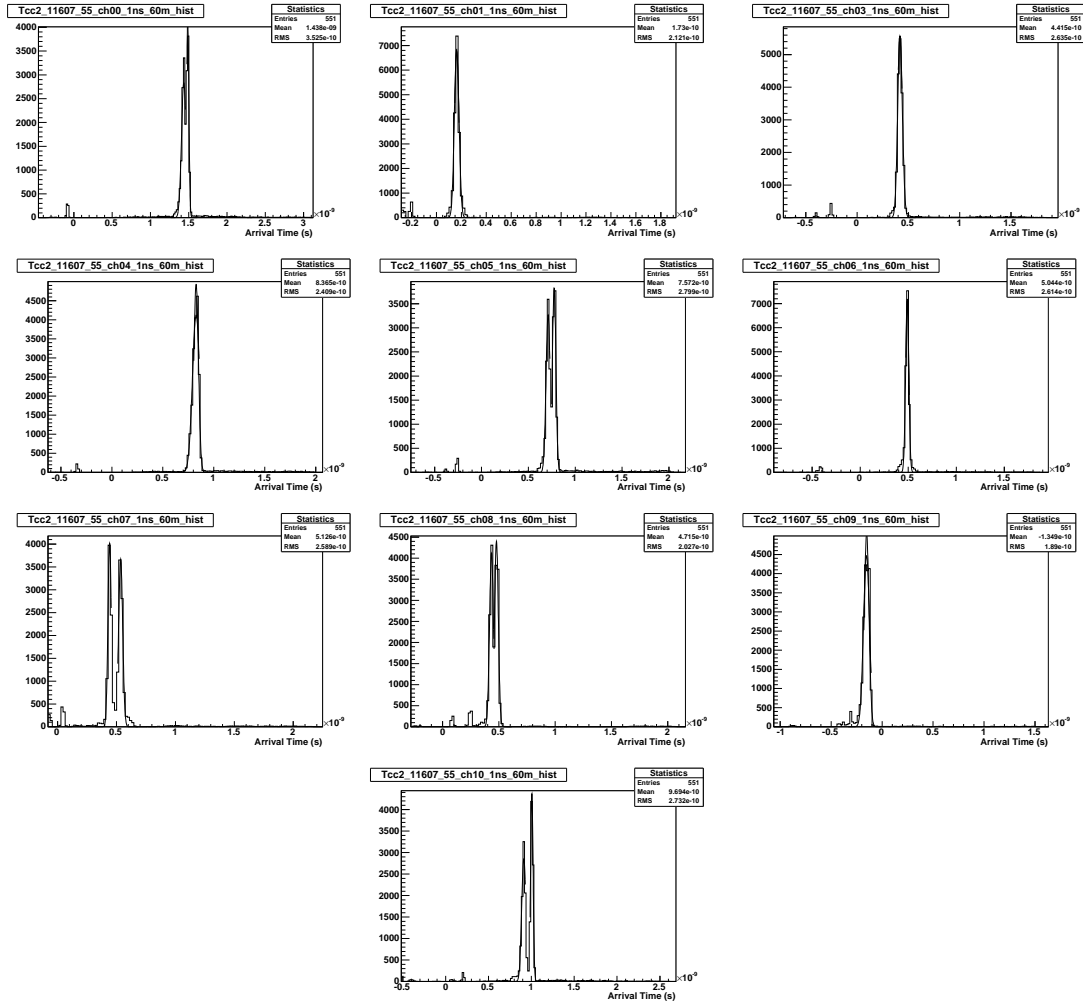


Figure F.6: Channel-to-Channel Jitter Relative to Channel 2, 60 m of Fibre.

Table F.4: Channel-to-Channel Jitter Relative to Channel 8, 2 m of Fibre.

Channel	$T_{cc8}$	p-p	RMS	RJ	DJ	TJ	$\delta TJ$
	( <i>ns</i> )	( <i>ns</i> )	( <i>ns</i> )	( <i>ps</i> )	( <i>ns</i> )	( <i>ns</i> )	( <i>ps</i> )
0	0.593	2.891	0.314	16.7	2.77	3.00	36.4
1	-0.644	3.200	0.183	22.7	3.02	3.35	36.8
2	-1.10	2.436	0.196	18.1	2.30	2.56	39.8
3	-0.346	3.018	0.203	18.3	2.88	3.14	38.6
4	0.109	2.691	0.254	27.6	2.48	2.88	38.7
5	0.085	2.636	0.259	18.3	2.50	2.76	40.2
6	-0.224	3.055	0.222	16.6	2.93	3.16	38.6
7	-0.276	2.273	0.156	15.8	2.15	2.38	37.8
9	-0.761	3.145	0.132	16.9	3.01	3.26	36.6
10	0.150	3.255	0.265	15.5	3.13	3.36	37.1

Table F.5: **Channel-to-Channel Jitter Relative to Channel 8, 60 m of Fibre.**

Channel	$T_{cc8}$	p-p	RMS	RJ	DJ	TJ	$\delta TJ$
	( <i>ns</i> )	( <i>ns</i> )	( <i>ns</i> )	( <i>ps</i> )	( <i>ns</i> )	( <i>ns</i> )	( <i>ps</i> )
0	0.589	3.265	0.357	20.4	3.10	3.39	39.0
1	-0.662	2.91	0.179	19.2	2.76	3.03	37.2
2	-1.187	2.29	0.212	26.8	2.08	2.47	40.7
3	-0.361	2.86	0.218	18.8	2.71	2.98	40.9
4	0.041	2.58	0.279	18.7	2.44	2.70	36.2
5	-0.037	2.93	0.276	20.2	2.77	3.06	38.9
6	-0.297	2.98	0.249	23.5	2.80	3.13	40.2
7	-0.306	2.04	0.155	15.4	1.92	2.14	37.1
9	-0.928	3.24	0.175	13.5	3.13	3.32	41.4
10	0.150	3.26	0.265	15.5	3.13	3.36	36.5

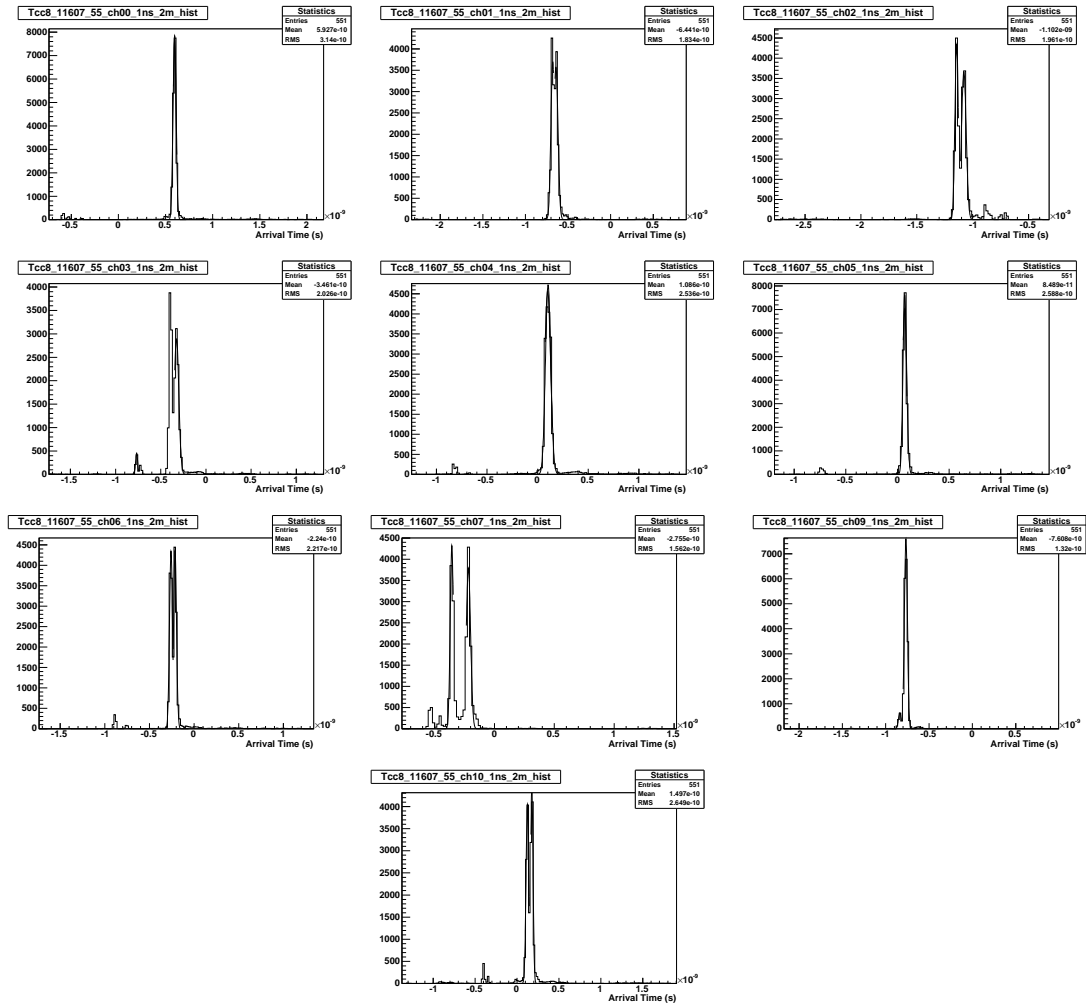


Figure F.7: Channel-to-Channel Jitter Relative to Channel 8, 2 m of Fibre.

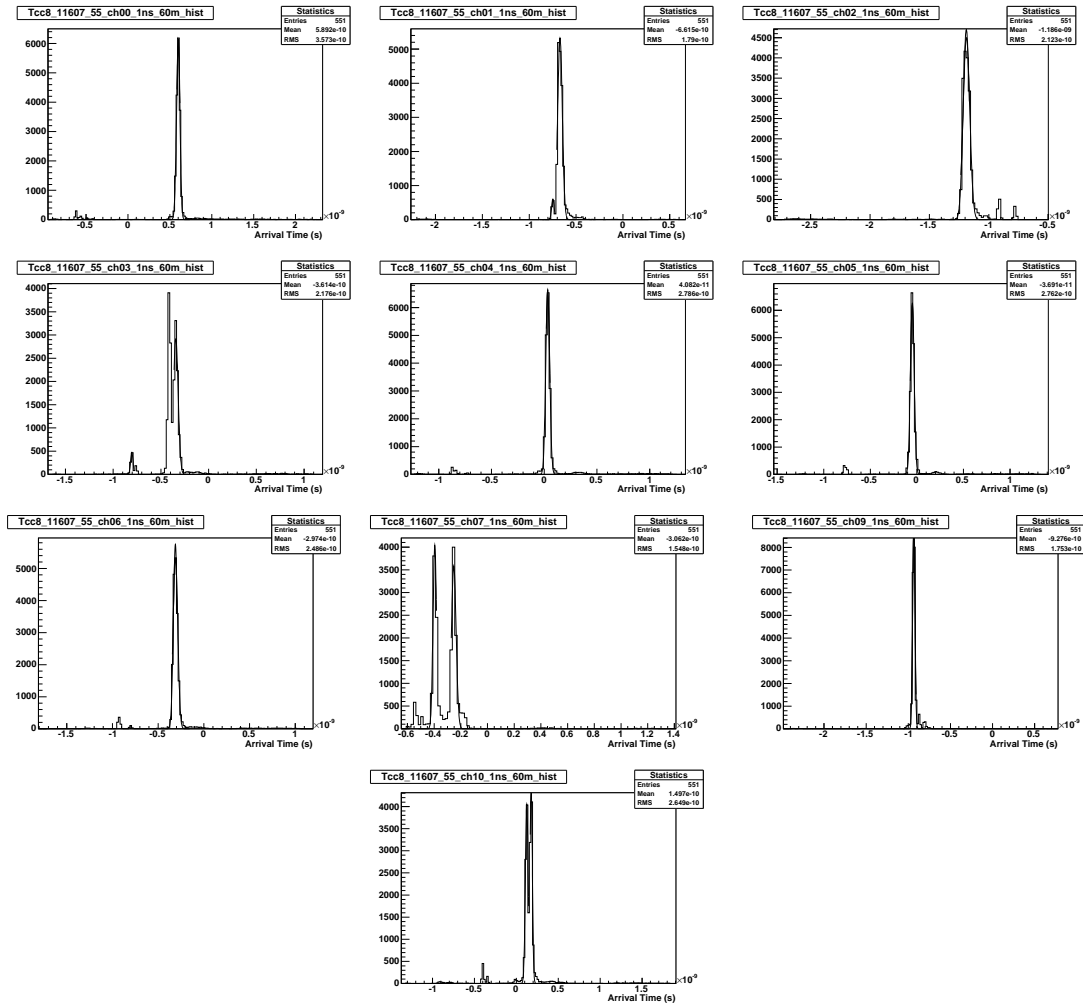


Figure F.8: Channel-to-Channel Jitter Relative to Channel 8, 60 m of Fibre.

## Appendix G

# Integration of the DAT within VERITAS

---

In this appendix the onsite installation software for the DAT modules is expanded upon.

### G.1 Onsite Installation and Evaluation of the DAT

Two pairs of DAT-v2 modules were installed between VERITAS telescopes 1 and 2 in January 2006. Several channels in each direction showed noise indicative of a misalignment between the clock and encoded data at the receivers. The problem was traced to the fibre interconnect system between the telescopes.

During laboratory tests a 12 channel MPO terminated ribbon cable was used to connect the modules. Each of the fibres in the ribbon cable was constrained to be of near identical length by the manufacturing process. Onsite armoured multi-fibre cables were laid in conduits between the telescopes. Such cables provide many fibres and were used for equipment other than the DAT modules, such as the laser calibration system. A set of 30 fibres were individually terminated with E2000 connectors at a patch-panel in each telescope. Then an E2000 to MPO fanout cable is connected to the DATs. Figure G.1(a) shows the layout of this cabling scenario. If a given fibre-splice to an E2000 connector

is unsuccessful the fibre must be shortened by around 5 cm before another attempt can be made [177]. At 5 ns/m such a difference in fibre lengths results in an additional skew of 250 ps between the 11 encoded data channels and the clock at the receiver. This is enough to knock the worst effected channels out of alignment.

In addition the temporary measure of using cables with the rubber bend protection removed to establish a secure connection between the PAROLI and the DB proved ineffective in a working environment. Out of 11 data channels two were not useable due to the PAROLI seating, and a further 5 in one pair and, 7 in the other pair, were misaligned. Thus there were only two working connections sending data from T1 to T2 and four sending data back. This minimal setup was however sufficient for the successful operation of a two telescope array. In late April 2006 the remaining two DAT-V2 pairs were shipped from Leeds and a vist was made to base camp to install them and diagnose the existing setup.

The skew induced by the difference in fibre lengths between the telescopes at the patch panels in each telescope was measured by recording the average arrival time of a pulse down each fibre relative to a fixed point. A much larger than previously expected skew of  $5.3 \pm 0.1$  ns was recorded across the 30 different available patch-panel channels [176]. Since the differences were primarily due to splicing errors the channels could be grouped according to delay as shown in Figure G.2. The E2000 connectors on the end of the MPO fanout cables were re-mapped at the patch panel to minimise the skew between DAT channels arriving at the receiver. By taking into account the known distribution in arrival times of signals at the DAT receiver from lab measurements with a equal length fibre ribbon cable, the shortest individual fibres within a group of similar lengths were mapped to DAT channels with the latest arrival times. Using this simple method 8 of a possible 11 channels in both directions between T1 and T2 were correctly aligned. Two of the other three channels remained misaligned due to the PAROLI seating.

The patch-panel mapping is specific to a given DAT pair. No modules could be replaced without remapping the fibres. However, it only takes an afternoon to re-map the fibres and individual fibres are a cheap option, excluding the cost of the fibre-splicing machine. The alternative method is to use a 150 m equivalent length fibre ribbon cable. A custom

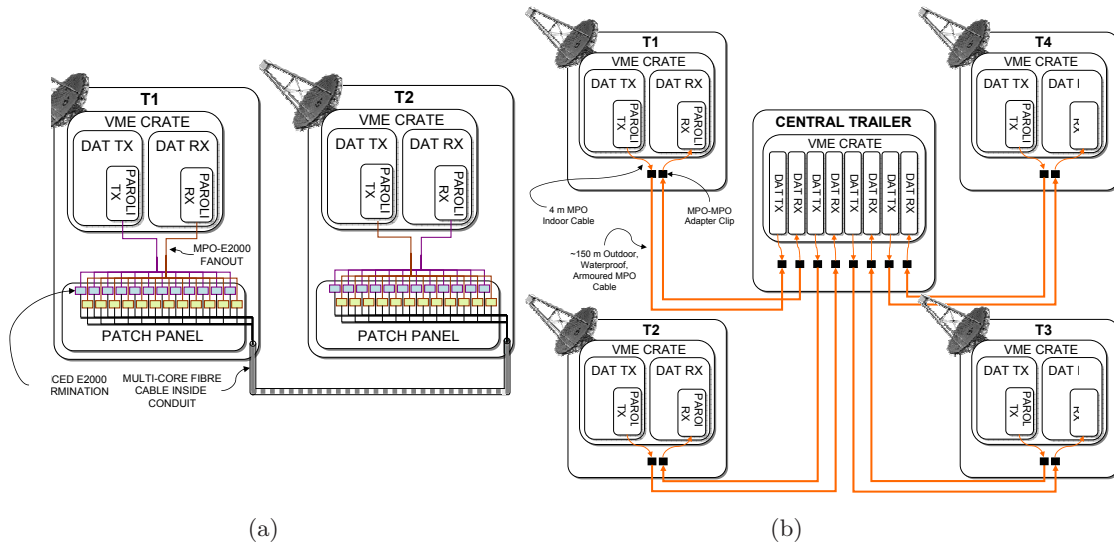


Figure G.1: (a) The DAT connection layout between T1 and T2 using E2000 patch-panels. (b) The alternative solution of using 12 channel MPO ribbon-fibre cables for all four telescopes.

made, armoured, waterproof cable is required<sup>1</sup>, so this option is expensive. Figure G.1(b) shows the four telescope layout for this scenario. To guarantee all channels of the DAT work, and to allow DAT pairs to be moved around the array and be replaced by spares the fibre ribbon-cable proved the only viable option.

In September 2006 150 m pairs of 12 channel MPO terminated fibre ribbon cables were laid between the central trailer and the four telescopes. Additional indoor, 4 m, MPO terminated fibre ribbon cables were installed at either end of the 150 m cables for direct connection to the DATs. These shorter cables, constantly unplugged from the DATs during development work, offer protection against potential damage to the longer, more expensive and difficult to replace, cable.

By March 2007 all DAT-V2 and DAT-V3 pairs were installed and working reliably enough to enable the operation of the VERITAS-4 array.

<sup>1</sup>Any cables laid outside of the telescope trailers must be robust to the temperature cycling (as specified in Section C.2, flooding during the monsoon season, and rodents.

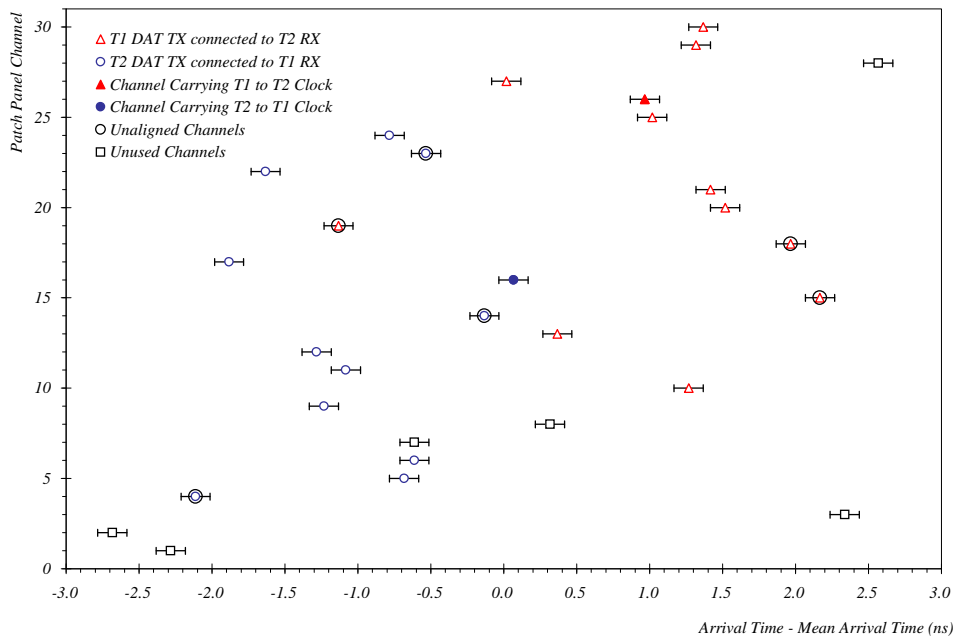


Figure G.2: Skew across the 30 fibres between T1 and T2 after termination in the E2000 patch panels. Here the channels are labelled from 1 (patch-panel top left) to 16 (patch-panel top right) the 17 (patch-panel bottom left) to 30 (patch-panel bottom, third from right), see [176] for details. A range of 5.3 ns is observed.

## G.2 Software for the DAT

Software is required to control and monitor the DAT modules over the FPGA implemented VME interface. Initially VME communication was achieved using a pc and serial port via a VME interface board courtesy of Hytec Electronics Ltd. which sat in the VME crate in place of the CPU controller. The board accepted commands using the VICKY interpreted language developed by Hytec [68]. Once the VME interface was confirmed to be working a standalone program was written in C++ utilising the VME Universe drivers to control the modules. In this scenario the user was asked to enter a slot number containing a DAT and the program read back the device code (0xFF7F) and model ID (0x0921 for Tx and 0x0922 for Rx). The user could then read, clear or set a given bit in the CSR.

The software was adapted to integrate into the VDAQ structure. The VDAQ structure is highly object orientated and relies on daemons running during system start-ups and shuts-downs as well as remote commands from external control software. The class `VDAQ_DAT` contains all the methods required to read and write to the DATs. It uses `VDAQ_Interface` to establish a VME interface and `VDAQ_Module` to create an instance of a generic VME module. `VDAQ_DAT` provides methods specific to the DAT to enable and disable bits in the CSR to, for example, disable the clock, or enable the laser. `VDAQ_DATCrate` creates an instance of `VDAQ_DAT` for every DAT module in a given VME crate, and hence requires a crate ID parameter (crate ID 0 corresponds to the central trailer, then crate ID 1-4 to T1-T4). When an instance of `VDAQ_DATCrate` is created registers at the base addresses within the crate are read to verify the presence of DAT modules. The base address of a given DAT module is not board specific, but rather set geographically by the slot in which it is place according to Eq. 6.1. The veritas data base contains a table of VME crates and DAT slot addresses. `VDAQ_DATCrate` attempts to obtain the slot addresses containing DATs from the data base before reverting to a local configuration file. If neither the data base nor the configuration file is accessible the base-address of every slot in the geographical addressing scheme is scanned, and if `0xFF7F` is returned the slot is assumed to contain a DAT. This option is the most user friendly, but may cause problems with other modules in the VME crate. `VDAQ_DATCrate` provides two methods to automatically initiate and shutdown the DATs. The VDAQ main program then simply calls these two methods at the appropriate time as it does for all other sub-systems, such as the FADC crates. The initialising method resets the CSRs, enables the lasers and sets the transmitter inputs to either IDC header or Lemo on a channel to channel basis. The input settings are stored in the data base. If the settings can not be read from the data base the software will look for a local configuration file, if this is also inaccessible, then the input settings will default to IDC header. The shutdown method simply disables the laser and turns the LEDs off.

Under normal operating conditions when a VME crate is powered up the shutdown procedure will be run as a daemonised process to disable the DAT lasers making the modules safe and extending the lifespan of the PAROLIs. When the VERITAS array control software, used during observing to control the telescope subsystems and monitor data recording, issues a 'start-night' command VDAQ will initiate the DATs in all four

telescopes and the central trailer. Similarly at the close of observing VDAQ will receive an 'end-night' command and shut-down the DAT modules. During development work a utility program, DAT\_Diagnostic provides the user with the ability to change and monitor all CSR bits with a user friendly interface.

# References

- [1] Seasonal weather averages for tucson. <http://www.wunderground.com/Norms> (2006). Accessed August 29, 2006.
- [2] Ageron, M. and ANTARES Collaboration. The ANTARES Optical Beacon System. *ArXiv Astrophysics e-prints*, (2007).
- [3] Agilent Technologies. *Jitter Analysis: The dual-Dirac Model, RJ/DJ, and Q-Scale* (2004).
- [4] Agilent Technologies (now Avago). *Agilent HFBR-772B/BE and HFBR-782B/BE Pluggable Parallel Fiber Optic Modules, Transmitter and Receiver Data Sheet* (2003).
- [5] Aguilar, J. A., et al. First results of the Instrumentation Line for the deep-sea ANTARES neutrino telescope. *Astroparticle Physics*, 26 (2006), 314.
- [6] Aguilar, J. A., et al. The data acquisition system for the ANTARES neutrino telescope. *Nuclear Instruments and Methods in Physics Research A*, 570 (2007), 107.
- [7] Aharonian, F., et al. Is the giant radio galaxy M 87 a TeV gamma-ray emitter? *A&A*, 403 (2003), L1.
- [8] Aharonian, F., et al. Calibration of cameras of the H.E.S.S. detector. *Astroparticle Physics*, 22 (2004), 109.
- [9] Aharonian, F., et al. The Crab Nebula and Pulsar between 500 GeV and 80 TeV: Observations with the HEGRA Stereoscopic Air Cerenkov Telescopes. *ApJ*, 614 (2004), 897.

- [10] Aharonian, F., et al. A New Population of Very High Energy Gamma-Ray Sources in the Milky Way. *Science*, 307 (2005), 1938.
- [11] Aharonian, F., et al. Detection of TeV  $\gamma$ -ray emission from the shell-type supernova remnant RX J0852.0-4622 with HESS. *A&A*, 437 (2005), L7.
- [12] Aharonian, F., et al. A detailed spectral and morphological study of the gamma-ray supernova remnant RX J1713.7-3946 with HESS. *A&A*, 449 (2006), 223.
- [13] Aharonian, F., et al. Observations of the Crab nebula with HESS. *A&A*, 457 (2006), 899.
- [14] Aharonian, F., et al. The H.E.S.S. Survey of the Inner Galaxy in Very High Energy Gamma Rays. *ApJ*, 636 (2006), 777.
- [15] Aharonian, F., et al. First ground-based measurement of atmospheric Cherenkov light from cosmic rays. *Phys. Rev. D*, 75 (2007)(4), 042004.
- [16] Aharonian, F. A. TeV Astrophysics with HESS. *Bulletin of the American Astronomical Society*, 1403 (2005).
- [17] Aharonian, F. A., Konopelko, A. K., Völk, H. J., and Quintana, H. 5@5 - a 5 GeV energy threshold array of imaging atmospheric Cherenkov telescopes at 5 km altitude. *Astroparticle Physics*, 15 (2001), 335.
- [18] Aharonian, F. A., et al. A possible association of the new VHE  $\gamma$ -ray source HESS J1825 137 with the pulsar wind nebula G 18.0 0.7. *A&A*, 442 (2005), L25.
- [19] Amenomori, M., et al. Observation of PeV Gamma Rays from the Monogem Ring with the Tibet Air Shower Array. *ApJ*, 635 (2005), L53.
- [20] Atmel Corporation. *FPGA Configuration EEPROM Memory* (2005).
- [21] Aynutdinov, V., et al. BAIKAL experiment: Main results obtained with the neutrino telescope NT200. *Nuclear Instruments and Methods in Physics Research A*, 567 (2006), 423.
- [22] Baixeras, C. et al. MAGIC Phase II. *29th ICRC* (2005).

- [23] Baro, J. Z. *Characterization of laser diodes for the new Optical Links of the MAGIC II Telescope*. Ph.D. thesis, Universitat Autònoma de Barcelona (2006).
- [24] Barr, M. Programmable logic: What's it to ya? *Embedded Systems Programming*, (1999), 75.
- [25] Bartko, H., et al. Tests of a prototype multiplexed fiber-optic ultra-fast FADC data acquisition system for the MAGIC telescope. *Nuclear Instruments and Methods in Physics Research A*, 548 (2005), 464.
- [26] Bastieri, D., et al. A two-level pattern trigger for the MAGIC telescope. *Nuclear Instruments and Methods in Physics Research A*, 461 (2001), 521.
- [27] Benbow, W. and Hess Collaboration. The Status and Performance of H.E.S.S. Aharonian, F. A., Völk, H. J., and Horns, D., editors, *AIP Conf. Proc. 745: High Energy Gamma-Ray Astronomy*, 611 (2005).
- [28] Berge, D., Funk, S., and Hinton, J. Background modelling in very-high-energy  $\gamma$ -ray astronomy. *A&A*, 466 (2007), 1219.
- [29] Bernlohr, K., Carmona, E., and Schweizer, T. Mc simulation and layout studies for a future cherenkov telescope array. *30th ICRC, Merida, Mexico* (2007).
- [30] Blandford, R. Particle acceleration at astrophysical shocks: A theory of cosmic ray origin. *Physics Reports*, 154 (1987), 1.
- [31] Bogatin, E. and Garat, G. Analysis of board layout helps cure jitter problems. *EDN Magazine*, 5th August (2004).
- [32] Bond, I. H., Hillas, A. M., and Bradbury, S. M. An island method of image cleaning for near threshold events from atmospheric Čerenkov telescopes. *Astroparticle Physics*, 20 (2003), 311.
- [33] Bradbury, S. and Rose, H. Pattern recognition trigger electronics for an imaging atmospheric cherenkov telescope. *Nucl. Instr. & Meth. A*, 481 (2002), 521.
- [34] Brooks, D. Crosstalk, emi, and differential z: Good, bad, or ugly? *Printed Circuit Design*, (2001).

- [35] Buckley, J. H., Dowkontt, P., Kosack, K., and Rebillot, P. F. The VERITAS Flash ADC Electronics System. *28th ICRC*, 2827 (2003).
- [36] Buckwalter, J. F. and Hajimiri, A. Cancellation of crosstalk-induced jitter. *IEEE Journal of Solid State Circuits*, 41 (2006)(3).
- [37] Burr-Brown Products from Texas Instruments. *OPA695 Ultra-Wideband, Current-Feedback Operational Amplifier with Disable, Datasheet* (2004).
- [38] Carlsson, C. and Martinsson, H. Analog Modulation Properties of Oxide Confined VCSELs at Microwave Frequencies. *Journal of Lightwave Technology*, 20 (2002)(9), 1740.
- [39] CAT Collaboration. Observations of the Crab Nebula with the CAT imaging atmospheric Čerenkov telescope. Aharonian, F. A. and Völk, H. J., editors, *American Institute of Physics Conference Series*, volume 558 of *American Institute of Physics Conference Series*, 753 (2001).
- [40] Coarasa, J. A. et al. The Data Acquisition of the MAGIC II Telescope. *ICRC*, volume 3 of *ICRC*, 281–+ (2005).
- [41] Cogan, P. *Nanosecond Sampling of Atmospheric Cherenkov Radiation Applied to TeV Gamma-Ray Observations of Blazars with VERITAS*. Ph.D. thesis, University College Dublin (2007).
- [42] Colin, P., LeBohec, S., and Holder, J. Experimental approaches for 100 TeV gamma-ray astronomy. *ArXiv Astrophysics e-prints*, (2006).
- [43] Cornils, R., et al. Point spread function and long-term stability of the H.E.S.S. reflectors. Aharonian, F. A., Völk, H. J., and Horns, D., editors, *AIP Conf. Proc. 745: High Energy Gamma-Ray Astronomy*, 736 (2005).
- [44] Cortina, J. et al. Technical Performance of the MAGIC Telescope. *ICRC*, 359 (2005).
- [45] Cox, C. H. *Analog Optical Links Theory and Practice*. Cambridge University Press (2004).
- [46] Cronin, J., Gaisser, T. K., and Swordy, S. P. *Sci. America.*, 276 (1997), 44.

- [47] Daum, A., et al. First results on the performance of the HEGRA IACT array. *Astroparticle Physics*, 8 (1997), 1.
- [48] Davies, J. and Cotton, E. *Journal of Solar Energy*, 1 (1957), 16.
- [49] de La Calle, I., et al. Design and performance of analog fiber optic links used on the Whipple 10 meter air Cherenkov telescope. *ICRC*, 2904 (2001).
- [50] de la Calle Perez, I. *Detection of High Energy Gamma-Rays from X-Ray Selected Blazars*. Ph.D. thesis, University of Leeds (2003).
- [51] de Naurois, M., et al. Measurement of the Crab Flux above 60 GeV with the CELESTE Cerenkov Telescope. *ApJ*, 566 (2002), 343.
- [52] de Wit, W. J., et al. The potential for intensity interferometry with gamma-ray telescope arrays. *Proceedings of HTRA, Edinburgh* (2007).
- [53] Dinkespiler, B., et al. Development of an analogue optical link for the front-end read-out of the ATLAS electromagnetic calorimeter. *Nuclear Instruments and Methods in Physics Research A*, 431 (1999), 531.
- [54] Drury, L. An introduction to the theory of diffusive shock acceleration of energetic particles in tenuous plasmas. *Rep. Prog. Phys.*, 46 (1983), 973.
- [55] Duke, C. and Lebohec, S. <http://www.physics.utah.edu/gammaray/grisu/>.
- [56] Enomoto, R., et al. A Search for Sub-TeV Gamma Rays from the Vela Pulsar Region with CANGAROO-III. *ApJ*, 638 (2006), 397.
- [57] Falcone, A. D., et al. STAR: Very Large Aperture Telescope Array Using Many Small IACTs. Aharonian, F. A., Völk, H. J., and Horns, D., editors, *AIP Conf. Proc. 745: High Energy Gamma-Ray Astronomy*, 748 (2005).
- [58] Fegan, S. *A VHE Survey of Unidentified EGRET Sources*. Ph.D. thesis, University of Arizona (2003).
- [59] Fermi, E. On the origin of the cosmic radiation. *Physical Review*, 75 (1949), 1169.
- [60] Fiber Options, I. *Learning About Options in Fiber*. Technical report, 80 Orville Drive, Bohemia, New York (2000).

- [61] Funk, S., et al. The Central Trigger System of the H.E.S.S. Telescope Array. Aharonian, F. A., Völk, H. J., and Horns, D., editors, *AIP Conf. Proc. 745: High Energy Gamma-Ray Astronomy*, 753 (2005).
- [62] Gaisser, T. K. *Cosmic Rays and Particle Physics*. Cambridge University Press (1990).
- [63] Galbraith, W. *Extensive Air Showers*. Butterworths Scientific Publications (1958).
- [64] Galbraith, W. and Jelley, J. *Nature*, 171 (1953), 349.
- [65] Gibbs, K., et al. The VERITAS Atmospheric Cerenkov Telescopes: Positioner, Optics and Associated Components. *28th ICRC*, 2823 (2003).
- [66] Ginzburg, V. L. and Syrovatskii, S. I. *The origin of cosmic rays*. Pergamon Press (1964).
- [67] Goldblatt, K. *The 3.3V Configuration of Spartan-3 FPGAs*. Xilinx, Inc (2005).
- [68] Golding, F. *VIKY A Language for VME Systems*. Hytec Electronics Ltd. (1992).
- [69] Greisen, K. *Rev. Mod. Phys.*, 13 (1956), 240.
- [70] Greisen, K. *Phys. Rev. Lett.*, 16 (1966), 748.
- [71] Gustavsson, J. S. et al. High-speed digital modulation characteristics of oxide-confined vertical-cavity surface-emitting lasers - numerical simulations consistent with experimental results. *IEEE Journal of Quantum Electronics*, 38 (2002)(8), 1089.
- [72] Gustavsson, J. S. et al. Harmonic and Intermodulation Distortion in Oxide-Confined Vertical Cavity Surface Emitting Lasers. *IEEE Journal of Quantum Electronics*, 39 (2003)(8), 941.
- [73] Hajimiri, A., Limotyrakis, S., and Lee, T. H. *IEEE Journal of Solid State Circuits*, 34 (1999)(6).
- [74] Hall, J., et al. Veritas CFDs. *28th ICRC*, 2851 (2003).
- [75] Halzen, F. and Hooper, D. AMANDA Observations Constrain the Ultrahigh Energy Neutrino Flux. *Physical Review Letters*, 97 (2006)(7), 071101.

- [76] Hancock, J. Identifying sources of jitter. *Euro DesignCon* (2004).
- [77] Hanna, D. and Mukherjee, R. The laser calibration system for the space ground-based gamma-ray detector. *Nucl. Instr. & Meth. A*, 482 (2002), 271.
- [78] Hayashida, M. et al. Development of HPDs with an 18-mm-diameter GaAsP photocathode for the MAGIC-II project. *29th ICRC* (2005).
- [79] Hays, E. The Track Imaging Cerenkov Experiment. *AAS/High Energy Astrophysics Division*, volume 9 of *AAS/High Energy Astrophysics Division*, 21.05 (2006).
- [80] Heck, D. et al. *CORSIKA: A Monte Carlo Code to simulate Extensive Air Showers*. Forschungszentrum Karlsruhe (1998).
- [81] Hess, V. Observation of penetrating radiation in seven balloon flights. *Phys. Zeitschr.*, 13 (1912), 1084.
- [82] Hillas, A. M. Angular and energy distributions of charged particles in electron-photon cascades in air. *J. Phys. G: Nucl. Phys.*, 8 (1982), 1461.
- [83] Hillas, A. M. The sensitivity of cerenkov radiation pulses to the longitudinal development of cosmic-ray showers. *J. Phys. G: Nucl. Phys.*, 8 (1982), 1475.
- [84] Hillas, A. M. Cerenkov light images of EAS produced by primary gamma. Jones, F. C., editor, *19th ICRC*, 445 (1985).
- [85] Hillas, A. M. Cosmic Rays: Recent Progress and some Current Questions. *ArXiv Astrophysics e-prints*, (2006).
- [86] Hinton, J. and the Hess Collaboration. The H.E.S.S. View of the Central 200 Parsecs. *Journal of Physics Conference Series*, 54 (2006), 140.
- [87] Hinton, J. A. The status of the HESS project. *New Astronomy Review*, 48 (2004), 331.
- [88] Hoffman, C. M., Sinnis, C., Fleury, P., and Punch, M. Gamma-ray astronomy at high energies. *Rev. Mod. Phys.*, 71 (1999)(4), 897.
- [89] Holder, J. Exploiting VERITAS Timing Information. *29th ICRC*, 383 (2005).

- [90] Holder, J. Status and Performance of the First VERITAS telescope. *29th ICRC*, 379 (2005).
- [91] Holder, J., et al. The first VERITAS telescope. *Astroparticle Physics*, 25 (2006), 391.
- [92] Honeywell. *HFE4080-321/XBA VCSEL Datasheet* (1998).
- [93] Horns, D. Ground-based gamma-ray observations with H.E.S.S.: status and future. *Ground-based and Airborne Telescopes. Edited by Stepp, Larry M.. Proceedings of the SPIE, Volume 6267, pp. 62670H (2006).* (2006).
- [94] Humensky, T. B. et al. Calibration of VERITAS Telescope 1 via Muons. *ArXiv Astrophysics e-prints*, (2005)(astro-ph/0507449).
- [95] Hunter, S. D., et al. EGRET Observations of the Diffuse Gamma-Ray Emission from the Galactic Plane. *ApJ*, 481 (1997), 205.
- [96] Infineon Technologies. *PAROLI 2 Preliminary Data Sheet* (2003).
- [97] Itoh, C., et al. Detection of diffuse TeV gamma-ray emission from the nearby starburst galaxy NGC 253. *A&A*, 396 (2002), L1.
- [98] Jelley, J. V. *Čerenkov Radiation and its applications*. Pergamon Press (1958).
- [99] Kabuki, S. and Cangaroo Collaboration. Performance of the Atmospheric Cherenkov Imaging Camera for the CANGAROO-III Experiment. (2003), 2859.
- [100] Karg, T. and et al. Sensitivity estimates for an underwater acoustic neutrino telescope. *ICRC*, 195 (2005).
- [101] Karle, A. Status of IceCube in 2005. *Nuclear Instruments and Methods in Physics Research A*, 567 (2006), 438.
- [102] Kieda, D., Swordy, S. P., Wakely, S. P., and Virshup, A. High resolution charge measurements of UH cosmic ray nuclei using a direct imaging Cherenkov ground-based observatory. Gorham, P. W., editor, *Particle Astrophysics Instrumentation. Edited by Peter W. Gorham. Proceedings of the SPIE, Volume 4858, pp. 338-346 (2003).*, volume 4858 of *Presented at the Society of Photo-Optical Instrumentation Engineers (SPIE) Conference*, 338 (2003).

- [103] Kieda, D. B., Swordy, S. P., and Wakely, S. P. A high resolution method for measuring cosmic ray composition beyond 10 TeV. *Astroparticle Physics*, 15 (2001), 287.
- [104] Kieda, D. B., Swordy, S. P., and Wakely, S. P. Exotic PeV particle detection using Direct Cerenkov Light. *ICRC*, volume 4 of *ICRC*, 1533 (2001).
- [105] Kieda, D. B., et al. Calibration Systems for the VERITAS Observatory. *ICRC*, 2831 (2003).
- [106] Kieda, D. B., et al. Signal Cable Selection for the VERITAS Observatory. *28th ICRC*, 2835 (2003).
- [107] Koyama, K., et al. 378 (1995), 255.
- [108] Kravchenko, I., et al. RICE limits on the diffuse ultrahigh energy neutrino flux. *Physical Review D.*, 73 (2006)(8), 082002.
- [109] Kubo, H., et al. Status of the CANGAROO-III project. *New Astronomy Review*, 48 (2004), 323.
- [110] Kuch, S. Simulation for KM3NeT using ANTARES-software. *Nuclear Instruments and Methods in Physics Research A*, 567 (2006), 498.
- [111] Le Bohec, S. and Sleege, G. Design of the preamplifier for veritas, internal note (2004).
- [112] Lessard, R. W., Buckley, J. H., Connaughton, V., and Le Bohec, S. A new analysis method for reconstructing the arrival direction of TeV gamma rays using a single imaging atmospheric Cherenkov telescope. *Astroparticle Physics*, 15 (2001), 1.
- [113] Li, T.-P. and Ma, Y.-Q. Analysis methods for results in gamma-ray astronomy. *ApJ*, 272 (1983), 317.
- [114] Lin, S. Misalignment tolerance analysis of combined thick convex lens and lensed fiber scheme between vertical-cavity surface-emission lasers and single-model fibers. 43 (2004)(9), 2087.
- [115] Longair, M. S. *High energy astrophysics. Vol. 1 Particles, photons and their detection*. Cambridge University Press, 2nd edition (1992).

- [116] Lorenz, E. Status of the 17 m MAGIC telescope. *New Astronomy Review*, 48 (2004), 339.
- [117] Lorenz, E., Maier, R., Tran, T. S., and Weissbach, P. A fast, large dynamic range analog signal transfer system based on optical fibers. *Nuclear Instruments and Methods in Physics Research A*, 461 (2001), 517.
- [118] Lozano-Bahilo, J., Rudge, A., and Zsenei, A. A linear optical link using radiation hard VCSELs. *Nuclear Instruments and Methods in Physics Research A*, 461 (2001), 530.
- [119] Lucarelli, F., et al. Observations of the Crab Nebula with the HEGRA system of IACTs in convergent mode using a topological trigger. *Astroparticle Physics*, 19 (2003), 339.
- [120] MAGIC Collaboration. VHE Gamma-Ray Observation of the Crab Nebula and Pulsar with MAGIC. *ArXiv e-prints*, 705 (2007).
- [121] Maier, G. and et al. Monte Carlo studies of possible upgrades of current arrays of imaging Cherenkov telescopes. *29th ICRC*, 391 (2005).
- [122] Maier, G. and Knapp, J. Cosmic-Ray Events as Background in Imaging Atmospheric Cherenkov Telescopes. *ArXiv e-prints*, 704 (2007).
- [123] Mannheim, K. The proton blazar. *A&A*, 269 (1993), 67.
- [124] Marshall, P. *Hytec VME DAT RX 2338: 12 Channel LVDS/Optical Data Receiver Module, Technical Manual and Circuit Description*. Hytec Electronics Ltd (2004).
- [125] Marshall, P. *Hytec VME DAT TX 2337: 12 Channel LVDS/Optical Data Transmitter Module, Technical Manual and Circuit Description*. Hytec Electronics Ltd (2004).
- [126] Maxim. *HFTA-05.0: Statistical Confidence Levels for Estimating BER Probability* (2000).
- [127] Maxim High-Frequency/Fiber Communications Group. *MAX3735A Laser Driver Output Configurations, Part 4: Driving VCSELs Design Note: HFDN-26.3* (2004).

- [128] Maxim Integrated Products, 120 San Gabriel Drive, Sunnydale, CA. *Maxim MAX3740A 3.2Gbps SFP VCSEL Driver with Diagnostic Monitors Datasheet* (2004).
- [129] Maxim Integrated Products, 120 San Gabriel Drive, Sunnydale, CA. *Maxim DS1859 Dual, Temperature-Controlled Resistors with Internally Calibrated Monitors Datasheet* (2006).
- [130] Merck, M. H., Lorenz, E., and Mirzoyan, R. MAGIC 2: an ultimate imaging Cherenkov telescope. Gorham, P. W., editor, *Particle Astrophysics Instrumentation. Edited by Peter W. Gorham. Proceedings of the SPIE, Volume 4858, pp. 327-337 (2003).*, 327 (2003).
- [131] Meucci, M., et al. The trigger system of the MAGIC telescope: on-line selection strategies for Cherenkov telescopes. *Nuclear Instruments and Methods in Physics Research A*, 518 (2004), 554.
- [132] Mirzoyan, R. et al. Technical Innovations for the MAGIC Project. *28th ICRC*, 2963 (2003).
- [133] Mitel Semiconductor. *1A354 High-Performance PIN Photodiode Datasheet* (2004).
- [134] Nagai, T. *Search for TeV gamma-ray emission from nearby starburst galaxies*. Ph.D. thesis, The University of Utah, United States – Utah (2005).
- [135] Nagesh Gupta, M. G. *Creating High-Speed Memory Interfaces with Virtex-II and Virtex-II Pro FPGAs*. Xilinx, Inc (2004).
- [136] OECA. *ZL60052 VCSEL Datasheet* (2004).
- [137] OECA. *ZL60002 VCSEL Preliminary Datasheet* (2005).
- [138] ON Semiconductor Components Industries, LLC. *MC10EP90, MC100EP90: -3.3V / -5V Triple ECL Input to LVPECL/PECL Output Translator* (2004).
- [139] ON Semiconductor Components Industries, LLC. *MC100EL91: 5 V Triple PECL Input to 5 V ECL Output Translator* (2005).
- [140] Palais, J. C. *Fiber Optic Communications*. Prentice Hall (1998).

- [141] Paneque, D. *The MAGIC Telescope: development of new technologies and first observations*. Ph.D. thesis, Max-Planck-Institut für Physik (2004).
- [142] Paneque, D. et al. Analogue signal transmission by an optical fiber system for the camera of the MAGIC telescope. *28th ICRC*, 2927 (2003).
- [143] Paneque, D. et al. A method to enhance the sensitivity of photomultipliers for air cherenkov telescopes by applying a lacquer that scatters light. *Nuclear Instruments and Methods in Physics Research A*, 518 (2004), 619.
- [144] Pedroni, V. A. *Circuit Design with VHDL*. MIT Press (2004).
- [145] Pepeljugoski, P., Abbott, J., and Tatum, J. Effect of launch conditions on power penalties in gigabit links using 62.5  $\mu\text{m}$  core fibers operating at short wavelength. *NIST Symposium on Fiber Optic Measurements*. Boulder, CO (1998).
- [146] Picolight. *12 x 0.5-2.5 Gbps Parallel Optical Receiver Data Sheet* (2006).
- [147] Picolight. *12 x 0.5-2.5 Gbps Parallel Optical Transmitter Datasheet* (2006).
- [148] Pragasam, R. *Spartan FPGAs The Gate Array Solution*. Xilinx, Inc (2001).
- [149] Pühlhofer, G., et al. The technical performance of the HEGRA system of imaging air Cherenkov telescopes. *Astroparticle Physics*, 20 (2003), 267.
- [150] Punch, M., et al. Detection of TeV photons from the active galaxy Markarian 421. *Nature*, 358 (1992), 477.
- [151] Quinn, J., et al. Detection of Gamma Rays with  $E_{\gamma} > 300$  GeV from Markarian 501. *ApJ*, 456 (1996), L83.
- [152] Rissons, A., Perchoux, J., Mollier, J.-C., and Grabherr, M. Noise and signal modeling of various VCSEL structures. Lei, C., Choquette, K. D., and Kilcoyne, S. P., editors, *Vertical-Cavity Surface-Emitting Lasers VIII*. Edited by Lei, Chun; Choquette, Kent D.; Kilcoyne, Sean P. *Proceedings of the SPIE, Volume 5364*, pp. 80-91 (2004)., volume 5364 of *Presented at the Society of Photo-Optical Instrumentation Engineers (SPIE) Conference*, 80 (2004).
- [153] Roberts, A. The birth of high-energy neutrino astronomy: A personal history of the DUMAND project. *Reviews of Modern Physics*, 64 (1992), 259.

- [154] Roberts, M. D. et al. Auger GAP note, GAP-2003-010. <http://www.auger.org>, (2003).
- [155] Rose, J., et al. Fast analog signal transmission for an air Cherenkov photomultiplier camera using optical fibers. *Nuclear Instruments and Methods in Physics Research A*, 442 (2000), 113.
- [156] Rossi, B. *High Energy Particles*. Prentice-Hall (1952).
- [157] Rossi, B. and Greisen, K. *Rev. Mod. Phys.*, 13 (1941), 240.
- [158] Rott, C. and for the IceCube Collaboration. IceCube: Performance, Status, and Future. *ArXiv Astrophysics e-prints*, (2006).
- [159] Sawyer, N. *Data to Clock Phase Alignment*. Xilinx, Inc (2002).
- [160] Shepherd, N. et al. Absolute calibration of imaging atmospheric Cherenkov telescopes. *29th ICRC*, 427 (2005).
- [161] Sinnis, G. et al. *Nucl. Phys. B (Proc. Suppl.)*, 43 (1995), 141.
- [162] Spurio, M. and for the ANTARES Collaboration. Status report (2006) of the ANTARES project. *ArXiv High Energy Physics - Phenomenology e-prints*, (2006).
- [163] Sreekumar, P., et al. EGRET Observations of the Extragalactic Gamma-Ray Emission. *ApJ*, 494 (1998), 523.
- [164] STACEE Collaboration: D. M. Gingrich, et al. The STACEE Ground-Based Gamma-Ray Detector. *ArXiv Astrophysics e-prints*, (2005).
- [165] Stamerra, A., et al. The Trigger System of the MAGIC Telescope: On-Line Selection Strategies for Cherenkov Telescopes. *ICRC*, volume 5 of *ICRC*, 2959–+ (2003).
- [166] Stenger, V. J. DUMAND: progress and status. Schneps, J., Kafka, T., Mann, W. A., and Nath, P., editors, *Neutrino Physics and Astrophysics*, 344 (1988).
- [167] Tan, C., Stern, M., and Bhargava, V. Vertical Cavity Surface Emission Laser Focusing using a Miniature Precision Molded Plastic Lens. *Opt. Eng.*, 43 (2004)(10), 2478.

- [168] Tapp, S. *Configuration Quickstart Guidelines*. Xilinx, Inc (2003).
- [169] Vacanti, G., et al. Muon ring images with an atmospheric Čerenkov telescope. *Astroparticle Physics*, 2 (1994), 1.
- [170] Wakely, S. P. and VERITAS Collaboration. The VERITAS Prototype. *28th ICRC*, 2803 (2003).
- [171] Walker, T. P. Making the Most of Supernova 1987A. *Nature*, 330 (1987), 609.
- [172] Weekes, T. C. and Turver, K. E. Gamma-ray astronomy from 10-100 GeV: A new approach. Wills, R. D. and Battrick, B., editors, *ESA SP-124: Recent Advances in Gamma-Ray Astronomy*, 279 (1977).
- [173] Weekes, T. C., et al. Observation of TeV gamma rays from the Crab nebula using the atmospheric Čerenkov imaging technique. *ApJ*, 342 (1989), 379.
- [174] Weekes, T. C., et al. VERITAS: the Very Energetic Radiation Imaging Telescope Array System. *Astroparticle Physics*, 17 (2002), 221.
- [175] Weinstein, A. et al. The veritas trigger system. *30th ICRC, Merida, Mexico* (2007).
- [176] White, R. Summary of on site work completed on the dats (2006).
- [177] White, R. and Kieda, D. Cable splicing. private communication (2006).
- [178] White, R. and Marshall, P. Dat power consumption. private communication (2006).
- [179] White, R. J. Simulated rise time of the veritas 12 m reflector. *AIP Conf. Proc. 745: High Energy Gamma-Ray Astronomy*, 797 (2005).
- [180] White, R. J., Rose, H. J., Bradbury, S. M., and Marshall, P. Parallel distribution of asynchronous optical signals. *Nuclear Instruments and Methods in Physics Research A*, 577 (2007), 708.
- [181] Wilkes, R. J. and et al. DUMAND-II Progress Report. Jones, L., editor, *AIP Conf. Proc. 276: Very High Energy Cosmic-Ray Interactions*, 636 (1993).

- [182] Williams, W. S. C. *Nuclear and Particle Physics*, 247–253. Clarendon Press (1991).
- [183] Wood, M. *Interfacing LVPECL 3.3V Drivers With Xilinx 2.5V Differential Receivers*. Xilinx, Inc (2005).
- [184] Xilinx, Inc. *Spartan and Spartan-XL Families Field Programmable Gate Arrays: Complete Data Sheet* (2002).
- [185] Xilinx, Inc. *Using Digital Clock Managers (DCMs) in Spartan-3 FPGAs* (2003).
- [186] Xilinx, Inc. *Using Embedded Multipliers in Spartan-3 FPGAs* (2003).
- [187] Xilinx, Inc. *Using the ISE Design Tools for Spartan-3 FPGAs* (2003).
- [188] Xilinx, Inc. *644-MHz SDR LVDS Transmitter/Receiver* (2004).
- [189] Xilinx, Inc. *Spartan-II 2.5V FPGA Family: Complete Data Sheet* (2004).
- [190] Xilinx, Inc. *Xilinx In-System Programming Using an Embedded Microcontroller* (2004).
- [191] Xilinx, Inc. *High-Speed Clock Architecture for DDR Designs Using Local Inversion* (2005).
- [192] Xilinx, Inc. *Using Block RAM in Spartan-3 Generation FPGAs* (2005).
- [193] Xilinx, Inc. *Using Look-Up Tables as Distributed RAM in Spartan-3 Generation FPGAs* (2005).
- [194] Xilinx, Inc. *Using Look-Up Tables as Shift Registers (SRL16) in Spartan-3 Generation FPGAs* (2005).
- [195] Xilinx, Inc. *Spartan-3 FPGA Family: Complete Data Sheet* (2006).
- [196] Zarlink. *ZL60101/2 12 x 2.7 Gbps Parallel Fiber Optic Link Transmitter and Receiver Data Sheet* (2004).
- [197] Zatsepin, G. and Kuzmin, V. *JETP Lett.*, 4 (1966), 78.
- [198] Zivny, P. *Tektronix CSA/TDS8200 Jitter Analysis Application: Jitter and Noise Analysis, BER Estimation Descriptions*. Tektronix, Inc. (2005).

- [199] Zweerink, J., et al. Solar Two Gamma-Ray Observatory: a high-sensitivity telescope for intermediate high-energy gamma-ray astronomy. Siegmund, O. H. and Flanagan, K. A., editors, *Proc. SPIE Vol. 3765, p. 524-529, EUV, X-Ray, and Gamma-Ray Instrumentation for Astronomy X*, Oswald H. Siegmund; Kathryn A. Flanagan; Eds., 524 (1999).